

Published by Empress Catherine II
Saint Petersburg Mining University

SINCE 1907

E-ISSN 2541-9404
ISSN 2411-3336

JOURNAL OF MINING INSTITUTE

ZAPISKI GORNOGO INSTITUTA

SCIENTIFIC JOURNAL



Volume 271

N1 • 2025

INDEXING IN
SCOPUS (Q1)
WEB OF SCIENCE (ESCI)

WWW.PMI.SPMI.RU



The scientific periodical “Journal of Mining Institute” is published since 1907 by Empress Catherine II Saint Petersburg Mining University – the first higher technical educational institution in Russia, founded in 1773 by the decree of Catherine II as the embodiment of the ideas of Peter I and M.V. Lomonosov on the training of engineers for the development of mining business.

The International Competence Center for Mining Engineering Education under the auspices of UNESCO operates on the basis of Empress Catherine II Saint Petersburg Mining University and contributes to active interaction of the Journal with the international scientific community.

The purpose of the Journal is to create an information space in which Russian and foreign scientists can present results of their theoretical and empirical research on the problems of the mining sector.

Published articles cover the issues of geology, geotechnical engineering and engineering geology, mining and petroleum engineering, mineral processing, energy, geoecology and life safety, economics of raw materials industries.

The Journal is indexed by Scopus (Q1), Web of Science Core Collection (ESCI), DOAJ Seal, RSCI, GeoRef, Google Scholar, RSCI. It is included in the White list of the Ministry of Education and Science of the Russian Federation.

The Journal is published six times a year. The average first decision time is one month.

Articles are published free of charge. Translation is provided by the author.

The cover shows an exhibit of the Mining Museum – a core with fauna – a cephalopod mollusk (*Cephalopoda*), a bivalve mollusk (*Bivalvia*) from the Lower Pechora. Collections by L.A. Popugaeva, a pioneer of primary diamond deposits in the USSR. Nenets expedition, Naryan-Mar.

The Mining Museum is the world's third largest natural-science exposition, it contains more than 230 thousand exhibits, including precious metals and stones, unique collections of minerals, ores, rocks, paleontological remains, meteorites, a collection of models and prototypes of mining equipment, pieces of stone-cutting and jewelry art.



Journal founder: Empress Catherine II Saint Petersburg Mining University

CHIEF EDITOR

V.S.Litvinenko, Doctor of Engineering Sciences, Professor, Member of the International Academy of Higher Education, RANS, RAHS, MANEB, Rector (Empress Catherine II Saint Petersburg Mining University, Saint Petersburg, Russia)

DEPUTY CHIEF EDITOR

S.G.Skublov, Doctor of Geological and Mineralogical Sciences, Professor, Member of the Russian Mineralogical Society, Expert of the RSF and RAS (Empress Catherine II Saint Petersburg Mining University, Saint Petersburg, Russia)

EXECUTIVE SECRETARY

S.V.Sinyavina, Candidate of Engineering Sciences, Director of the Publishing House (Empress Catherine II Saint Petersburg Mining University, Saint Petersburg, Russia)

EDITORIAL TEAM

O.Ye.Aksyutin, Doctor of Engineering Sciences, Corresponding Member of the RAS, Board Member, Head of Department (PAO Gazprom, Moscow, Russia)

A.A.Baryakh, Doctor of Engineering Sciences, Professor, Member of the RAS, Director (Perm Federal Research Center Ural Branch RAS, Perm, Russia)

V.N.Brichkin, Doctor of Engineering Sciences, Professor, Vice Rector for Scientific Personnel Training (Empress Catherine II Saint Petersburg Mining University, Saint Petersburg, Russia)

S.G.Gendler, Doctor of Engineering Sciences, Professor, Member of the RANS, Head of Department of Occupational Safety (Empress Catherine II Saint Petersburg Mining University, Saint Petersburg, Russia)

O.M.Ermilov, Doctor of Engineering Sciences, Professor, Member of the RAS, RAHS, Deputy Engineer-in-Chief of Science Programmes (OOO Gazprom Development Nadym, Nadym, Russia)

V.P.Zubov, Doctor of Engineering Sciences, Professor, Head of Department of Underground Mining (Empress Catherine II Saint Petersburg Mining University, Saint Petersburg, Russia)

G.B.Kleiner, Doctor of Economics, Professor, Corresponding Member of the RAS, Deputy Director (Central Research Institute of Economics and Mathematics of the RAS, Moscow, Russia)

A.V.Kozlov, Doctor of Geological and Mineralogical Sciences, Member of the Russian Mineralogical Society, Head of Department of Geology and Exploration of Mineral Deposits (Empress Catherine II Saint Petersburg Mining University, Saint Petersburg, Russia)

Yu.B.Marin, Doctor of Geological and Mineralogical Sciences, Professor, Corresponding Member of the RAS, Honorary President (Russian Mineralogical Society, Saint Petersburg, Russia)

V.A.Morenov, Candidate of Engineering Sciences, Associate Professor (Empress Catherine II Saint Petersburg Mining University, Saint Petersburg, Russia)

M.A.Pashkevich, Doctor of Engineering Sciences, Professor, Head of Department of Geoecology (Empress Catherine II Saint Petersburg Mining University, Saint Petersburg, Russia)

T.V.Ponomarenko, Doctor of Economics, Professor (Empress Catherine II Saint Petersburg Mining University, Saint Petersburg, Russia)

O.M.Prishchepa, Doctor of Geological and Mineralogical Sciences, Member of the RANS, Head of Department of Geology of Oil and Gas (Empress Catherine II Saint Petersburg Mining University, Saint Petersburg, Russia)

A.G.Protosenya, Doctor of Engineering Sciences, Professor, Head of Department of Construction of Mining Enterprises and Underground Structures (Empress Catherine II Saint Petersburg Mining University, Saint Petersburg, Russia)

V.E.Somov, Doctor of Economics, Candidate of Engineering Sciences, Member of the RANS, Director (OOO Kinef, Kirishi, Russia)

A.A.Tronin, Doctor of Geological and Mineralogical Sciences, Director (Saint Petersburg Scientific-Research Centre for Ecological Safety RAS, Saint Petersburg, Russia)

V.L.Trushko, Doctor of Engineering Sciences, Professor, Member of the International Higher Education Academy of Sciences, RANS, RAHS, MANEB, Head of Department of Mechanics (Empress Catherine II Saint Petersburg Mining University, Saint Petersburg, Russia)

P.S.Tsvetkov, Candidate of Economics, Associate Professor (Empress Catherine II Saint Petersburg Mining University, Saint Petersburg, Russia)

A.E.Cherepovitsyn, Doctor of Economics, Professor, Head of Department of Economics, Organization and Management (Empress Catherine II Saint Petersburg Mining University, Saint Petersburg, Russia)

Ya.E.Shklyarskii, Doctor of Engineering Sciences, Professor, Head of the Department of General Electric Engineering (Empress Catherine II Saint Petersburg Mining University, Saint Petersburg, Russia)

Oleg Antzutkin, Professor (University of Technology, Lulea, Sweden)

Gabriel Weiss, Doctor of Sciences, Professor, Pro-Rector for Science and Research (Technical University, Kosice, Slovakia)

Hal Gurgenci, Professor (School of Mining Machine-Building in University of Queensland, Brisbane, Australia)

Edwin Kroke, Doctor of Sciences, Professor (Institute of Inorganic Chemistry in Freiberg Mining Academy, Freiberg, Germany)

Zhou Fubao, Doctor of Sciences, Professor, Vice President (China University of Mining and Technology, Beijing, PR China)

Zhao Yuemin, Doctor of Sciences, Professor, Director of Academic Committee (China University of Mining and Technology, Beijing, PR China)

Sections

• Geology • Geotechnical Engineering and Engineering Geology • Economic Geology • Energy

Registration Certificate PI N FS77-70453 dated 20.07.2017

PH License N 06517 dated 09.01.02

Editorial staff: Head of the Editorial Center V.L.Lebedev; Editors: E.S.Dribinskaya, M.G.Khachirova, L.V.Nabieva, A.I.Yakovleva

Computer Design: N.N.Sedykh, V.I.Kashirina, E.A.Golovinskaya

© Empress Catherine II Saint Petersburg Mining University, 2025

Passed for printing 25.02.2025. Format 60 × 84/8. Academic Publishing Division 41.

Circulation: 300 copies. Order 65. Printed by RIC of Empress Catherine II Saint Petersburg Mining University. Free sale price.

Mailing address of the Journal Founder and the Editorial Board

21st Linia V.O., N 2, St. Petersburg, Russia, 199106

Phone: +7 (812) 328-8416; Fax +7 (812) 327-7359;

E-mail: pmi@spmi.ru

Journal website: pmi.spmi.ru



CONTENTS

Mariya V. Chudakova, Kirill A. Ovchinnikov, Dmitrii N. Ulyanov, Anisa M. Kunakova, Liniza R. Saifutdinova, Andrei A. Pimenov, Anton L. Maximov. Carbon dioxide corrosion inhibitors: current state of research and development.....	3
Dmitrii V. Kuznetsov, Sergei Yu. Stepanov, Andrei V. Butnyakov, Viktoriya S. Igosheva. Lamprophyres of the Peshchernoe gold deposit, their geological position, material composition, and metasomatic alterations (Northern Urals)	22
Yurii A. Kashnikov, Denis V. Shustov, Sergei Yu. Yakimov. Consideration of the geomechanical state of a fractured porous reservoir in reservoir simulation modelling	42
Mariya A. Chukaeva, Tatyana V. Sapelko. Assessment of the ecological state of aquatic ecosystems by studying lake bottom sediments	53
Andrei A. Abrosimov. Study of wormhole channel formation resulting from hydrochloric acid treatment in complex-type reservoirs using filtration and X-ray computed tomography methods	63
Elena E. Kameneva, Viktoriya S. Nikiforova. Study of the pore structure in granite and gabbrodolerite crushed stone grains of various sizes.....	74
Tatiana V. Minnikova, Sergey I. Kolesnikov. Environmental assessment of biochar application for remediation of oil-contaminated soils under various economic uses	84
Mikhail Ya. Bryn, Murat G. Mustafin, Dinara R. Bashirova, Bogdan Yu. Vasilev. Investigation of the accuracy of constructing digital elevation models of technogenic massifs based on satellite coordinate determinations.....	95
Viktoriya V. Lisai, Yurii D. Smirnov, Andrei V. Ivanov, Gabriel Borowski. Investigation of the effectiveness of the use of various substances for dust suppression during the transshipment of granular sulfur.....	108
Bui Thi Hong Tham, Phi Truong Thanh. Crustal movement model in the ITRF2020 – a case study in Northern Vietnam	120
Nadezhda L. Aluker, Boris P. Aduiev, Denis R. Nurmukhametov. Radiation characteristics of coals at different stages of metamorphism.....	131
Andrei M. Bramm, Stanislav A. Eroshenko. Evaluation of the impact of the distance determination function on the results of optimization of the geographical placement of renewable energy sources-based generation using a metaheuristic algorithm.....	141
Pavel V. Matrenin, Alina I. Stepanova. Enhancing the interpretability of electricity consumption forecasting models for mining enterprises using SHapley Additive exPlanations	154
Aleksandra A. Volchikhina, Mariya A. Vasilyeva. Development of equipment and improvement of technology for inertial thickening of backfill hydraulic mixtures at the final stages of transportation	168
Tatyana E. Litvinova, Stepan A. Gerashev. Behaviour of cerium (III) phosphate in a carbonate-alkaline medium	181



Carbon dioxide corrosion inhibitors: current state of research and development

Mariya V. Chudakova^{1,2}✉, Kirill A. Ovchinnikov³, Dmitrii N. Ulyanov¹, Anisa M. Kunakova⁴,
Liniza R. Saifutdinova⁵, Andrei A. Pimenov⁶, Anton L. Maximov²

¹ PAO Gazprom Neft, Saint Petersburg, Russia

² A.V. Topchiev Institute of Petrochemical Synthesis, RAS, Moscow, Russia

³ Peoples's Friendship University of Russia named after Patrice Lumumba, Moscow, Russia

⁴ Gazprom Neft Scientific and Technical Center, Saint Petersburg, Russia

⁵ GCSS Neftepromhim LLC, Kazan, Republic of Tatarstan, Russia

⁶ Tatar Oil Research and Design Institute (TatNIPIneft) of PJSC TATNEFT, Almeteyevsk, Republic of Tatarstan, Russia

How to cite this article: Chudakova M.V., Ovchinnikov K.A., Ulyanov D.N., Kunakova A.M., Saifutdinova L.R., Pimenov A.A., Maximov A.L. Carbon dioxide corrosion inhibitors: current state of research and development. *Journal of Mining Institute*. 2025. Vol. 271. N 15984, p. 3-21.

Abstract

Among the methods of corrosion control in the oil and gas production industry the leading place belongs to inhibitor protection, since there is no need for technological and technical changes in the existing equipment. The combination of high variability of inhibitor composition with changing conditions of its application and low capital investments makes it an indispensable reagent at oil and gas fields. The main classes of compounds used as active bases of carbonic acid corrosion inhibitors for the protection of oil and gas equipment are described. Classical organic active bases containing heteroatoms (oxygen, sulfur, nitrogen) are examined. Special attention was paid to alkylimidazolines and other nitrogen-containing compounds as the most frequently used as active bases of carbonic acid corrosion inhibitors in Russia and abroad. A wide range of possibilities to achieve the desired properties of corrosion inhibitors by varying the substitutes has been demonstrated. Nowadays, in addition to the traditional requirements for corrosion inhibitors, their safety for the environment is equally important. The information on prospective research and development aimed at improving the environmental characteristics of the reagents used is given. Plant extracts, synthetic and biological polymers involved in traditional corrosion inhibitors or used as new independent compounds are considered. It is shown that the effectiveness of corrosion inhibitors significantly depends on the pH of the medium, temperature, partial pressure of CO₂, flow rate, and other factors.

Keywords

corrosion inhibitor; carbonic acid corrosion; imidazoline; CO₂; green inhibitors; plant inhibitors; polymeric inhibitors; synthetic polymers; biopolymers

Received: 30.09.2022

Accepted: 07.11.2024

Online: 25.02.2025

Published: 25.02.2025

Introduction

Oil and gas industry equipment is subject to aggressive influence of the external environment. One of the main factors of accidents (up to 80 %) and failure of oilfield equipment is corrosion of external and internal pipe walls. When the metal surface is in contact with a medium (a mixture of liquid and gaseous hydrocarbons), the corrosion process is significantly accelerated in the presence of hydrogen sulfide, carbon dioxide, water, oxygen, and mechanical impurities [1].

Factors having maximum influence on the mechanism and intensity of corrosion of field oil and gas pipelines [2, 3]: high water content of transported products; high content of corrosive-aggressive gases (carbon dioxide and/or hydrogen sulfide); high temperature of transported products; high content of mechanical impurities.

Previously, carbon dioxide was not considered as an active corrosive agent; hydrogen sulfide and oxygen posed a significant threat. However, the situation has changed dramatically with the



development of deep-lying seam. The simultaneous presence of bicarbonate and carbonate ions in the aqueous phase causes carbonic acid corrosion, which leads to failure of oil and gas field equipment. [4]. The simultaneous presence of bicarbonate and carbonate ions in the aqueous phase causes carbonic acid corrosion, which leads to failure of oil and gas field equipment [2]. At 25-35 % content of the water phase in the oil-water mixture, the surface of steel equipment is wetted by water, which causes corrosion stimulated by CO₂ dissolved in the mixture [5]. The rate of corrosion damage is 3-4 mm/year and in some cases reaches 6-8 mm/year. When predicting corrosion rates, it should be assumed that the carbon dioxide content in the aqueous phase is closely related to the partial pressure of carbon dioxide ($p\text{CO}_2 > 0.2$ MPa – severe corrosion, $p\text{CO}_2 = 0.02-0.2$ MPa – moderate, $p\text{CO}_2 < 0.02$ MPa – insignificant [6]), and the partial pressure is temperature dependent [7].

One solution to the environmental problem of carbon dioxide emission and decarbonization of the industrial sector is the use of carbon capture, utilization and storage (CCUS) technology. However, carbon dioxide corrosion is a serious problem that has hindered the widespread development and application of this technology [8, 9].

Three temperature areas can be distinguished in the carbon dioxide corrosion process [10]:

- low temperature area (below 60 °C) – corrosion is mostly uniform and its rate increases with increasing temperature; small amounts of FeCO₃ are formed on the metal surface;
- medium temperature area (about 100 °C) – the formed iron carbonate film is uneven in thickness; local corrosion intensifies, the rate of which reaches a maximum;
- high temperature area (above 150 °C) – corrosion rate decreases (by an order of magnitude or more) due to the formation of a dense coating of iron oxide (Fe₃O₄) with high adhesion.

Carbon dioxide can cause both uniform and more dangerous localized (moss-like and meso-like pitting) corrosion of steel. In the process of localized corrosion, an irregular and/or unstable protective film of corrosion products is formed on the metal surface (FeCO₃, Fe₃O₄, etc.).

Methods of corrosion control in the oil industry:

- technological methods of protection, i.e. creation and maintenance of corrosion-safe conditions of equipment operation;
- use of corrosion-resistant/non-metallic materials [11];
- application of corrosion inhibitors (CI);
- use of protective coatings.

Among the listed methods of corrosion control in the oil and gas production industry in Russia and abroad, the leading place is currently occupied by inhibitor protection, as it does not require significant capital investments and a serious restructuring of the technology of oil production, gathering and treatment [10]. CI are fast acting and cost effective, so no field containing aggressive components is operated without the use of corrosion inhibitor protection. The advantage of this method is its simplicity and cost-effectiveness, possibility to use it both on new and operated wells, which allows in the process of field development to easily replace the existing inhibitor with a more effective one without disturbing the production technology at the fields. In the Russian Federation, corrosion inhibitors are used during the development of oil and gas fields as prescribed by Gosgortekhnadzor [2].

Inhibitors are supplied to pipeline systems with periodic or continuous dosing. During periodic dosing, contact of the pipeline metal surface with the commercial form of inhibitor or its concentrated solution is organized. At the same time, inhibitors should have an effect of after-action, i.e. the protective layer formed by their application should retain its integrity for a long time. At constant dosing the formation and maintenance of the protective layer is realized due to diffusion of the active



component of the inhibitor from the liquid volume on the metal surface of the pipeline wall. The effectiveness of pipeline protection with corrosion inhibitors depends on the chemical composition, adsorption capacity and the amount of inhibitor injected [12-14].

Carbon dioxide corrosion inhibitors

Corrosion inhibitors are chemical compounds that reduce the rate of corrosion without significantly changing the concentration of any corrosion reagent. The ability of inhibitors to retard corrosion is mainly due to the following properties: adsorption of CI on the metal surface; change in the rate of anodic/cathodic reactions; slowing down the rate of CI diffusion to the metal surface; decrease in the electrical resistance of the metal surface.

The corrosion inhibitor acts at the metal/solution interface to form a film of various types – passivating, precipitating and adsorptive.

The most widespread use of passivators is for corrosion control in neutral or near-neutral pH environments. The chemical composition and structure of inhibitors largely determines their mechanism of action. Among inhibitors one can find inorganic substances with oxidizing properties (nitrites, molybdates, tungstate, chromates), which are able to create protective oxide films on the surface of the corroding metal. Currently, the use of inhibitors of this type has been abandoned due to toxicity; they are used only in the aviation industry and construction.

Precipitating film inhibitors are chemicals that form insoluble protective films by reacting with soluble substances in the environment (e.g., phosphonates and polyphosphates that form protective films with calcium ions in solution) or with the protected medium – metal ions (e.g., copper-benzotriazole salt film (BTA) [1].

Inhibitors that form adsorptive protective films are mainly organic substances (surfactants), which often have a surfactant molecular structure with a hydrophilic group capable of binding to the metal surface and a hydrophobic part of the molecule protruding towards the solution volume. The adsorbed inhibitor molecules restrict oxygen diffusion and water access to the metal surface, which reduces the corrosion rate.

Modern adsorption-type corrosion inhibitors are usually a solution of one or more organic compounds with high inhibitory properties (active base) in a hydrocarbon or water-alcohol solvent.

There are a number of requirements for corrosion inhibitors used in the oil industry:

- protective effect in a wide range of temperatures and pressures (from normal to high), as well as in conditions of high flow velocities and the presence of abrasive particles;
- low solidification temperature (not less than $-50\text{ }^{\circ}\text{C}$);
- good solubility and/or dispersibility in working media (water-soluble, hydrocarbon-soluble, hydrocarbon-soluble-water-dispersible, insoluble in neither water nor hydrocarbons);
- absence of influence on the stability of oil-water emulsions;
- fire and explosion safety, compliance with the requirements of sanitary norms;
- compatibility with other reagents used in the technological process and absence of influence on the quality and processes of subsequent oil refining, etc.

Also, when developing effective corrosion inhibitors, it is worth considering the environmental impact, the possibility of use at low concentrations (100-200 mg/l), and chemical stability in corrosive environments.

All commercially available corrosion inhibitors have an optimal area of application depending on the industry segment, composition of corrosive media and technological features of the protected objects [15]. Table 1 shows the most common composition of corrosion inhibitors used in various fields.



Table 1

Composition of inhibitors used in various segments of the oil and gas industry

Segment	Inhibitors	Composition	Medium
Oil field	Corrosion inhibitors	Linear amines and imidazolines in various solvents (kerosene, methanol, neonol, etc.)	Oil emulsion
Chemical-technological equipment protection	Corrosion inhibitors	Oxyethylated fatty amines and imidazolines	Petroleum products with various impurities
Water treatment	Complex inhibitors	Organophosphorus substances	Water
Water treatment of recycled industrial water enterprises	Complex inhibitors	Phosphorus-containing components, sodium polyphosphates. Zinc sulphates etc.	Water with various impurities

The main volume of reagents is used in the processes of production (for protection of pressure, oil gathering, in-field pipelines and water lines) and transportation of crude oil (Fig. 1).

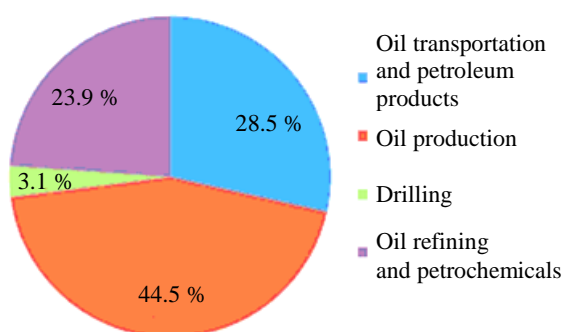


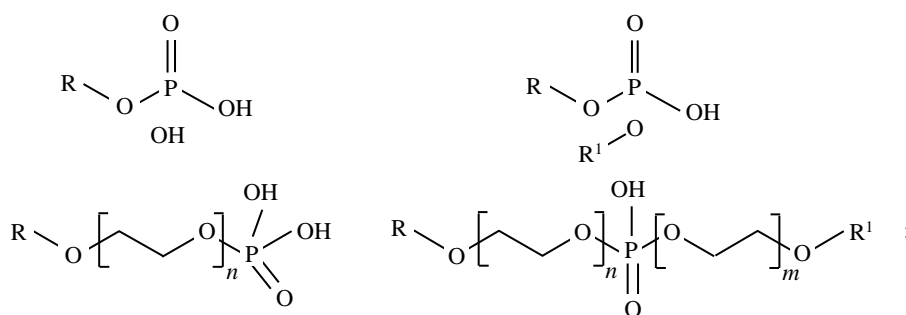
Fig. 1. Use of corrosion inhibitors in various segments of the oil and gas industry

Therefore, the most urgent is the development of new and improvement of currently used corrosion inhibitors, including carbon dioxide, used in the oil industry.

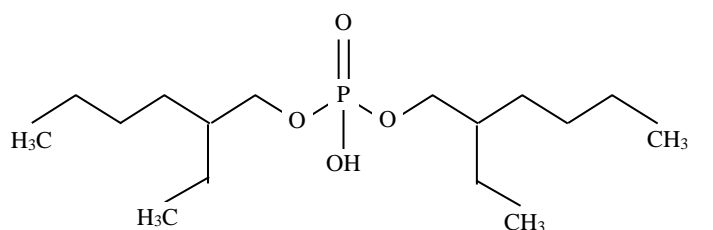
Organic corrosion inhibitors

Organic compounds containing heteroatoms (O, P, N, S) are being actively studied as corrosion inhibitors [16, 17]. Structures of the main phosphorus-, oxygen- and sulfur-containing compounds used in industry as active bases of carbon dioxide corrosion inhibitors:

- esters of phosphoric acid [16]

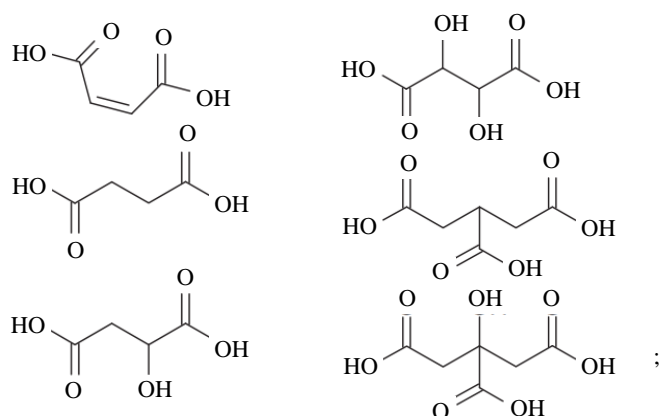


- bis(2-ethylhexyl) phosphate [18]

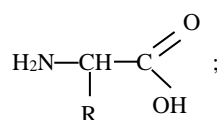




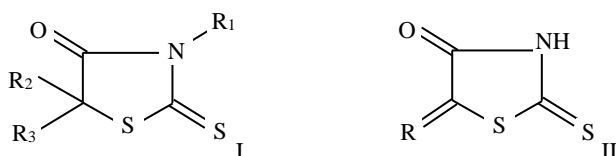
• carboxylic acids [19]



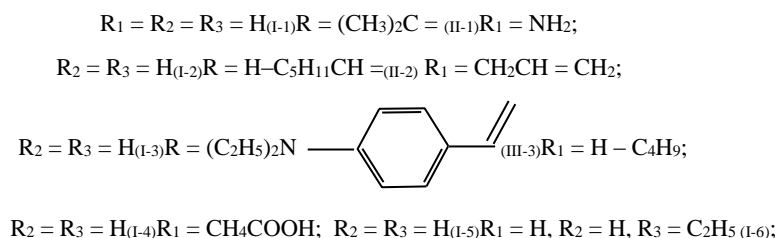
• amino acids and their derivatives [20]



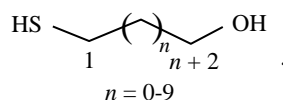
• rhodanine and derivatives [21]



where



• ω-mercaptoalcohols [22]



Phosphorus-containing compounds

The mechanism of adsorption of inhibitor molecules on the metal surface can be considered as donor-acceptor: heteroatoms containing π -electrons act as donors, and free d -orbitals of metal surfaces act as acceptor [16]. This interaction leads to the formation of a protective layer on the metal surface. The ability of phosphorus atoms to form adsorption bonds at the expense of π -electrons and vacant d -orbitals of transition metals determines the chemisorption and inhibitory properties of phosphorus-containing compounds, which are used as corrosion inhibitors individually or in mixtures.

Mono- and diethers of phosphoric acid form sparingly soluble salts with ions Fe^{2+} and Ca^{2+} , which form a protective layer on the metal surface, thereby reducing the rate of corrosion.



Corrosion inhibitors based on organic phosphorus compounds, such as N-heterocyclic alkylphosphonic acid $\text{HtC(R}_1\text{R}_2\text{)P(O)(OH)}_2$, where Ht – is a heterocyclic fragment with a nitrogen atom in the ring – pyrrolidine or morpholine, showed a high degree of protection against local corrosion; R_1 , R_2 – are hydrogen atoms (alkyl radicals CH_3 or CH_3 and C_2H_5) [23]. The presence of the acid residue P(O)(OH)_2 in the molecule provides the formation of a nanoscale self-organizing layer on the metal surface at the inhibitor concentration in aqueous solution from 30 to 60 mg/l.

In the research [18] the possibility of using bis(2-ethylhexyl)phosphate to inhibit carbon dioxide corrosion is reported. It is shown that P-O-Fe and P-Fe bonds are formed on the metal surface, due to which the corrosion inhibitor shows high efficiency – 93 % at a concentration of 500 ppm.

Oxygen-containing compounds

Carboxylic acids show high protective ability (above 90 %) in conditions of carbonic acid corrosion [19], while the inhibition efficiency is primarily associated with adsorption of carbonyl groups -C=O on the metal surface and significantly increases with increasing their amount. Tricarboxylic acids exhibit maximum efficacy even at low inhibitor concentrations. The presence and number of hydroxyl groups in the structure of the inhibitor molecule has a significant effect on its efficiency – succinic and maleic acids, which have no hydroxyl groups in their composition, showed better inhibition efficiency than malic and tartaric acids.

Amino acids, particularly glutamic acid, are effective corrosion inhibitors, but the concentration should be carefully selected depending on the environmental conditions, as the opposite effect can be achieved [20]. Amino acids are environmentally friendly compounds that are completely soluble in aqueous media, non-toxic and cheap, so more and more research has been directed towards the synthesis of amino acids and their more complex derivatives to improve the effectiveness of corrosion inhibitors [24].

In the research [25], the esterification reaction of natural petroleum acids with allylic alcohol in the presence of an ionic liquid, N-methylpyrrolidone hydrosulfate, was studied. Based on of the obtained allyl alcohol of petroleum acid nitro derivatives were synthesized, their salts and complexes were obtained and the influence of solutions of these compounds on the kinetics of the corrosion process was investigated. The nature of salts and complexes was found to affect the effectiveness of CO_2 corrosion inhibitors and varies in a series: potassium salt > monoethanolamine complex > diethanolamine complex. Potassium salt and monoethanolamine complex based on nitro product of natural petroleum acids showed the highest anticorrosion efficiency at a concentration of 300 ppm, which amounted to 98.4 and 98.9 %, respectively.

Sulfur-containing compounds

The authors of the source [21] suggest the use of rhodanine and its 3- or 5-derivatives of general formula I or II as a corrosion inhibitor. It was found that inhibitors exhibit high protective properties (up to 99 %) in carbonic acid corrosion of iron at very low concentrations (0.1-2.5 mg/l).

Decanthal can be an effective inhibitor of localized corrosion in carbonate media due to the formation of adsorption monolayer [26] and reduction of adsorption/desorption processes of intermediate compounds on the metal surface resulting from the slowing down of cathodic and anodic reactions. It was found that the introduction of 10-400 ppm decanthal can reduce the local corrosion of carbon steel. Investigations of the metal surface by physicochemical methods made it possible to establish that corrosion protection is provided by physical adsorption of the inhibitor on the metal surface rather than by chemisorption, since no Fe-S bonds were detected.

The relationship between the structure of a number of mercaptoalcohols and their anticorrosion efficacy as corrosion inhibitors was studied in [22]. While using molecular dynamic modeling, it was found that the high efficiency of mercaptoalcohols is due to their ability to adsorb on the Fe (110) surface with both -SH- and -OH- groups. As the carbon chain lengthens, the corrosion resistance properties improve and the optimum chain length is C_{11} .



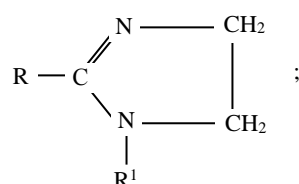
When straight, branched, cyclic or heterocyclic alkylene, arylene, alkylarylene, arylalkylene or hydrocarbon fragments containing from 1 to 30 carbon atoms of carbon-containing radicals with the general formula $(HS)_n-R-(OH)_m$ ($n, m = 1-3$), are introduced into mercaptoalcohols, the anticorrosive efficiency increases [27]. The best reduction in both uniform and localized corrosion rates was achieved in the presence of 2-mercaptoethanol, 2-mercaptopropanol, 1-mercapto-2-propanol and 2-mercaptobutanol.

Nitrogen-containing compounds

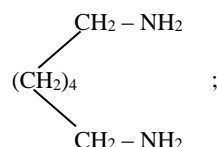
Inhibitors based on nitrogen-containing compounds are the most widespread among all organic compounds containing heteroatoms [17, 28].

Structures of the main nitrogen-containing compounds used as active bases of carbon dioxide corrosion inhibitors:

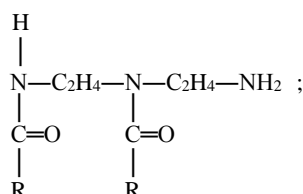
- imidazolines



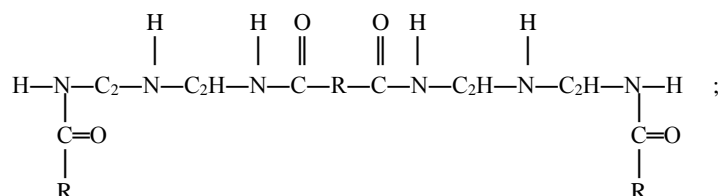
- primary amines $\text{R}-\text{NH}_2$;
- diamines



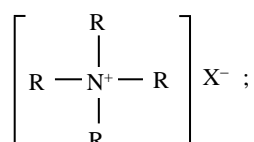
- amidoamines



- dimerized amidoamines

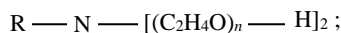


- quaternary ammonium bases (QAS)

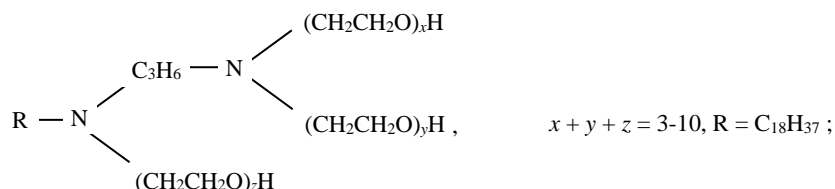




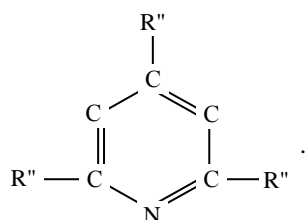
- oxyethylated primary amines



- polyethoxyalkyldiamines



- alkylpyridines



Amines, amides, imidazolines and their derivatives are used as the active base of corrosion inhibitors. Analysis of corrosion inhibitors used on the territory of the Russian Federation and produced by domestic companies shows that complex mixtures of nitrogen-containing compounds are predominantly used as the active base. Effectiveness of active bases of carbon dioxide corrosion inhibitors of domestic manufacturers: mixture of nitrogen-containing surfactants – 90 %; reaction product of tall oil with tetraethylenepentamine – 90 %; mixture of alkylimidazolines – 91 %; amido-imidosoline of fatty acids – 90 %; condensation product of fatty acids of tall oil with aminoethyl-ethanoamine – 91 %; mixture of alkylimidazolines of fatty acids C₈-C₁₂ – 90 %; alkyldimethylbenzylammonium chloride – 92 %.

Amines and QAS

Primary, secondary, tertiary amines and tertiary derivatives containing a positively charged nitrogen atom covalently bonded to four organic radicals and ionically bonded to an anion are used as corrosion inhibitors. The radicals commonly used are fatty acid residues, alkyl (C₈-C₃₀), phenyl, oxy- and polyoxyalkyl.

QAS are cationic type surfactants. This means that in aqueous solutions, QAS dissociate into a positively charged radical and an acid anion. QAS have been used for a long time and widely in the oil and gas industry. They are used as individual active bases or in mixtures with other classes of compounds. Dimethyldodecylbenzylammonium chloride is an example of QAS-based CI. N-alkyl quaternary ammonium compounds with different anions have the structure of amphiphilic cationic surfactants and are therefore potential metal corrosion inhibitors.

In the research [29] a series of pyrrolidine-based quaternary ammonium salts containing hydrophobic C₁₂-C₁₆ alkyl moieties and hydrophilic oxygen-containing substitutes (propargyl, dodecyl and their combination) were synthesized. High inhibitory properties of the studied ammonium compounds are primarily due to the presence of several adsorption centers. Hydrophilic fragments are chemisorbed on the metal surface to form a protective film (coating), and hydrophobic substitutes displace the adsorbed water layer to form a protective layer on the metal surface. As the alkyl chain length increases, the inhibition efficiency increases. Aliphatic hydrocarbon radicals contained in ammonium cations as well as in organic acid anions provide adsorption interaction with the metal surface.

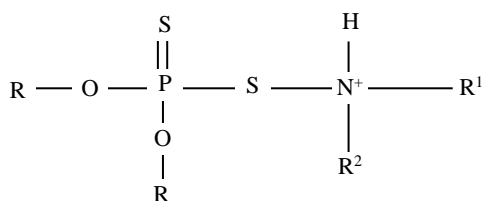


Fig.2. Structure of the O,O-diethers of dithiophosphoric acids
R is iso-C₉H₁₉C₆H₄, iso-C₉H₁₉C₆H₄(OCH₂CH₂)₆, iso-C₄H₉,
iso-C₈H₁₇; R¹ – H, C₂H₅, C₁₂H₂₅, CH₂CH₂OH; R²– H, CH₃,
C₂H₅, C₁₂H₂₅, CH₂CH₂OH

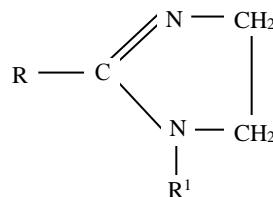


Fig.3. Structure of alkylimidazoline
R is hydrophobic, R¹ – hydrophilic

In addition, it is known that the simultaneous presence in aqueous solutions of a mixture of inhibitors exhibiting the properties of both cationic (containing ammonium cation) and anionic (containing hydrocarbon anion) surfactants can provide special properties that can significantly increase the effectiveness of anticorrosion action.

The length of alkyl substitute of dimethylbenzylammonium affects the effectiveness of corrosion inhibitor based on it [30]. The molecular structure of the model compounds includes the same polar group, dimethylbenzylammonium, and four different hydrophobic moieties with different lengths of alkyl tails (butyl (–C₄H₉), oktyl (–C₈H₁₇), dodecyl (–C₁₂H₂₅) and hexadecyl (–C₁₆H₃₃). It was found that the longer the length of the alkyl moiety, which has good adhesion to the metal surface, the higher the corrosion reduction efficiency for the homologous series evaluated. The main role of the leading group of model quaternary ammonium compounds is to form bonds of the inhibitor molecule with the metal surface, while the hydrophobicity of the alkyl tail plays a determining role in the inhibition process by displacing water molecules from the surface.

Ammonium salts of O, O-dialkyl dithiophosphoric acids (Fig.2) are effective inhibitors of carbonic acid corrosion, in the presence of which a protective effect of up to 99 % is achieved [31]. In the case of carbon dioxide corrosion, the inhibitory activity is independent of the nature of the amine and the length of the alkyl substitute in the ester group. An important feature is that the inhibitory effect of these compounds increases with increasing temperature.

Imidazolines

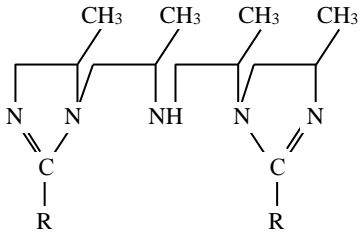
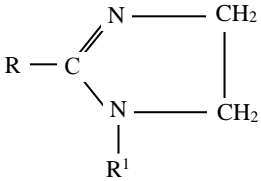
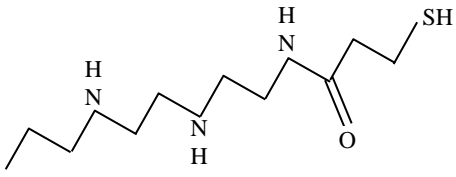
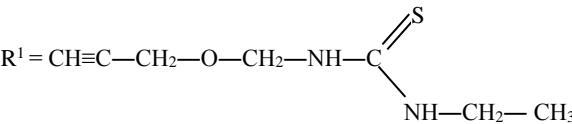
Imidazolines and their derivatives (Fig.3) are widely used as organic corrosion inhibitors in the oil and gas industry worldwide to effectively suppress CO₂ corrosion.

Imidazoline can be readily synthesized from natural fatty acids and ethylenediamines, as well as from aldehydes and diamines [20]. The use of natural fatty acids make imidazolines environmentally friendly. Imidazolines can also be derived from plant material. Thus, in [32] a hydroxyethyl imidazoline derivative was synthesized based on coffee oil and found to be highly effective in reducing carbon dioxide corrosion rate, 99.9 % at a concentration of 10 ppm. In the research [33] a novel N-(3-(2-fatty-4,5-dihydro-1H-imidazol-1-yl)propyl) – fatty amide-type surfactant was derived from fatty acids (C₁₆–C₁₈), contained in mango seeds and showed high performance under corrosive conditions of CO₂. It was previously determined that adsorption of olein-substituted imidazoline on steel surfaces creates a fully hydrophobic surface, forming a watertight barrier between the corrosive aqueous phase and the steel surface, which provides effective corrosion protection. To improve the efficiency of corrosion inhibitors, the authors [34] synthesized a number of imidazoline derivatives from oleic acid and various amines (ethylenediamine, diethylenetriamine, triethylenetetramine, tetraethylenepentamine, hydroxyethyl ethylenediamine, and polyethylenepolyamine) and showed that the efficiency of CI based on them is 97-98 %. The inhibition efficiency of imidazolines obtained by condensation of soybean oil fatty acid and various amines (DETA, TETA, TEPA) was 50-90 % [35]. Imidazoline derivatives derived from semi-purified rice bran oil exhibited high inhibitory properties up to 99.69 % for carbon steel [36].



Table 2

Structures of the main imidazoline compounds used as active bases of inhibitors of carbonic acid corrosion

Compound	Structure	Substitutes	Reference
Bis-imidazoline		$R = C_{17}H_{33}$	[37]
Alkylimidazoline		$R = C_{17}H_{33}$ $R^1 = H$ $C_2H_4NH_2$ $C_3H_6NH_2$ $C_2H_4NHC_2H_4NH_2$ $(C_2H_4NH)_2C_2H_4NH_2$ $(C_2H_4NH)_x C_2H_4NH_2$ ($x \geq 3$) C_2H_4OH $R = C_2H_5, C_{18}H_{37}$ $R^1 = C_2H_4OH$	[34], [38]
		$R = C_{17}H_{33}$	[38]
			[39]
		$R = C_{17}H_{33}$	[40]
			

The presence of several nitrogen atoms in the structure of compounds increases their anti-corrosion ability. The authors of [37] developed a method of obtaining a corrosion inhibitor based on ethylene oxide and bis-imidazoline obtained by interaction of tetrapropylene pentamine and oleic acid, which demonstrated high efficiency of corrosion reduction in carbonate medium – 97-98 % at a concentration of 30-50 mg/g.

A number of researches are aimed at studying the adsorption and anticorrosion properties of alkylimidazolines depending on the nature of substitutes R and R^1 (Table 2). Substitutes exhibit different properties and perform different functions. The hydrophilic part provides orientation and bonding of the corrosion inhibitor to the metal surface, while the hydrophobic part provides formation of a protective adsorption barrier between the metal surface and the corrosive medium. It is still debated which substitute has a greater influence on the effectiveness of corrosion inhibitors. For example, a number of alkylimidazolines have been synthesized in the research [38] by varying the nature of both hydrophilic and hydrophobic substitutes, the most representative examples are shown in Table 2.

It was established that at the same R ($C_{17}H_{33}$) replacing the hydrogen with aminoethylene ($C_2H_4NH_2$) in the position R^1 significantly increases the CI efficiency, from 77 to 92 %. Increasing the chain length of the amine substitute does not affect the efficiency as much, and in some cases



($C_3H_6NH_2$) decreases it. The introduction of a hydroxyethyl group into the imidazoline ring weakens the inhibitory ability of imidazoline due to an increase in its hydrophilicity, which leads to an increase in water solubility with a decrease in the insulating ability of the inhibitor film. Whereas, for the same R^1 (C_2H_4OH) replacing the alkyl chain C_{17} with C_2 decreases the CI efficiency sharply from 90 to 13 %, confirming the important role of the hydrophobic part length. The chain branching slightly changes the effectiveness of the inhibitor.

The authors [34] synthesized a series of imidazolines using oleic acid and various nitrogen- and oxygen-containing groups as substitutes (Table 2) and showed that the introduction of hydroxyethyl group increases the hydrophilicity of imidazoline, while aminoethylene increases the hydrophobicity. The effectiveness of a corrosion inhibitor is directly related to the combination of its hydrophobic and hydrophilic properties. Another important factor affecting the properties of corrosion inhibitors is the operating conditions, particularly the flow rate. Thus, at low speeds (0.3-0.6 m/s), alkylimidazolines with side substitutes $-C_2H_4NH_2$ and $-C_2H_4NHC_2H_4NH_2$ showed the highest performance, whereas at higher speeds (5.5 m/s), alkylimidazoline without side substitute R^1 had the highest efficiency.

In the research [41] a synergistic effect was found – when oleic imidazoline and mercaptoethanol were used in a 3:1 ratio, the efficiency reached 96.56 %.

In early researches it was shown that olein-substituted imidazoline is an effective base for corrosion inhibitors, and in order to improve the anticorrosion properties, the authors [39] introduced a sulfhydryl substitute into olein-substituted imidazoline (Table 2), which led to an increase in inhibition efficiency up to 95.58 %. This difference is due to the presence of an additional active adsorption center.

An inhibitor of carbon dioxide corrosion based on imidazoline derived from polyamine (triethanoltetramine, polyethylene polyamine) with carboxylic acid (oleic acid, stearic acid, acetic acid) was proposed in the research [42]. An important feature of this inhibitor is the addition of copper-containing carbon nanostructures to the obtained imidazoline, which makes it possible to reduce the working concentration of the corrosion inhibitor from 40 to 15 mg/l without loss of efficiency.

In studying the effectiveness of imidazoline-containing inhibitor of uniform and localized corrosion in the medium CO_2 [43] two main factors affecting the inhibition efficiency, i.e., inhibitor adsorption/film formation and the presence of corrosion products, were identified. The presence of corrosion products had a significant effect on both the adsorption of the inhibitor and the depth of the corrosion pit. This effect was most pronounced in the formation of a layer consisting predominantly of $FeCO_3$, while the corrosion inhibitor provided only ~25 % of the total protection.

Imidazolinthioureidooleic acid is widely used in the oil and gas industry as the basis of an effective carbon dioxide corrosion inhibitor for carbon steel, but due to the increasing depth of oil fields, improvement of its anticorrosion characteristics is required. One way of improvement is the modification of imidazolinthioureidooleic acid. For example, in [40] a modified imidazolinthioureidooleic acid (Table 2) was obtained by reaction with formaldehyde and propargyl alcohol c, which showed improved anticorrosion properties.

It was found that due to the additional adsorption center and higher hydrophobicity, the modified imidazoline forms a more stable and effective adsorption film, increasing the efficiency of the corrosion inhibitor based on it. In the research [44] branched tetraimidazoline derivatives that contain four adsorption centers were synthesized (Fig.4).

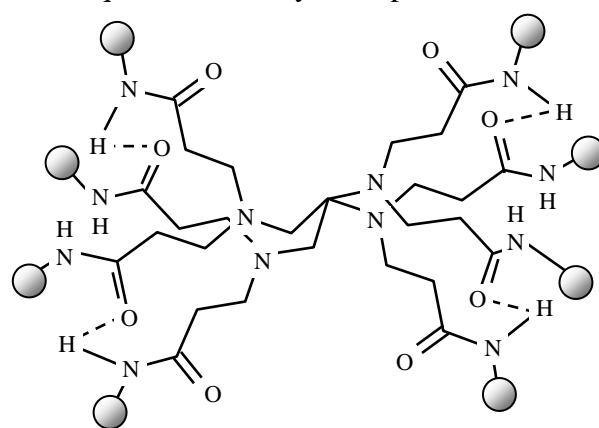


Fig.4. Structure of a branched derivative tetraimidazoline



Fig.5. Structure of 3- and 4-pyridinecarboxaldehyde-4-phenylthiosemicarbazides

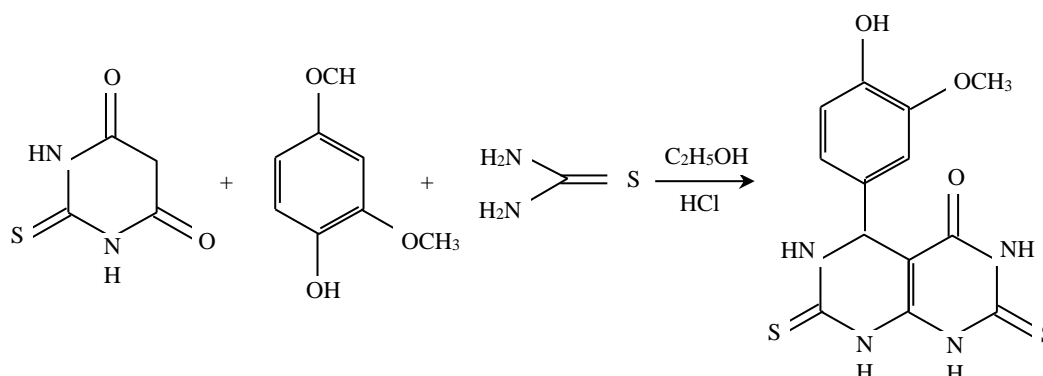


Fig.6. Synthesis scheme

5-(4-hydroxy-3-methoxyphenyl)-2,7-dithioxo-2,3,5,6,7,8-hexahydropyrimido[4,5-*d*]pyrimidin-4(1H)-one

It was found that the efficiency of the corrosion inhibitor based on the synthesized compound increases with increasing concentration and temperature and reaches 98.29 %. Scanning electron microscopy data confirm the formation of dense dendrimer-like protective films that ensure the absence of contact between the aggressive medium and the metal surface.

The pyridine Schiff base derivatives, namely 3-pyridinecarboxaldehyde-4-phenylthiosemicarbazide (3-PCPHC) and 4-pyridinecarboxaldehyde-4-phenylthiosemicarbazide (4-PCPHC) (Fig.5), showed efficacy as carbonic acid corrosion inhibitors [45]. At the same concentration, the inhibition efficiency of 3-PCPHC is higher than that of 4-PCPHC, increasing sharply with increasing concentration and remaining constant at different temperatures. According to the results of molecular dynamic simulations, both protonated and non-protonated 3-PCPHC and 4-PCPHC adsorb on Fe (110) almost parallel to the surface, forming an adsorption layer.

Pyrimidine-based compounds can exhibit high corrosion resistance activity. Thus, in [46] 5-(4-hydroxy-3-methoxyphenyl)-2,7-dithioxo-2,3,5,6,7,8-hexahydropyrimido[4,5-*d*]pyrimidin-4(1H)-one was synthesized (Fig.6) and used as a carbon dioxide corrosion inhibitor.

It was found that the high efficiency (up to 90 % at a concentration of 20 ppm) was mainly due to two factors, namely, the large number of adsorption centers (N, S and O, as well as π -electrons in the aromatic ring) and the selectivity of adsorption on the Fe (110) surface, which significantly reduced the local corrosion rate on the steel surface during sweet corrosion. This is consistent with earlier studies showing that the initiation of localized corrosion occurs in the sequence of iron crystal faces (110) > (100) > (111) given that the propagation of uniform corrosion occurs in the following order of iron crystal faces: (100) > (110) > (111) [47].

Polymer-containing compounds

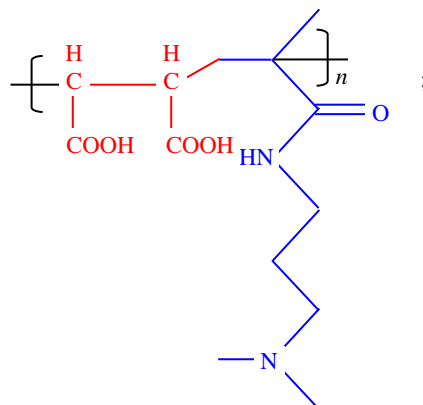
Polymeric corrosion inhibitors have a number of advantages over inhibitors with small organic molecules – easy formation of multilayer adsorption films on the metal surface and a greater number of molecule sites involved in adsorption and higher temperature resistance. According to



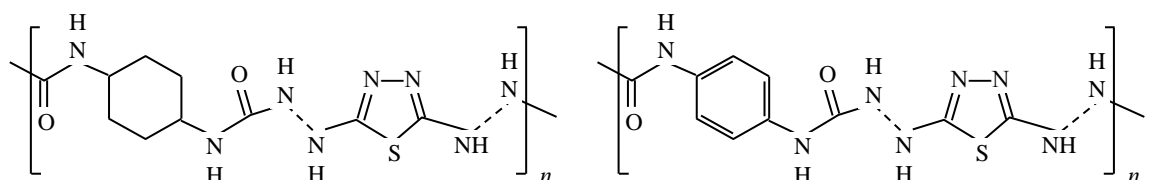
a review [48], most polymer-containing corrosion inhibitors are polyamines modified with carboxylate and heterocyclic moieties, thiols, disulfides and phosphorus-containing functional groups.

Structure of polymers used as corrosion inhibitors:

- poly(maleic acid-co-N-[3-(dimethylamino)propyl]-methacrylamide [49].



- poly(urethane-semicarbazides) containing thiadiazoles,



In the research [50] poly(maleic acid-co-N-[3-(dimethylamino)propyl]-methacrylamide) synthesized by polymerization in aqueous solution was used as the base of the corrosion inhibitor. The results showed that the polymeric corrosion inhibitor exhibited high corrosion inhibition efficiency (90.1 % at a dosage of 200 mg/l) and acted as an anodic type inhibitor by forming an adsorptive polymeric film on the metal surface.

Polysemicarbazides have good thermal and mechanical properties due to hydrogen bonding. Poly(urethane-semicarbazides) containing a chain of 1,3,4-thiadiazoles were synthesized. It was found that corrosion inhibitors based on them show high efficiency, forming a strong adsorbed film. The polymer containing aromatic rings showed more activity, which is probably due to its higher stiffness and stability [51].

In [49] polyacrylamide, poly(2-methoxyaniline) and copolymer of polyacrylamide and poly(2-methoxyaniline) were synthesized and investigated as corrosion inhibitors. Among all the polymers studied, poly(2-methoxyaniline) showed the highest anticorrosion efficiency, which was 80 % versus 63-74 %. The higher adsorption capacity may be due to the presence of more donor groups, which improves the coordination of the polymer to the metal surface.

The authors [52] compared the effectiveness of polypropylene glycol and polymethacrylic acid based corrosion inhibitors in the concentration range of 50-1000 ppm. The polymers were found to be mixed type inhibitors and the effectiveness of polypropylene glycol was higher, with corrosion activity increasing with increasing inhibitor concentration and decreasing with increasing temperature.

In recent years, inorganic porous materials and polymers have been widely studied for encapsulation of active substances, i.e., under certain environmental conditions, the capsules are destroyed with the release of a corrosion inhibitor [53]. For example, in work [54] the polymeric material was combined with classical organic corrosion inhibitors (Fig.7).

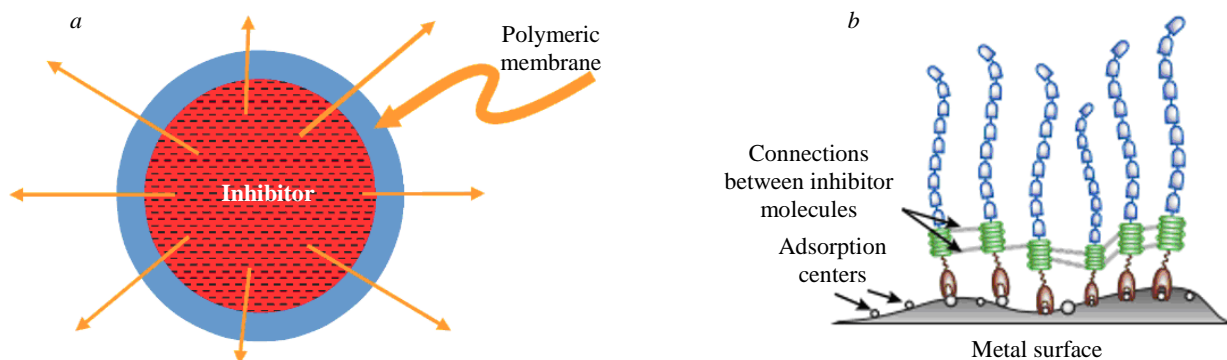


Fig.7. Structure of capsule polymer-containing corrosion inhibitor (diffusion of the active component of the inhibitor through the polymer membrane) (a), polymer-crosslinked surfactants (b)

The polymer can be used as a shell for a capsule covering the corrosion inhibitor concentrate (Fig.7, a). When exposed to the medium, slow uniform diffusion of the corrosion inhibitor through the organic polymer membrane of the capsule occurs. Additional components such as weighting agent and capsule wall modifier can be used to provide the required density, resistance to external influences and reagent diffusion rate through the membrane. Polymer cross-linked surfactants are polymer corrosion inhibitor molecules that have specific sites (spacers) that form an additional stable bond between them, reinforcing the film (Fig.7, b).

These approaches allow, on the one hand, to reduce the concentration of corrosion inhibitor without loss of efficiency, and on the other hand, to achieve a high aftereffect due to the creation of a stable film.

“Green” corrosion inhibitors

Another class of compounds actively used as environmentally safe corrosion inhibitors are substances of plant origin, which are promising due to biodegradability, availability and non-toxicity. The use of plant extracts can achieve inhibition efficiencies in excess of 80 %, making them attractive targets for research. The use of plant extracts as a crude corrosion inhibitor has been widely reported in the literature [55-57] as an alternative to classical corrosion inhibitors. The anticorrosive activity of many of the studied extracts may be related to the presence of heterocyclic components such as alkaloids, flavonoids, etc., which contribute to the formation of adsorption layer. A review of the literature on “green” corrosion inhibitors shows that the main criterion for inhibitor selection is the presence of heteroatoms (N, O, P, and S) in the composition, since hydroxyl, carboxyl and amino groups are mainly responsible for chelation and adsorption efficiency.

For example, alcoholic extracts of plants *Lycium shawii*, *Teucrium oliverianum*, *Ochradenus baccatus*, *Anvillea garcinii*, *Cassia italica*, *Artemisia sieberi*, *Carthamus tinctorius* and *Tripleurospermum auriculatum* were used as corrosion inhibitors. It is confirmed that these plant extracts exhibit high efficacy, which is 62-91 %. The extract of water hyacinth, a type of water weed that is often a problem for hydroelectric power plants, was also used, its effectiveness increases with increasing concentration, the optimum value being 50 ppm.

Biopolymers, especially water-soluble ones, are effective corrosion inhibitors in various aqueous environments [58]. Due to their massive functional groups, biopolymers are able to form complexes with a large area of the metal surface, providing a high degree of protection. The effectiveness of biopolymers used as corrosion inhibitors varies depending on their molecular weight, aromaticity, and the presence of groups forming bonds and adsorption centers.



Biopolymers such as lignin [59], inulin [60], cellulose [61], starch, pectin, chitosan [62], and their mixtures are considered as promising materials for “green” corrosion inhibitors for various environments.

Natural polymers can act as additives to traditionally used nitrogen-containing corrosion inhibitors, resulting in improved efficacy through synergistic effects [63].

Natural polysaccharides can be modified with different groups to obtain highly effective corrosion inhibitors. For example, two carboxymethyl chitosan derivatives were synthesized and used in [64], which exhibited maximum efficiency (87.97 and 93.95 %) at a concentration of 100 mg/l.

When considering plant extracts and biopolymers as corrosion inhibitors, it is necessary to take into account points related to the preparation of raw materials (drying, dehydration), to the conditions and reagents for extraction, as well as to the utilization of solvents, which are often highly acidic and alkaline media. Factors such as solvent to solid ratio, solvent polarity, extraction time and temperature can significantly affect the chemical composition and physical properties of the samples and, consequently, the efficacy of the corrosion inhibitors. In addition, development of mathematical models including kinetic and mechanistic studies is required in predicting the corrosion inhibitory effect from plant extracts to increase their efficiency.

Conclusion

Modern adsorption-type corrosion inhibitors are usually a solution of one or more organic compounds with high inhibitory properties (active base) in a hydrocarbon or water-alcohol solvent. All commercially available corrosion inhibitors have an optimal area of application depending on the industry segment, composition of corrosive media and technological features of the protected objects.

The efficiency of corrosion inhibitor action is mainly determined by its adsorption properties, which depend on physical and chemical properties, functional groups, aromaticity, steric effect, electron density on donor atoms. Metal surface composition, microstructure and temperature also affect the adsorption and hence the effectiveness of the inhibitor.

Organic compounds containing heteroatoms (O, P, N, S) are currently the most studied as corrosion inhibitors to effectively suppress CO₂ corrosion. The most widely spread in Russia and in the world are corrosion inhibitors, where alkylimidazolines and other nitrogen-containing compounds act as an active base, which show high anticorrosion properties in the range of conditions. The effectiveness of commercial inhibitors from different manufacturers varies between 90-92 %. It is shown that the anticorrosion properties can be significantly improved by selecting substitutes of nitrogen-containing compounds by varying their nature, chain length, structure, etc. This approach allows not only to increase the protection efficiency up to 98-99 %, but also to reduce the corrosion inhibitor concentration up to 10 ppm. In addition, one of the effective approaches to increase the anticorrosion properties of the bases used is to increase the number of adsorption centers mainly by introducing heteroatoms and aromatic structures. Corrosion inhibitors based on sulfur-containing compounds are used less frequently, but can also exhibit high corrosion protection properties, e.g. the use of rhodanine and its derivatives can achieve protection efficiencies of up to 99 % at very low concentrations (0.1-2.5 mg/l). Phosphorus-containing corrosion inhibitors show comparable anticorrosion properties at higher concentrations (up to 60 mg/g).

One of the actual directions of research in the field of corrosion inhibitors is the use of polymeric materials, which have advantages over inhibitors with small organic molecules, which include easier formation of multilayer adsorption films on the metal surface, a greater number of adsorption sites



and higher temperature resistance. The polymer-containing components are mostly polyamines modified with carboxylate and heterocyclic moieties, thiols, disulfides and phosphorus-containing functional groups and are used as an active base, exhibiting efficacy above 90 % at dosages up to 200 mg/l. Also polymeric materials can be used in combination with classical organic compounds, where they act as a shell for more uniform diffusion of the corrosion inhibitor, which allows to increase the efficiency of the anticorrosion process.

In recent years, substances of plant origin, which are promising due to biodegradability, availability and nontoxicity, have been actively investigated for use as environmentally safe corrosion inhibitors. The possibility of using biopolymers and polysaccharides, such as lignin, cellulose, starch, pectin, chitosan, etc., as well as their mixtures, the use of which allows achieving effective protection above 93 %, is considered. This class of compounds is used as an additive to traditionally used nitrogen-containing corrosion inhibitors, which increases the effectiveness due to synergistic effect, and as a main component, due to massive functional groups, which, adsorbed on the larger surface of the metal, provide a high degree of protection. Plant extracts also exhibit high anti-corrosion activity (above 91 %), which is attributed to the presence of heterocyclic components such as alkaloids, flavonoids, etc., which contribute to the formation of a strong adsorption layer.

Two main approaches have been proposed to improve corrosion protection in the petroleum industry. The first one is based on modification of currently used corrosion inhibitors based on nitrogen-containing compounds, which has advantages as this class is well studied in a wide range of conditions and has been successfully applied in the fields for many years. At the same time, “classical” corrosion inhibitors can be supplemented with new polymeric, biological, and nanoscale additives. Another approach is aimed at using alternative corrosion inhibitors, including those based on plant extracts and polymers, which requires more directed research and testing in real conditions, but is attractive from the point of view of the environmental performance of the applied objects.

REFERENCES

1. Ormellese M. Corrosion in Oil and Chemical Industry. Encyclopedia of Interfacial Chemistry: Surface Science and Electrochemistry. Elsevier, 2018. Vol. 6.1: Corrosion and Passivation, p. 145-154. DOI: [10.1016/B978-0-12-409547-2.13434-1](https://doi.org/10.1016/B978-0-12-409547-2.13434-1)
2. Koryakin A.Yu., Kobychev V.F., Kolichenko I.V., Yusupov A.D. Conditions of the carbon dioxide corrosion on the production facilities of Achimovskie deposits, methods of monitoring and forecasting. *Gas Industry*. 2017. N 12, p. 84-89 (in Russian).
3. Kasyanov A.V., Belousov A.E., Popov G.G., Bolobov V.I. Determination of factors affecting on grooving corrosion. Topical Issues of Rational Use of Natural Resources. CRC Press. 2019. Vol. 1, p. 393-399. DOI: [10.1201/9781003014577-49](https://doi.org/10.1201/9781003014577-49)
4. Kantyukov R.R., Zapevalov D.N., Vagapov R.K. Analysis of the application and impact of carbon dioxide media on the corrosion state of oil and gas facilities. *Journal of Mining Institute*. 2021. Vol. 250, p. 578-586. DOI: [10.31897/PMI.2021.4.11](https://doi.org/10.31897/PMI.2021.4.11)
5. Tkacheva V.E., Markin A.N., Presnyakov A.Y. et al. Localized carbon dioxide (CO₂) corrosion of the carbon and low-alloyed steels in oilfield systems. *Bulletin of the Technological University*. 2020. Vol. 23. N 12, p. 65-75 (in Russian).
6. Vagapov R.K., Fedotova A.I., Zapevalov D.N., Strelnikova K.O. Corrosion aggressiveness of various operational factors in hydrocarbon deposits containing carbon dioxide. *Vesti gazovoy nauki*. 2019. N 2 (39), p. 129-135 (in Russian).
7. Kahyarian A., Nesic S. A New Narrative for CO₂ Corrosion of Mild Steel. *Journal of the Electrochemical Society*. 2019. Vol. 166. N 11. C3048-C3063. DOI: [10.1149/2.0071911jes](https://doi.org/10.1149/2.0071911jes)
8. Ting Yan, Liang-Chen Xu, Zhuo-Xiong Zeng, Wei-Guo Pan. Mechanism and anti-corrosion measures of carbon dioxide corrosion in CCUS: A review. *iScience*. 2024. Vol. 27. Iss. 1. N 108594. DOI: [10.1016/j.isci.2023.108594](https://doi.org/10.1016/j.isci.2023.108594)
9. Ilinova A.A., Romasheva N.V., Stroykov G.A. Prospects and social effects of carbon dioxide sequestration and utilization projects. *Journal of Mining Institute*. 2020. Vol. 244, p. 493-502. DOI: [10.31897/PMI.2020.4.12](https://doi.org/10.31897/PMI.2020.4.12)
10. Askari M., Aliofkhazraei M., Jafari R. et al. Downhole corrosion inhibitors for oil and gas production – a review. *Applied Surface Science Advances*. 2021. Vol. 6. N 100128. DOI: [10.1016/j.apsadv.2021.100128](https://doi.org/10.1016/j.apsadv.2021.100128)
11. Petrova T.A., Epishina A.D. Anti-corrosion protection of pipelines at mining and processing enterprises. *Obogashchenie rud*. 2023. N 6, p. 52-58. DOI: [10.17580/or.2023.06.09](https://doi.org/10.17580/or.2023.06.09)
12. Shaposhnikov N.O., Golubev I.A., Khorobrov S.V. et al. Autoclave modeling of corrosion processes occurring in a gas pipeline during transportation of an unprepared multi-phase medium containing CO₂. *Journal of Mining Institute*. 2022. Vol. 258, p. 915-923. DOI: [10.31897/PMI.2022.92](https://doi.org/10.31897/PMI.2022.92)



13. Aminova D.F., Valiakhmetov R.I. Improving the efficiency of field pipeline protection using inhibitory protection. *Transport and Storage of Oil Products and Hydrocarbon Materials*. 2021. N 1, p. 58-61 (in Russian). DOI: [10.24412/0131-4270-2021-1-58-61](https://doi.org/10.24412/0131-4270-2021-1-58-61)
14. Vagapov R.K., Zapevalov D.N. Criteria for assessing the corrosion hazard and effectiveness of inhibitory protection during operation of gas production facilities in the presence of carbon dioxide. *Nauka i tekhnika v gazovoi promyshlennosti*. 2020. N 2 (82), p. 60-70 (in Russian).
15. Kulakov P.A., Rubtsov A.V., Afanasenko V.G. et al. Influence of technical condition parameters on the residual resource of capacitive equipment. *Journal of Physics: Conference Series*. 2019. Vol. 1399. Iss. 5. N 055052. DOI: [10.1088/1742-6596/1399/5/055052](https://doi.org/10.1088/1742-6596/1399/5/055052)
16. Verma D.K., Dewangan Y., Dewangan A.K., Asatkar A. Heteroatom-Based Compounds as Sustainable Corrosion Inhibitors: An Overview. *Journal of Bio- and Tribo-Corrosion*. 2021. Vol. 7. Iss. 1. N 15. DOI: [10.1007/s40735-020-00447-7](https://doi.org/10.1007/s40735-020-00447-7)
17. Winkler D.A., Hughes A.E., Özkan C. et al. Impact of inhibition mechanisms, automation, and computational models on the discovery of organic corrosion inhibitors. *Progress in Materials Science*. 2025. Vol. 149. N 101392. DOI: [10.1016/j.pmatsci.2024.101392](https://doi.org/10.1016/j.pmatsci.2024.101392)
18. Junying Hu, Qi Xiong, Longjun Chen et al. Corrosion inhibitor in CO₂-O₂-containing environment: Inhibition effect and mechanisms of Bis(2-ethylhexyl) phosphate for the corrosion of carbon steel. *Corrosion Science*. 2021. Vol. 179. N 109173. DOI: [10.1016/j.corsci.2020.109173](https://doi.org/10.1016/j.corsci.2020.109173)
19. Wysocka J., Cieslik M., Krakowiak S., Ryl J. Carboxylic acids as efficient corrosion inhibitors of aluminium alloys in alkaline media. *Electrochimica Acta*. 2018. Vol. 289, p. 175-192. DOI: [10.1016/j.electacta.2018.08.070](https://doi.org/10.1016/j.electacta.2018.08.070)
20. Hamadi L., Mansouri S., Oulmi K., Kareche A. The use of amino acids as corrosion inhibitors for metals: A review. *Egyptian Journal of Petroleum*. 2018. Vol. 27. Iss. 4, p. 1157-1165. DOI: [10.1016/j.ejpe.2018.04.004](https://doi.org/10.1016/j.ejpe.2018.04.004)
21. Reznik V.S., Khodyrev J.P., Akamsin V.D., Galiakberov R.M., Giniyatullin R.K., Semenov V.E., Galjametdinova I.V. Patent N 2351690 RF. Method of sweet iron corrosion inhibition. Publ. 10.04.2009. Bul. N 10 (in Russian).
22. Yuanqiang Zhu, Qingqing Sun, Yuan Wang et al. A Study on Inhibition Performance of Mercaptoalcohols As Corrosion Inhibitors by First Principle and Molecular Dynamics Simulation. *Russian Journal of Physical Chemistry A*. 2020. Vol. 94. N 9, p. 1877-1886. DOI: [10.1134/S0036024420090356](https://doi.org/10.1134/S0036024420090356)
23. Zubritskaja N.G., Baltser A.E., Bazanov A.G., Babenko T.G., Ivanova T.V., Shukan I.V., Barskova E.N., Gromov A.V., Podobaev A.N., Reformatskaja I.I., Ashcheulova I.I. Patent N 2430997 RF. Corrosion Inhibitor. Publ. 10.10.2011. Bul. N 28 (in Russian).
24. El Ibrahim B., Jmiai A., Bazzi L., El Issami S. Amino acids and their derivatives as corrosion inhibitors for metals and alloys. *Arabian Journal of Chemistry*. 2020. Vol. 13. Iss. 1, p. 740-771. DOI: [10.1016/j.arabjc.2017.07.013](https://doi.org/10.1016/j.arabjc.2017.07.013)
25. Mamedova N.A., Mamedkhanova S.A., Shakhmamedova A.G. The Synthesis and Application of Salts and Complexes on the Basis of Petroleum Acid Allyl Ester as Carbon Dioxide Corrosion Inhibitors. *Petroleum Chemistry*. 2019. Vol. 59. N 2, p. 213-219. DOI: [10.1134/S0028242119020114](https://doi.org/10.1134/S0028242119020114)
26. Belarbi Z., Dominguez Olivo J.M., Farelis F. et al. Decanethiol as a Corrosion Inhibitor for Carbon Steels Exposed to Aqueous CO₂. *Corrosion*. 2019. Vol. 75. Iss. 10, p. 1246-1254. DOI: [10.5006/3233](https://doi.org/10.5006/3233)
27. Young Soo Ahn, Jovancicevic V. Patent N WO 01/12878 A1. Mercaptoalcohol corrosion inhibitors. Publ. 22.02.2001.
28. Monticelli C. Corrosion Inhibitors. *Encyclopedia of Interfacial Chemistry: Surface Science and Electrochemistry*. Elsevier, 2018. Vol. 6.1: Corrosion and Passivation, p. 164-171. DOI: [10.1016/B978-0-12-409547-2.13443-2](https://doi.org/10.1016/B978-0-12-409547-2.13443-2)
29. Haque J., Jafar Mazumder M.A., Quraishi M.A. et al. Pyrrolidine-based quaternary ammonium salts containing propargyl and hydrophobic C-12 and C-16 alkyl chains as corrosion inhibitors in aqueous acidic media. *Journal of Molecular Liquids*. 2020. Vol. 320. Part B. N 114473. DOI: [10.1016/j.molliq.2020.114473](https://doi.org/10.1016/j.molliq.2020.114473)
30. Moradighadi N., Lewis S., Dommguez Olivo J.M. et al. Effect of Alkyl Tail Length on CMC and Mitigation Efficiency Using Model Quaternary Ammonium Corrosion Inhibitors. *Corrosion*, 24-28 March 2019, Nashville, TN, USA. OnePetro, 2019. N NACE-2019-13004.
31. Badeeva E.K., Batyeva E.S., Nizamov I.S. et al. Ammonium salts of *O,O'*-dialkyldithiophosphoric acids: Effective inhibitors for carbon dioxide corrosion of mild steel on the basis of red phosphorus. *Phosphorus, Sulfur, and Silicon and the Related Elements*. 2016. Vol. 191. Iss. 11-12, p. 1640-1641. DOI: [10.1080/10426507.2016.1223662](https://doi.org/10.1080/10426507.2016.1223662)
32. Porcayo-Calderon J., Martínez de la Escalera L.M., Canto J., Casales-Diaz M. Imidazoline Derivatives Based on Coffee Oil as CO₂ Corrosion Inhibitor. *International Journal of Electrochemical Science*. 2015. Vol. 10. Iss. 4, p. 3160-3176. DOI: [10.1016/S1452-3981\(23\)06528-8](https://doi.org/10.1016/S1452-3981(23)06528-8)
33. Sanchez-Salazar E., Vazquez-Velez E., Uruchurtu J. et al. Use of a Gemini-Surfactant Synthesized from the Mango Seed Oil as a CO₂-Corrosion Inhibitor for X-120 Steel. *Materials*. 2021. Vol. 14. Iss. 15. N 4206. DOI: [10.3390/ma14154206](https://doi.org/10.3390/ma14154206)
34. Jing-Mao Zhao, Feng Gu, Tong Zhao, Rui-Jing Jiang. Corrosion inhibition performance of imidazoline derivatives with different pedant chains under three flow rates in high-pressure CO₂ environment. *Research on Chemical Intermediates*. 2016. Vol. 42. Iss. 6, p. 5753-5764. DOI: [10.1007/s11164-015-2401-y](https://doi.org/10.1007/s11164-015-2401-y)
35. Muktiarti N., Ditama I., Soegijono B. Characterization of imidazoline derivatives synthesized from soybean oil fatty acids as corrosion inhibitors on mild steel. *AIP Conference Proceedings*. 2020. Vol. 2242. Iss. 1. N 020023. DOI: [10.1063/5.0007980](https://doi.org/10.1063/5.0007980)
36. Salinas-Solano G., Porcayo-Calderón J., Martínez de la Escalera L.M. et al. Development and evaluation of a green corrosion inhibitor based on rice bran oil obtained from agro-industrial waste. *Industrial Crops and Products*. 2018. Vol. 119, p. 111-124. DOI: [10.1016/j.indcrop.2018.04.009](https://doi.org/10.1016/j.indcrop.2018.04.009)
37. Zagidullin R.N., Mustafin A.G., Khusainova K.G., Sadykov T.T. Patent N 2756210 RF. Method for obtaining corrosion inhibitor based on polypropylene polyamine and carboxylic acid for oilfield, mineralized and hydrogen sulfide-containing media. Publ. 28.09.2021. Bul. N 28 (in Russian).



38. Usman B.J., Ali S.A. Carbon Dioxide Corrosion Inhibitors: A review. *Arabian Journal for Science and Engineering*. 2018. Vol. 43. Iss. 1, p. 1-22. DOI: [10.1007/s13369-017-2949-5](https://doi.org/10.1007/s13369-017-2949-5)
39. Ziqi Zheng, Junying Hu, Noam Eliaz et al. Mercaptopropionic acid-modified oleic imidazoline as a highly efficient corrosion inhibitor for carbon steel in CO₂-saturated formation water. *Corrosion Science*. 2022. Vol. 194. N 109930. DOI: [10.1016/j.corsci.2021.109930](https://doi.org/10.1016/j.corsci.2021.109930)
40. Yuan Lu, Wei Wang, Chen Zhang, Jingmao Zhao. A Novel Imidazoline Derivative Used as an Effective Corrosion Inhibitor for Carbon Steel in a CO₂/H₂S Environment. *International Journal of Electrochemical Science*. 2019. Vol. 14. Iss. 9, p. 8579-8594. DOI: [10.20964/2019.09.06](https://doi.org/10.20964/2019.09.06)
41. Yuanqiang Zhu, Shidong Qu, Yang Shen et al. Investigation on the synergistic effects and mechanism of oleic imidazoline and mercaptoethanol corrosion inhibitors by experiment and molecular dynamic simulation. *Journal of Molecular Structure*. 2023. Vol. 1274. Part 2. N 134512. DOI: [10.1016/j.molstruc.2022.134512](https://doi.org/10.1016/j.molstruc.2022.134512)
42. Zakharov A.I., Demianchenko A.O., Shevnev A.A. Patent N 2769118 RF. Corrosion inhibitor. Publ. 28.03.2022. Bul. N 10 (in Russian).
43. Amir Shamsa, Richard Barker, Yong Hua et al. Impact of corrosion products on performance of imidazoline corrosion inhibitor on X65 carbon steel in CO₂ environments. *Corrosion Science*. 2021. Vol. 185. N 109423. DOI: [10.1016/j.corsci.2021.109423](https://doi.org/10.1016/j.corsci.2021.109423)
44. Yi He, Yanqiu Zhou, Ranran Yang et al. Imidazoline derivative with four imidazole reaction centers as an efficient corrosion inhibitor for anti-CO₂ corrosion. *Russian Journal of Applied Chemistry*. 2015. Vol. 88. N 7, p. 1192-1200. DOI: [10.1134/S1070427215070149](https://doi.org/10.1134/S1070427215070149)
45. Yue Meng, Wenbo Ning, Bin Xu et al. Inhibition of mild steel corrosion in hydrochloric acid using two novel pyridine Schiff base derivatives: a comparative study of experimental and theoretical results. *RSC Advances*. 2017. Vol. 7. Iss. 68, p. 43014-43029. DOI: [10.1039/c7ra08170g](https://doi.org/10.1039/c7ra08170g)
46. Onyeachu I.B., Quraishi M.A., Obot I.B., Haque J. Newly synthesized pyrimidine compound as CO₂ corrosion inhibitor for steel in highly aggressive simulated oilfield brine. *Journal of Adhesion Science and Technology*. 2019. Vol. 33. Iss. 11, p. 1226-1247. DOI: [10.1080/01694243.2019.1585029](https://doi.org/10.1080/01694243.2019.1585029)
47. Arafin M.A., Szpunar J.A. A new understanding of intergranular stress corrosion cracking resistance of pipeline steel through grain boundary character and crystallographic texture studies. *Corrosion Science*. 2009. Vol. 51. Iss. 1, p. 119-128. DOI: [10.1016/J.CORSCI.2008.10.006](https://doi.org/10.1016/J.CORSCI.2008.10.006)
48. Tiu B.D.B., Advincula R.C. Polymeric corrosion inhibitors for the oil and gas industry: Design principles and mechanism. *Reactive and Functional Polymers*. 2015. Vol. 95, p. 25-45. DOI: [10.1016/j.reactfunctpolym.2015.08.006](https://doi.org/10.1016/j.reactfunctpolym.2015.08.006)
49. Azzam E.M.S., Abd El-Salam H.M., Mohamed R.A. et al. Control the corrosion of mild steel using synthesized polymers based on polyacrylamide. *Egyptian Journal of Petroleum*. 2018. Vol. 27. Iss. 4, p. 897-910. DOI: [10.1016/j.ejpe.2018.01.006](https://doi.org/10.1016/j.ejpe.2018.01.006)
50. Tianqi Chen, Zhan Chen, Mengjin Chen, Chaoyang Fu. Evaluation of anti-corrosion performance of poly(maleic acid-co-N-[3-(dimethylamino)propyl]-methacrylamide) as novel copolymer inhibitor for carbon steel in neutral medium. *Journal of Molecular Liquids*. 2021. Vol. 338. N 116638. DOI: [10.1016/j.molliq.2021.116638](https://doi.org/10.1016/j.molliq.2021.116638)
51. Al-Shihry S.S., Sayed A.R., El-Lateef H.M.A. Design and assessment of a novel poly(urethane-semicarbazides) containing thiadiazoles on the backbone of the polymers as inhibitors for steel pipelines corrosion in CO₂-saturated oilfield water. *Journal of Molecular Structure*. 2020. Vol. 1201. N 127223. DOI: [10.1016/j.molstruc.2019.127223](https://doi.org/10.1016/j.molstruc.2019.127223)
52. Umoren S., Solomon M.M., Israel A.U. et al. Comparative Study of the Corrosion Inhibition Efficacy of Polypropylene Glycol and Poly (Methacrylic Acid) for Mild Steel in Acid Solution. *Journal of Dispersion Science and Technology*. 2015. Vol. 36, p. 1721-1735. DOI: [10.1080/01932691.2015.1004411](https://doi.org/10.1080/01932691.2015.1004411)
53. Sun A., Cui G., Liu Q. Capsule corrosion inhibitor loaded with hyperbranched chitosan: Carbon dioxide corrosion protection for downhole pipelines in oil fields. *Colloids and Surfaces A: Physicochemical and Engineering Aspects*. 2023. Vol. 664. N 131106. DOI: [10.1016/j.colsurfa.2023.131106](https://doi.org/10.1016/j.colsurfa.2023.131106)
54. Dzhanelidze S.Z., Zhuravlev V.V., Zhukov A.Yu. et al. Scale control at production wells of Gazpromneft Vostok LLC: results of field tests and technical and economic assessment of the use of encapsulated inhibitor. *PROneft. Professionally about Oil*. 2021. Vol. 6. N 1, p. 95-101. DOI: [10.51890/2587-7399-2021-6-1-94-101](https://doi.org/10.51890/2587-7399-2021-6-1-94-101)
55. Salleh S.Z., Yusoff A.H., Zakaria S.K. et al. Plant extracts as green corrosion inhibitor for ferrous metal alloys: A review. *Journal of Cleaner Production*. 2021. Vol. 304. N 127030. DOI: [10.1016/j.jclepro.2021.127030](https://doi.org/10.1016/j.jclepro.2021.127030)
56. Popoola L.T. Organic green corrosion inhibitors (OGCIs): a critical review. *Corrosion Reviews*. 2019. Vol. 37. Iss. 2, p. 71-102. DOI: [10.1515/correv-2018-0058](https://doi.org/10.1515/correv-2018-0058)
57. Reza N.A., Akhmal N.H., Fadil N.A., Taib M.F.M. A Review on Plants and Biomass Wastes as Organic Green Corrosion Inhibitors for Mild Steel in Acidic Environment. *Metals*. 2021. Vol. 11. Iss. 7. N 1062. DOI: [10.3390/met11071062](https://doi.org/10.3390/met11071062)
58. Shahini M.H., Ramezanzadeh B., Eivaz Mohammadloo H. Recent advances in biopolymers/carbohydrate polymers as effective corrosion inhibitive macro-molecules: A review study from experimental and theoretical views. *Journal of Molecular Liquids*. 2021. Vol. 325. N 115110. DOI: [10.1016/j.molliq.2020.115110](https://doi.org/10.1016/j.molliq.2020.115110)
59. de Haro J.C., Magagnin L., Turri S., Griffini G. Lignin-Based Anticorrosion Coatings for the Protection of Aluminum Surfaces. *ACS Sustainable Chemistry & Engineering*. 2019. Vol. 7. Iss. 6, p. 6213-6222. DOI: [10.1021/acssuschemeng.8b06568](https://doi.org/10.1021/acssuschemeng.8b06568)
60. Gowraraju N.D., Jagadeesan S., Ayyasamy K. et al. Adsorption characteristics of Iota-carrageenan and Inulin biopolymers as potential corrosion inhibitors at mild steel/sulphuric acid interface. *Journal of Molecular Liquids*. 2017. Vol. 232, p. 9-19. DOI: [10.1016/j.molliq.2017.02.054](https://doi.org/10.1016/j.molliq.2017.02.054)
61. Umoren S.A., AlAhmary A.A., Gasem Z.M., Solomon M.M. Evaluation of chitosan and carboxymethyl cellulose as eco-friendly corrosion inhibitors for steel. *International Journal of Biological Macromolecules*. 2018. Vol. 117, p. 1017-1028. DOI: [10.1016/j.ijbiomac.2018.06.014](https://doi.org/10.1016/j.ijbiomac.2018.06.014)



62. Umoren S.A., Eduok U.M. Application of carbohydrate polymers as corrosion inhibitors for metal substrates in different media: A review. *Carbohydrate Polymers*. 2016. Vol. 140, p. 314-341. DOI: [10.1016/j.carbpol.2015.12.038](https://doi.org/10.1016/j.carbpol.2015.12.038)
63. Brindha T., Malarvizhi M., Mallika J. Kinetic and thermodynamic adsorption study of mild steel corrosion and inhibition of Azadirachta Indica gum in hydrochloric acid solution. *International Journal of Current Research*. 2015. Vol. 7. Iss. 9, p. 20510-20518.
64. Qing Zhao, Jixiang Guo, Guodong Cui et al. Chitosan derivatives as green corrosion inhibitors for P110 steel in a carbon dioxide environment. *Colloids and Surfaces B: Biointerfaces*. 2020. Vol. 194. N 111150. DOI: [10.1016/j.colsurfb.2020.111150](https://doi.org/10.1016/j.colsurfb.2020.111150)

Authors: **Mariya V. Chudakova**, Candidate of Chemical Sciences, Senior Researcher, Chudakova.MV@gazprom-neft.ru, <https://orcid.org/0000-0001-9211-9970> (PAO Gazprom Neft, Saint Petersburg, Russia; A.V.Topchiev Institute of Petrochemical Synthesis, RAS, Moscow, Russia), **Kirill A. Ovchinnikov**, Candidate of Chemical Sciences, PhD Candidate, <https://orcid.org/0000-0002-9298-3475> (Peoples's Friendship University of Russia named after Patrice Lumumba, Moscow, Russia), **Dmitrii N. Ulyanov**, Head of Department, <https://orcid.org/0000-0002-3995-3605> (PAO Gazprom Neft, Saint Petersburg, Russia), **Anisa M. Kunakova**, Candidate of Chemical Sciences, Head of the Center, <https://orcid.org/0000-0003-4311-5273> (Gazprom Neft Scientific and Technical Center, Saint Petersburg, Russia), **Liniza R. Saifutdinova**, Candidate of Chemical Sciences, Contractor, <https://orcid.org/0000-0002-9062-4794> (GCSS Neftepromhim LLC, Kazan, Republic of Tatarstan, Russia), **Andrei A. Pimenov**, Doctor of Engineering Sciences, Director, <https://orcid.org/0000-0001-8923-2550> (Tatar Oil Research and Design Institute (TatNIPIneft) of PJSC TATNEFT, Almet'yevsk, Republic of Tatarstan, Russia), **Anton L. Maximov**, Doctor of Chemical Sciences, Corresponding Member of RAS, Director, <https://orcid.org/0000-0001-9297-4950> (A.V.Topchiev Institute of Petrochemical Synthesis, RAS, Moscow, Russia).

The authors declare no conflict of interests.



Lamprophyres of the Peshchernoe gold deposit, their geological position, material composition, and metasomatic alterations (Northern Urals)

Dmitrii V. Kuznetsov¹✉, Sergei Yu. Stepanov², Andrei V. Butnyakov³, Viktoriya S. Igosheva¹

¹ The Zavaritsky Institute of Geology and Geochemistry of the Ural Branch of the RAS, Ekaterinburg, Russia

² South Urals Federal Research Center of Mineralogy and Geoecology of the Urals Branch of the RAS, Ilimenskii State Nature Reserve, Miass, Russia

³ Ural Branch of Polymetal UK, Ekaterinburg, Russia

How to cite this article: Kuznetsov D.V., Stepanov S.Yu., Butnyakov A.V., Igosheva V.S. Lamprophyres of the Peshchernoe gold deposit, their geological position, material composition, and metasomatic alterations (Northern Urals). Journal of Mining Institute. 2025. Vol. 271. N 16393, p. 22-41.

Abstract

The article presents the first data on biotite-hornblende lamprophyres discovered at the Peshchernoe gold deposit. We consider the geological position of lamprophyre dikes in the deposit structure and the relationship of these rocks with tectonically weakened and mineralized zones. The data on the structural position of mineralized zones, faults, dike bodies, metasomatic halos, and host volcanogenic-sedimentary rocks confirm the tectonic nature of the Peshchernoe deposit alteration system. Lamprophyre dikes are pre-ore, as evidenced by the superimposed metasomatic mineral associations. We assume that dikes of andesitic rocks, lamprophyres, and subsequently hydrothermal fluids, including ore-bearing ones, were intruded along the fault zone of northeastern strike at different geological times. The description of mineralogical and chemical transformations of lamprophyres, which occurred as a result of alteration, is given. Two stages of metasomatism are distinguished: carbon dioxide (beresitization-listvenitization) and subsequent alkaline (sodic metasomatism). During carbon dioxide metasomatism, dark-coloured minerals are replaced by chlorite, albitization and sericitization of plagioclase occur, and ferruginous dolomite is formed under the influence of a significant supply of CO₂. Alkaline (sodic) metasomatism is superimposed on the mineral metasomatic paragenesis of the first stage. We consider metasomatic zoning during sodic metasomatism, manifested in one of the spessartite dikes. Chlorite and relics of magmatic dark-coloured minerals are replaced by magnesite, the supply of Na leads to the appearance of newly formed albite, and the supply of S leads to the formation of pyrite, which concentrates iron from other minerals. As a result of the sodic metasomatism, iron content in carbonates decreases in the direction from the outer metasomatic zone to the inner one. We conclude that it was the alkaline-sulphide sodium solutions that performed the ore-bearing function, and beresitization and listvenitization prepared a favourable environment for ore deposition.

Keywords

gold; Peshchernoe deposit; lamprophyres; beresitization-listvenitization; sodic metasomatism; Krasnoturinskii ore cluster; Northern Urals

Funding

The work was carried out under the state budget-funded research of the Institute of Geology and Geochemistry of the Ural Branch of the RAS (N 123011800009-9); part of the analytical work and field studies were performed at the expense of the state budget-funded research of the South Urals Federal Research Center of Mineralogy and Geoecology of the Urals Branch of the RAS (N 122040600006-1).

Received: 01.03.2023

Accepted: 03.06.2024

Online: 30.09.2024

Published: 25.02.2025

Introduction

Dike swarms of various compositions, including lamprophyres, are often present within the ore fields of gold deposits. Lamprophyres are found in gold deposits of various genetic types: orogenic [1, 2], controversial type between orogenic or intrusion-related [3-5], epithermal [6-8], Carlin-type [9-11], reduced intrusion-related RIRGS [12, 13], etc. [14, 15]. Based on frequent spatio-temporal connections between lamprophyres and gold mineralization, it was suggested that they might play a key role in ore formation in mesothermal gold deposits [16-18].



In the Urals, examples of deposits with widespread biotite-hornblende lamprophyre dikes are the Kochkarskoe [19], Berezovskoe [20-22], and Vorontsovskoe [23-25] gold deposits. As a rule, lamprophyre dikes are pre-gold ore [19, 21, 23], as evidenced by the superimposed alteration types. In the case of the Kochkarskoe deposit, most of the gold mineralization occurs in metasomatically altered lamprophyre dikes [19], which have received their own name “tabashki”. At the Vorontsovskoe deposit, the gold content in the dikes does not exceed 0.2 g/t [26].

The Peshchernoe deposit is on the eastern slope of the Northern Urals, 4.5 km southwest of the town of Krasnoturinsk. Mineralogically, it belongs to the Krasnoturinsk ore cluster, which includes skarn-magnetite and copper-skarn deposits, as well as the large Vorontsovskoe gold deposit [23, 27]. The deposit area is on the western limb of the Turinskaya brachysyncline, composed of volcanogenic-sedimentary rocks of the Turinskaya Fm. (S₂-D_{1tr}), which have a gentle (10-20°) eastern, northeastern dip (Fig.1, *b*). The Turyinskaya brachysyncline, in turn, is in the eastern part of the Tagil-Magnitogorsk megazone (Fig.1, *a*), in the southern segment of the Auerbakhovskii volcano-plutonic belt, composed of the Late Silurian-Devonian volcanogenic-sedimentary rocks of intermediate composition [28]. 800 m to the east of the deposit is the Poludenskii diorite massif (Fig.1, *c*) of the Early-Middle Devonian gabbro-diorite-granite Auerbakhovskii complex [29]. Small diorite bodies, presumably of the same complex, are present at the deposit.

The Peshchernoe gold deposit was discovered by the Ural Branch of AO Polymetal UK and is currently being mined by ZAO Zoloto Severnogo Urala. The deposit mineralization is classified as gold-low-sulphide-quartz [30]. Volcanogenic-sedimentary rocks in the deposit structure include tuffaceous siltstones and tuffaceous sandstones with interlayers of tuff gritstones, which are intruded by numerous dikes of mafic and intermediate rocks. In terms of chemical composition, tuffaceous siltstones and tuffaceous sandstones correspond to intermediate volcanics of the normal petrochemical series. Gold mineralization is represented by mineralized zones in metasomatically altered volcanogenic-sedimentary rocks (tuffaceous siltstones and tuffaceous sandstones), less often in andesites and basaltic andesites. The most productive ore areas contain minerals of polymetallic paragenesis (pyrite, arsenopyrite, galena, fahlore, chalcopyrite, sphalerite), and gold is found mainly in the form of native segregations, often filling fractures in sulphides.

The position of mineralized zones at the deposit is controlled by northeastern-trending faults occurring subconformably with the contact of volcanogenic-sedimentary rocks of the Turinskaya Fm. and the coeval basalt sequence (Fig.2, *a, b*). The faults are accompanied by cataclasis and crushing zones and, according to observations, are marked by lamprophyre dikes. Attitude was measured for several lamprophyre dikes by sampling azimuthally oriented cores. The dip azimuth (d.a.) of the dikes is 120-125° with a dip angle of 55-60°, which is subconformable with the direction and dip angle of the ore zone. The lamprophyre bodies intersect a tuffaceous siltstone sequence, which, according to the bedding (Fig.2, *c*), dips northeast at an angle of 10-15°. Dike thickness ranges from a few tens of centimetres to three metres. Dike contacts and the host tuffaceous siltstones are sharp, with hardening zones to 5 cm thick.

Gold mineralization may have spatial, temporal, structural, paragenetic, or genetic relation to dike complexes. Study of lamprophyres as a component of dike clusters at gold deposits can provide information on the age boundaries of ore formation, the nature and character of metasomatizing fluids, including ore-bearing ones. Since lamprophyres have a consistent mineral and chemical composition, they are more representative for the study of superimposed mineralogical and chemical metasomatic alterations compared to volcanogenic-sedimentary rocks.

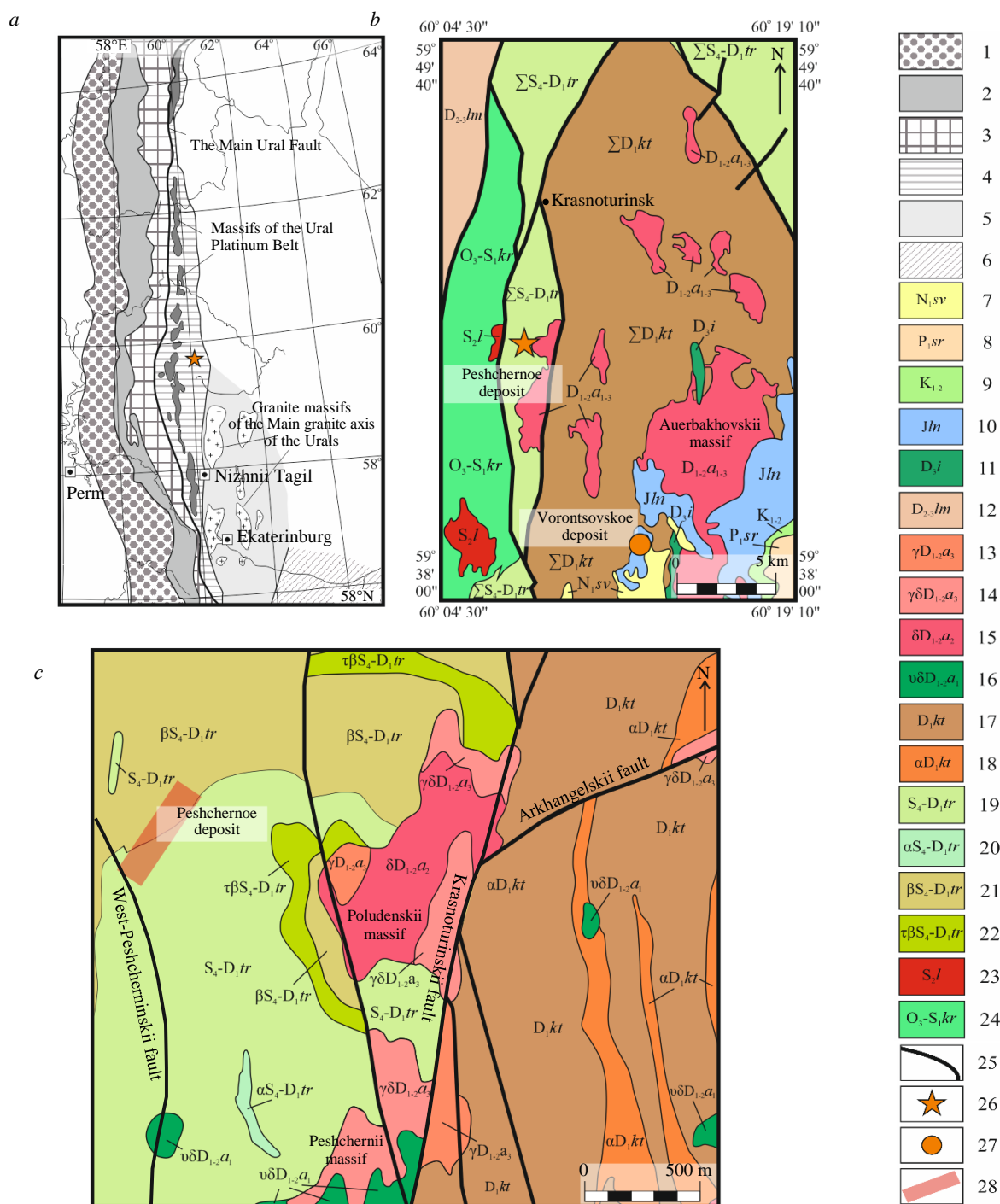


Fig.1. Tectonic zoning of the Middle and Northern Urals (a) according to [31], geological map of the Turyinskaya brachysyncline (b) and the Peshchernoe deposit area (c), compiled based on the report¹ materials and [29, 30] with additions

- 1 – Cis-Ural foredeep; 2-6 – zones: West Ural (2), Central Ural (3), Tagil-Magnitogorsk (4), East Ural (5), Trans-Ural (6); 7-10 – formations: Svetlinskaya (7), Serovskaya (8), Mysovskaya, Kamyshlovskaya, and Zaikovskaya (9), Langurskaya (10); 11 – gabbrodolerites of the Ivdel complex; 12 – Limkinskaya Fm.; 13-16 – granitoids of the Auerbachovskii complex ($D_{1-2}a_{1-3}$): granites (13), granodiorites (14), diorites (15), gabbrodiorites and gabbro (16); 17, 18 – rocks of the Krasnoturinskaya Fm. (ΣD_{1kt}): tuffaceous sandstones and tuffaceous siltstones (17), andesites and their tuffs (18); 19-22 – rocks of the Turinskaya Fm. (ΣS_4-D_{1tr}): tuffaceous sandstones and tuffaceous siltstones (19), andesites and their tuffs (20), basalts and their tuffs (21), trachybasalts and their tuffs (22); 23 – granitoids of the Levinskii complex; 24 – Krasnouralskaya Fm.; 25 – faults; 26 – Peshchernoe deposit; 27 – Vorontsovskoe deposit; 28 – Peshchernoe deposit area

¹ Report of the Serov geological survey party on extensive additional geological study at 1:50,000 scale of the Serov prospect within sheets O-41-1-A (eastern half), O-41-1-B (western half), O-41-1-V, O-41-1-G (western half), O-41-13-A, O-41-13-B (north-western quarter), O-41-13-V, conducted in 1974-1978.

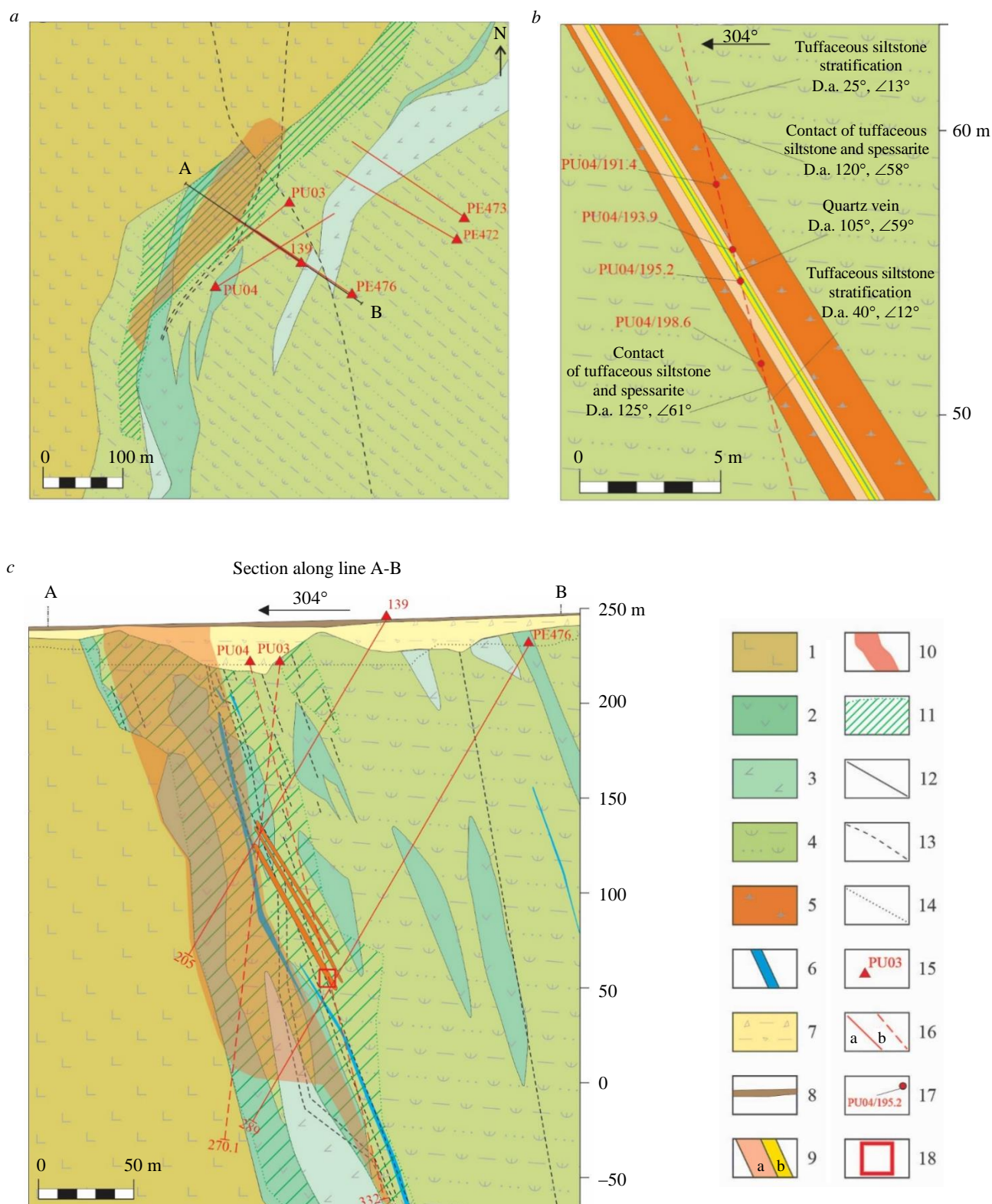


Fig.2. Sketch geological map (a) and section (b, c) of the Peshchernoe deposit
 (based on materials from OOO Krasnoturinsk-Polymetal with additions)

- 1 – basalts; 2 – andesites; 3 – andesibasalts; 4 – tuffaceous siltstones; 5 – spessartites; 6 – quartz veins; 7 – weathering crust;
 8 – deluvial deposits; 9 – transition (a) and inner (b) metasomatic zones in a spessartite dike; 10 – ore zone;
 11 – metasomatic alterations; 12 – geological boundaries; 13 – tectonic faults; 14 – lower boundary of the quarry at the time of drilling exploratory
 wells in 2022; 15 – exploratory wells; 16 – projections of exploratory well axes in the section plane (a) and across (b); 17 – sampling points
 (PU04/191.4 – dike margin, hanging wall, outer metasomatic zone; PU04/193.9 – transition metasomatic zone; PU04/195.2 – dike central part,
 inner metasomatic zone; PU04/198.6 – dike margin, footwall, outer metasomatic zone); 18 – section area shown at an enlarged scale in Fig.2, b



Research methods and materials

The material composition of lamprophyres was studied on samples from several dikes selected from the core of exploratory wells. Their location is indicated in the sketch geological map of the deposit (Fig.2, *a*). The first part of the sample number corresponds to the designation of the exploratory well, and the second, to the sampling depth. The composition of minerals was determined in polished sections on a TESCAN Mira LMS scanning electron microscope using an EDS detector at the Geoanalytic Collective Use Centre of the IGG UB RAS, Ekaterinburg. The following setups were used for surveying: accelerating voltage of 20 kV, electron beam current of 0.8 nA, beam diameter of 8-9 nm. The contents of petrogenic components in rocks were determined by X-ray fluorescence analysis on an SRM-35 multichannel spectrometer. The detection limits for the main part of petrogenic components using this method are in the range of 0.006-0.09 wt.%. The microelement composition of rocks was studied by the ICP-MS method on an Agilent 7700x mass spectrometer at the South Urals Federal Research Center of Mineralogy and Geoecology of the Urals Branch of the RAS, Miass. Thermal analysis was performed on a Diamond TG-DTA thermal analyser and semi-quantitative X-ray phase analysis on an XRD-7000 X-ray diffractometer at the Geoanalyst Collective Use Centre. Gold contents were determined for several samples by atomic absorption spectrometry with electrothermal atomization on a ContrAA 700 spectrometer. The gold detection limit was 0.8 mg/t, and the error did not exceed 40 rel.%.

Research results

Petrographic and mineralogical characteristics of rocks. The rocks of the studied dikes have a dark grey colour, massive texture, porphyritic, lamprophyre, and ocellar structures. Almost all the lamprophyres that make up the dikes are metasomatically altered to varying degrees, which is expressed in the replacement of intermediate plagioclase by albite, the development of dolomite, chlorite, and sericite. Of the preserved primary (magmatic) mineral paragenesis, amphibole, biotite and plagioclase relics are present in the rocks. According to the set of preserved primary minerals, as well as textural and structural features, lamprophyres of the Peshchernoe deposit correspond to spessartites and kersantites [18]. Porphyritic phenocrysts in spessartites are represented by amphibole (Fig.3, *b, c*), and in kersantites – by biotite, which is replaced by a mineral aggregate of chlorite and sericite (Fig.3, *a*). Ocelli have a rounded shape, 1-2 mm in size, and are composed of an aggregate of dolomite, quartz, and albite (Fig.3, *c*). The rock bulk consists of plagioclase, dolomite, quartz, chlorite, and sericite. The pyrite content in the studied samples varies from 0.5 to 5 vol.%. Sphalerite, pentlandite, and chalcopyrite are present in pyrite as small inclusions. Monazite, apatite, rutile, and chrome spinelide were found among the accessory minerals.

In the central part of one of the spessartite dikes there is a fracture filled with quartz, probably marking the permeability zone. Along the well axis the thickness of this dike was 12.2 m, with a true thickness of 3.1 m (see Fig.2, *c*). The fracture dip azimuth is 105°, with a dip angle of 60°, which is subconformable with the dip direction of the dike itself. From the permeable zone towards the edge of the dike there are several zones of metasomatic alterations: inner, transition, and outer. The boundaries between the metasomatic zones are distinct. Sometimes quartz veinlets 1-2 mm thick run along them. The rock in the outer metasomatic zone is dark grey. The mineral composition is similar to that of metasomatically altered spessartites from other dikes, except that amphibole, in addition to chlorite, begins to be replaced by magnesite (Fig.3, *d*). In the transition zone, spessartites acquire a light grey colour with a greenish tint. In this zone, amphibole and biotite are no longer preserved, chlorite disappears, plagioclase is completely albitized, and the magnesite content increases. A characteristic feature of the rocks in the transition metasomatic zone is an increase in sericite proportion in mineral composition (Fig.3, *e*). Part of sericite is represented by bright green fuchsite, which causes the greenish tint of the rock. In the transition metasomatic zone relative to the outer zone, the pyrite content increases from 0.5 to 2 vol.%. Spessartites in the inner metasomatic zone are light grey with a beige tint. The mineral composition of the rocks in the inner metasomatic zone is simplified, chlorite and

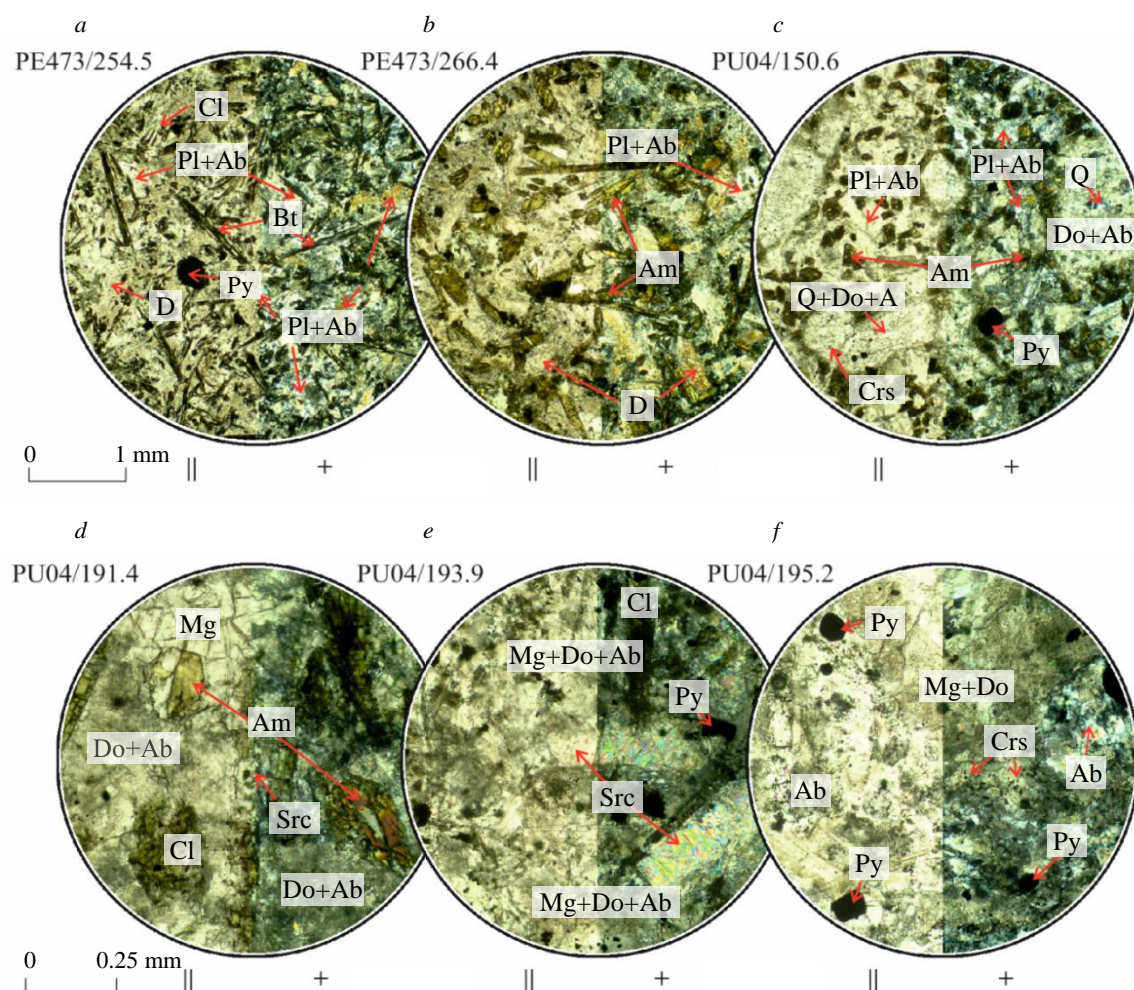


Fig.3. Micrographs of thin sections of kersantite (a), spessartite (b, c)

and metasomatic zones in a dike of altered spessartites: outer (d), transition (e), and inner (f) zone

|| – nicols are parallel, + – nicols are crossed; Ab – albite, Am – amphibole, Bt – biotite, Cl – chlorite, Crs – chrome spinelide, Do – dolomite, Mg – magnesite, Pl – plagioclase, Py – pyrite, Q – quartz, Src – sericite

sericite almost disappear (Fig.3, f). Albite content in the rocks in this zone exceeds 50 vol.%. In addition to albite, developing after plagioclase, independent grains appear – aggregates of this mineral. Pyrite content in the inner metasomatic zone increases to 5 vol.%. The proportion of quartz in the mineral composition of spessartites during the transition from the outer metasomatic zone to the inner one slightly decreases.

Magmatic mineral paragenesis. Amphibole of spessartites is widespread in the form of grains of prismatic habit, to 2 mm in elongation, pleochroic from pale greenish-yellow to brownish-green. In chemical composition (Table 1) it corresponds to magnesiohastingsite [32]. Biotite is present in spessartites and kersantites, forms tabular grains to 1.5 mm in size along the pinacoid plane with a thickness of no more than 0.1 mm (Fig.4, a). In thin section it is pleochroic from greyish-green to dark greenish-brown. Biotite belongs to the annite-phlogopite isomorphous series with an admixture of eastonite-siderophyllite component (see compositions in Table 1). Plagioclase is preserved as relics in the bulk (Fig.4, b) and has an andesine composition. Accessory chrome-spinel, which is preserved at all stages of metasomatic alterations, can also be attributed to the minerals of magmatic paragenesis. Chrome-spinel is usually observed inside ocelli in the form of rounded, isometric grains (Fig.4, d), as well as octahedrons measuring 0.01-0.05 mm, less often in the bulk in the form of grains with a square cross-section, to 0.2 mm in size (Table 1). According to the classification by end members [33], this mineral from spessartites corresponds to aluminous magnesiochromite. Another ubiquitous



accessory mineral, which is present in all studied lamprophyre samples, is apatite. Apatite consists of grains elongated in one direction, to 0.1 mm long and 0.01-0.02 mm wide (Fig.4, c). In chemical composition it corresponds to fluorapatite [34], has increased SiO₂ and SO₃ contents, low P₂O₅ contents, and reduced sum values. Low sum values may indicate enrichment of apatite in hydroxyl group and carbon, but the used electron microscopy method only enables to assume such a conclusion. Apatite composition changes insignificantly depending on the location in a particular zone of metasomatic alteration of spessartites. From the outer metasomatic zone to the inner one, CaO, P₂O₅ contents and the sum values statistically increase in apatite, which may indicate a decrease in CO₂ and OH proportion in it. A mineral containing Sr, Ba and S, probably a sulphate of the barite-celestine series, is present in apatite in the form of small inclusions.

Table 1

Representative chemical compositions of minerals of metasomatically altered spessartites, wt. %

Sample	PU04/ 191.4	PU04/ 191.4	PU04/ 191.4	PU04/ 191.4	PU04/ 191.4	PU04/ 191.4	PU04/ 191.4	PU04/ 195.2	PU04/ 191.4	PU04/ 191.4	PU04/ 191.4	PU04/ 195.2
Mineral	Am	Am	Bt	Bt	Cl	Cl	Crs	Crs	An	Ab	Ap	Ap
SiO ₂	41.04	40.23	37.14	37.81	33.93	34.55	0.83	0.42	53.53	67.62	1.74	1.53
TiO ₂	1.48	1.86	0.93	0.92	—	—	0.3	0.43	—	—	—	—
Al ₂ O ₃	14.14	14.30	16.70	16.98	15.86	14.95	18.94	20.32	29.74	20.31	0.27	0.19
Cr ₂ O ₃	—	—	—	—	—	—	47.82	44.02	—	—	—	—
FeO*	11.28	11.87	12.89	12.14	15.61	14.38	17.64	21.67	0.56	—	0.66	0.35
MnO	0.23	0.16	—	0.16	—	—	—	—	—	—	—	—
MgO	13.82	13.53	18.41	18.40	21.52	23.71	13.41	12.98	—	—	0.50	0.43
CaO	11.82	11.90	0.18	0.18	0.11	0.35	—	—	10.41	0.08	52.11	55.28
Na ₂ O	2.43	2.47	0.65	0.90	—	—	—	—	5.34	11.99	0.73	0.46
K ₂ O	1.04	1.02	7.66	8.00	—	—	—	—	0.42	—	—	—
P ₂ O ₅	—	—	—	—	—	—	—	—	—	—	34.79	37.14
SO ₃	—	—	—	—	—	—	—	—	—	—	2.16	1.57
SrO	—	—	—	—	—	—	—	—	—	—	1.01	0.98
F	—	—	—	—	—	—	—	—	—	—	2.16	2.1
Cl	—	—	—	—	—	—	—	—	—	—	0.44	0.47
O = F, Cl*	—	—	—	—	—	—	—	—	—	—	1.01	0.99
H ₂ O*	2.05	2.04	4.06	4.11	12.09	12.27	—	—	—	—	—	—
Total	99.33	99.38	98.62	99.60	99.12	100.2	98.94	99.84	100*	100*	95.56	99.51

Estimated formula units

	24 O atoms		22 cations		10 cations		4 O atoms		5 cations and 8 anions		17 cations and 26 anions	
Si	6.04	5.94	2.74	2.76	3.37	3.38	0.03	0.01	2.41	2.94	0.31	0.26
Ti	0.16	0.21	0.05	0.05	0.00	0.00	0.01	0.01	—	—	—	—
Al ^{IV}	1.96	2.06	1.26	1.24	0.63	0.62	—	—	—	—	—	—
Al ^{VI}	0.49	0.43	0.19	0.22	1.22	1.10	—	—	—	—	—	—
Al	—	—	—	—	—	—	0.70	0.74	1.41	1.04	0.06	0.04
Cr	—	—	—	—	—	—	1.18	1.08	—	—	—	—
Fe ²⁺	1.05	1.12	0.80	0.74	1.29	1.18	0.41	0.42	0.02	—	0.10	0.05
Fe ³⁺	0.34	0.35	0.00	0.00	0.00	0.00	0.05	0.14	—	—	—	—
Mn	0.03	0.02	0.00	0.01	0.00	0.00	—	—	—	—	—	—
Mg	3.03	2.98	2.02	2.00	3.18	3.45	0.63	0.60	—	—	0.13	0.11
Ca	1.86	1.88	0.01	0.01	0.01	0.04	—	—	0.31	0.00	9.78	9.99
Na	0.69	0.71	0.09	0.13	0.00	0.00	—	—	0.61	1.01	0.25	0.15
K	0.20	0.19	0.72	0.74	0.00	0.00	—	—	0.04	—	—	—
P	—	—	—	—	—	—	—	—	—	—	5.16	5.30
S	—	—	—	—	—	—	—	—	—	—	0.28	0.20
Sr	—	—	—	—	—	—	—	—	—	—	0.10	0.10
F	—	—	—	—	—	—	—	—	—	—	1.20	1.12
Cl	—	—	—	—	—	—	—	—	—	—	0.13	0.13

Note. FeO* – total iron FeO and Fe₂O₃. O = F, Cl*, H₂O* – estimated values. 100* – contents are normalized to 100 %. The estimation of formula units was performed by the MineralCalc software with the determination of the Fe²⁺ and Fe³⁺ indices using the G.T.R. Droop method [35].

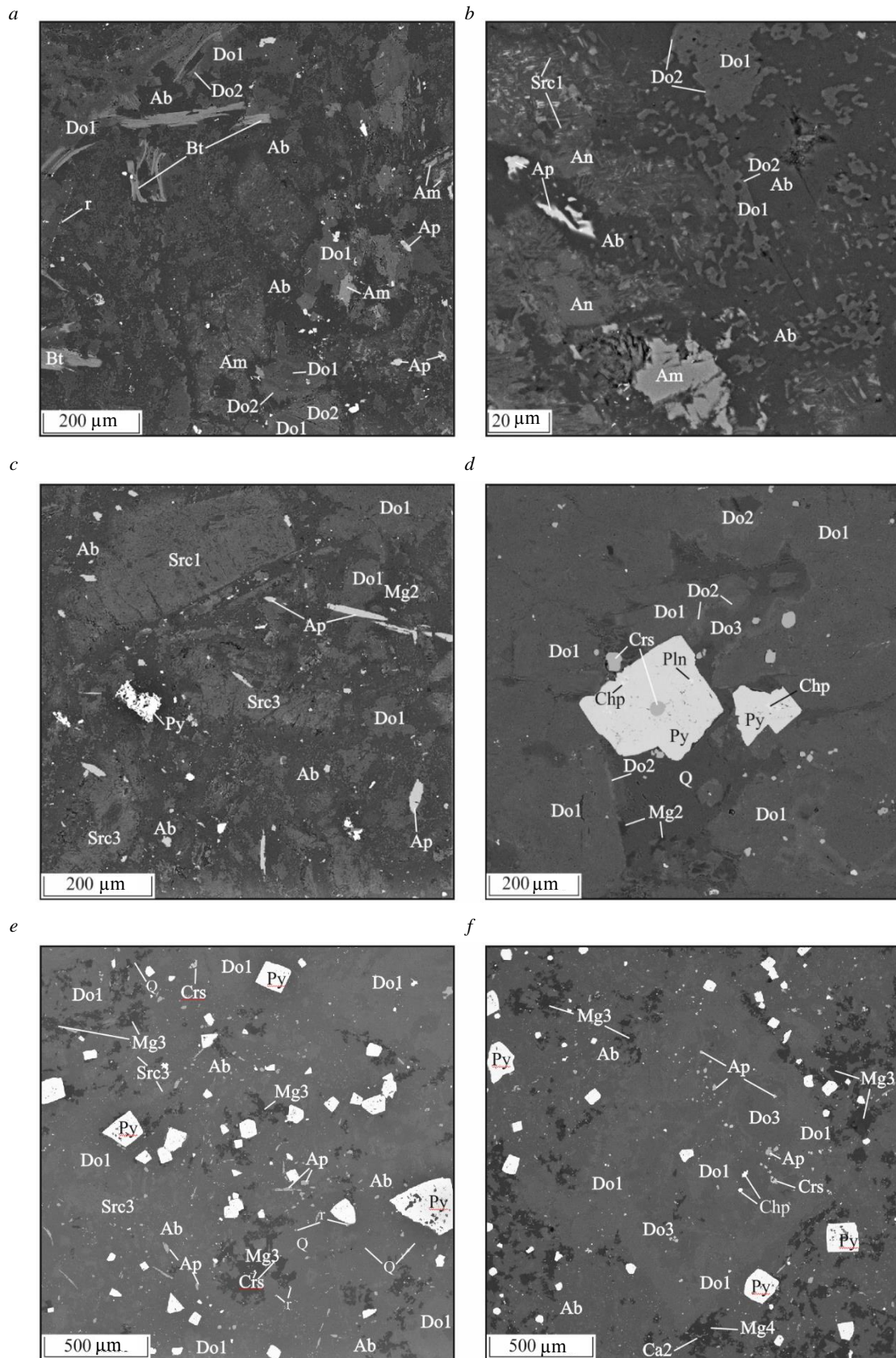


Fig.4. Backscattered electron micrographs of metasomatically altered spessartites.
 Outer metasomatic zone, sample PU04/191.4 (a, b); transition metasomatic zone, sample PU04/193.9 (c, d);
 inner metasomatic zone, PU04/195.2 (e, f)

An – anorthite, Ap – apatite, Ca – calcite, Chp – chalcopryrite, Pln – pentlandite. For other symbols, see Fig.3



Metasomatic mineral parageneses. Chlorite in lamprophyres of the Peshchernoe deposit replaces amphibole and biotite and corresponds to clinocllore in chemical composition (Table 1). Replacement of amphibole and biotite by chlorite is accompanied by the formation of fine dissemination of rutile with individual grains less than 0.01 mm in size. The main metasomatic mineral in altered spessartites is albite, which makes up about 40 vol.% in the rocks and is a primary plagioclase replacement product. It is found both in independent segregations and in intergrowths with sericite and plagioclase relics with individual grains measuring 0.01-0.02 mm. In metasomatites after spessartites with pronounced metasomatic zoning, albite content in the transition zone increases to 50 vol.% and in the inner zone to 55 vol.%. In the transition and inner metasomatic zones, newly formed albite appears. Unlike the similar mineral replacing andesine, it has independent larger grains to 0.1 mm in size. Carbonate in altered lamprophyres is represented by ferruginous dolomite (Table 2) and makes up 35-40 vol.% in the rocks. Zoning is observed in dolomite grains, in which the central part of the dolomite grains is less ferruginous than the marginal part (Fig.4, *b, d, f*).

Table 2

Chemical composition of carbonates, wt.%

N	Sample	Mineral	FeCO ₃	MnCO ₃	MgCO ₃	CaCO ₃	SrCO ₃	Total
1	PE472/264.8	Do1	10.43	1.18	30.64	57.75	0.00	100.0
2	PU04/191.4	Do1	9.20	0.82	30.81	59.17	0.00	100.0
3	PU04/191.4	Do1	10.98	0.87	30.48	57.67	0.00	100.0
4	PU04/191.4	Do1 c	8.83	1.71	31.26	58.20	0.00	100.0
5	PU04/191.4	Do2 e	17.99	0.67	27.20	53.01	1.12	100.0
6	PU04/193.9	Do1	9.90	0.52	30.56	59.02	0.00	100.0
7	PU04/193.9	Do1	10.16	0.66	29.24	59.95	0.00	100.0
8	PU04/193.9	Do1 c	9.61	1.87	31.49	57.03	0.00	100.0
9	PU04/193.9	Do2 e	14.60	2.76	28.19	53.12	1.33	100.0
10	PU04/193.9	Do1 c	11.00	0.51	31.07	57.09	0.32	100.0
11	PU04/193.9	Do2 e	12.49	3.23	29.23	53.84	1.20	100.0
12	PU04/193.9	Do3	5.67	1.02	35.38	56.40	1.53	100.0
13	PU04/195.2	Do1	8.94	1.40	31.11	58.56	0.00	100.0
14	PU04/195.2	Do3 c	3.66	1.31	35.79	57.87	1.37	100.0
15	PU04/195.2	Do1 e	8.49	1.18	32.56	57.77	0.00	100.0
16	PU04/195.2	Do3 c	4.26	1.03	35.77	57.59	1.36	100.0
17	PU04/195.2	Do1 e	10.90	1.79	29.65	57.38	0.29	100.0
18	PU04/191.4	Mg1	59.03	0.98	37.99	2.00	0.00	100.0
19	PU04/191.4	Mg1	56.50	1.30	40.48	1.73	0.00	100.0
20	PU04/193.9	Mg2	36.47	0.55	62.49	0.49	0.00	100.0
21	PU04/193.9	Mg2	33.94	1.94	62.89	1.23	0.00	100.0
22	PU04/195.2	Mg3	13.98	0.47	85.05	0.50	0.00	100.0
23	PU04/195.2	Mg3	13.12	0.00	86.67	0.22	0.00	100.0
24	PU04/195.2	Mg4	8.38	0.00	90.72	0.91	0.00	100.0
25	PU04/195.2	Ca1	1.88	0.00	4.09	94.03	0.00	100.0
26	PU04/195.2	Ca1	1.71	0.00	4.55	93.10	0.63	100.0
27	PU04/195.2	Ca2	1.49	0.39	1.03	97.10	0.00	100.0

Notes: c – grain centre; e – grain edge; 18, 19 – replaces amphibole; 25, 26 – at the boundary between dolomite and magnesite; 27 – fills a fracture in magnesite.

In addition to dolomite chemical composition change within a single grain, variations in composition are observed during the transition from one metasomatic zone to another. Three types of dolomite can be distinguished by chemical composition. In the outer and transition metasomatic zones, the grains centre is represented by dolomite-1 (Do1 in Table 2) with 8.5-11.0 wt.% FeCO₃. Dolomite-2 (Do2) from the marginal part of the grains is more ferruginous. In the outer metasomatic zone, FeCO₃ content in it reaches 18.0 wt.%, in the transition zone – 12.5-14.6 wt.%. In addition to a higher iron content, Do2 has a SrCO₃ content of 1.1-1.3 wt.%, while in Do1 the content of this component



is to 0.3 wt.%. In the inner metasomatic zone, the central part of the grains is dolomite-3 (Do3), with a FeCO_3 content of 3.7-4.3 wt.% and SrCO_3 of about 1.5 wt.%. The marginal part of the dolomite grains in the inner metasomatic zone is similar in chemical composition to Do1. In addition to dolomite, magnesite appears in the outer metasomatic zone. Magnesite replaces porphyritic phenocrysts of amphibole and in chemical composition corresponds to breunnerite (Mg1 in Table 2), with FeCO_3 content of 56-59 wt.%. In the transition metasomatic zone, magnesite becomes less ferruginous (Mg2) and has FeCO_3 content of 34-36.5 wt.%. In the inner metasomatic zone, two types of magnesite (Mg3 and Mg4) are present, differing in iron content. In the first type FeCO_3 is from 13 to 14 wt.%, in the second – about 8.4 wt.%.

Thus, in the direction from the outer metasomatic zone to the inner one, the iron content of carbonates in altered spessartites decreases. In the inner metasomatic zone, in addition to dolomite and magnesite, small calcite segregations were found. In one case, calcite is located between dolomite and magnesite (Ca1 in Table 2), in the other it fills a microfracture in magnesite (Ca2, Fig.4, f). Sericite in metasomatically altered spessartites belongs to the muscovite – paragonite isomorphous series (Table 3). In different parts of the metasomatic halo, the percentage of sericite varies and its chemical composition changes. In the outer metasomatic zone, sericite makes up 5 vol.%. It is dominated by the paragonite end member with Na_2O and K_2O contents of 5 wt.% each (Src1 in Table 3). In the transition metasomatic zone, the amount of sericite increases to 10 vol.% with the size of individual grains being 0.5-1 mm (Fig.4, c).

According to the chemical composition, three types of sericite are distinguished in this zone. The first type is close to sericite from the outer zone with a slight predominance of the paragonite end member and Na_2O and K_2O contents of 3.2 and 7.0 wt.%, respectively. In the second type of sericite (Src2), the muscovite end member predominates, and to 10 mol.% of the fuchsite end member is observed. The contents in it are, wt.%: Na_2O 1.6-1.8, K_2O 5.5-5.7, and Cr_2O_3 to 1.6. Sericite of the third type is muscovite (Src3) with Na_2O content of about 0.6 wt.% and K_2O 9.4 wt.%. In the inner metasomatic zone, sericite content is 1-2 vol.% and it is represented by muscovite.

Table 3

Chemical composition of sericite, wt. %

Component	PU04/191.4	PU04/193.9	PU04/193.9	PU04/193.9	PU04/193.9	PU04/195.2	PU04/195.2	PU04/195.2
	Src1	Src1	Src2	Src2	Src3	Src3	Src3	Src3
SiO_2	54.66	52.49	49.80	49.69	48.63	48.98	49.38	49.65
Al_2O_3	28.62	30.14	35.25	35.34	32.64	32.05	32.98	31.15
Cr_2O_3	–	–	1.59	1.46	–	–	–	–
FeO^*	1.13	1.39	0.30	0.45	2.5	2.48	1.85	2.98
MgO	0.36	1.25	0.82	0.83	1.74	2.29	1.98	1.81
CaO	0.92	–	0.30	0.28	–	–	–	–
Na_2O	4.72	3.16	1.60	1.83	0.58	0.45	0.31	0.28
K_2O	4.95	6.96	5.68	5.48	9.39	9.22	8.94	9.60
H_2O^*	4.64	4.60	4.60	4.61	4.53	4.54	4.57	4.52
Total	100.0	100.0	100.0	100.0	100.0	100.0	100.0	100.0
Content of end-members, mol. %								
Muscovite	33	44	52	49	74	73	79	77
Paragonite	62	46	34	38	11	10	7	6
Celadonite	5	10	5	5	15	17	14	17
Fuchsite	–	–	9	8	–	–	–	–

Note. Muscovite $\text{KAl}_2(\text{AlSi}_3\text{O}_{10})(\text{OH}_2)$, paragonite $\text{NaAl}_2(\text{AlSi}_3\text{O}_{10})(\text{OH}_2)$, celadonite $\text{K}(\text{Mg}, \text{Fe}^{3+})(\text{Si}_4\text{O}_{10})(\text{OH}_2)$, fuchsite $\text{K}(\text{Al}, \text{Cr})_3(\text{Si}_3\text{O}_{10})(\text{OH}_2)$ were used as end members.



Sulphides. In the metasomatically altered lamprophyres of the Peshchernoe deposit, sulphides are mainly represented by pyrite, the content of which averages 0.5 vol.%. Pyrite has sections of predominantly complex shape, less often rectangular, with an average size of 0.01 mm, rarely to 0.05 mm. In different metasomatic zones developed along the spessartite dike, the amount and morphology of pyrite vary. In the outer metasomatic zone, the content and character of pyrite are similar to those observed in the other lamprophyre dikes. In the transition metasomatic zone, pyrite increases to 2 vol.%, the sections also have a predominantly complex shape with the presence of rectangles, the size of the sections is on average 0.01-0.03 mm, rarely to 0.2 mm. In the inner metasomatic zone, pyrite increases to 5 vol.%, the average grain size increases to 0.05 mm. The shape of the pyrite sections in the inner zone is mainly rectangular, sections corresponding to the shape of grains in the form of pyritohedra appear (Fig.4, *e*). The chemical composition of pyrite is quite consistent, with small variations in the content of Co and Ni impurities. An As impurity was found in a single grain from the inner metasomatic zone. Sphalerite, chalcopyrite, and pentlandite are present in the form of inclusions in pyrite, as well as small independent grains (Fig.4, *d, f*).

Petrochemical characteristics of rocks. The contents of petrogenic components and rare elements in lamprophyres of the Peshchernoe gold deposit are given in Table 4. Low SiO₂ contents and high loss on ignition (LOI) values in lamprophyres indicate metasomatic alterations and can serve as a criterion for assessing their manifestation scale. In the least altered spessartites, the SiO₂ contents are 40-41 wt.% with a LOI of 12.5-13.5. In the most altered samples, these values are 34.7-36 wt.% and 15.5-17.1 wt.%, respectively. In kersantites from the Peshchernoe deposit, the SiO₂ values are higher than in spessartites, from 42 to 45 wt.%, and the LOI is lower – 8-10 wt.%.

Table 4

**Content of petrogenic components (wt.%), gold (mg/t), and rare elements (g/t)
in lamprophyres from the Peshchernoe gold deposit**

Component	Sample											
	PU03/ 96.6	PU04 150.6	PU04/ 167.9	PE472/ 264.8	PU04/ 191.4	PU04/ 193.9	PU04/ 195.2	PU04/ 198.6	PE472/ 179.5	PE473/ 254.5	Spec_B	Kers_B
	1	2	3	4	5	6	7	8	9	10	11	12
SiO ₂	34.72	40.66	36.03	39.82	38.52	35.65	38.89	40.89	44.81	42.39	46.04	52.55
TiO ₂	0.64	0.83	0.55	0.73	0.67	0.78	0.71	0.78	1.22	1.18	0.72	1.19
Al ₂ O ₃	11.85	12.79	10.27	11.81	10.45	12.02	11.18	11.58	14.62	14.18	12.54	12.08
FeO*	5.17	7.54	6.20	7.53	7.76	6.39	5.27	7.54	7.34	7.24	9.82	5.90
MnO	0.12	0.13	0.13	0.16	0.14	0.13	0.11	0.13	0.19	0.14	0.16	0.12
MgO	8.12	9.62	12.23	13.44	12.44	10.22	11.28	10.46	9.59	8.04	13.02	8.34
CaO	15.38	10.60	11.68	10.12	10.75	10.29	9.89	11.43	8.03	9.48	8.17	6.7
Na ₂ O	4.67	3.04	3.92	2.72	2.75	4.24	5.01	3.07	3.19	4.98	2.1	2.4
K ₂ O	0.15	0.58	0.42	0.18	0.40	0.77	0.21	0.56	1.32	0.24	0.66	5.0
P ₂ O ₅	0.15	0.40	0.21	0.30	0.29	0.31	0.27	0.34	0.71	0.72	0.15	0.84
LOI	15.42	13.05	16.06	12.44	15.02	17.11	13.37	12.57	7.96	10.21	5.8	4.3
S	3.15	0.33	1.94	0.30	0.28	1.73	3.24	0.21	0.44	0.64	0.22	0.16
Total	99.56	99.57	99.64	99.54	99.47	99.63	99.44	99.56	99.41	99.43	99.75	99.78
Au	–	–	–	<0.8	2.8	4.3	23.0	8.2	–	–	–	–
Li	0.86	25.1	11.4	22.5	22.2	2.77	7.82	17.6	6.53	14.6	–	–
Be	0.46	0.89	0.59	0.80	0.74	0.81	0.44	0.91	1.18	1.19	–	–
Sc	20.6	24.2	26.9	26.8	28.0	25.4	26.2	25.8	20.2	20.4	–	–
V	129	183	128	164	148	168	116	170	212	219	–	–
Cr	178	333	480	535	501	454	273	348	307	292	–	–
Co	30.6	34.1	38.6	39.3	41.4	36.2	39.6	36.4	28.3	29.7	–	–
Ni	175	185	265	254	253	215	254	232	136	131	–	–
Cu	40.9	54.7	49.1	49.3	35.6	53.8	55.4	50.1	85.2	80.6	–	–
Zn	45.6	56.8	47.3	58.5	50.1	51.2	46.0	58.0	64.8	69.9	–	–
Ga	11.6	13.0	10.0	11.7	11.0	11.0	10.8	12.4	14.8	15.2	–	–
As	212	9.07	110	3.80	2.93	63.7	191.1	2.55	9.32	6.67	–	–
Rb	2.51	9.15	6.16	1.91	6.52	10.7	3.08	6.46	6.37	19.8	–	–



End of Table 4

Component	Sample											
	PU03/ 96.6	PU04 150.6	PU04/ 167.9	PE472/ 264.8	PU04/ 191.4	PU04/ 193.9	PU04/ 195.2	PU04/ 198.6	PE472/ 179.5	PE473/ 254.5	Spec_B	Kers_B
	1	2	3	4	5	6	7	8	9	10	11	12
Sr	1618	1060	851	665	969	732	820	1236	1091	702	–	–
Y	10.5	14.5	10.6	14.1	12.9	13.4	13.4	14.9	17.8	18.0	–	–
Zr	66.7	91.8	72.4	91.2	90.2	75.3	74.6	93.7	134	132	–	–
Nb	1.74	2.87	1.43	1.30	1.57	1.10	0.85	2.48	4.41	7.58	–	–
Mo	0.70	0.18	0.54	0.13	0.10	<0.10	<0.10	0.42	1.18	1.00	–	–
Cd	0.24	0.25	0.16	0.15	0.16	0.17	0.15	0.15	0.19	0.17	–	–
Sn	0.31	0.55	0.39	0.64	0.44	0.45	0.31	0.53	0.87	0.80	–	–
Sb	2.78	2.64	1.19	0.43	0.38	0.87	8.46	1.14	0.36	0.84	–	–
Cs	0.07	0.84	0.41	0.65	0.88	0.63	0.29	0.53	0.68	0.61	–	–
Ba	351	829	321	872	472	244	531	954	368	678	–	–
La	34.0	47.8	35.3	42.1	39.8	34.6	36.4	45.7	54.7	43.5	32.6	–
Ce	67.4	101	68.3	86.3	83.6	69.8	70.7	93.8	110	93.2	69.8	–
Pr	8.61	12.5	8.48	11.2	10.3	8.87	9.09	11.9	13.5	11.0	9.22	–
Nd	35.6	49.0	34.4	43.8	40.4	36.9	38.7	46.0	50.9	41.7	36.3	–
Sm	6.17	8.15	5.92	7.39	6.89	6.51	6.74	7.69	7.87	6.98	6.08	–
Eu	1.68	2.34	1.63	2.18	1.93	1.70	1.88	2.28	2.21	2.31	1.85	–
Gd	5.03	6.69	4.94	6.20	5.62	5.34	5.48	6.43	6.85	6.12	4.41	–
Tb	0.54	0.71	0.52	0.66	0.60	0.60	0.59	0.69	0.75	0.73	0.48	–
Dy	2.48	3.23	2.40	3.00	2.82	2.75	2.74	3.20	3.53	3.65	2.74	–
Ho	0.42	0.54	0.43	0.54	0.49	0.47	0.46	0.56	0.64	0.66	0.51	–
Er	1.23	1.55	1.20	1.49	1.42	1.38	1.36	1.58	1.81	1.82	1.43	–
Tm	0.14	0.18	0.16	0.18	0.17	0.15	0.15	0.19	0.22	0.23	0.20	–
Yb	0.99	1.19	0.97	1.16	1.11	1.05	1.07	1.25	1.48	1.50	1.36	–
Lu	0.14	0.17	0.13	0.18	0.16	0.17	0.15	0.18	0.22	0.20	0.21	–
Hf	1.80	2.21	1.68	2.15	2.24	1.80	1.85	2.26	3.07	2.96	–	–
Ta	2.65	0.64	0.37	0.33	0.34	0.31	0.34	0.40	0.39	0.53	–	–
W	0.82	0.14	0.09	<0.08	<0.08	0.16	0.21	<0.08	0.22	0.32	–	–
Pb	9.04	7.51	4.39	4.93	2.67	3.39	4.16	6.69	5.10	5.82	–	–
Th	5.00	6.54	5.00	5.69	5.60	5.16	4.97	6.43	5.53	5.55	–	–
U	1.10	1.49	1.17	1.34	1.29	1.15	1.10	1.45	1.28	1.30	–	–

Notes: 1-4 – spessartite dikes; 5-8 – samples from one spessartite dike: 5 – marginal part, hanging wall, outer metasomatic zone, 6 – transition metasomatic zone, 7 – central part, inner metasomatic zone, 8 – marginal part, footwall, outer metasomatic zone; 9, 10 – kersantite dikes; 11, 12 – rocks of the Vorontsovskoe gold ore deposit according to [25, 36]: 11 – spessartite (petrogenic elements – sample N 933, REE – sample N 34-2/17), 12 – kersantite. FeO* – total iron FeO and Fe₂O₃.

Another pair of components that correlates with the degree of metasomatic alteration of lamprophyres are Na₂O and S. In less altered rocks, the Na₂O content is 2.7-3.1 wt.%, and S is about 0.3 wt.%, in more altered samples 4.7-5 wt.% and 3.2 wt.%, respectively. The two pairs of petrogenic components listed above do not always correlate with each other. For example, spessartites from the inner metasomatic zone, which actually underwent the greatest metasomatic processing, have high Na₂O and S contents with average SiO₂ and LOI values.

TiO₂ content in lamprophyres varies depending on the rock type, amounting to 1.2 wt.% in kersantites and 0.5-0.8 wt.% in spessartites. In addition, kersantites have higher Al₂O₃ contents compared to spessartites. Widely varying K₂O contents in kersantites from 0.2 to 1.3 wt.% indicate the replacement of biotite by secondary minerals during metasomatism with the removal of potassium from the rock, which is confirmed by petrographic observations. In altered spessartites, K₂O is 0.2-0.8 wt.%. MnO, FeO, MgO, and CaO contents in kersantites and less altered spessartites of the Peshchernoe deposit have similar values. Variations in the total FeO content in spessartites correlate with the degree of metasomatic alteration. In the least altered spessartites, FeO is 7.5 wt.%, decreasing with increasing metasomatic alteration to 5.2 wt.%.



Thermal analysis was performed for samples from a spessartite dike with evident metasomatic zoning. It allows estimating the contents of OH and CO₂ components in these rocks. Mass losses during decomposition of dolomite and magnesite were 12-17 %, which leads to the conclusion that the CO₂ content in the rocks is 12-17 wt.%. The OH contents were estimated from the mass change during chlorite decomposition and amounted to 1.3 wt.%. Part of the mass decrease during thermal analysis is due to adsorption moisture in the preparation and pyrite decomposition. The total mass changes in the studied samples were 14.2-18 wt.%, which is quite close to the obtained values of loss on ignition measured as part of the X-ray fluorescence analysis.

Geochemical characteristics of rocks. Spessartites and kersantites of the Peshchernoe gold deposit differ in the content of individual rare elements (Table 4, Fig.5 and 6). Kersantites have higher values of Be, V, Cu, Zn, Y, HREE, Zr, Hf, Nb, Mo, Sn, W relative to spessartites, while the latter have higher Cr, Co, and Ni contents. Variations in the rare element contents are observed in spessartites depending on the degree of metasomatic alteration of rocks. More altered spessartites have lower Li, Zr, Hf, and REE contents and higher As, Sb, and W contents. The above-mentioned geochemical features of lamprophyres are reflected in Fig.5 and 6, where the absolute contents of the element in the rock are normalized to chondrite C1 [37] and the average content in calc-alkaline lamprophyres according to [18], respectively. Spessartites in these diagrams are divided into three groups: weakly, moderately, and strongly metasomatically altered. Distribution of samples by the degree of metasomatic alteration was made according to petrographic, petrochemical, and geochemical data. Au contents were measured in one of the dikes of less altered spessartites, as well as in metasomatites after a dike of spessartites with pronounced metasomatic zoning. In weakly altered spessartites, Au content was below the detection limit. The rocks of the inner metasomatic zone contain, mg/t: 23 gold, in the transition zone 4, in the outer zone in the hanging wall of the dike 3, in the outer zone in the footwall 8. Note that the metasomatites of the outer zone in the footwall of the dike have higher Sb, Zn, Pb, Ba, Mo, Th, and U contents than in the hanging wall.

Discussion of the results

According to petrographic and petrochemical observations, lamprophyres of the Peshchernoe deposit correspond to spessartites and kersantites that underwent significant metasomatic alterations. In addition to lamprophyre dikes, the deposit also contains andesitic dikes. A similar compositionally diverse dike complex was described at the Vorontsovskoe gold deposit [25, 36], located approximately 8 km southeast of the Peshchernoe deposit. The observed spatial relationship between gold mineralization and dike series, including spessartites, kersantites, and andesitic rocks, can serve as a prospecting criterion for this region.

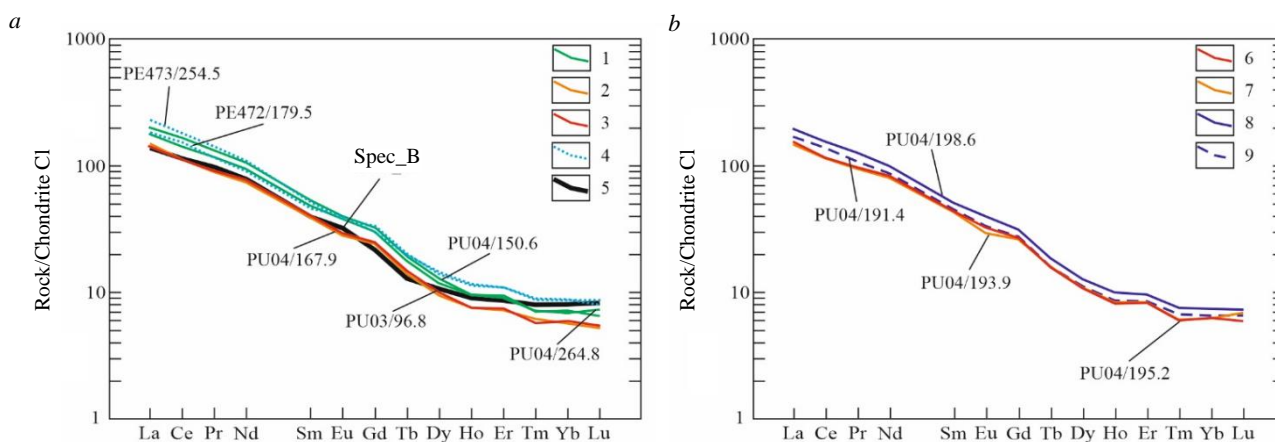


Fig.5. Rare earth element contents in lamprophyres of the Peshchernoe deposit, normalized to chondrite C1 [37]:

- a* – individual dikes of spessartites and kersantites (1-3 – spessartites of the Peshchernoe deposit: 1 – weakly metasomatically altered, 2 – moderately altered, 3 – strongly altered; 4 – kersantites of the Peshchernoe deposit; 5 – spessartites of the Vorontsovskoe deposit according to [36]);
b – metasomatic zones in the dike of altered spessartites (6 – central part of the dike, inner metasomatic zone; 7 – transitional metasomatic zone; 8 – marginal part of the dike, footwall, outer metasomatic zone; 9 – marginal part of the dike, hanging wall, outer metasomatic zone)

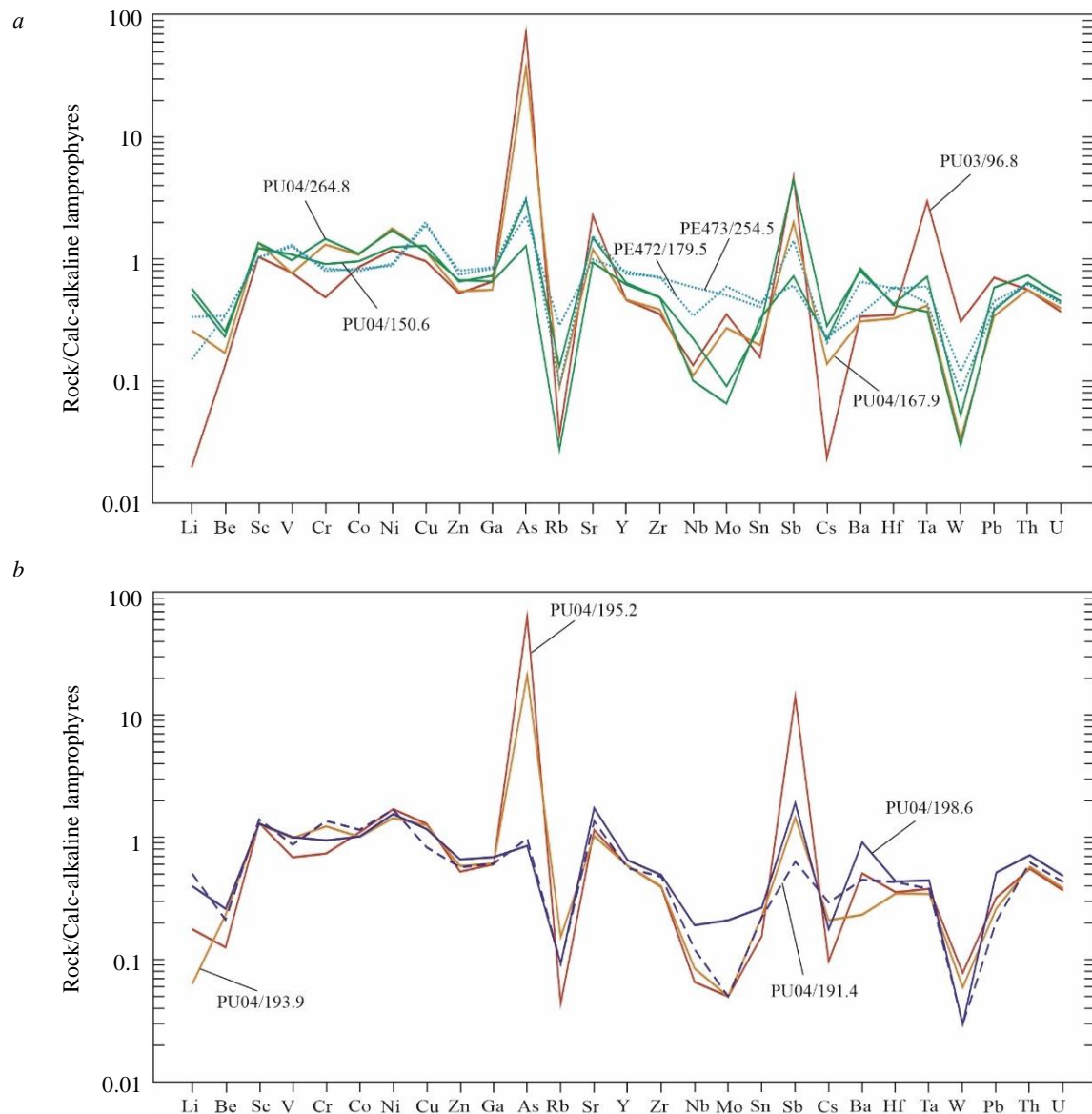


Fig.6. Rare element contents in lamprophyres of the Peshchernoe deposit, normalized to the average content in calc-alkaline lamprophyres according to [18]:
a – individual spessartite and kersantite dikes; *b* – metasomatic zones in a dike of altered spessartites
 See Fig.5 for legend

The measured attitude of the lamprophyre dike coincides with the direction and dip angle of the ore-controlling faults. The presence of discontinuous faults, which are fluid conductors and usually filled with lamprophyre dikes, is noted at many gold deposits [11, 17]. Dikes of lamprophyres and andesitic rocks are pre-ore, as evidenced by the superimposed metasomatic mineral associations. Metasomatic alterations at the Peshchernoe deposit are controlled mainly by a series of faults striking northeast, forming a metasomatic halo enveloping the fault zone. Structurally, faults dipping south-east at an angle of about 60°, dike bodies, metasomatic halos and mineralized zones represent one system, and the host volcanogenic-sedimentary rocks gently dipping to the northeast represent another one.

The diagram of the arrangement of additive geochemical halos of Ag + Sb + As [30] to the south of the Peshchernoe deposit reflects a series of linear, near N-S elongated geochemical anomalies, which spatially coincide with the Zapadno-Peshcherninskii fault. It can be assumed that the geochemical halos



record the influence of fluids entering through fault systems. In the deposit area, elongation of the geochemical halos takes on a northeastern direction and coincides with the orientation of the faults in which the mineralized zones are localized. The northeast striking fault zone occurs subconformably with the contact of the volcanogenic-sedimentary rocks of the Turinskaya Fm. and the coeval basalt strata. Probably, basalts served as a screening structure for hydrothermal solutions.

The data on the structural position of mineralized ore zones, faults, dike bodies, metasomatic halos, and host volcanogenic-sedimentary rocks suggest that the alteration system of the Peshchernoe deposit is tectonogenic. Probably, dikes of rocks of andesitic composition, lamprophyres were intruded along the northeast striking fault zone at different geological times, and subsequently it became a channel for hydrothermal fluids, including ore-bearing ones. The influence of primary orientation of volcanogenic-sedimentary rocks for gold, as was proposed for Vorontsovskoe [24], seems unlikely in the Peshchernoe deposit area.

To assess the influence of metasomatism on the chemical composition of lamprophyres, it is necessary to determine the primary rock composition. It was not possible to detect unaltered lamprophyres in the Peshchernoe deposit drillhole core. The average composition of lamprophyres from the Vorontsovskoe ore field [25, 36] and calc-alkaline lamprophyres according to [18] are quite close, which may indicate an insignificant degree of their alteration by metasomatism. Therefore, we accepted the compositions of spessartites and kersantites from the Vorontsovskoe deposit [25, 36] as a possible educt. Individual compositions of these rocks are given in Table 4.

The least altered spessartites and kersantites from the Peshchernoe deposit differ from similar rocks of the Vorontsovskoe deposit by a lower SiO_2 content and higher CaO , Na_2O , and LOI values. In addition, spessartites from Peshchernoe have a lower total FeO content, compared with spessartites from the Vorontsovskoe deposit. Kersantites from Peshchernoe contain less K_2O , relative to kersantites from the Vorontsovskoe deposit. The REE contents in spessartites from the Peshchernoe and Vorontsovskoe deposits are almost identical (see Fig.5). The differences in the contents of petrogenic components in lamprophyres from the Peshchernoe and Vorontsovskoe deposits are the result of a higher degree of metasomatic alterations in the former. Accordingly, the initial metasomatic stage observed in lamprophyres from the Peshchernoe deposit was accompanied by SiO_2 , FeO , K_2O removal from the rocks and CaO , Na_2O , CO_2 supply. REE contents remained without significant changes.

A more detailed analysis can be made of the substance balance during the next stage of metasomatism, expressed in the development of metasomatic mineral parageneses that form individual metasomatic zones in one of the dikes of altered spessartites. The alterations that occurred when metasomatites formed at this stage led to a change in the rock density. Spessartites of the outer metasomatic zone (sample PU04/191.4) have a density of 2.8 g/cm^3 , in the transition zone (sample PU04/193.9) it increases to 2.85 g/cm^3 , and in the inner zone (sample PU04/195.2) it is 2.86 g/cm^3 . The estimation results are presented in Table 5; N_i^v is the number of element atoms in a geometric volume of rock in $10,000 \text{ \AA}^3$: N_i^v in metasomatically altered spessartites of the outer, N_i^v in the transition, and N_i^v in the inner zones; ΔN_i^v is the difference between the number of element atoms in a geometric volume of rock in $10,000 \text{ \AA}^3$ of the source and resulting rock: ΔN_i^v in the outer and transition, ΔN_i^v in the transition and inner, ΔN_i^v in the outer and inner zones; ΔN_i^v is designated with a plus if the element is supplied and with a minus if it is removed; $\Delta N_i^v/N_i^v$ is the relative change in the number of element atoms as a percentage of the number of element atoms in the source rock, in our case, the number of element atoms in metasomatically altered spessartites of the outer zone. Figure 7 shows the relative changes in the number of element atoms when passing from the outer metasomatic zone to the transition zone and from the transition zone to the inner one, the line is the result of these changes, corresponding to the difference in the number of element atoms between the outer and inner metasomatic zones.



Table 5

Estimation of the substance balance during the alteration of spessartites at the sodic stage of metasomatism

Elements	Number of atoms per 10,000 Å ³			Supply-removal per 10,000 Å ³					
	PU04/191.4	PU04/193.9	PU04/195.2	Absolute differences			Relative to N _i ^v ₁ , %		
	N _i ^v ₁	N _i ^v ₂	N _i ^v ₃	ΔN _i ^v ₁₋₂	ΔN _i ^v ₂₋₃	ΔN _i ^v ₁₋₃	ΔN _i ^v ₁₋₂ /N _i ^v ₁	ΔN _i ^v ₂₋₃ /N _i ^v ₁	ΔN _i ^v ₁₋₃ /N _i ^v ₁
Si	110	103	112	-7	+9	+2	-6.36	+8.18	+1.82
Ti	1.43	1.70	1.57	+0.27	-0.13	+0.14	+18.88	-9.09	+9.79
Al	35.0	40.9	38.5	+5.9	-2.4	+3.5	+16.86	-6.86	+10.00
Fe ²⁺	18.5	15.5	12.9	-3.0	-2.6	-5.6	-16.22	-14.05	-30.27
Mn	0.33	0.31	0.27	-0.02	-0.04	-0.06	-6.06	-12.12	-18.18
Mg	52.7	44.0	49.1	-8.7	+5.1	-3.6	-16.51	+9.68	-6.83
Ca	32.8	31.9	30.9	-0.9	-1.0	-1.9	-2.74	-3.05	-5.79
Na	15.2	23.8	28.3	+8.6	+4.5	+13.1	+56.58	+29.61	+86.18
K	1.47	2.84	0.77	+1.37	-2.07	-0.70	+93.20	-140.82	-47.62
P	0.69	0.75	0.68	+0.06	-0.07	-0.01	+8.70	-10.14	-1.45
S	1.47	9.37	17.72	+7.90	+8.35	+16.25	+537.41	+568.03	+1105.44
CO ₂	56.7	64.3	48.2	+7.6	-16.1	-8.5	+13.40	-28.40	-14.99
OH	12.4	-	-	-12.4	-	-12.4	-100.00	-	-100.00
O	526	502	481	-24	-21	-45	-4.56	-3.99	-8.56
Total +	-	-	-	+31.7	+26.95	+34.99	+3.67	+3.12	+4.05
Total -	-	-	-	-56.02	-45.41	-77.77	-6.48	-5.25	-8.99
Total	864.69	840.37	821.91	-24.32	-18.46	-42.78	-2.81	-2.13	-4.94

Note. The estimation was performed using the atomic volume conversion by Yu.V.Kazitsyn and V.A.Rudnik [38].

Four groups of elements can be distinguished after a matter analysis. The first group is represented by S and Na, which are supplied into the rocks of the transition and inner metasomatic zones. The second group consists of relatively inert elements at this stage of metasomatism: Al, Ti, Si, P, Ca, Mg. Elements of the third group are removed from the rocks. They include Mn, Fe, and OH. The fourth group of elements is represented by K and CO₂. The amounts of these components increase in the transition zone and decrease significantly in the inner one. We have concluded that this is the result of K and CO₂ redistribution from the inner metasomatic zone to the rocks of the transition zone, and not their removal by metasomatizing solutions. Negative values of the resulting relative changes in K and CO₂ contents can be due to the fact that the transition metasomatic zone is twice thick as the inner one.

The supply and removal of rare elements at the sodic stage of metasomatism is illustrated in Fig.5, b. The rocks in the inner metasomatic zone have higher Au, As, Sb, and W contents relative to spessartites in the outer zone, which indicates the supply of these elements as a result of metasomatism, while Li is removed from the rocks. Spessartites with a moderate and strong degree of metasomatic alterations demonstrate a slight depletion in REE relative to less altered rocks with the preservation of the REE spectra shape (see Fig.5). The studied spessartite dike is outside the ore zone (see Fig.2, b). However, the distribution of elements observed in it may reflect general patterns. The rocks in the dike footwall have higher Au, Sb, Zn, Pb, Ba, Mo, Th, and U contents compared to the rocks in the hanging wall. This is consistent with the position of ore zones in the footwall of ore-controlling faults and the absence of mineralization in metasomatically altered rocks of the hanging wall.

Two stages of metasomatism can be distinguished in metasomatic alterations observed in the Peshchernoe deposit spessartites: carbon dioxide and subsequent sodic. During carbon dioxide metasomatism, dark-coloured minerals are replaced by chlorite, albitization and sericitization of plagioclase occur. Ferruginous dolomite is formed under the influence of a significant supply of CO₂. The forming mineral paragenesis corresponds to the outer metasomatic zone during listvenization of gabbro [20, 39, 40]. Alkaline (sodic) metasomatism is superimposed on the mineral metasomatic

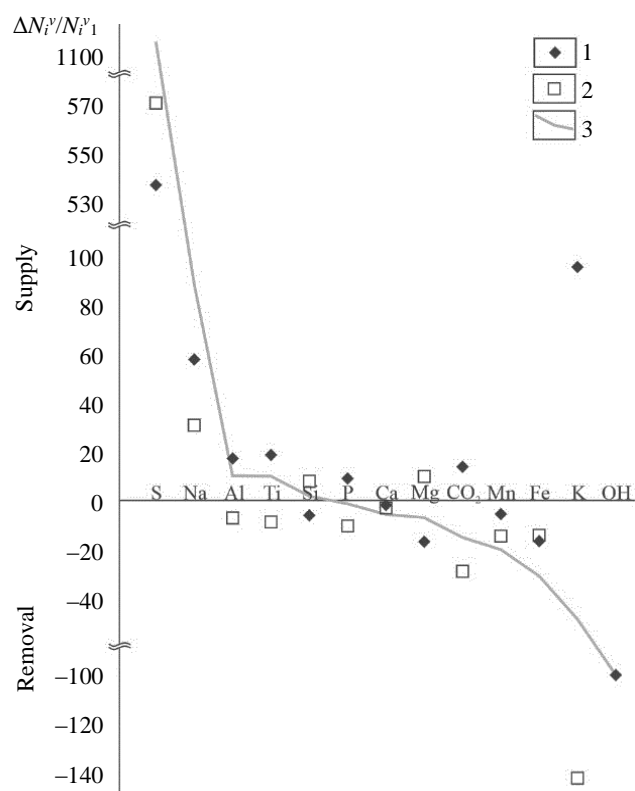


Fig.7. Supply-removal of elements during the sodic stage of metasomatic alteration of spessartites
 ΔN_i^v – difference between the number of element atoms in 10,000 Å³ of the source and resulting rocks;
 N_i^v1 – number of element atoms in 10,000 Å³ of metasomatically altered spessartites of the outer zone

Alterations during transition:

- 1 – from the outer metasomatic zone to the transition zone;
- 2 – from the transition metasomatic zone to the inner one;
- 3 – the resulting line of alterations corresponding to the difference in the number of element atoms between the outer and inner metasomatic zones

paragenesis of the first stage. Chlorite and relics of magmatic dark-coloured minerals are replaced by magnesite, the supply of Na leads to the appearance of newly formed albite, and as a result of the supply of S, pyrite is formed, which concentrates iron from other minerals. As a result of the sodic stage of metasomatism, the iron content in carbonates decreases in the direction from the outer metasomatic zone to the inner one, whereas the opposite trend was described for listvenization [40]. By high sodium content, formed metasomatites are similar to eisites. They differ from the latter by a significant supply of S and the absence of hematite [41, 42]. The absence of hematization and the binding of iron into pyrite may indicate a higher felsicity of metasomatizing solutions than during the formation of classical eisites [41].

In addition to alterations observed in lamprophyres, propylitized rocks are present in the peripheral areas of the deposit. Propylites and metasomatic alterations of the carbon dioxide stage are widespread in the Peshchernoe deposit area, and the influence of sodic metasomatism has a more local distribution near permeable fault zones. The limitation of eisitization halos by the sizes of solution-supplying channels can be explained by the positive volumetric effect of mineral alterations, leading to the blockage of fractures and pores [41].

The set of metasomatic styles at the Peshchernoe deposit generally corresponds to the propylite-beresite eisite-bearing alteration type, characteristic of tectonic alteration systems. According to the model by E.V.Plyushchev et al. [43], due to the high volatility of carbon dioxide in the upper levels of the hydrothermal system, a carbonatization area can form, which corresponds to the high content of carbonates in metasomatites from the Peshchernoe deposit. A combination of beresite-listvenites and eisites in connection with mineralization is observed at the Kochkarskoe, Chudnoe, Kumakskoe and other gold deposits [44].

The study of metasomatically altered spessartites of the Peshchernoe deposit showed that Au, As, Sb, and W accumulate as a result of late sodic metasomatism. This stage is associated with a significant supply of sulphur and sulphide formation. Beresitized rocks of the Peshchernoe deposit with a superimposed association of alkaline (sodic) metasomatites have the highest gold concentrations [45]. It was the alkaline-sulphide sodium solutions that had the ore-bearing or ore-mobilizing function during gold mineralization development at the deposit. Beresitization-listvenitization created a favourable environment for ore deposition [40]. Beresitization-listvenitization, according to the metasomatic zoning theory [46], corresponds to the “felsic stage”, and eisitization may represent the “late alkaline stage”. The solubility and transport of gold in sodic hydrothermal solutions were considered by various authors [47, 48]. Recently, the possibility of extracting gold from ore using alkaline



solutions of sodium polysulphide has been actively discussed [49, 50]. Gold ore deposition from alkaline solutions into relatively felsic rocks (listvenites, beresites) and quartz veins is considered in detail by V.N.Sazonov [40]. The data obtained confirm the previously identified direct relationship between mineralization related to the gold-low-sulphide-quartz formation and Ag, As, and Sb in rocks of the central segment of the East Tagil tectono-stratigraphic area, to which the Peshchernoe deposit area belongs [30].

The spatial proximity to the massif of the gabbro-diorite-granite complex, the connection of mineralization with fault zones and lamprophyre dikes, high CO₂ contents in metasomatically altered rocks, and an increased content of As, Sb, and W as a result of ore-accompanying metasomatic processes indicate that the Peshchernoe deposit can be classified as a gold prospect associated with intrusive massifs and formed in the area of their hydrothermal influence [12, 51].

Conclusion

Lamprophyres at the Peshchernoe gold deposit are represented by spessartites and kersantites. Lamprophyre dikes mark faults that later became channels for hydrothermal fluids, including ore-bearing ones. Two stages of metasomatism are distinguished in the metasomatic alterations observed in spessartites: carbon dioxide and subsequent sodic. Geochemical orientation of sodic metasomatites after spessartites indicates that it was the sodic stage of metasomatism that accompanied ore. Identification of sodic metasomatism halos in the field of widespread metasomatites of the propylite-beresite formation may be promising for more accurate localization of ore zones.

REFERENCES

1. Dirks P.H.G.M., Sanislav I.V., van Ryt M.R. et al. Chapter 8: The World-Class Gold Deposits in the Geita Greenstone Belt, Northwestern Tanzania. *Geology of the World's Major Gold Deposits and Provinces*. Society of Economic Geologists, 2020. Special Publication. N 23, p. 163-183. DOI: [10.5382/SP.23.08](https://doi.org/10.5382/SP.23.08)
2. Dubé B., Mercier-Langevin P., Ayer J. et al. Chapter 3: Gold Deposits of the World-Class Timmins-Porcupine Camp, Abitibi Greenstone Belt, Canada. *Geology of the World's Major Gold Deposits and Provinces*. Society of Economic Geologists, 2020. Special Publication. N 23, p. 53-80. DOI: [10.5382/SP.23.03](https://doi.org/10.5382/SP.23.03)
3. Mueller A.G., Hagemann S.G., McNaughton N.J. Neoproterozoic orogenic, magmatic and hydrothermal events in the Kalgoorlie-Kambalda area, Western Australia: constraints on gold mineralization in the Boulder Lefroy-Golden Mile fault system. *Mineralium Deposita*. 2020. Vol. 55. Iss. 4, p. 633-663. DOI: [10.1007/s00126-016-0665-9](https://doi.org/10.1007/s00126-016-0665-9)
4. Seltmann R., Goldfarb R.J., Zu B. et al. Chapter 24: Muruntau, Uzbekistan: The World's Largest Epigenetic Gold Deposit. *Geology of the World's Major Gold Deposits and Provinces*. Society of Economic Geologists, 2020. Special Publication. N 23, p. 497-521. DOI: [10.5382/SP.23.24](https://doi.org/10.5382/SP.23.24)
5. Goldfarb R.J., Pitcairn I. Orogenic gold: is a genetic association with magmatism realistic? *Mineralium Deposita*. 2023. Vol. 58. Iss. 1, p. 5-35. DOI: [10.1007/s00126-022-01146-8](https://doi.org/10.1007/s00126-022-01146-8)
6. Rock N.M.S., Finlayson E.J. Petrological affinities of intrusive rocks associated with the giant mesothermal gold deposit at Porgera, Papua New Guinea. *Journal of Southeast Asian Earth Sciences*. 1990. Vol. 4. Iss. 3, p. 247-257. DOI: [10.1016/S0743-9547\(05\)80018-2](https://doi.org/10.1016/S0743-9547(05)80018-2)
7. Kadel-Harder I.M., Spry P.G., Layton-Matthews D. et al. Paragenetic relationships between low- and high-grade gold mineralization in the Cripple Creek Au-Te deposit, Colorado: Trace element studies of pyrite. *Ore Geology Reviews*. 2020. Vol. 127. N 103847. DOI: [10.1016/j.oregeorev.2020.103847](https://doi.org/10.1016/j.oregeorev.2020.103847)
8. Kelley K.D., Jensen E.P., Rampe J.S., White D. Chapter 17: Epithermal Gold Deposits Related to Alkaline Igneous Rocks in the Cripple Creek District, Colorado, United States. *Geology of the World's Major Gold Deposits and Provinces*. Society of Economic Geologists, 2020. Special Publication. N 23, p. 355-373. DOI: [10.5382/SP.23.17](https://doi.org/10.5382/SP.23.17)
9. Bettles K. Chapter 13: Exploration and Geology, 1962 to 2002, at the Goldstrike Property, Carlin Trend, Nevada. *Integrated Methods for Discovery: Global Exploration in the Twenty-First Century*. Society of Economic Geologists, 2002. Special Publication. N 9, p. 275-298. DOI: [10.5382/SP.09.13](https://doi.org/10.5382/SP.09.13)
10. Emsbo P., Hofstra A.H., Lauha E.A. et al. Origin of High-Grade Gold Ore, Source of Ore Fluid Components, and Genesis of the Meikle and Neighboring Carlin-Type Deposits, Northern Carlin Trend, Nevada. *Economic Geology*. 2003. Vol. 98. N 6, p. 1069-1105. DOI: [10.2113/gsecongeo.98.6.1069](https://doi.org/10.2113/gsecongeo.98.6.1069)
11. Dobak P.J., Robert F., Barker S.L.L. et al. Chapter 15: Goldstrike Gold System, North Carlin Trend, Nevada, USA. *Geology of the World's Major Gold Deposits and Provinces*. Society of Economic Geologists, 2020. Special Publication. N 23, p. 313-334. DOI: [10.5382/SP.23.15](https://doi.org/10.5382/SP.23.15)



12. Hart C. Reduced Intrusion-Related Gold Systems. Mineral Deposits Division. A Synthesis of Major Deposit Types, District Metallogeny, the Evolution of Geological Provinces and Exploration Methods. Geological Association of Canada, Mineral Deposits Division, 2007. Special Publication. N 5, p. 95-112.
13. Korobeinikov A.F., Gusev A.I., Krasova A.S. Reduced intrusive-alteration gold ore systems. *Izvestiya Tomskogo politekhnicheskogo universiteta*. 2012. Vol. 321. N 1, p. 16-22 (in Russian).
14. Shatova N.V., Molchanov A.V., Terekhov A.V. et al. Ryabinovoe copper-gold-porphyry stock (Southern Yakutia): geology, noble gases isotope systematics and isotopic (U-Pb, Rb-Sr, Re-Os) dating of wallrock alteration and ore-forming processes. *Regional Geology and Metallogeny*. 2019. Vol. 77, p. 75-97 (in Russian).
15. Artemiev D.S., Krymsky R.Sh., Belyatsky B.V., Ashikhmin D.S. The age of mineralization of Mayskoe gold ore deposit (Central Chukotka): results of Re-Os isotopic dating. *Journal of Mining Institute*. 2020. Vol. 243, p. 266-278. DOI: [10.31897/PMI.2020.3.266](https://doi.org/10.31897/PMI.2020.3.266)
16. Hodgson C.J., Troop D.G. A new computer-aided methodology for area selection in gold exploration; a case study from the Abitibi greenstone belt. *Economic Geology*. 1988. Vol. 83. N 5, p. 952-977. DOI: [10.2113/gsecongeo.83.5.952](https://doi.org/10.2113/gsecongeo.83.5.952)
17. Rock N.M.S., Groves D.I., Perring C.S., Golding S.D. Gold, Lamprophyres, and Porphyries: What Does Their Association Mean? The Geology of Gold Deposits: The Perspective in 1988. The Economic Geology Publishing Company, 1989. Economic Geology Monograph 6, p. 609-625. DOI: [10.5382/Mono.06.47](https://doi.org/10.5382/Mono.06.47)
18. Rock N.M.S. Lamprophyres. New York: Springer, 1991, p. 285. DOI: [10.1007/978-1-4757-0929-2](https://doi.org/10.1007/978-1-4757-0929-2)
19. Fershtater G.B., Znamenskii S.E., Borodina N.S. Age and geochemistry of the Plastovskii gold massif. *Ezhegodnik-2008. Trudy Instituta geologii i geokhimii UrO RAN*. 2009. Iss. 156, p. 276-282 (in Russian).
20. Borodaevskii N.I., Borodaevskaya M.B. Berezovskoe ore field (geological structure). Moscow: Metallurgizdat, 1947, p. 264 (in Russian).
21. Spiridonov E.M., Baksheev I.A., Filimonov S.V. Chrome spinels and genesis of pre-gold ore spessartites of the Berezovskoe ore field, Middle Urals. Magmatizm, metamorfizm i glubinnoe stroenie Urala. Tezisy dokladov VI Uralskogo petrograficheskogo soveshchaniya. V 2 tomakh. T. 2. Ekaterinburg: Institut geologii i geokhimii UrO RAN, 1997, p. 228-229 (in Russian).
22. Baksheev I.A., Belyatsky B.V. Sm-Nd and Rb-Sr isotope systems of scheelite of Berezovsky gold deposit, Middle Urals. *Lithosphere*. 2011. Vol. 4, p. 110-118 (in Russian).
23. Sazonov V.N., Murzin V.V., Grigorev N.A., Gladkovskii B.A. Endogenous mineralization of the Devonian andesitic volcano-plutonic complex (Urals). Sverdlovsk: UrO AN SSSR, 1991. 183 c (in Russian).
24. Vikentyev I.V., Tyukova E.E., Murzin V.V. et al. Vorontsovsk gold deposit. Geology, gold modes, genesis. Ekaterinburg: Fort Dialog-Iset, 2016, p. 204 (in Russian).
25. Azovskova O.B., Rovnushkin M.Yu., Soroka E.I. Petrochemical features of the dike complex of the Vorontsovskoe gold-ore deposit (Northern Urals). *News of the Ural State Mining University*. 2019. Iss. 1 (53), p. 18-27. DOI: [10.21440/2307-2091-2019-1-18-27](https://doi.org/10.21440/2307-2091-2019-1-18-27)
26. Nechkin G.S., Rovnushkin M.Yu. Sulphide near-dike mineralization at the Vorontsovskoe gold deposit (Auerbakhovskii complex, Northern Urals). *Ezhegodnik-2010. Trudy Instituta geologii i geokhimii UrO RAN*. 2011. Iss. 158, p. 187-190 (in Russian).
27. Minina O.V. Auerbakhovskii complex ore-magmatic system in the Middle Urals. *Otechestvennaya geologiya*. 1994. N 7, p. 17-23 (in Russian).
28. Ogereleva A.V., Arifulov Ch.H., Arsenteva I.V. Gold potential of Auerbakhovskii volcanic-plutonic belt (North, Subpolar, Polar Ural). *National Geology*. 2014. N 2, p. 4-19 (in Russian).
29. State Geological Map of the Russian Federation. Scale 1:200,000 (2nd generation). Seriya Sredne-Uralskaya. List O-41-I (Serov). Obyasnitelnaya zapiska. St. Petersburg: VSEGEI, 2017, p. 260 (in Russian).
30. Nesis V.N., Motov A.P., Butnyakov A.V. Geochemical characteristics and boundaries of gold ore fields of the region including Gornychka and Peschernoe deposits, Northern Urals. *Ores and Metals*. 2020. N 1, p. 32-38 (in Russian). DOI: [10.24411/0869-5997-2020-10003](https://doi.org/10.24411/0869-5997-2020-10003)
31. Puchkov V.N. Geology of the Urals and Cis-Urals (actual problems of stratigraphy, tectonics, geodynamics and metallogeny). Ufa: DesignPoligraphService, 2010, p. 280 (in Russian).
32. Hawthorne F.C., Oberti R., Harlow G.E. et al. Nomenclature of the amphibole supergroup. *American Mineralogist*. 2012. Vol. 97. N 11-12, p. 2031-2048. DOI: [10.2138/am.2012.4276](https://doi.org/10.2138/am.2012.4276)
33. Bosi F., Biagioni C., Pasero M. Nomenclature and classification of the spinel supergroup. *European Journal of Mineralogy*. 2019. Vol. 31. N 1, p. 183-192. DOI: [10.1127/ejm/2019/0031-2788](https://doi.org/10.1127/ejm/2019/0031-2788)
34. Pasero M., Kampf A.R., Ferraris C. et al. Nomenclature of the apatite supergroup minerals. *European Journal of Mineralogy*. 2010. Vol. 22. N 2, p. 163-179. DOI: [10.1127/0935-1221/2010/0022-2022](https://doi.org/10.1127/0935-1221/2010/0022-2022)
35. Droop G.T.R. A general equation for estimating Fe³⁺ concentrations in ferromagnesian silicates and oxides from microprobe analyses, using stoichiometric criteria. *Mineralogical Magazine*. 1987. Vol. 51. Iss. 361, p. 431-435. DOI: [10.1180/minmag.1987.051.361.10](https://doi.org/10.1180/minmag.1987.051.361.10)
36. Azovskova O.B., Soroka E.I., Rovnushkin M.Yu., Soloshenko N.G. Sm-Nd isotopy of the dikes of the Vorontsovskoe gold-ore deposit (Northern Urals). *Vestnik of Geosciences*. 2020. N 9 (309), p. 3-6. DOI: [10.19110/geov.2020.9.1](https://doi.org/10.19110/geov.2020.9.1)
37. Sun S.-S., McDonough W.F. Chemical and isotopic systematics of oceanic basalts: implications for mantle composition and processes. Magmatism in the Ocean Basins. London: Geological Society, 1989. Special Publication. N 42, p. 313-345. DOI: [10.1144/GSL.SP.1989.042.01.19](https://doi.org/10.1144/GSL.SP.1989.042.01.19)
38. Kazitsyn Yu.V., Rudnik V.A. Guide to estimating the balance of matter and internal energy in the formation of metasomatic rocks. Moscow: Nedra, 1968, p. 364 (in Russian).
39. Zavaritskii A.N. Selected Works. In 4 volumes. Vol. 4. Moscow: Akademiya nauk SSSR, 1963, p. 727 (in Russian).



40. Sazonov V.N. Listvenitization and mineralization. Moscow: Nauka, 1975, p. 172 (in Russian).
41. Omelyanenko B.I. Wallrock hydrothermal alterations of rocks. Moscow: Nedra, 1978, p. 215 (in Russian).
42. Sazonov V.N. Gold-producing metasomatic formations of mobile belts (geodynamic settings and RTX parameters of formation, prognostic value). Ekaterinburg: Uralskaya gosudarstvennaya gorno-geologicheskaya akademiya, 1998, p. 181 (in Russian).
43. Plyushchev E.V., Shatov V.V., Kashin S.V. Metallogeny of alteration types. St. Petersburg: VSEGEI, 2012. Vol. 354, p. 560 (in Russian).
44. Sazonov V.N., Ogorodnikov V.N., Koroteev V.A., Polenov Yu.A. Gold deposits of the Urals. Ekaterinburg: Uralskaya gosudarstvennaya gorno-geologicheskaya akademiya, 2001, p. 622 (in Russian).
45. Tolochko S.A., Desyuk M.A. Geological features of the Peshchernoe gold deposit (Sverdlovsk region). *Praktika geologov na proizvodstve: Sbornik trudov VII Vserossiiskoi studencheskoi nauchno-prakticheskoi konferentsii, 3 dekabrya 2022, Rostov-na-Donu, Rossiya*. Rostov-na-Donu; Taganrog: Izdatelstvo Yuzhnogo federalnogo universiteta, 2022, p. 46-48 (in Russian).
46. Korzhinskii D.S. Theory of metasomatic zoning. Moscow: Nauka, 1982, p. 104 (in Russian).
47. Zvyagintsev O.E., Paulsen I.A. On the solubility of gold in alkali hydrosulphides. *Izvestiya sektora po izucheniyu platiny*. 1940. Iss. 17, p. 101-110 (in Russian).
48. Letnikov F.A., Vilor N.V. Gold in a hydrothermal process. Moscow: Nedra, 1981, p. 224 (in Russian).
49. Qingjuan Wen, Yufeng Wu, Xiu Wang et al. Researches on preparation and properties of sodium polysulphide as gold leaching agent. *Hydrometallurgy*. 2017. Vol. 171, p. 77-85. DOI: [10.1016/j.hydromet.2017.04.008](https://doi.org/10.1016/j.hydromet.2017.04.008)
50. Sudova M., Kanuchova M., Sisol M. et al. Possibilities for the Environmental Processing of Gold-Bearing Ores. *Separations*. 2023. Vol. 10. Iss. 7. N 384. DOI: [10.3390/separations10070384](https://doi.org/10.3390/separations10070384)
51. Baker T., Lang J.R. Fluid inclusion characteristics of intrusion-related gold mineralization, Tombstone–Tungsten magmatic belt, Yukon Territory, Canada. *Mineralium Deposita*. 2001. Vol. 36. Iss. 6, p. 563-582. DOI: [10.1007/s001260100189](https://doi.org/10.1007/s001260100189)

Authors: **Dmitrii V. Kuznetsov**, Leading Engineer, kuznetsov@igg.uran.ru, <https://orcid.org/0009-0003-3261-7742> (The Zavaritsky Institute of Geology and Geochemistry of the Ural Branch of the RAS, Ekaterinburg, Russia), **Sergei Yu. Stepanov**, Candidate of Geological and Mineralogical Sciences, Senior Researcher (South Urals Federal Research Center of Mineralogy and Geoecology of the Urals Branch of the RAS, Ilmenskii State Nature Reserve, Miass, Russia), **Andrei V. Butnyakov**, Deputy Director (Ural branch of Polymetal UK, Yekaterinburg, Russia), **Viktoriya S. Igosheva**, Research Engineer, <https://orcid.org/0000-0002-9158-4958> (The Zavaritsky Institute of Geology and Geochemistry of the Ural Branch of the RAS, Ekaterinburg, Russia).

The authors declare no conflict of interests.



Consideration of the geomechanical state of a fractured porous reservoir in reservoir simulation modelling

Yurii A. Kashnikov, Denis V. Shustov, Sergei Yu. Yakimov✉

Perm National Research Polytechnic University, Perm, Russia

How to cite this article: Kashnikov Yu.A., Shustov D.V., Yakimov S.Yu. Consideration of the geomechanical state of a fractured porous reservoir in reservoir simulation modelling. *Journal of Mining Institute*. 2025. Vol. 271. N 16217, p. 42-52.

Abstract

This paper presents reservoir simulation modeling of a hydrocarbon accumulation with a fractured porous reservoir, incorporating the geomechanical effects of fracture closure during variations in formation pressure. The fracture permeability parameter is derived from the impact of stress on fracture walls. The fracturing parameter is determined based on 3D seismic data analysis. A permeability reduction model is implemented in the tNavigator reservoir simulation platform. The proposed approach improves the convergence of formation pressure dynamics in well data while maintaining flow rate and water cut adaptation accuracy. This results in enhanced formation pressure prediction and optimization of the pressure maintenance system.

Keywords

geomechanical modelling; reservoir simulation modelling; mathematical modelling; fracturing; permeability; machine learning

Received: 10.04.2023

Accepted: 07.11.2024

Online: 25.02.2025

Published: 25.02.2025

Introduction

During the development of a fractured reservoir, significant decreases in formation pressure trigger processes that are difficult to capture using single-medium models. Widely discussed in the literature, these processes include fracture closure and variations in fracture permeability, both of which affect the reservoir's geomechanical state [1-3].

Currently, reservoir simulation models of oil and gas accumulations, even those containing fractured porous reservoirs, are often built using single-porosity models. These models are well-established and relatively straightforward to adapt to initial development conditions. However, well flow rates and bottomhole pressures depend heavily on the permeability and porosity of the near-wellbore formation. High water production is a function of phase permeabilities and aquifer activity. One of the most complex and crucial aspects of model calibration is the accurate simulation of formation pressure dynamics, as it impacts well performance, equipment selection, and stimulation planning. The well operating mode, the choice of downhole equipment, and the planning of inflow stimulation measures depend on formation pressure. From the point of view of reservoir physics, the content of free gas in the pores and, as a result, phase permeabilities, as well as fractures opening in the reservoir and absolute permeability depend on formation pressure¹.

¹ Guidelines for the development of permanent geotechnical models of oil and gas fields. In 2 parts. Part 2. Filtration models. Moscow: OAO VNIOENG, 2003, p. 224.



The most accurate approach for modeling fractured reservoirs involves developing a discrete fracture network (DFN) model coupled with a dual-porosity/dual-permeability reservoir simulation. However, such models require extensive parametric input and are challenging to implement [4].

The article proposes an approach to geological reservoir simulation modelling of hydrocarbon accumulations with a fractured porous reservoir based on the geomechanical effects of the fracture space closure during changes in formation pressure. The permeability distribution along the section is dynamic. In the initial formation conditions, the reservoir is represented by both a pore medium and open fracture systems. With a decrease in formation pressure, an intensive decrease in fracture permeability occurs, as a result of which entire areas of the formation, previously considered a reservoir, cease to filter hydrocarbons. The initial value of permeability, as well as its change, are a function of stresses.

The study was conducted on the Tournaisian–Famennian formation (TFm) in one of the fields in the Perm Region. This formation consists of a massive carbonate bed with up to 19 layers and a total thickness of 50-75 m. The wells initially exhibit high flow rates (up to 100 m³/day or more), but most experience a several-fold decline in flow rates within the first 5-10 years.

Methods

To consider the dynamic behaviour of the permeability and porosity properties of a fractured reservoir during reservoir simulation modelling, modelling can be divided into several stages in accordance with the new approach:

- analysis of production data and well flow tests, identification of areas with the permeability reduction effect;
- selection of geological and geophysical criteria that determine the intensity of fracture permeability reduction or the absence of this process;
- development of a 3D geomechanical model of the formation and surrounding rocks;
- preparation for reservoir simulation modelling, simulation of the permeability cubes and fracture compressibility parameters;
- adjustment and adaptation of the new reservoir simulation model considering the effect of fracture closure and new permeabilities.

To identify the effect of changing the filtration properties of the reservoir, the results of well flow studies as well as industrial data on well operation were analyzed at the first stage. The fact of a change in filtration properties can be preliminarily observed by a decrease in well permeability, determined by pressure recovery curves, by well indicator diagrams concave to the flow rate axis, as well as by the negative dynamics of the productivity coefficient [5, 6]. The first method of identifying this effect is the most reliable, since the permeability dynamics are analyzed on the well contour, where the colmation is absent. According to widespread practice, the dependence of permeability on pressure is approximated by an exponential function

$$k = k_0 e^{\beta(p - p_0)},$$

where k_0 and k – the initial and current permeability; p_0 and p – the initial and current formation pressures; β – the permeability reduction degree.

The unknown values are the initial permeability under formation conditions k_0 and the permeability reduction parameter β . Such an analysis is possible in the presence of a sufficiently wide range of formation pressures of well studies in non-stationary modes, at low water cut values and formation pressures exceeding the saturation pressure. At the pay under consideration, 10 wells correspond to these conditions, for which β was subsequently determined.



When selecting geological and geophysical criteria for the 3D distribution of the permeability reduction parameter, several approaches can be used. For example, in [7], ranking was performed by the P-wave travel time. The compressibility of the fracture walls was determined by the strength properties of the rock, which, in turn, depended on the P-wave velocity. The advantage of this method is the prevalence of acoustic logging materials for most pays. Its main disadvantage is the lack of reference to fracturing. In the case of a porous fractured reservoir, where fracturing is not widespread, based on the interval travel time of the P-wave, high rock compressibility can be falsely identified even in areas with a porous reservoir.

In this regard, the present work investigated the formation fracturing distribution based on well data and core studies. Since the number of wells covered by the fracturing studies is insufficient for simple interpolation, a search for a relationship between fracturing and 3D seismic materials was performed. A set of research data related to the identification of fractures was collected and analyzed [8]. Fracturing of eight wells in the Tfm pay of the analyzed field was studied. The studies included a geophysical investigation of wells using the EMS by KarSar MS-110 and MicroScope devices, as well as fracturing determination in an oriented core.

The distribution of near-vertical fracturing with predominant strike azimuths of 90-130° and dip angles of 70-85° stands out from the entire data set. The results did not depend on the device used. The obtained distributions were further used to build a volumetric probabilistic model of fracturing in the studied pay. Classification was performed by machine learning methods in Python. The angle stack cubes of 3D seismic survey amplitudes were used directly (without conversion to attributes) as the initial parameters for training the model. The idea was to take a segment of the seismic trace passing through the studied point in the interval of ± 50 m relative to this point using compression methods (principal vector methods, singular value decomposition, etc.) as input parameters of machine learning methods. Various boostings were used as machine learning models.

The classification quality was assessed by the cross-validation method using the ROC AUC metric and reached values of 0.88-0.91 for different models. Two classes (types) of void space were identified based on actual data: without fractures (0) and with fractures (1). Figure 1 shows the probability density distributions of the occurrence of these classes depending on the probability of predictions of machine learning models. The classes are well separated in such a way that with an increase in the predicted probability, the ratio of class 1 to class 0 increases.

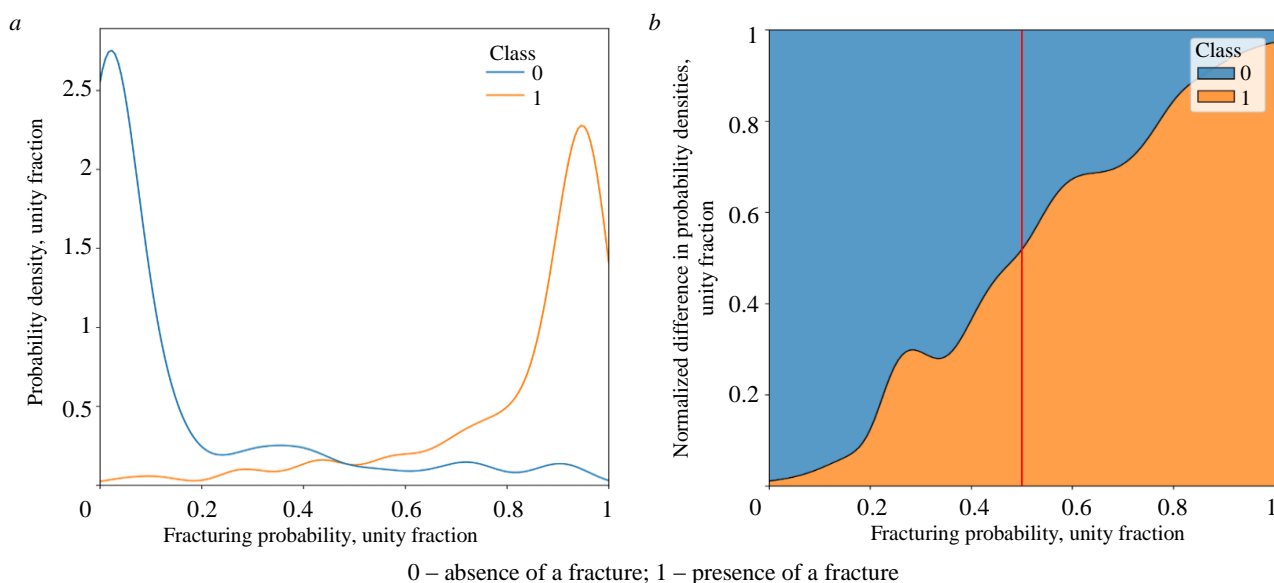


Fig.1. Distribution of probability densities of fracturing for the selected classes (a) and the normalized difference in probability densities (b)

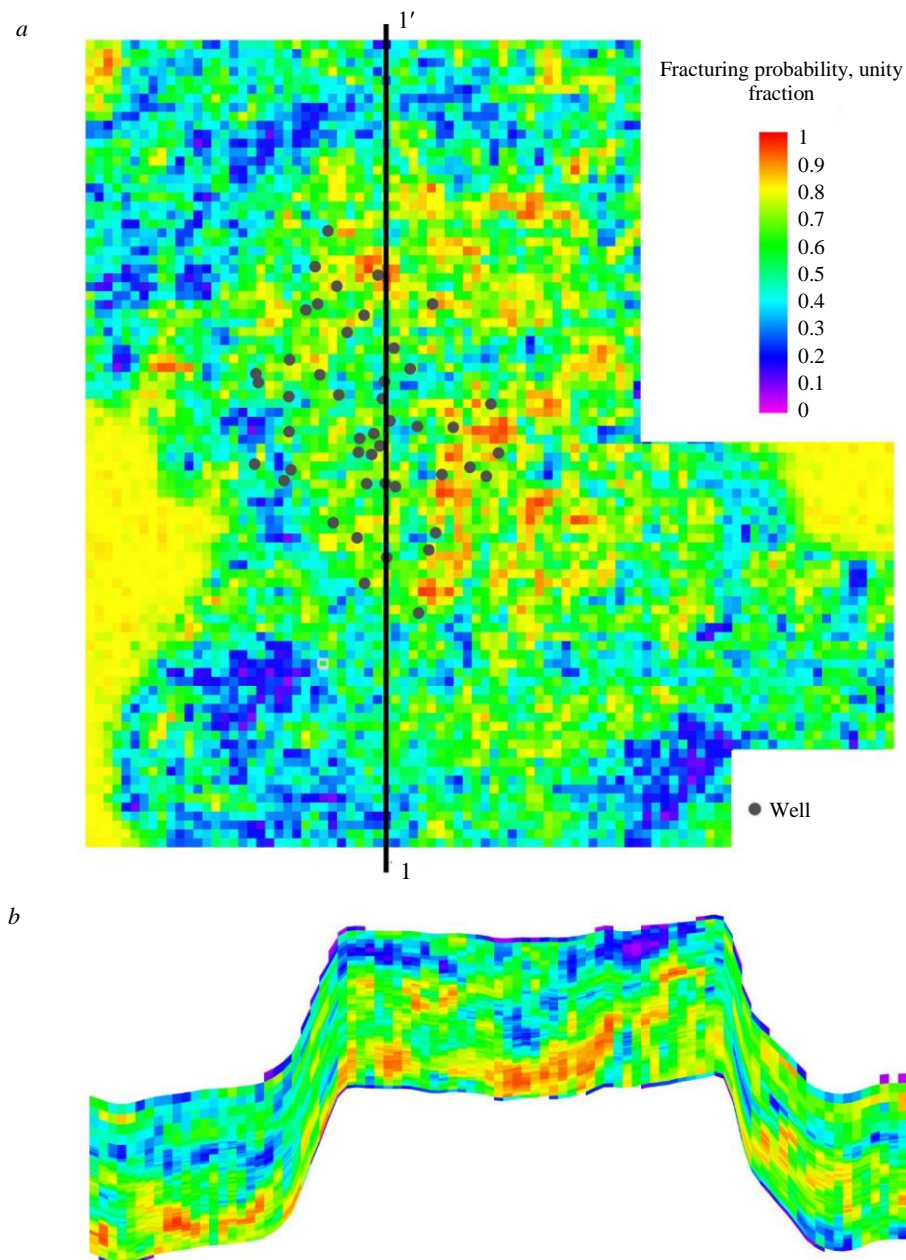


Fig.2. Probability of fracturing distribution along the roof of the TFm formation (a) and along section 1-1 (b)

Based on the obtained cube of a 3D fracturing probability distribution (Fig.2), the average value of this parameter in the perforation interval for all wells was determined. Further analysis of the parameter for a group of wells with a sufficient number of pressure build-up curves demonstrated its linear relationship with a decrease in permeability:

$$\beta = 0.0328CD, \quad (1)$$

where CD – the probability parameter of the presence of fracturing (variation range from 0 to 1).

This dependence was subsequently used to identify regions with decreased permeability in the reservoir simulation modeling, as well as to compile tables of the dependence of permeability and porosity properties on formation pressure in each identified region.

At present, to obtain a 3D distribution of permeability in a reservoir simulation model of fractured and fractured porous pays, in most cases, correlations on porosity are still used with subsequent



calibration to the results of well flow testing (WFT). A geomechanical approach was used to determine the permeability distribution.

There is a lot of information in scientific and technical literature about the influence of the stress state of rocks on the permeability of fractured porous and fractured reservoirs [9-11]. However, the permeability of porous reservoirs does not depend on the stress state as much as the permeability of fractured rock [12-14]. With this in mind, a search was performed for the relationship between the stress state of the massif [15, 16] and fracture permeability determined based on WFT.

It is clear that the permeability of fracture and fault systems is highly dependent on their orientation relative to the principal normal stresses. The critically stressed fault hypothesis [16, 17] states that “mechanically active faults are also hydraulically active, whereas mechanically inactive faults are not”, a view supported by numerous studies [16, 18, 19]. Mechanically active faults are under stresses that promote the opening of fractures, facilitating fluid flow. Thus, the permeability of a fracture system is influenced both by the normal stresses that compress it and by the tangential stresses that induce sliding [20]. Equations for estimating tangential and normal stresses acting along a fracture are widely known [1, 15].

The tendency for slip depends not only on these stresses but also on the rock's strength. In general, the stress state criterion for a weakening surface (fracture or fault) is given by:

$$T_{slip} = \frac{1}{\mu} \frac{\tau}{\sigma_n},$$

where μ – the friction coefficient; τ , σ_n – the tangential and normal stresses on the fracture surface, respectively.

Thus, having estimated the normal and shear stresses acting in the analysed fracture system and having compared them with the pay permeability data recorded in a certain interval, it is possible to judge the degree of the fracture system activity.

In the simplest model – assuming an impermeable matrix and a system of plane-parallel fractures – the fracture permeability is given by:

$$K_m = \frac{e^3}{12d},$$

where e – the fracture aperture; d – the spacing between fractures.

As a parameter characterizing the fracture density (the reciprocal of the distance between fractures), the third degree of the fracturing probability can be used.

If we take the fracturing probability as a measure of fracture density ($p = 1/d$) and assume that the fracture aperture is proportional to the stress ratio ($e = \tau/\sigma_n$), then an expression for the fractured reservoir permeability can be formulated as:

$$K_m = \frac{a \text{Prob}(\tau / \sigma_n)^3}{12},$$

where Prob – the fracturing probability value; τ/σ_n – the ratio of normal (σ_n) and tangential (τ) stresses along the fracture system; a – an empirical coefficient [20].

In simulating fracture permeability, two types of fracturing were considered: ordered, corresponding to the maximum fracture concentration (azimuth 115°, dip angle 80°), and conditionally ordered, associated with the stratigraphic layer curvature, the strike azimuth of which is normal to the direction of maximum curvature. The maximum curvature azimuth was determined as a physical direction (rather than by comparing vectors along mutually perpendicular axes, as many geological



modeling packages do). The dip angle for the conditionally ordered system was obtained by solving an optimization problem. Finally, the pore permeability from the geological model was added to the fracture permeability to yield the total reservoir permeability:

$$K = \frac{a \text{Prob}(\frac{\tau^{ym}}{\sigma_n^{ym}} + \frac{\tau}{\sigma_n})^3}{12} + K_{\text{por}}, \quad (2)$$

where K_{por} – the pore component of permeability.

For subsequent flow simulations, the fracture component of permeability obtained in the local fracture coordinate system must be transformed into the global coordinate system of the model (2). For each fracture system, the permeability tensor is estimated in the global coordinate system of the reservoir simulation model [15]:

$$K_D = K_M \begin{bmatrix} 1 - \cos^2 \alpha \sin^2 \theta & \cos \alpha \sin \alpha \sin^2 \theta & -\cos \alpha \cos \theta \sin \theta \\ \cos \alpha \sin \alpha \sin^2 \theta & 1 - \sin^2 \alpha \sin^2 \theta & \sin \alpha \cos \theta \sin \theta \\ -\cos \alpha \cos \theta \sin \theta & \sin \alpha \cos \theta \sin \theta & \sin^2 \theta \end{bmatrix}; \quad (3)$$

$$[K] = \sum_{i=1}^m [K_{Di}], \quad (4)$$

where α – the dip angle of a given fracture system; θ – the strike azimuth; m is the number of fracture systems.

Development of a geomechanical model. The tangential and normal stresses and the directions in which they act in each cell for permeability simulation were derived from our geomechanical model. Developing a geological-geomechanical model [1, 18, 19] for a pay or an entire field involves assessing the initial stress state by determining parameters such as: vertical stress; minimum and maximum horizontal stresses; azimuth of horizontal stress; pore pressure; spatial distribution of the mechanical properties of both the pay and the surrounding rocks [21-23].

A 3D geomechanical finite element mesh was constructed by exporting the geometry (as eight-node element coordinates) from geological modeling software and converting it into a format compatible with the geomechanical simulator.

The grid cells had lateral dimensions of 100×100 m. In the region of the studied pay, the mesh was vertically refined to a cell thickness of 0.4 m. Instead of modeling the overlying strata in full, a leveling layer was created and loaded with a weight corresponding to the overburden during geomechanical computations.

Since the vertical stress is determined by the weight of the overlying rocks, the density distribution was simulated by interpolating density logging data and integrating over cell thicknesses to compute vertical stress. The mechanical properties of the pay were assigned based on relationships between static and dynamic characteristics obtained from core tests [24-27].

Lateral stress components were simulated using an isotropic elastic porous medium model [16, 28, 29]:

$$S_h = \text{Biot} \cdot p + \frac{\nu}{1-\nu} (\sigma_v - \alpha p) + \frac{E}{1-\nu^2} [\varepsilon_h + \nu \varepsilon_H];$$

$$S_H = \text{Biot} \cdot p + \frac{\nu}{1-\nu} (\sigma_v - \alpha p) + \frac{E}{1-\nu^2} [\nu \varepsilon_h + \varepsilon_H],$$

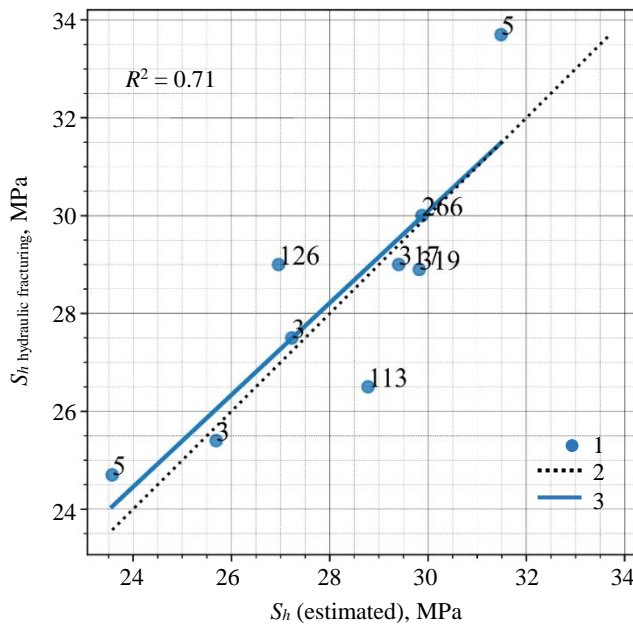


Fig.3. Comparison of estimated stresses with measured values of hydraulic fracture closure pressures

1 – values in wells; 2 – line of equal values; 3 – regressive straight line

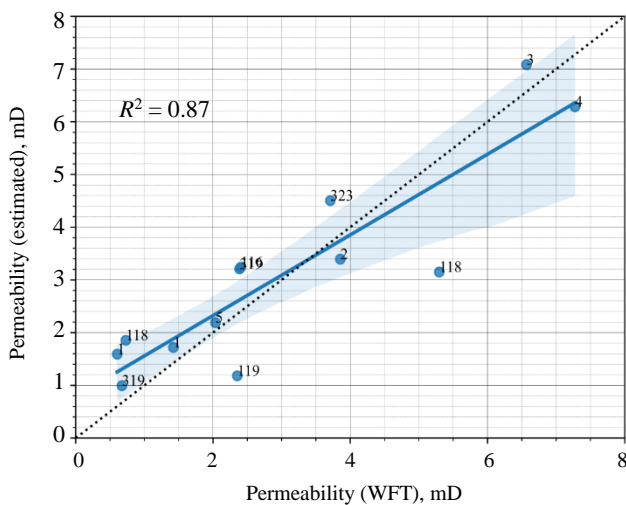


Fig.4. Crossplot of the cube root of the estimated and determined from WFT permeabilities

See Fig.3 for legend

where S_h , S_H – the minimum and maximum horizontal stresses, respectively; p – the formation (pore) pressure; σ_v – the vertical stress, $Biot$ – the Biot coefficient; ν – the Poisson ratio, E – the elastic modulus, ε_h , ε_H – the components of additional tectonic deformations.

The formation pressure distribution was adopted from the current reservoir simulation model and later adjusted using up-to-date pressure data (from well flow tests, hydraulic fracturing, etc.) [30].

Calibration of the simulated minimum horizontal stress profile was performed by comparing the estimated stresses with fracture closure pressures measured during hydraulic fracturing (Fig.3).

Subsequently, the finite element method (implemented in Ansys) was used to evaluate the stress-strain state of the rock mass. The simulation employed a coupled formulation that accounted for fluid flow in a deformable porous medium, with kinematic boundary conditions on the lower and lateral faces to incorporate tectonic deformations.

After completing the geomechanical computations (using equations (2)-(4), a permeability cube was generated and used in the reservoir simulation. The permeability values obtained by this method showed good agreement with WFT results (Fig.4).

In the final phase, reservoir simulation was conducted using the new permeability cubes and incorporating fracture closure concepts.

In the initial simulation, the reservoir was subdivided into many layers with limited hydrodynamic connectivity between interlayers. The fracture system-evident from core studies

and microimager logs-was not explicitly modeled. Although some sections might formally be classified as nonreservoir (owing to negligible total porosity), fluid flow can occur via fractures.

To account for fracturing, we propose an intermediate model between the original single-medium model and a dual-medium (dual-porosity/dual-permeability) model with the following features:

- inactive cells from the initial reservoir simulation model were set as active;
- insignificant porosity was set in the cells of the initial non-reservoir (0.2 %, while the initial oil reserves for the entire model increased by 3 %);
- permeability was determined by formulas (2)-(4) in all cells of the model;



- permeability anisotropy was simulated using the angular parameters of fracture systems identified and adopted in the computations [21];
- permeability reduction was assumed irreversible, as confirmed by numerous compression tests on core samples with single fractures.

Permeability reduction was implemented using 10 rocktab tables describing permeability change [31]. The regions of applying these tables were determined by the fracturing probability value. The first region corresponds to the accumulation areas with a minimum number of fractures, the tenth region – to the areas with the highest fracture density and maximum permeability reduction. The parameter β is determined by the linear dependence (1). The method for considering the effect of permeability reduction in flow simulations is implemented in the tNavigator software package.

Discussion of results

Flow simulations showed that when the formation pressure decreases, there are areas where permeability drops especially rapidly. In the case of low initial permeability and a rapid decrease in permeability, zones may arise where fluid filtration ceases. This indicates an inconstant (dynamic) character of the lithological section over time (Fig.5).

The new approach improved the match between simulated and actual formation pressures in the reservoir model (Fig.6). For example, in well 3 the decline in formation pressure was accompanied by a drop in liquid flow rate from 80 to 20 m³/day. In the original model, a reduction in liquid withdrawal, coupled with the operation of adjacent injection wells, would have been expected to restore formation pressure – a restoration not observed in the field. This discrepancy is attributable to the dynamic lithological structure in the drainage area of well 3. In the geomechanically based simulation, the pressure drop led to a significant and irreversible reduction in permeability over large portions of the accumulation, thereby disrupting reservoir-to-well connectivity among production, injection, and aquifer regions. These results emphasize the importance of timely formation pressure maintenance in fractured reservoirs and highlight the critical role of accurately determining rock compressibility in flow simulations [32, 33].

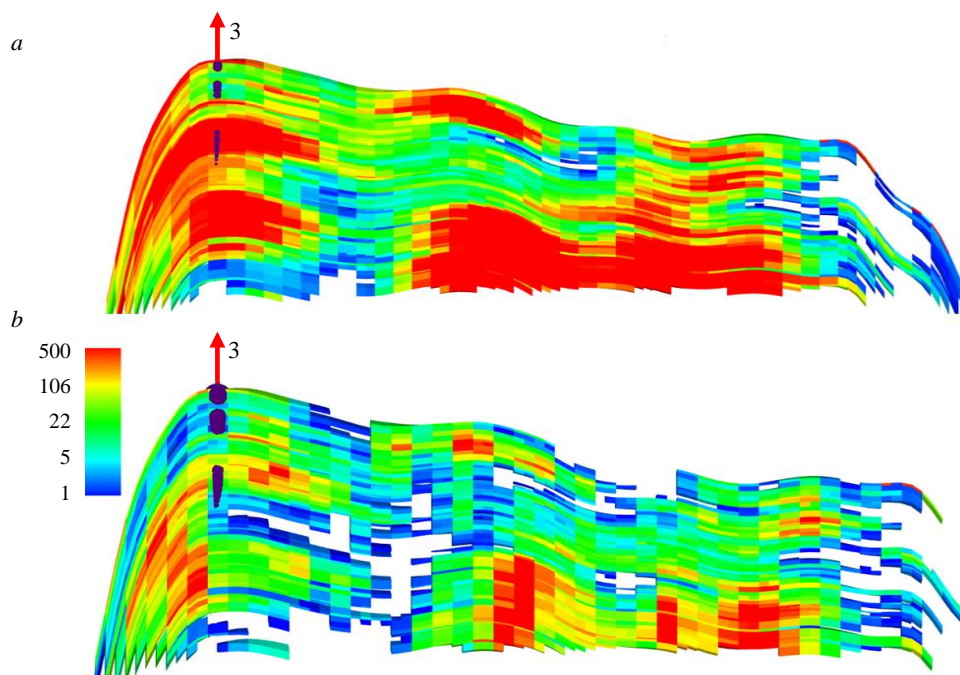


Fig.5. Distribution of well 3 rock permeability across the section at the beginning of development (a) and after 10 years (b)

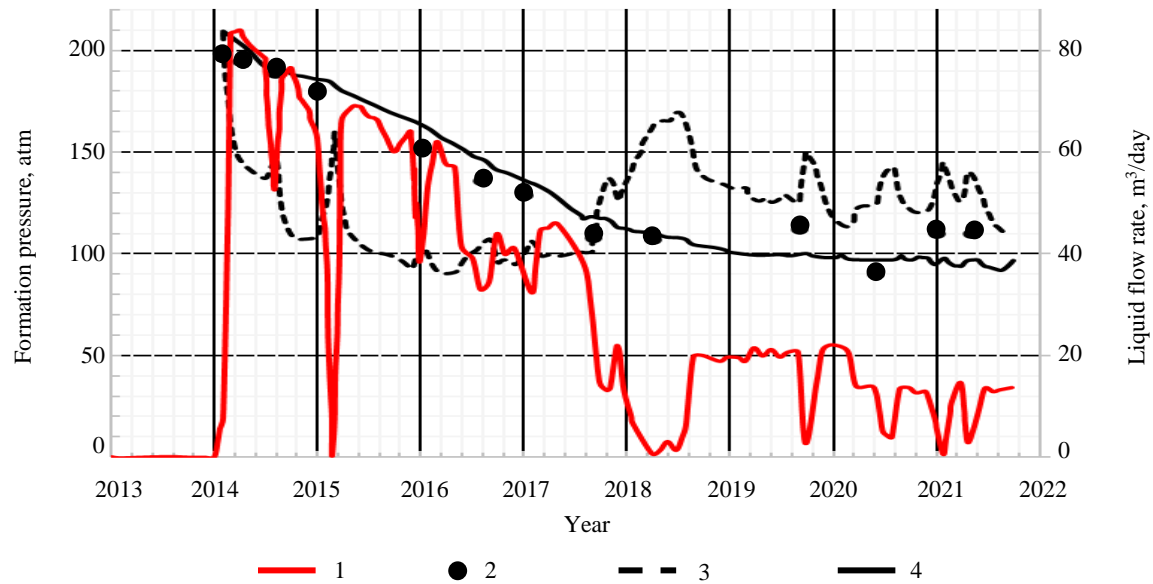


Fig.6. Dynamics of fluid flow rate and reservoir pressure of well 3

1 – fluid flow rate, m³/day; 2 – actual data; 3 – initial fluid flow model; 4 – fluid simulation model based on the geomechanical approach

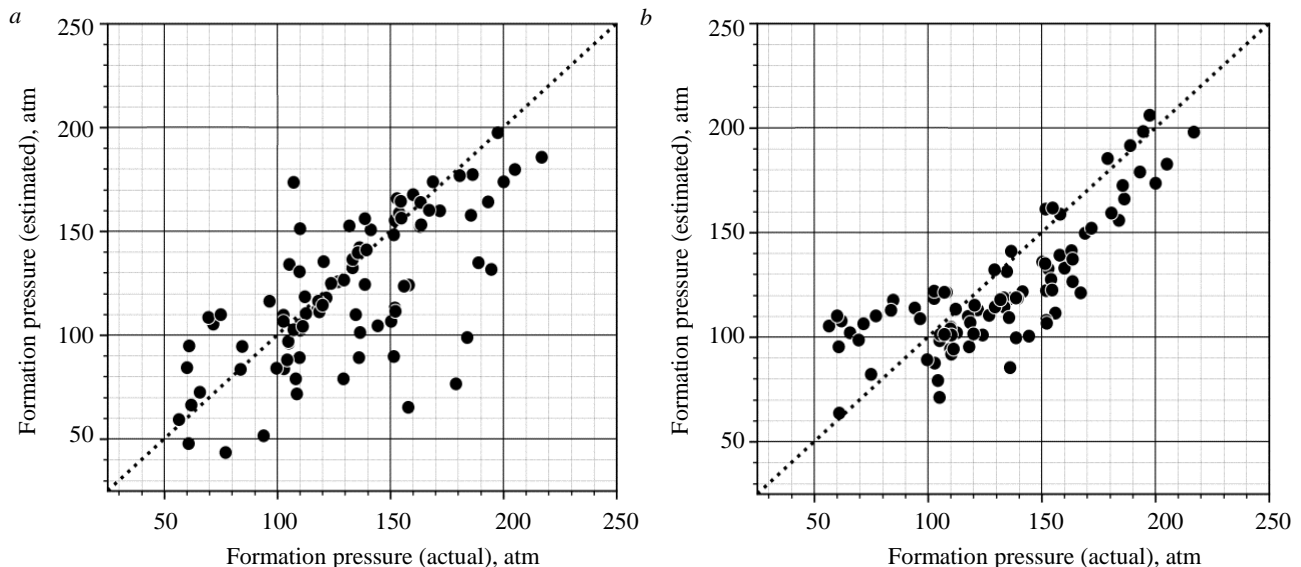


Fig.7. Crossplot of the correspondence between the actual and estimated reservoir pressures in wells for the initial model (a) and the model modified using geomechanical modelling (b)

Figure 7 shows crossplots of actual versus estimated formation pressures for all wells. The geomechanically modified model shows a closer match to the actual pressures compared to the original model, without any deterioration in the prediction quality for well flow rates or water cuts.

Overall, our simulations indicate that the proposed concept effectively improves the fidelity of reservoir simulation models for hydrocarbon accumulations with fractured reservoirs.

Conclusion

Developing new approaches for reservoir simulation of fractured reservoirs is crucial for the design and development of hydrocarbon fields.

Although a discrete fracture network (DFN) model coupled with a dual-porosity/dual-permeability simulation remains the most comprehensive method for representing fracturing, it requires extensive parametric input.



Recently, three-dimensional geomechanical models have become increasingly popular because they can simulate the spatial distribution of principal stresses based on initial physicomaterial properties using the finite element method. While geomechanical models are often developed to support well drilling and hydraulic fracturing operations, their results can also be used to assess fracture aperture in fractured reservoirs and, by extension, to generate 3D permeability cubes.

Generalization of the fracturing study results enabled us to determine the general angle parameters of the fracture systems for the pay under consideration. Machine learning classification using angle stack cubes from 3D seismic surveys yielded a fracturing probability cube. A strong correlation was found between reservoir permeability and the rock state as determined by geomechanical modeling, enabling us to derive the full permeability tensor for the TFm pay.

The tNavigator software package implements a method for considering the effect of permeability reduction in flow simulations. The overall decrease in reservoir permeability is modelled using the built-in keywords of the simulator.

Reservoir simulation modelling using the described approaches has made it possible to significantly improve the convergence of formation pressure dynamics with an acceptable quality of convergence of production dynamics and water cut. Increasing the reliability of formation pressure forecasting allows planning inflow stimulation activities with a more predictable result, creating more realistic fracture properties when developing hydraulic fracturing designs, and optimizing the formation pressure maintenance system.

REFERENCES

1. Kashnikov Yu.A., Ashikhmin S.G. Rock mechanics in the development of hydrocarbon accumulations. Moscow: Gornaya kniga, 2019, p. 496 (in Russian).
2. Shchipanov A.A. The influence of dynamic information of a fractured porous reservoir on the depression increasing effect. *Geologiya, geofizika i razrabotka neftyanykh i gazovykh mestorozhdenii*. 2003. N 2, p. 33-37 (in Russian).
3. Cheremisin N.A., Sonich V.P., Efimov P.A. The role of inelastic deformation of reservoirs in oil recovery. *Neftyanoe khozyaistvo*. 2001. N 9, p. 76-79 (in Russian).
4. Zakrevsky K.E., Kundin A.S. Features of geological 3D modeling of carbonate and cracked oilfields. Moscow: OOO "Belyi Veter", 2016, p. 404 (in Russian).
5. Viktorin V.D. The influence of carbonate reservoir properties on the oil field development efficiency. Moscow: Nedra, 1988, p. 149 (in Russian).
6. Lun Zhao, Zifei Fan, Mingxian Wang et al. Productivity Evaluation of Vertical Wells Incorporating Fracture Closure and Reservoir Pressure Drop in Fractured Reservoirs. *Mathematical Problems in Engineering*. 2020. Vol. 2020. Iss. 1. N 9356178. DOI: [10.1155/2020/9356178](https://doi.org/10.1155/2020/9356178)
7. Yakimov S.Yu. Geological and geomechanical principles of assessing changes in fracture permeability during changes in formation pressure in carbonate reservoirs: Avtoref. dis. ... kand. tekhn. nauk. Perm: Permskii natsionalnyi issledovatel'skii politekhnicheskii universitet, 2018, p. 26 (in Russian).
8. Cherepanov S.S., Ponomareva I.N., Erofeev A.A., Galkin S.V. Determination of fractured rock parameters based on a comprehensive analysis of the core studies data, hydrodynamic and geophysical well tests. *Oil Industry Journal*. 2014. N 2, p. 94-96 (in Russian).
9. Brace W.F. Permeability of crystalline and argillaceous rocks. *International Journal of Rock Mechanics and Mining Sciences & Geomechanics Abstracts*. 1980. Vol. 17. Iss. 5, p. 241-251. DOI: [10.1016/0148-9062\(80\)90807-4](https://doi.org/10.1016/0148-9062(80)90807-4)
10. Kranz R.L., Frankel A.D., Engelder T., Scholz C.H. The permeability of whole and jointed Barre Granite. *International Journal of Rock Mechanics and Mining Sciences & Geomechanics Abstracts*. 1979. Vol. 16. Iss. 4, p. 225-234. DOI: [10.1016/0148-9062\(79\)91197-5](https://doi.org/10.1016/0148-9062(79)91197-5)
11. Barton N., Bandis S., Bakhtar K. Strength, deformation and conductivity coupling of rock joints. *International Journal of Rock Mechanics and Mining Sciences & Geomechanics Abstracts*. 1985. Vol. 22. Iss. 3, p. 121-140. DOI: [10.1016/0148-9062\(85\)93227-9](https://doi.org/10.1016/0148-9062(85)93227-9)
12. Barton N., Bandis S. Effects of Block Size on the Shear Behavior of Jointed Rock. The 23rd U.S. Symposium on Rock Mechanics (USRMS), 25-27 August 1982, Berkeley, CA, USA. OnePetro, 1982. N ARMA-82-739.
13. Fischer K. Geomechanical reservoir modeling – workflow and case study from the North German Basin: vom Fachbereich Material- und Geowissenschaften der Technischen Universität Darmstadt zur Erlangung des akademischen Grades Doktor der Naturwissenschaften (Dr. rer. nat.) genehmigte Dissertation. Darmstadt: Technische Universität, 2013, p. 265.



14. Zhang Zhang, Shunli He, Daihong Gu et al. Effects of stress-dependent permeability on well performance of ultra-low permeability oil reservoir in China. *Journal of Petroleum Exploration and Production Technology*. 2018. Vol. 8. Iss. 2, p. 565-575. DOI: [10.1007/s13202-017-0342-2](https://doi.org/10.1007/s13202-017-0342-2)
15. Wittke W. Rock Mechanics Based on an Anisotropic Jointed Rock Model (AJRM). *Ernst & Sohn*. 2014, p. 876. DOI: [10.1002/9783433604281](https://doi.org/10.1002/9783433604281)
16. Zoback M.D. Reservoir Geomechanics. Cambridge: Cambridge University Press, 2007, p. 449. DOI: [10.1017/CBO9780511586477](https://doi.org/10.1017/CBO9780511586477)
17. Zoback M.D., Kohli A.H. Unconventional Reservoir Geomechanics. Shale Gas, Tight Oil, and Induced Seismicity. Cambridge University Press, 2019, p. 495. DOI: [10.1017/9781316091869](https://doi.org/10.1017/9781316091869)
18. Shustov D.V., Kashnikov Yu.A., Ashikhmin S.G., Kukhtinskiy A.E. 3D Geological Geomechanical Reservoir Modeling for the Purposes of Oil and Gas Field Development Optimization. *Geomechanics and Geodynamics of Rock Masses*. CRC Press, 2018. Vol. 2, p. 1425-1430.
19. Tavaf Saeed, Abdideh M. Using petrophysical and geomechanical modeling of reservoir rock in well completion. *Modeling Earth Systems and Environment*. 2022. Vol. 8. Iss. 4, p. 5639-5652. DOI: [10.1007/s40808-022-01440-4](https://doi.org/10.1007/s40808-022-01440-4)
20. Shustov D.V., Kashnikov Yu.A. Development of geological-geomechanical model of some part of Urubcheno-Tokhonskoe oil field. *Geology, geophysics and development of oil and gas fields*. 2015. N 4, p. 26-31 (in Russian).
21. Charlez Ph.A. Rock Mechanics. In 2 volumes. Vol. 2: Petroleum Applications. Technip Editions, 1997, p. 661.
22. Hampton J., Boitnott G. Integration of Fine-Scale, Plug, and Well-Log Geomechanical Properties. 53rd U.S. Rock Mechanics/Geomechanics Symposium, 23-26 June 2019, New York City, NY, USA. OnePetro, 2019. N ARMA-2019-2077.
23. Boitnott G., Louis L., Hampton J. et al. High Resolution Geomechanical Profiling in Heterogeneous Source Rock From the Vaca Muerta Formation, Neuquén Basin, Argentina. 52nd U.S. Rock Mechanics/Geomechanics Symposium, 17-20 June 2018, Seattle, WA, USA. OnePetro, 2018. N ARMA-2018-129.
24. Gowida A., Elkhatatny S., Moussa T. Comparative Analysis Between Different Artificial Based Models for Predicting Static Poisson's Ratio of Sandstone Formations. International Petroleum Technology Conference, 13-15 January 2020, Dhahran, Kingdom of Saudi Arabia. OnePetro, 2020. N IPTC-20208-MS. DOI: [10.2523/IPTC-20208-MS](https://doi.org/10.2523/IPTC-20208-MS)
25. Qi Li, Aguilera R., Cinco-Ley H. A Correlation for Estimating the Biot Coefficient. *SPE Drilling & Completion*. 2020. Vol. 35. Iss. 2, p. 151-163. DOI: [10.2118/195359-PA](https://doi.org/10.2118/195359-PA)
26. Rekoske J., Walton G. Estimating Mechanical Properties of Sandstone from Petrographic and Physico-Mechanical Indices. 53rd U.S. Rock Mechanics/Geomechanics Symposium, 23-26 June 2019, New York City, NY, USA. OnePetro, 2019. N ARMA-2019-0101.
27. Tariq Z., Mahmoud M.A., Abdulraheem A., Al-Shehri D.A. On Utilizing Functional Network to Develop Mathematical Model for Poisson's Ratio Determination. 52nd U.S. Rock Mechanics/Geomechanics Symposium, 17-20 June 2018, Seattle, WA, USA. OnePetro, 2018. N ARMA-2018-744.
28. Sone H. Mechanical Properties of Shale Gas Reservoir Rocks and its Relation to the in-Situ Stress Variation Observed in Shale Gas Reservoirs: Dissertation for the Degree of Doctor of Philosophy. Stanford University, 2012, p. 247.
29. Sone H., Zoback M.D. Mechanical properties of shale-gas reservoir rocks – Part 2: Ductile creep, brittle strength, and their relation to the elastic modulus. *Geophysics*. 2013. Vol. 78. N 5, p. D393-D402. DOI: [10.1190/geo2013-0051.1](https://doi.org/10.1190/geo2013-0051.1)
30. Zakharov L.A., Martyushev D.A., Ponomareva I.N. Predicting dynamic formation pressure using artificial intelligence methods. *Journal of Mining Institute*. 2022. Vol. 253, p. 23-32. DOI: [10.31897/PMI.2022.11](https://doi.org/10.31897/PMI.2022.11)
31. Indrupskiy I.M., Ibragimov I.I., Tsagan-Mandzhiev T.N. et al. Laboratory, numerical and field assessment of the effectiveness of cyclic geo-mechanical treatment on a Tournaisian carbonate reservoir. *Journal of Mining Institute*. 2023. Vol. 262, p. 581-593. DOI: [10.31897/PMI.2023.5](https://doi.org/10.31897/PMI.2023.5)
32. Zhukov V.S., Kuzmin Yu.O. Experimental evaluation of compressibility coefficients for fractures and intergranular pores of an oil and gas reservoir. *Journal of Mining Institute*. 2021. Vol. 251, p. 658-666. DOI: [10.31897/PMI.2021.5.5](https://doi.org/10.31897/PMI.2021.5.5)
33. Zhukov V.S., Kuzmin Yu.O. Comparison of the approaches to assessing the compressibility of the pore space. *Journal of Mining Institute*. 2022. Vol. 258, p. 1008-1017. DOI: [10.31897/PMI.2022.97](https://doi.org/10.31897/PMI.2022.97)

Authors: Yuri A. Kashnikov, Doctor of Engineering Sciences, Professor, <https://orcid.org/0000-0002-6168-7251> (Perm National Research Polytechnic University, Perm, Russia), Denis V. Shustov, Candidate of Engineering Sciences, Leading Researcher, <https://orcid.org/0000-0002-8404-7935> (Perm National Research Polytechnic University, Perm, Russia), Sergei Yu. Yakimov, Candidate of Engineering Sciences, Leading Researcher, geotech@pstu.ru, <https://orcid.org/0009-0004-4514-0370> (Perm National Research Polytechnic University, Perm, Russia).

The authors declare no conflict of interests.



Assessment of the ecological state of aquatic ecosystems by studying lake bottom sediments

Mariya A. Chukaeva¹✉, Tatyana V. Sapelko²

¹ Empress Catherine II Saint Petersburg Mining University, Saint Petersburg, Russia

² Institute of Limnology of the RAS – Saint Petersburg Federal Research Center of the RAS, Saint Petersburg, Russia

How to cite this article: Chukaeva M.A., Sapelko T.V. Assessment of the ecological state of aquatic ecosystems by studying lake bottom sediments. *Journal of Mining Institute*. 2025. Vol. 271. N 16225, p. 53-62.

Abstract

The article presents the results of coupled palynological and geochemical studies of five various genesis lakes, located along the route of the expedition “In the footsteps of Alexander von Humboldt in Siberia, Altai and Eastern Kazakhstan”, dedicated to the double anniversary: the 190th anniversary of the expedition across Russia of the famous scientist and his 250th birthday. A geochemical analysis of water and bottom sediments of Ik Lake (Siberia), Lakes Kolyvanskoe and Beloe (Altai), Lake Bezymyannoe (Kazakhstan) and Nagornyi Pond (Altai) was carried out. Based on their results an assessment of studied lakes ecological state was given through single and integral criteria. A high level of pollution was noted for Nagornyi Pond and Lake Bezymyannoe, which is caused by a significant technogenic load from nearby mines. This is consistent with the data of palynological research. The aquatic ecosystems of Lakes Kolyvanskoe and Beloe are characterized by a satisfactory ecological situation, but they experience an increased recreational load. The results of spore-pollen analysis and analysis of non-pollen palynomorphs showed the low ability of these lakes to self-healing. The most favorable ecological state and high self-cleaning capacity were noted for Lake Ik, which is consistent with the data of palynological studies. It is being confirmed with the results of palynological studies. It was therefore concluded about the ability to make a quick assessment of the aquatic ecosystems’ ecological state by studying lakes using coupled palynological and geochemical analysis.

Keywords

lakes; lake sediments; surface samples; technogenic impact; geochemical analysis; pollen analysis

Funding

Research is executed within the State task N FSRRW-2023-0002; FMNG-2019-0004.

Received: 13.04.2023

Accepted: 25.10.2023

Online: 23.01.2024

Published: 25.02.2025

Introduction

In May-June 2019, the Russian-German expedition “In the Footsteps of Alexander von Humboldt in Western Siberia, Altai and Eastern Kazakhstan”, dedicated to the 250th anniversary of the birth of the outstanding scientist and the 190th anniversary of his expedition to Russia, took place within the framework of a joint project of St. Petersburg Mining University, Freiberg Mining Academy and the St. Petersburg Union of Scientists. Among the various objects (outcrops, rocks, dumps, soils, landscapes) along the route of the expedition lakes were studied.

For a comprehensive assessment of an aquatic ecosystem, it is necessary to know the indicators of water and its biotic part [1]. Bottom sediments as a depositing medium are also instrumental in assessing the state of a water body [2]. They accumulate chemical elements and provide information about the ecological condition of the catchment area. Bottom sediments are an important source of information about past climatic and geochemical conditions, allowing assessing the ecological state of air and water [3, 4]. They actively accumulate pollutants and can become a source of secondary pollution of water bodies. Heavy metals intensively accumulating in bottom sediments are among the most dangerous pollutants [5]. Water and bottom sediments were sampled with subsequent chemical and spore-pollen analyses for express-assessment of the ecological state of lakes. Palynological studies of lake sediments provide additional information for assessment of the regional geochemical



background [6]. When comparing the results of surface samples analyses with modern vegetation, discrepancies are often revealed. Their analysis makes it possible to draw conclusions about changes in the vegetation cover under the influence of technogenesis [7, 8].

Study area. The authors investigated lakes of different types (in terms of genesis, size, water balance and chemical composition) on the border of forest and forest-steppe zones of Siberia, Ore Altai and Kazakhstan (Fig.1).

Ik Lake is located in Krutinskii District of Omsk Oblast in the south of the West Siberian Plain in the interfluvium of the Ishim and Irtysh Rivers. It is a part of the system of The Big Krutinsk Lakes (Ik, Saltaim, Tenis) belonging to the Irtysh Lake and River system. The shape of the lake is round, slightly elongated from southwest to northeast, length 12 km, width 8 km, length of the shoreline 36.2 km. The origin of the basin is glacial. The mirror area is 71.4 km² and the catchment area is 1190 km². The bottom is flat, the depth increases smoothly towards the middle, the average depth is 2.7 m, maximum 4.7 m. The shores are steep and composed of coastal-alluvial deposits of sands with interlayers of clays with underlying siltstones and sandstones [9]. Since southwesterly winds prevail on Ik Lake, the northeastern and eastern shores are subject to abrasion and serve as a source of Ca, Mg, Fe, and Al inputs to the water. Aquatic vegetation zonally encircles the lake. At the water's edge there are various species of sedges, arrowleaf, chasteberry, plantain, amphibian buckwheat, teloresis. Then there is a zone of cattail and reed. The water supply of the lake is supported by the Yaman and Krutikha Rivers, as well as by atmospheric precipitation. The mouth of the Krutikha River is heavily silted, and in dry years the water flow is insignificant. The Kiterma River flows out of the lake, connecting Ik Lake with Saltaim Lake. There is a dam at its source, which maintains the water level in the lake. The watershed is located in the forest-steppe zone [9]. The settlements of Kiterma, Ust-Kiterma, Krutinka and Yaman are located along the perimeter of the lake. Farms, summer cattle camps, cultivated fields and unauthorized dumps are concentrated in them. Surface runoff from these areas is a source of pollution of the lake with Al, Fe, Cu, Mn and nutrients. The lake is also experiences recreational load. Three surface samples of bottom sediments were taken from Ik Lake and water samples were taken at the same points.



Fig.1. Study area with sampling points (based on Google maps)



Kolyvanskoe Lake is located at the foot of the northern slope of the Kolyvanskii Ridge in the Zmeinogorskii District of Altai Region. The regional background of Zn, Cr, and Cu is elevated here as a result of many years of active mining of polymetallic ores. The lake has an irregular shape and stretches from north to south. Its length is 4 km with a width from 0.5 to 2.5 km, the average depth is 1.8 m and the maximum depth is 4.1 m [10]. The origin of the basin is presumably tectonic. The water mirror area is 4.5 km², the catchment area is 55.7 km². The shores are gentle, low, in some places overgrown with bushes. The Kolyvanka River flows into the Kolyvanskoe Lake from the east, the Pochtovyi Stream from the west and The Ust-Kolyvanka River flows out from the north [11]. Kolyvanskoe Lake is a geological and landscape natural monument of regional significance. It is characterized by rich and diverse flora and unique vegetation. It is inhabited by a rare species (tertiary relict) of water nut. The banks are dominated by pinnate sagebrush, hair grass, valis fescue, steppe bluegrass, goniolimon. There are dense thickets of bushes (common bird cherry, cotoneaster, Siberian barberry, Tatar honeysuckle); there are birch and common pine in some places. Ash-leaved maple, which belongs to the adventive species, is widespread. Kolyvanskoe Lake suffers from a high recreational load. As a result of many years of unorganized recreation and tourism, landscapes are significantly disturbed. The priority pollutants entering the lake with surface runoff are Fe, Cu, Al, Zn, Pb, Cr and biogenic elements. Three surface samples of bottom sediments and at one point a water sample were taken at the lake.

Nagorny Pond is located in Zmeinogorsk, Altai Krai, at the southern foot of the Kolyvan Ridge. It was created in the floodplain of the Zmeyevka River in 1786 according to the project of hydraulic engineer K.D.Frolov [12]. The dam built on it flooded an earlier dam upstream and formed a pond fed by the river, several springs and rain waters. The mirror area is 7.5 km². At present, the dam and part of the structures for ore lifting and mine water pumping have been preserved. The main source of anthropogenic impact is the Zmeinogorsk polymetallic mine, which operated in the XVIII-XX centuries and was mothballed. Recultivation of dumps and mine workings was not carried out, so the pollution of the pond has aerogenic (as a result of dusting) and hydrogenic (as a result of infiltration of atmospheric precipitation through the thickness of disturbed rocks) character [13, 14]. The main potential pollutants are Fe, Zn, Cu, Cr, Ni, Cd, Ti. One sample of bottom sediments and a water sample were taken from the Nagorny Pond.

Beloe Lake is located in a wide basin of the Kolyvanskii Ridge in the Kuryinskii District of Altai Krai. It has an oval shape with the size of 2.4 by 1.2 km, average depth of 4.5 m and maximum depth of 7.4 m [15]. The origin of the basin is tectonic. The mirror area is 2.7 km², the catchment area is 14.2 km². The lake lies in granite shores from the south and in shale shores from the east and north. Beloe Lake belongs to the basin of the Belaya River. Beloe Lake belongs to the basin of the Loktevka River, a left tributary of the Charysh River. It is connected with the Belaya River by an artificial canal. At the mouth of the canal there is a concrete dam regulating water flow [16]. Ozernyi Stream in the southeast and Bezymyannyi Stream in the northeast flow into the lake. Mountain-steppe vegetation is widespread in the vicinity, with a pine forest approaching from the northwest. The following plants grow along the banks: southern reed, lake reed, amphibian mountain, submerged hornwort, shiny and curly radish. In the recreational load on the lake ecosystem the share of unorganized tourism is high, especially in summer months. The southeastern part of the coast is used for hayfields. Since 2010 the lake has the status of a natural monument within the boundaries of the shoreline. Since 2013 the company "Eco-vector" has been extracting sapropel from the lake. Two samples of bottom sediments and a water sample were taken from the lake.

Bottom sediments were also sampled at Bezymyannoe Lake, located in the Rudnyi Altai in a mountain basin at the foot of the Ivanovskii Ridge, 30 km from Ridder (Kazakhstan). The lake is drainless and has no tributaries. From the western side it is framed by outcrops of calcareous and siliceous siltstones and microquartzites, presumably of the Kryukov Formation, up to 25-30 m thick. Along the faults, the rocks are locally altered by superimposed hydrothermal processes. In the Ridder district, they formed rich polymetallic ores mined by several mines [17]. Scattered disseminated mineralization of sphalerite, galena and chalcopyrite was recorded in the studied outcrop. In the oxidation zone, these minerals are actively decomposed and, as a result of wind and water erosion,



may serve as a source of Zn, Pb, Cu, and Fe contamination of surface waters [18]. The lake may also experience anthropogenic load from the existing mining enterprise in Ridder. The prevailing wind direction according to long-term meteorological observations is westerly (38 %), which contributes to the aerotechnogenic transfer of pollutants from the territory of mines and dumps [19]. The main potential pollutants are Fe, Zn, Cu, Mn, Pb, Cr, Cd, and Ni.

The sedimentation rate in the studied lakes is 0.3-0.35 cm/year [9].

Methods

Water samples were collected from a boat and from the shores of small lakes from a depth of 10-30 cm from the surface into polyethylene containers. Immediately at the sampling site, non-stable water quality indicators such as temperature, salinity and pH were determined using a WTW MULTI 350I multimeter with a set of electrodes. In accordance with GOST R 59024-2020, one part of the sample was acidified with nitric acid to pH less than 2, and the other part was left in its natural state. After that the samples were cooled to +4 °C for transportation and further analysis in laboratory conditions.

Bottom sediments were sampled with a Voronkov lot into polyethylene containers at the same points as the water samples, and then cooled to +4 °C for further transportation. The thickness of the sampled sediment layer was 2.5-3 cm. Palynological analysis of bottom sediments was carried out in laboratory conditions to characterize the vegetation of lakes and their catchments, and also their chemical composition was determined: organic, inorganic and total carbon C on TOC-V (Shimadzu), water-soluble, mobile and gross forms of heavy metals according to MVI-80-2008. Also for bottom sediments the losses on ignition and pH of water extract were determined according to GOST 26423-85.

Quantitative chemical analysis of water was performed in the accredited laboratory “Environmental Modeling” of Saint Petersburg Mining University. Metal concentrations were determined by atomic emission spectrometry with inductively coupled plasma on ICPE-9000 (Shimadzu) according to M-02-1109-09, anions – by chromatographic method on LC-20 Prominence (Shimadzu) by ion chromatography according to M-02-1805-09.

Spore-pollen analysis of bottom sediments was carried out at the Institute of Limnology of the Russian Academy of Sciences. Samples were processed using heavy liquid according to the method of V.P.Grichuk¹ and tested for carbonation using hydrochloric acid. Only the sample from Nagornyi Pond was found to be weakly carbonate. Pollen and spores were identified according to the identifiers of L.A.Kupriyanova, L.A.Alyoshin² and P.D.Moore, J.A.Webb, M.E.Collinson³, as well as with the help of material collections of the Institute of Limnology of the Russian Academy of Sciences. To reconstruct the state of the lake ecosystem, non-dust palynomorphs [20], green algae *Botryococcus braunii* and *Pediastrum*, fungal spores, plant stomata, remains of microfauna, rhizopods, microparticles of coals, etc. were determined in each sample [21].

Quantitative chemical analysis of bottom sediments was carried out in the accredited laboratory “Environmental Modeling” of Saint Petersburg Mining University. Bottom sediment samples were dried at room temperature to air-dry condition in a well-ventilated place and in the absence of direct sunlight, while minimizing the possibility of secondary contamination. After that, foreign particles (pebbles, debris, algae, etc.) were removed from the air-dry samples using tweezers. The cleaned sample was ground in an agate mortar. Determination of moisture content and losses on ignition was carried out on the thermogravimetric analyzer TGA 701 by LECO according to R 52.24.763-2012.

Metals were considered as priority pollutants in bottom sediments [22, 23]. Decomposition of samples to determine the gross content of metals was carried out in a microwave system with a mixture of hydrochloric, nitric, hydrofluoric and boric acids. The mobile forms were extracted with acetate and ammonium buffer solution with pH = 4.8. For determination of water-soluble forms, aqueous extracts

¹ Grichuk V.P. Methodology for processing sedimentary rocks poor in organic residues for the purposes of pollen analysis. *Problems of physical geography*. 1940. N 8, p. 53-58.

² Kupriyanova L.A., Aleshina L.A. Pollen and spores of plants of the flora of the European part of the USSR. Leningrad: Nauka, 1972, p. 171.

³ Moore P.D., Webb J.A., Collinson M.E. Pollen analysis. Oxford: Blackwell Scientific Publications, 1991, p. 216.



were prepared based on bidistilled water. Acid decomposition products and extracts were analyzed by atomic absorption and atomic emission spectrometry methods according to MVI-80-2008. The pH value was also determined in aqueous extracts.

Discussion of results

All the studied lakes are fresh with neutral pH level. According to O.A.Alekin's classification, by predominant anion they belong to hydrocarbonate; by predominant cation – Ik Lake belongs to sodium, the others – to calcium. Ik Lake and Kolyvanskoe Lake belong to the highest category, Beloe Lake – to the first category of fishery importance; Nagornyi Pond and Bezmyannoe Lake are water bodies of cultural and domestic importance. Comparison of the results with MACs for the respective categories of water use showed exceedances for Fe ($K_{MAC} = 3$), Mn (9), Al (3) and Cu (15) in Kolyvanskoe Lake; for Mn (3) and Cu (30) in Beloe Lake; for Sr (1.5) and Cu (60) in Ik Lake. No exceedances were recorded in Nagornyi Pond and Bezmyannoe Lake, which is associated with more “soft” norms for water bodies of cultural and domestic importance.

Relative to the conditionally background values for lakes of the forest-steppe zone of Western Siberia, obtained from the results of the study of the chemical composition of the 130 small lakes (that are not directly under the influence of anthropogenic impact) [24, 25], the following chemical elements were found: the increased content of Cu ($K_{background} = 6.8$), Co (2) and Cr (1.2) in Ik Lake; Al (2.6), Zn (2.3), Cu (2), Cr (1.8) and Fe (1.5) in Kolyvanskoe Lake; Co (1.5), Cr (2), Cu (3.3) and Zn (1.8) – in Beloe Lake; Fe (4), Al (3.1), Cu (4.5), Cr (4.5), Zn (2.2), and Ni (1.8) – in Pond Nagornyi; Cu (7), Cr (4.2), Zn (3.1) and Ni (2.4) – in Bezmyannoe Lake.

The results of the spore-pollen analysis (arithmetic mean values for three samples) are presented in Table 1, according to which the lake landscapes of Nagornyi Pond and Bezmyannoe Lake are classified as forest, and those of Ik Lake and Kolyvanskoe Lake as forest-steppe.

Table 1

Spore-pollen spectra composition of surface samples of the studied water bodies

Water body	Tree pollen, %	Grass pollen, %	Spores, %
Ik Lake	61	38	1
Kolyvanskoe Lake	43	53	4
Nagornyi Pond	73	25	2
Bezmyannoe Lake	70	30	0

Pollen of birch and pine prevails among tree species in the spore-pollen spectra of Ik Lake and Kolyvanskoe Lake. Pollen of fir and pine with a significant admixture of birch and a small admixture of spruce prevails in the spore-pollen spectra of Bezmyannoe Lake. Pine pollen absolutely dominates in Nagornyi Pond, which is partially introduced in all cases, as it is very volatile and is transported to the maximum distance relative to all other pollen grains. Grass pollen in Ik Lake and Kolyvanskoe Lake is represented mainly by cereals and artemisia, in Bezmyannoe Lake and Nagornyi Pond – by cereals and sedges. Pollen of ruderal grasses was detected in all samples, except for the bottom sediments of Ik Lake. The maximum pollen content of aquatic and coastal aquatic plants was detected in Kolyvanskoe Lake.

Non-pollen palynomorphs in all bottom sediment samples are represented by green algae *Pediastrum*, remains of microfauna, fungi spores and coal microparticles. No species of *Pediastrum* algae were found in the surface samples of

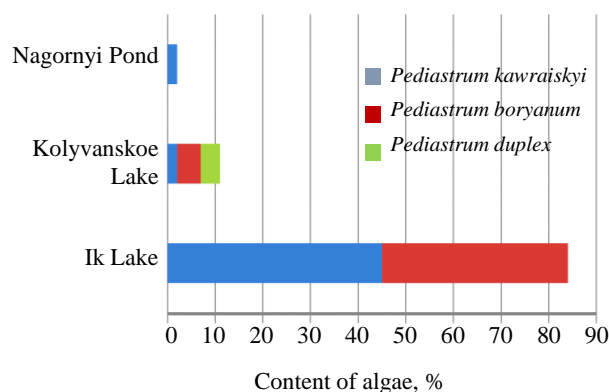


Fig.2. Content of different species of *Pediastrum* algae in surface samples of the studied water bodies



Bezmyannoe Lake. Their maximum content was found for Ik Lake, with the highest diversity of species noted for Kolyvanskoe Lake (Fig.2). In Kolyvanskoe Lake green algae are also represented by *Botryococcus braunii* and diatoms, in Nagornyi Pond – mainly by diatoms. Spores of ferns and horsetails were recorded in Ik Lake and Nagornyi Pond. A small number of shell amoebae was detected only in Nagornyi Pond. The maximum content of charcoal microparticles and minimum microfauna was noted for Bezmyannoe Lake, *Elodea* pollen was also detected there. *Plantago* and *Cerealia* were found in small amounts in the bottom sediments of Ik Lake.

The results of chemical analysis of bottom sediments for the content of gross, mobile and water-soluble forms of metals are presented in Table 2. The values of losses on ignitions and hydrogen index of water extract are presented in Table 3.

Table 2

Content of gross, mobile and water-soluble forms of metals in the studied bottom sediment samples

Element	MAC (APC)* gross / mobile form		Metal content: gross / mobile / water-soluble forms, ppm**											
			Ik Lake			Kolyvanskoe Lake			Nagornyi Pond			Bezmyannoe Lake		
Al	n/s		22850	13.1	11.3	45057	81	5.6	19624	27	26	34184	28	13
Ba	n/s		175	6.8	0.95	325	10	1.7	1731	76	1.1	170	22	0.67
Cd	0.5	n/s	1.4	0.49	0.17	2.4	1.2	0.16	3.8	1.2	0.12	4.4	1.1	0.095
Co	n/s	5.0	3.1	0.87	0.39	16	1.8	0.51	14	3.0	0.20	27	5.2	0.28
Cr	0.05	n/s	18	0.13	0.058	73	0.53	0.0093	46	0.38	0.088	49	0.43	0.060
Cu	33	3	3.6	0.57	0.079	42	1.9	0.20	34	2.6	0.48	83	11	0.75
Fe	n/s	n/s	7017	75	15	52152	1983	0.89	27352	680	37	46897	280	11
Mn	1500	80	171	16	0.44	481	77	19	785	523	1.4	1655	303	0.78
Ni	n/s	4.0	15	0.28	0.072	51	3.1	0.18	25	1.4	0.18	38	1.3	0.15
Pb	32	6.0	8.0	0.27	< 0.25	8.4	0.88	< 0.25	4.3	0.33	< 0.25	4.1	0.28	< 0.25
Sr	n/s		85	12	3.7	131	20	4.6	336	183	13	114	35	2.6
Ti	n/s		2523	0.92	0.89	5387	0.99	0.18	3834	0.52	0.28	4754	0.57	0.30
Zn	55	23	6.7	1.7	0.058	81	6.8	1.0	86	7.1	0.25	366	72	0.24

* The MAC and APC values are adopted according to SanPiN “On approval of sanitary regulations and standards SanPiN 1.2.3685-21 “Hygienic standards and requirements for ensuring the safety and (or) harmlessness of environmental factors to humans”; n/s – the indicator is not standardized.

** Arithmetic mean values for three samples; bold numbers – values exceeding MAC (APC) values.

Table 3

Losses on ignition and pH of aqueous extract of the studied bottom sediment samples

Indicator	Ik Lake	Kolyvanskoe Lake	Nagornyi Pond	Bezmyannoe Lake
Losses on ignition, %	16.3	14.4	9.04	6.04
pH	6.66	6.36	7.17	6.88

Bottom sediments sampled at Beloe Lake are more than 90 % sandy fraction ($d > 0.05$ mm). This is due to the sapropel mining at the lake. Their further chemical and spore-pollen analysis was not carried out, since it is proved [26, 27] that it is necessary to analyze the finest particles ($d < 0.01$ mm) to obtain representative information on the state of water bodies.

Assessment of the degree of impact of bottom sediments on the ecological state of water bodies presents certain methodological difficulties [28]. First of all, this is due to the lack of norms for them. The Water Code of the Russian Federation defines lakes as an aggregate of surface waters and the land covered by them within the shoreline. In this regard, at first, a comparison of the concentrations of gross forms of metals with MAC (APC) for soils was carried out [29, 30]. However, taking into account only the gross forms of metals, does not allow estimating their migration capacity and, consequently, the potential contribution of bottom sediments to surface water pollution. Reliable interpretation of the results of bottom sediment analysis should be based on information about the forms of pollutants [28]. For this reason, as well as for the reason of potentially possible secondary pollution of the studied water bodies as a result of wind agitation, changes in redox conditions, increased activity of microorganisms, etc., special attention was paid to the assessment of mobile and water-soluble forms of metals [31, 32].



Bezmyannoe Lake is the only one of the studied water bodies, in which exceeding of the established normative values for mobile forms of metals (Co, Cu, Zn) was recorded, but their content is insignificant as a percentage of the gross forms. A high percentage of water-soluble and mobile forms of heavy metals relative to their gross content (Table 2) was noted in bottom sediments of Ik Lake (Cd, Co, Cr, Ni, Sr and Ti), Kolyvanskoe Lake (Co, Sr, Mn) and Nagornyi Pond (Cr, Cu, Ti). Presumably, it is connected with different genesis of bottom sediments: in the first case, the share of rock weathering products prevails; in the second case – the share of plant remains, microorganisms, etc. Thus, for Ik Lake, Krutinskoe Lake and Nagornyi Pond, the bottom sediments have a higher content of organic component (Table 3), compared to Bezmyannoe Lake.

To establish the degree and nature of contamination of bottom sediments, the bottom accumulation coefficient was used, which was calculated using the formula according to R 52.24.763-2012:

$$BAC = \frac{C_{BS}}{C_{water}} \quad (1)$$

where C_{BS} – concentration of pollutants in bottom sediments, $\mu\text{g/g}$ dry residue; C_{water} – concentration of pollutants in water respectively in the same period of time, mg/dm^3 .

Bottom accumulation coefficients calculated for the studied water bodies are presented in Fig.3 in graphical form. The following factors will also influence the value of BAC: the nature of the pollutant and its solubility in water, specific gravity, specificity of the ongoing processes of sorption – desorption in the system “water – bottom sediments”, geomorphologic features of the water body [26, 27].

As can be seen from Fig.3, the lowest level of chronic pollution among the studied water bodies is characterized by Ik Lake, for which the calculated values of BAC do not exceed $n = 1-10$ for all considered metals, except Mn. Taking into account low concentrations of pollutants in water samples from this lake, it is possible to assess the situation here as satisfactory.

According to the results of spore-pollen analysis and analysis of non-pollen palynomorphs, the most favorable conditions were also established for Ik Lake. The correspondence of the composition of palynospectra to the zonal type of vegetation indicates minimal change of vegetation cover as a result of anthropogenic impact. The distribution of two *Pediastrum* species indicates its oligotrophic state, and *Plantago* and *Cerealia Plantago* species associated with human activity along the shores of the lake indicates increasing anthropogenic load.

Significant anthropogenic impact on Kolyvanskoe Lake is evidenced by the BAC values for Ni, Zn and Ba within the range $10-10^2n$. Elevated concentrations of Fe ($K_{MAC} = 3$), Mn (9), Al (3) and Cu (15) in water indicate recent pollution entering the water body. Three species of *Pediastrum* algae founded here in small, as compared to Ik Lake, amounts indicate the previously favorable and currently deteriorating condition of the water body.

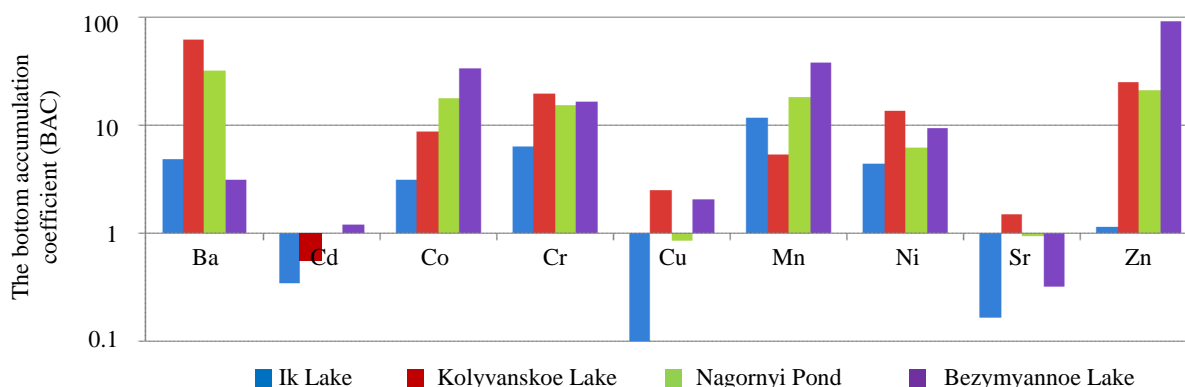


Fig.3. Bottom accumulation coefficients calculated for the studied water bodies



In Nagornyi Pond and Bezymyannoe Lake high values of BAC for Cr, Zn, Co and Mn are observed, which is associated with the close location of polymetallic ore deposits. These water bodies are characterized as low polluted according to BAC. The high content of coal microparticles found in these water bodies indicates that there were fires in the surrounding landscapes. According to the data of spore-pollen analysis and analysis of non-pollen palynomorphs, the most unfavorable conditions of evolution of the lake and surrounding landscapes were obtained for Bezymyannoe Lake. The inconsistency of palynospectra of modern vegetation and high content of fungi spores in the bottom sediments of Bezymyannoe Lake testify to the anthropogenic impact on the vegetation cover. The shell amoebae found in the Nagornyi Pond indicate periodic watering of the area, which is probably related to the disturbance of the groundwater table because of anthropogenic activities in the vicinity and may lead to waterlogging over time.

Single assessments, such as BAC, are usually not sufficient to obtain a reliable overall picture of the level of contamination of bottom sediments, so the integral criterion – total pollution index (Z_c) [33] is widely used. Its calculation was performed for all analyzed heavy metals for all studied water bodies, except Beloe Lake, for which bottom sediments were not analyzed:

$$Z_c = \sum_{i=1}^n K_i (n-1), \quad (2)$$

where n – the number of accounted metals; K – the contrast coefficient.

Contrast coefficients for each metal were calculated as the ratio of its concentration in the study area to the corresponding background concentration, and the MAC (APC) values for soils were taken as background concentrations (see Table 2).

The total pollution index (Z_c) by gross and mobile forms of metals calculated for bottom sediments of the studied water bodies are presented graphically in Fig.4.

Based on the methodology of Yu.E.Saet⁴, the calculated values of total pollution indexes for mobile and gross forms of metals (Fig.4) and the ratio between them allow us to assess the pollution level of Nagornyi pond and Bezymyannoe Lake as high, Kolyvanskoe Lake – as medium, Ik Lake – as low. In addition, for the Nagornyi Pond and Bezymyannoe Lake total indicators of pollution by mobile forms of metals significantly exceeding the total indicators of pollution by gross forms, which characterizes the bottom sediments of the considered water bodies as a dangerous source of secondary pollution, and determines their high danger for hydrobionts.

Conclusion

Geochemical studies of water and bottom sediments allowed assessing the ecological state of water bodies in the south-west of Siberia and Altai and in the eastern part of Kazakhstan. Thus, Nagornyi Pond and Bezymyannoe Lake were classified as water bodies with a high level of pollution caused by prolonged anthropogenic load from underground and open-pit mines located near active or worked-out underground and open-pit mines. The data of spore-pollen analysis and analysis of non-pollen palynomorphs confirm these results. Maximum values of ruderal grasses, fungal spores and coal microparticles were noted here. Kolyvanskoe Lake and Beloe

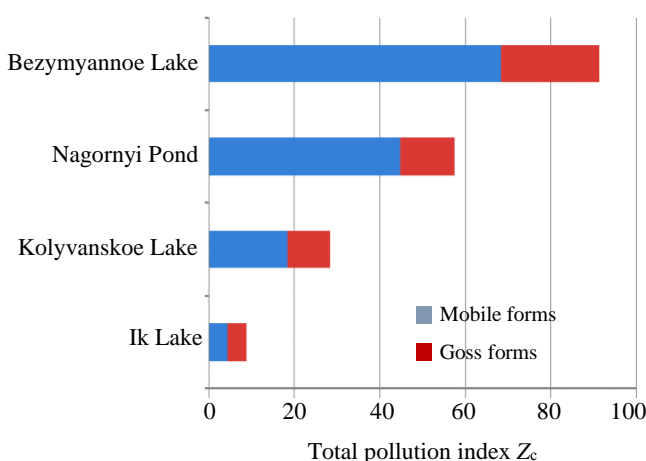


Fig.4. Values of the total pollution index of bottom sediments of the studied water bodies by gross and mobile forms of metals

⁴ Saet Yu.E. Geochemistry of the environment. Moscow: Nedra, 1990, p. 333.



Lake are characterized by the average level of pollution. It is also important to note that in the bottom sediments of Kolyvanskoe Lake high values of indicators of total pollution by mobile forms of heavy metals relative to their gross forms were recorded, which shows a low self-purifying capacity of the water body. Taking into account the rapid growth rate of recreational load, one can predict a sharp deterioration of the ecological state of the lake. Ik Lake is characterized by the most favorable ecological condition from of all studied lakes. According to the results of palynological analysis, the highest percentage of *Pediastrum* algae was noted here, which allows us to conclude that the lake has a high self-purifying capacity and low anthropogenic load.

The conducted studies indicate the possibility of using a new method of express assessment of the ecological state of aquatic ecosystems by studying lakes with the help of spore-pollen and geochemical analyses of the upper layer of lake bottom sediments. If geochemical indicators of water provide information about the ecological state of water bodies themselves, the results of spore-pollen analysis and analysis of non-pollen palynomorphs of lake bottom sediments, as well as geochemical analysis of lake sediments show the effect of anthropogenic impact in a wider aspect (lake and its catchment). The combined use of the methods allows to assess not only lake water quality, but also lake ecosystems in general, as well as to make retrospective analysis of the sources of impact. This method does not imply an in-depth investigation of the causes of pollution and forecasting of possible consequences, but it can be used to obtain a quick assessment for further large-scale studies.

REFERENCES

1. Tusupbekov J.A., Ryapolova N.L. Assessment of the environmental sustainability of surface waters in Western Siberia. *Proceedings of Voronezh State University. Series: Geography. Geoecology*. 2019. N 3, p. 55-60 (in Russian). DOI: [10.17308/geo.2019.3/2324](https://doi.org/10.17308/geo.2019.3/2324)
2. Sabatier P., Moernaut J., Bertrand S. et al. A Review of Event Deposits in Lake Sediments. *Quaternary*. 2022. Vol. 5. Iss. 3. N 34. DOI: [10.3390/quat5030034](https://doi.org/10.3390/quat5030034)
3. Volkodaeva M.V., Kiselev A.V. On development of System for Environmental Monitoring of Atmospheric Air Quality. *Journal of Mining Institute*. 2017. Vol. 227, p. 589-596. DOI: [10.25515/PMI.2017.5.589](https://doi.org/10.25515/PMI.2017.5.589)
4. Dauvalter V.A., Denisov D.B., Slukovskii Z.I., Dinu M.I. Biogeochemical Features of Functioning of Small Arctic Lakes of the Khibiny Mountains under Climatic and Environmental Changes. *Geochemistry International*. 2022. Vol. 60. N 6, p. 560-574. DOI: [10.1134/S0016702922050044](https://doi.org/10.1134/S0016702922050044)
5. Slukovskii Z.I., Guzeva A.V., Dauvalter V.A. Rare earth elements in surface lake sediments of Russian arctic: Natural and potential anthropogenic impact to their accumulation. *Applied Geochemistry*. 2022. Vol. 142. N 105325. DOI: [10.1016/j.apgeochem.2022.105325](https://doi.org/10.1016/j.apgeochem.2022.105325)
6. Sapelko T.V. Paleolimnological research: new possibilities and possible mistakes. Paleolimnology of Northern Eurasia: experience, methodology, current status and young scientists school in microscopy skills in paleolimnology, 1-4 October 2018, Kazan, Russia. Proceedings of the 3rd International Conference, 2018, p. 104-105.
7. Lukanina E., Blyakharchuk T. A comparison of spore-pollen spectra of forest, forest-steppe and steppe of Western Siberia. 12th International Meeting Pollen Monitoring Programme. Abstract book, 20-23 August 2019, Riga, Latvia, 2019, p. 21-24.
8. Popolzin A.G. Lakes of the south of the Ob-Irtysh basin. Novosibirsk: Zapadno-Sibirskoe knizhnoe izd-vo, 1967, p. 350 (in Russian).
9. Strakhovenko V.D., Kabannik V.G., Malikova I.N. Geochemical features of the ecosystem of Lake Kolyvan (Altai territory) and related technogenic impact. *Lithology and Mineral Resources*. 2014. Vol. 49. N 3, p. 220-234. DOI: [10.1134/S0024490214030055](https://doi.org/10.1134/S0024490214030055)
10. Poznyakov A.A. On the history of Kolyvan Lake. *Bulletin of the Altay Branch of the Russian Geographical Society*. 2015. Vol. 38. N 3, p. 93-98 (in Russian).
11. Korotaeva A.E., Pashkevich M.A. Spectrum survey data application in ecological monitoring of aquatic vegetation. *Mining Informational and Analytical Bulletin*. 2021. N 5-2, p. 231-244 (in Russian). DOI: [10.25018/0236_1493_2021_52_0_231](https://doi.org/10.25018/0236_1493_2021_52_0_231)
12. Iakovleva E., Belova M., Popov A. Mining and Environmental Monitoring at Open-Pit Mineral Deposits. *Journal of Ecological Engineering*. 2019. Vol. 20. Iss. 5, p. 172-178. DOI: [10.12911/22998993/105438](https://doi.org/10.12911/22998993/105438)
13. Ponomarenko M.R., Kutepov Y.I. Complexity Assessment to Substantiate Deformation Monitoring at Open Pit Mines. *Journal of Mining Science*. 2021. Vol. 57. Iss. 6, p. 986-994. DOI: [10.1134/S1062739121060119](https://doi.org/10.1134/S1062739121060119)
14. Yagnachkova N.I. Natural monuments of Mountain Kolyvan. The Altai Territory is proud of this: based on materials from a creative competition. Barnaul: Azbuka, 2008, p. 24-26 (in Russian).
15. Kuzmenkin D.V., Ivanova E.S. Quantitative characteristic of macrozoobenthos in littoral zone of Kolyvanskoe and Beloe lakes (North-Western Altai) according to research in 2019. *Proceedings of the Tigirek State Natural Reserve*. 2020. Iss. 12, p. 100-104 (in Russian). DOI: [10.53005/20767390_2020_12_100](https://doi.org/10.53005/20767390_2020_12_100)
16. Suiekpayev Y.S., Sapargaliyev Y.M., Dolgopolova A.V. et al. Mineralogy, geochemistry and U-Pb zircon age of the Karaotkel Ti-Zr placer deposit, Eastern Kazakhstan and its genetic link to the Karaotkel-Preobrazhenka intrusion. *Ore Geology Reviews*. 2021. Vol. 131. N 104015. DOI: [10.1016/j.oregeorev.2021.104015](https://doi.org/10.1016/j.oregeorev.2021.104015)



17. Nigmatova S.A., Bayshashov B.U., Pirogova T.E. et al. Geology, stratigraphy and palaeontology of the Eocene Shynzhyly locality (Eastern Kazakhstan) and comparison with the continental Eocene of Italy. *Gortania. Geologia, Paleontologia, Paleontologia*. 2020. Vol. 42, p. 37-53.
18. Pashkevich M.A., Danilov A.S., Matveeva V.A. Remote sensing of chemical anomalies in the atmosphere in influence zone of Korkino open pit coal mine. *Eurasian Mining*. 2021. N 1, p. 79-83. DOI: [10.17580/em.2021.01.16](https://doi.org/10.17580/em.2021.01.16)
19. Shelekhova T.S., Lavrova N.B. Paleogeographic reconstructions of the Northwest Karelia region evolution in the holocene based on the study of small lake sediments. *Trudy Karelskogo nauchnogo tsentra Rossiiskoi akademii nauk*. 2020. N 9, p. 101-122 (in Russian). DOI: [10.17076/lim1268](https://doi.org/10.17076/lim1268)
20. Sapelko T.V., Tsyganov A.N., Mazei Yu.A. et al. New approaches to complex paleolimnological studies of the Holocene history of lakes. *Trudy Paleontologicheskogo obshchestva*. 2018. Vol. 1, p. 118-124 (in Russian).
21. Blyakharchuk T.A., Mitrofanova E.Y., Eirikh A.N. Integrated palaeoecological investigation of bottom sediments from lake Manzhherokskoye in the piedmont Altai region. *Trudy Karelskogo nauchnogo tsentra Rossiiskoi akademii nauk*. 2015. N 9, p. 81-99 (in Russian). DOI: [10.17076/lim166](https://doi.org/10.17076/lim166)
22. Sarapulova G.I. Geochemical approach in assessing the technogenic impact on soils. *Journal of Mining Institute*. 2020. Vol. 243, p. 388-392. DOI: [10.31897/PMI.2020.3.388](https://doi.org/10.31897/PMI.2020.3.388)
23. Salamov A.M., Mammadov V.A., Khalilova H.Kh. Study of the Anthropogenic Impact on the Change of Geoecological Conditions of the Khojahasan Lake, Azerbaijan. *Journal of Mining Institute*. 2019. Vol. 239, p. 603-610. DOI: [10.31897/PMI.2019.5.603](https://doi.org/10.31897/PMI.2019.5.603)
24. Borodina E.V., Borodina U.O. Factors affecting chemical composition of lake water of specially protected areas in Altai mountains, Russia, based on Multa river basin study. *Vodnye resursy*. 2019. Vol. 46. N 4, p. 405-416 (in Russian). DOI: [10.31857/S0321-0596464405-416](https://doi.org/10.31857/S0321-0596464405-416)
25. Kremleva T.A., Moiseyenko T.I., Khoroshavin V.Y., Shavnin A.A. Geochemical features of natural waters of West Siberia: microelement composition. *Tyumen State University Herald*. 2012. N 12, p. 71-80.
26. Valiev V.S., Shamaev D.E., Khasanov R.R., Malanin V.V. Heavy metals mobility in sediments and peculiarities of variability interpretation. *Russian Journal of Applied Ecology*. 2022. N 2, p. 61-67 (in Russian). DOI: [10.24852/2411-7374.2022.2.61.67](https://doi.org/10.24852/2411-7374.2022.2.61.67)
27. Mazur V.V., Dorovskikh G.N. Accumulation of metals in the bottom sediments. *Syktvykar University Bulletin. Series 2. Biology, geology, chemistry, ecology*. 2013. N 3, p. 159-177 (in Russian).
28. Legostaeva Y.B., Gololobova A.G. Bottom Sediments as an Indicator of the Geoecological State of Natural Water Currents. *Ecology and Industry of Russia*. 2022. Vol. 26. N 11, p. 66-71 (in Russian). DOI: [10.18412/1816-0395-2022-11-66-71](https://doi.org/10.18412/1816-0395-2022-11-66-71)
29. Pashkevich M.A., Bech J., Matveeva V.A., Alekseenko A.V. Biogeochemical assessment of soils and plants in industrial, residential and recreational areas of Saint Petersburg. *Journal of Mining Institute*. 2020. Vol. 241, p. 125-130. DOI: [10.31897/PMI.2020.1.125](https://doi.org/10.31897/PMI.2020.1.125)
30. Kharko P.A., Matveeva V.A. Bottom sediments in a river under acid and alkaline wastewater discharge. *Ecological Engineering and Environmental Technology*. 2021. Vol. 22. Iss. 3, p. 35-41. DOI: [10.12912/27197050/134870](https://doi.org/10.12912/27197050/134870)
31. Piirainen V.Y., Mikhaylov A.V., Barinkova A.A. The concept of modern ecosystem for the Ural Aluminium Smelter. *Tsvetnye metall*. 2022. N 7, p. 39-45 (in Russian). DOI: [10.17580/tsm.2022.07.04](https://doi.org/10.17580/tsm.2022.07.04)
32. Pashkevich M.A., Bykova M.V. Methodology for thermal desorption treatment of local soil pollution by oil products at the facilities of the mineral resource industry. *Journal of Mining Institute*. 2022. Vol. 253, p. 49-60. DOI: [10.31897/PMI.2022.6](https://doi.org/10.31897/PMI.2022.6)
33. Valiev V.S., Ivanov D.V., Shagidullin R.R. A method for integrated assessment of sediment pollution. *Trudy Karelskogo nauchnogo tsentra Rossiiskoi akademii nauk*. 2019. N 9, p. 51-59 (in Russian). DOI: [10.17076/lim1122](https://doi.org/10.17076/lim1122)

Authors: **Mariya A. Chukaeva**, Candidate of Technical Sciences, Senior Researcher, chukaeva.mariia@gmail.com, <https://orcid.org/0000-0003-3643-6757> (Empress Catherine II Saint Petersburg Mining University, Saint Petersburg, Russia), **Tatyana V. Sapelko**, Candidate of Geography, Senior Researcher, <https://orcid.org/0000-0003-0933-7091> (Institute of Limnology of the RAS – Saint Petersburg Federal Research Center of the RAS, Saint Petersburg, Russia).

The authors declare no conflict of interests.



Study of wormhole channel formation resulting from hydrochloric acid treatment in complex-type reservoirs using filtration and X-ray computed tomography methods

Andrei A. Abrosimov*National University of Oil and Gas "Gubkin University", Moscow, Russia*

How to cite this article: Abrosimov A.A. Study of wormhole channel formation resulting from hydrochloric acid treatment in complex-type reservoirs using filtration and X-ray computed tomography methods. *Journal of Mining Institute*. 2025. Vol. 271. N 16270, p. 63-73.

Abstract

The primary function of hydrochloric acid treatment (HAT) is to create the maximum number of high-conductivity channels in the near-wellbore zone of the reservoir to restore its permeability and enhance hydraulic connectivity between the undisturbed part of the formation and the well. The objective of this study is to physically model HAT on core samples from the Orenburg oil and gas condensate field and to research the impact of such treatment on the structure of the pore space of rocks related to complex-type reservoirs. The complexity of the rock's pore space and the low permeability of the formations are distinguishing features of the study object. For this reason, HAT is a widely applied method for production intensification, necessitating the verification of acid injection rates, where the success criterion is the formation of high-conductivity filtration channels (wormholes) in the near-wellbore zone. These channels significantly expand the drainage area of wells, thereby bringing additional reservoir sections into development. The study examined the characteristics of filtration channel development resulting from acid treatment. Their structure was characterized and analyzed using X-ray computed tomography. The complex study confirmed the accuracy of the selected injection rate and provided practical recommendations for enhancing the efficiency of HAT.

Keywords

X-ray tomography; hydrochloric acid treatment; pore space; reservoir properties; carbonate reservoir; wormhole

Received: 25.06.2023**Accepted:** 07.11.2024**Онлайн:** 25.02.2025**Published:** 25.02.2025**Introduction**

There is a trend towards a decline in hydrocarbon (HC) production from terrigenous reservoirs and the development of carbonate deposits, which are characterized by low reservoir properties (RP) and complex pore space structures. The process of HC extraction from such reservoirs is more labor-intensive and economically costly than from traditional reservoirs. To ensure successful field development in such conditions, various geological and technical measures are carried out to increase the efficiency of oil and gas production and accelerate the production rates of recoverable reserves [1-3].

Chemical methods are most commonly used for carbonate reservoirs, particularly hydrochloric acid treatment (HAT), which is one of the main methods for enhancing oil production. The technology was developed by chief chemist Herman Frasch, who worked at a Standard Oil refinery in Ohio, USA, and patented the method in 1896 [4]. Since then, the method has been actively used in the oil and gas industry, and currently, there are numerous variations depending on the acid composition [5-7] and treatment technology [8-10]. During HAT, the acid dissolves the solid phase and creates deep, highly permeable channels with a wormhole-like structure [11-13]. Some studies have



shown that wormholes can form even at very low acid concentrations, which may indicate their deep penetration into the reservoir [14, 15].

Most foreign publications focus on mathematical modeling of acid treatment, while the work of domestic researchers is primarily directed towards service support for acidizing operations. There are only a few publications dedicated to studying the processes and mechanisms occurring during the interaction of reservoir rock with acid solutions, which is a fundamental factor for proper planning of the treatment and maximizing its effectiveness. Laboratory core studies are the only foundation that provides preliminary insights into the research object and the processes occurring in the rock. The majority of theoretical and experimental research is focused on determining the regimes of acid treatment and the composition of acid mixtures for more effective rock dissolution and treatment. For example, in the article [16] the results of studies on selecting the acid composition for treatment of the near-wellbore zone in low-permeability terrigenous reservoir rocks of Jurassic deposits are presented. It was found that a two-stage treatment of core material, first with hydrochloric acid and then with clay-acid compositions, is the most effective. In another study [17] the process of secondary precipitate formation during acid treatment in terrigenous reservoirs of Western Siberia is studied in more detail. To prevent its formation, based on the results of experiments, it is recommended to strictly control the contact time between the acid composition and the reservoir rock, as well as to use modifying additives that affect the surfactant properties of the acid compositions. A similar issue was addressed in the study for reservoirs with high temperatures [18], where the process of pre-flushing the well is proposed as one of the most effective stages of acid treatment for oil wells, significantly reducing the issue of secondary precipitate formation. The pre-flushing stage cools the rock surface and reduces the acid's reaction rate with the rock at high reservoir temperatures.

There is a growing number of publications dedicated to the topic of modeling hydrochloric acid treatment at the pore level [19-21]. For example, in the article [19] the results of a developed mathematical model for simulating acid treatment using X-ray computed tomography data are presented. The research focused on core samples from a carbonate reservoir of Cretaceous deposits. The simulation of acid treatment at different injection rates demonstrated the heterogeneous nature of the dissolution process, leading to wormhole formation within a specific range of injection rates.

Acid treatment simulation is also conducted at a higher level – for reservoirs and fields – using acidizing simulators. In the study [22] for polymictic reservoirs in Western Siberia, a series of calculations were performed within the framework of improving the effectiveness of near-wellbore zone treatment using clay-acid compositions. These calculations were aimed at determining the optimal volume of acid composition injection, and recommendations were provided for enhancing the efficiency of acid treatment. In the article [23] the problem of mathematical modeling of acid treatment on the near-wellbore zone (NWZ) of gas fields with carbonate fractured-porous reservoirs is discussed. Based on the proposed model, the progression of the acid and the change in the filtration characteristics of the bottom-hole formation zone (BFZ) were studied during acid injection under various regimes. In the article [24] a model of multiple acid treatments is presented, taking into account the complex structure of the NWZ, combining submodels of the wellbore, pressure and flow rate calculations, fluid distribution in the NWZ, wormhole development, skin factor calculation, and the consideration of flow diverters.

A significantly smaller number of studies are dedicated to exploring the impact of acid treatment on the pore space and reservoir properties of real carbonate rocks. In the study [25] a comparison of the impact of acid treatment on high- and low-permeability carbonate reservoirs was conducted. The results of acid treatment on core samples showed that, when treating low-permeability samples, the equivalent dissolution channel area was larger than with acid treatment on high-permeability samples, indicating higher effectiveness of acid treatment on low-permeability reservoirs. In the study [26] the



effect of hydrochloric acid concentration on the pore size distribution of core samples from a carbonate reservoir and its reservoir properties was studied. It was found that the use of 15 % hydrochloric acid leads to an increase in porosity, in some cases up to 2.5 times, and the median pore diameter Md_p increases up to three times. In the article [27] the effect of self-diverting acid compositions on reservoir properties and the channels formed as a result of acid treatment was studied. The effect of forming a network of etched channels through the injection of self-diverting acid compositions was demonstrated. It was found that the use of such compositions reduces the acid penetration rate, which can later ensure more uniform treatment.

Even fewer studies are dedicated to exploring the structure of the formed wormholes, particularly in samples belonging to complex reservoir types [28-30]. It is necessary to study in more detail the process of hydrochloric acid treatment on rock samples to improve the effectiveness of acidizing. This need has defined the objective of the present study – to analyze the changes in the structure of the pore space of rocks belonging to a complex reservoir type under the influence of acid treatment, using the productive section of the Orenburg oil and gas condensate field (OGCF) as an example, with the application of X-ray computed tomography and laboratory core studies. The specific feature of the research object is the complexity of the pore structure of the rocks and the low permeability of the reservoirs. Since acid treatment is a widely applied method for enhancing production, there is a need for direct verification of the justification for the acid injection rates used, with the success criterion being the formation of highly conductive filtration channels (wormholes) in the near-wellbore zone, which significantly expand the drainage area of wells and, thereby, involve additional areas of the reservoir in the development.

Objects and methods

The work utilized samples of real reservoir rocks of the pore-cavernous and fractured types, which are most characteristic for the Eastern section of the Orenburg oil and gas condensate field. Sample KP-01 represents an organic-detrital limestone with thin (up to 1 mm) lenses of bituminous material oriented across the core axis. The detritus in the limestone consists of shell fragments of brachiopods, gastropods, and crinoids, ranging from 0.2 to 1.5 mm, cemented with fine-grained calcite and dolomite. The cement type is basaltic-pore, porous. Sample T-02 represents a chemogenic limestone with inclusions of rounded faunal fragments up to 0.5 mm, dolomitic, and sulfated. Two stylolitic seams are observed, oriented across the core axis, filled with clayey-bituminous material. The fractures in the sample are weakly undulating, rarely branching, sometimes with a collisional pattern, oriented subparallel to the core axis, with occasional brownish oil accumulations along them. The fracture density parameter for the core sample is 0.2 units/mm³.

The research on these samples was conducted in several stages. The first stage involved studying the structure of the pore space using X-ray computed tomography (CT) and determining the core's filtration characteristics before acid treatment. The second stage involved the injection of hydrochloric acid solution through the core samples. The final stage included re-scanning and laboratory studies of the core after hydrochloric acid treatment.

X-ray computed tomography has been used to study the structure of the pore space of rocks since the 1980s. Today, CT is one of the developing and informative methods in the oil and gas industry, allowing for the visualization and quantitative characterization of the composition, structure of rocks, and their pore space [31-33], and is also used for modeling hydrodynamic processes occurring within the pore space [34-36]. In this study, X-ray tomographic investigations were conducted using the SkyScan 1172 computed tomography scanner (Belgium). The scanning parameters were as follows: rotation step of 0.2 deg; averaging over eight frames; rotation angle of 360 deg; X-ray tube voltage of 100 kV; current of 100 μ A; and resolution of 10 μ m. One of the main advantages of computed tomography is its ability to study the structure of the pore space of various types of reservoir samples without compromising their integrity, meaning the same core cylinders can be used for modeling acid treatment. During scanning, the samples were strictly spatially oriented to ensure



accurate post-acid treatment imaging, allowing for comparisons between the studied objects and tomographic results.

On the HP-CFS setup, hydrochloric acid solution was pumped through samples KP-01 and T-02, and their filtration properties were determined before, during, and after the injection of the solution. This setup enables high-level experimentation to study fluid filtration through porous media under reservoir thermobaric conditions. It allows filtration experiments on packed porous media models and core samples at temperatures up to 150 °C. A backpressure system is used when necessary, supporting a maximum pressure of 7.0 MPa. For core sample testing, the confining pressure can reach up to 50.0 MPa. Fluid filtration is conducted at fixed flow rates of up to 600 cm³/h. Heating of the core sample inside the core holder to the experimental temperature is achieved using a liquid thermostat.

The experiment was conducted under conditions as close as possible to real acid treatment operations in wells. A 12 % hydrochloric acid solution with the necessary inhibitors, prepared for acid treatment in one of the wells of the Orenburg oil and gas condensate field, was used for injection. The experiments were carried out at the actual reservoir temperature of 20 °C. The viscosity of the reservoir water was 1.024 mPa·s, and its density was 1.012 g/cm³.

Results and discussion

At the first stage of the tomographic study of sample KP-01, the following findings were revealed: the pore space of the sample is represented by intercrystalline pores and caverns. The pore and cavern sizes range from 3.3 μm to 1.9 mm, with a median value of 78.65 μm. The pore density parameter Pd_p for the sample is 277 units/mm³; the pore surface area S_p is 6138.3 mm²/mm³; and the porosity K_p is 10.53 %. The majority of the sample's capacity – 68.84 % – is accounted for by ellipsoidal pores, while rounded and slit-shaped pores constitute 17.74 and 13.42 %, respectively.

The tomographic analysis of sample T-02 revealed the following: the pore space is characterized by intercrystalline pores, fractures, and residual pores within a stylolite seam. The pore size ranges from 3.3 to 448 μm, with Md_p – 57.6 μm; Pd_p – 21 units/mm³; S_p – 3.4 mm²/mm³; K_p – 1.07 %. Although visually the fracture on the sample and tomographic slices appears as a plane of rock continuity disruption, it is actually a system of cavities ranging from 75 to 448 μm in size with an ellipsoidal-tubular shape. Among them, 95 % of supercapillary cavities are interconnected through smaller ones. The fracture cavities differ from intercrystalline pores in the rock matrix by size, shape, and orientation. Fracture cavities are more elongated (shape coefficient 0.5-0.7 in the fracture vs. 0.7-0.8 in the matrix) and oriented along the fracture dip. Residual cavities within the stylolite seam are mostly ellipsoidal, largely isolated from each other, and exhibit weak hydrodynamic connectivity. Next, formation water was pumped through the samples until stable filtration was obtained under a pressure differential (ΔP) of 4.81 atm at the ends of sample KP-01 and 19.2 atm for sample T-02 (Fig.1). The initial permeability k_{perm} of the samples with water was 0.82 mD for KP-01 and 0.21 mD for T-02.

During the second stage, instead of formation water, technological hydrochloric acid solution was injected. The flow rate (FIR) remained constant throughout the entire experiment at 20 cm³/h. As shown in the pressure change graph during the experiment (Fig.1), the breakthrough time of the hydrochloric acid solution through the sample, marked by a sharp decrease in FIR and a corresponding increase in permeability, was significantly different for the two types of reservoirs. For the pore-cavernous reservoir (KP-01), the breakthrough occurred in 66 min, for the fractured reservoir (T-02), it was much faster, at 17 min. The final permeability values after the acid treatment were 5902 mD and 5930 mD, respectively, demonstrating a substantial improvement in permeability for both types of collectors.

At the third stage, X-ray tomography of the core samples was performed after the HAT. The permeability values and filtration resistance of the samples clearly indicated changes in the reservoir properties of the samples, with the formation of through dissolution channels. Structural changes in the pore space of the rock samples were scanned using X-ray computed tomography, conducted under the same imaging parameters as before the injection.

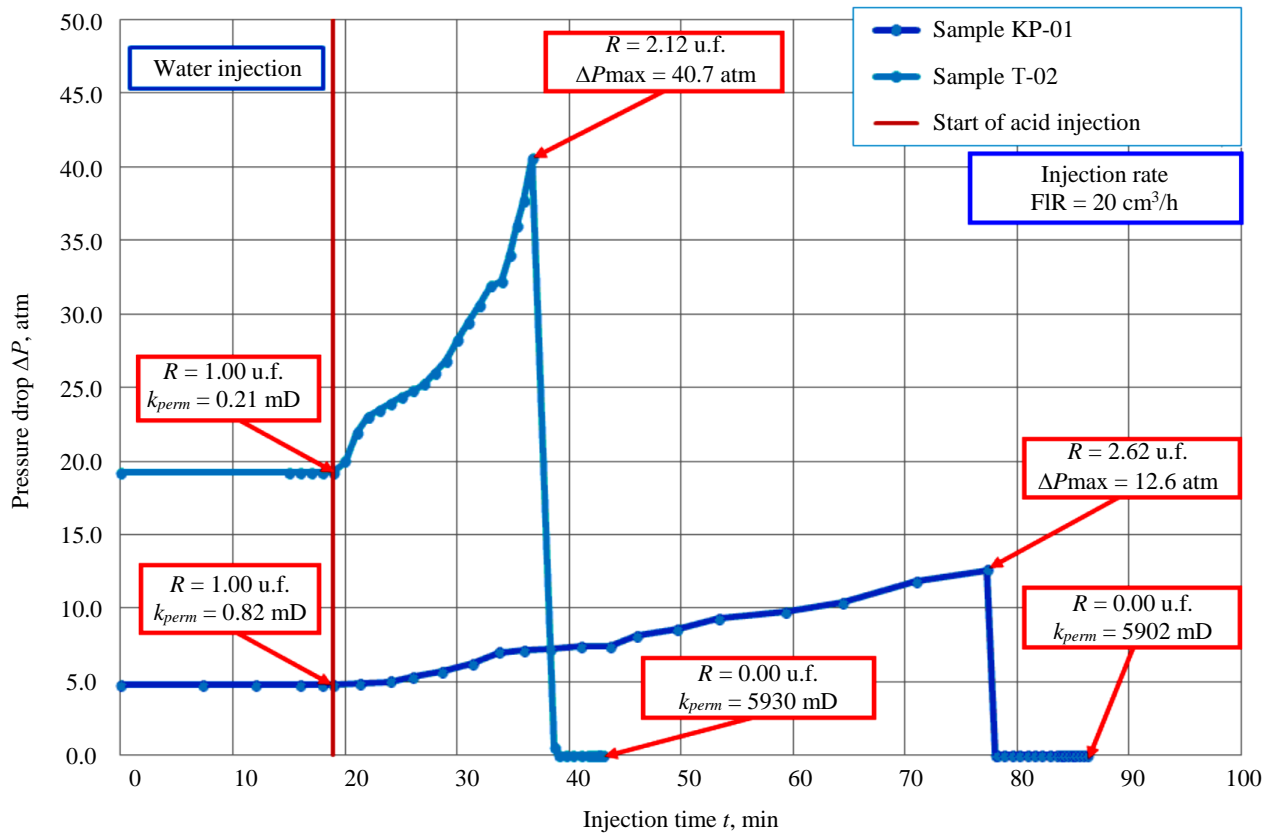


Fig.1. Pressure change characteristics during injection of technological acid solution into water-saturated core samples KP-01 and T-02

The graph in Fig.2 illustrates the changes in porosity along the entire length of the KP-01 sample and the X-ray tomography of the extended dissolution channel formed. During the acid treatment process, constant contact between the carbonate material and the acid solution was observed at the inlet end, leading to the formation of a complete dissolution segment – zone I. Further within the sample volume, zone II was formed, characterized by changes in the primary structure of the pore space due to the creation of new cavities and short channels, with a depth of 7 mm in the sample.

Fig.3 represents tomographic slices of zone II of the samples before and after HAT. For sample KP-01, significant changes in the structure of the pore space are observed in absolute values: the maximum pore and cavity sizes increased from 250 to 861 μm (3.4 times); the porosity of this zone changed from 1 to 6.53 % (6.5 times); the density parameter also increased from 233 to 379 units/ mm^3 (1.6 times), and the specific void surface area grew from 62.4 to 225.5 mm^2/mm^3 (3.6 times), indicating the formation of not only large dissolution voids but also smaller ones.

Sample T-02, characterized by a fractured-type void space, initially exhibited low reservoir properties, but it is in this sample that significant changes in pore space are observed compared

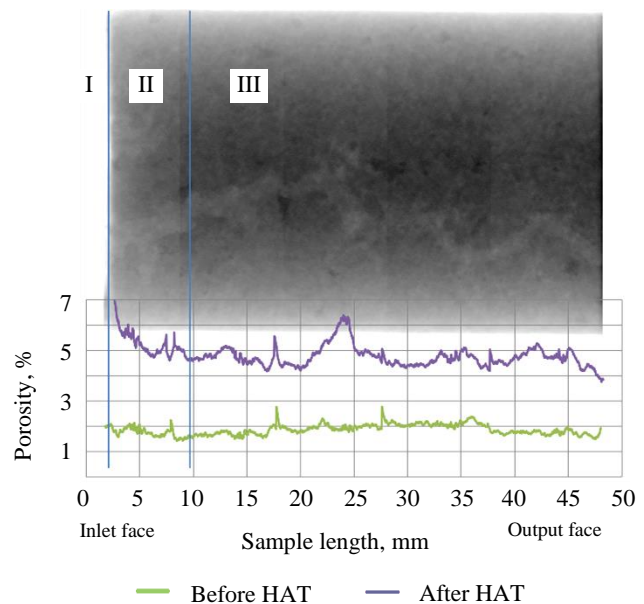


Fig.2. Graph of porosity distribution along the length of cylinder sample KP-01 before and after acid treatment

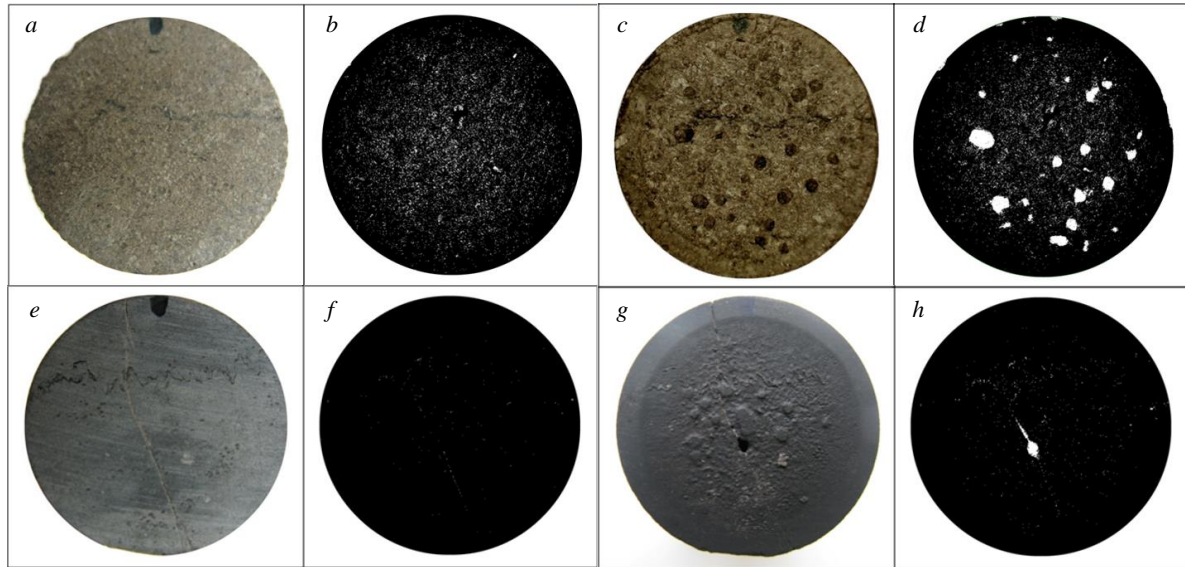


Fig.3. External view of the inlet face of sample KP-01 before (a) and after (c) HAT, and the structure of the hollow voids within it (b, d); T-02 before (e) and after (g) HAT, and the structure of the hollow voids within it (f, h):
a, b – $N_p = 10593$ units, $S_p = 62.4 \text{ mm}^2/\text{mm}^3$, $K_p = 1.00 \%$, $Pd_p = 233 \text{ units}/\text{mm}^3$, d_p : min $13.9 \text{ } \mu\text{m}$, max $249.9 \text{ } \mu\text{m}$;
c, d – $N_p = 17231$ units, $S_p = 225.53 \text{ mm}^2/\text{mm}^3$, $K_p = 6.53 \%$, $Pd_p = 379 \text{ units}/\text{mm}^3$, d_p : min $13.9 \text{ } \mu\text{m}$, max $861.7 \text{ } \mu\text{m}$;
e, f – $N_p = 761$ units, $S_p = 2.86 \text{ mm}^2/\text{mm}^3$, $K_p = 0.04 \%$, $Pd_p = 18 \text{ units}/\text{mm}^3$, d_p : min $13.9 \text{ } \mu\text{m}$, max $129.0 \text{ } \mu\text{m}$;
g, h – $N_p = 2828$ units, $S_p = 17.40 \text{ mm}^2/\text{mm}^3$, $K_p = 0.45 \%$, $Pd_p = 65 \text{ units}/\text{mm}^3$, d_p : min $13.9 \text{ } \mu\text{m}$, max $566.9 \text{ } \mu\text{m}$

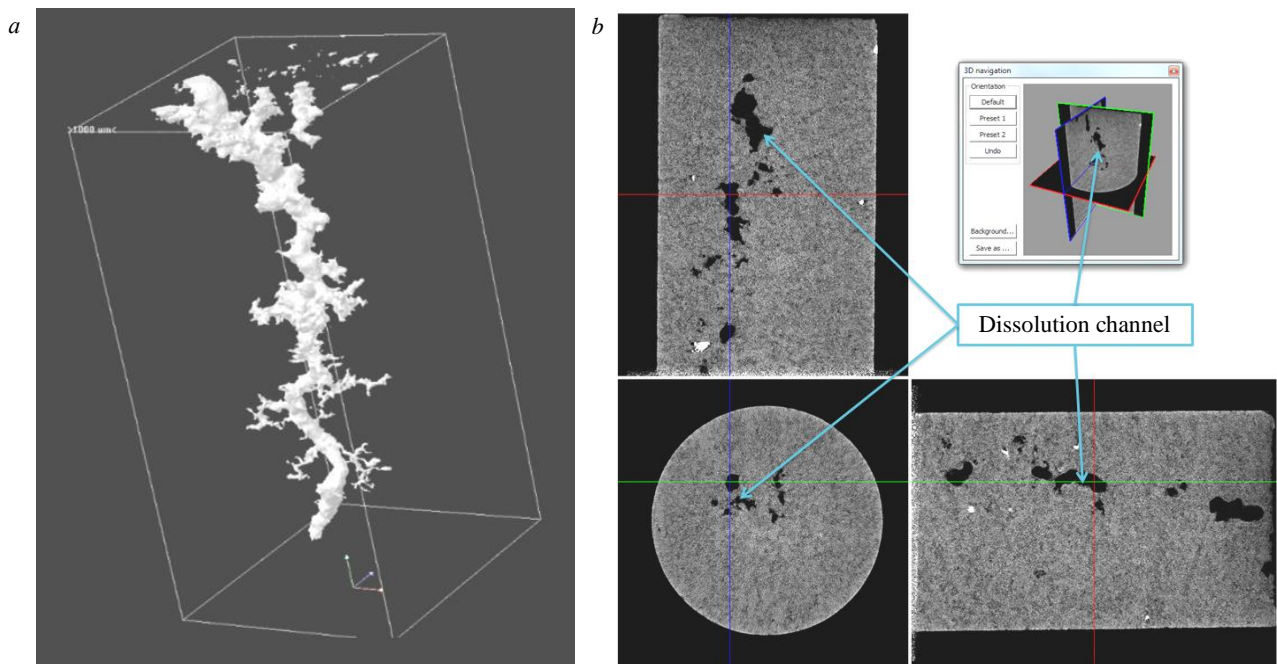


Fig.4. Internal volume of dissolution channels: a – 3D system and its view on X-ray tomographic slices; b – 2D system

to the initial sample: the number of pores increased by 3.7 times (from 761 to 2828); the maximum void size grew by 4.4 times (from 129 to 567 μm); and porosity increased by 11.2 times (from 0.04 to 0.45 %).

Next, zone III is observed, characterized by the development of a single extended dissolution channel (98.8 mm). The channel has a winding conical shape, measuring $1.9 \times 2.8 \text{ mm}$ at the entrance and $1.3 \times 1.4 \text{ mm}$ at the exit, with separate sections featuring the development of smaller and shorter lateral channels (Fig.4). The channel tortuosity T_c is 4.3 u.f.; the surface area S_c is $2.62 \text{ mm}^2/\text{mm}^3$, and



the volume V_c is 0.37 cm^3 . Overall, a significant structural change in the pore space of the sample is observed: pore and cavern sizes increased to 3.4 mm, with the median diameter nearly doubling. Porosity changed slightly to 11.5 %, the pore density parameter increased by 1.4 times, and the sample's permeability increased significantly – by four orders of magnitude.

For the second sample, characterized by a fracture-type reservoir, CT scanning revealed the presence of zones I and II (Fig.5), similar to the first sample but of smaller size. Additionally, a dissolution channel development zone (zone III) was observed, extending along the fractures. Unlike the pore-cavern type sample, the fracture-type sample exhibited two dissolution channels at the inlet face (see Fig.3, *h*), which merged into a single channel over a short distance (Fig.6, *a*). CT scanning showed that in this sample, the channel extended solely along the fracture and had a feather-like shape, with a more rounded entrance measuring $1.3 \times 1.9 \text{ mm}$ and an exit size of $0.8 \times 2.5 \text{ mm}$ (Fig.6). T_c is 3 u.f.; S_c is $7.9 \text{ mm}^2/\text{mm}^3$, and V_c is 0.092 cm^3 .

A significant structural change in the pore space is observed: the sizes of pores and caverns increased to 2.15 mm, with the median diameter increasing nearly fourfold. Porosity increased by 2.2 %, the pore density parameter tripled, and the sample's permeability significantly increased – by four orders of magnitude. The obtained morphological and petrophysical characteristics of the acid-affected zones in the samples, before and after HAT, are presented in the Table.

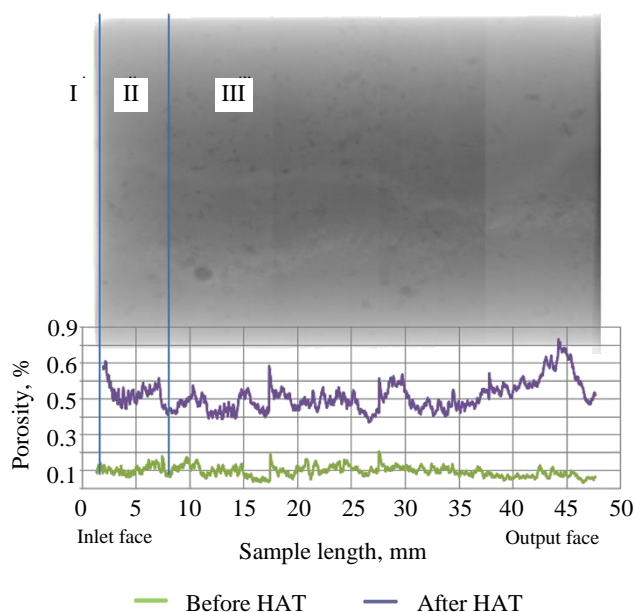


Fig.5. Graph of porosity distribution along the length of petrophysical sample T-02 before and after acid treatment

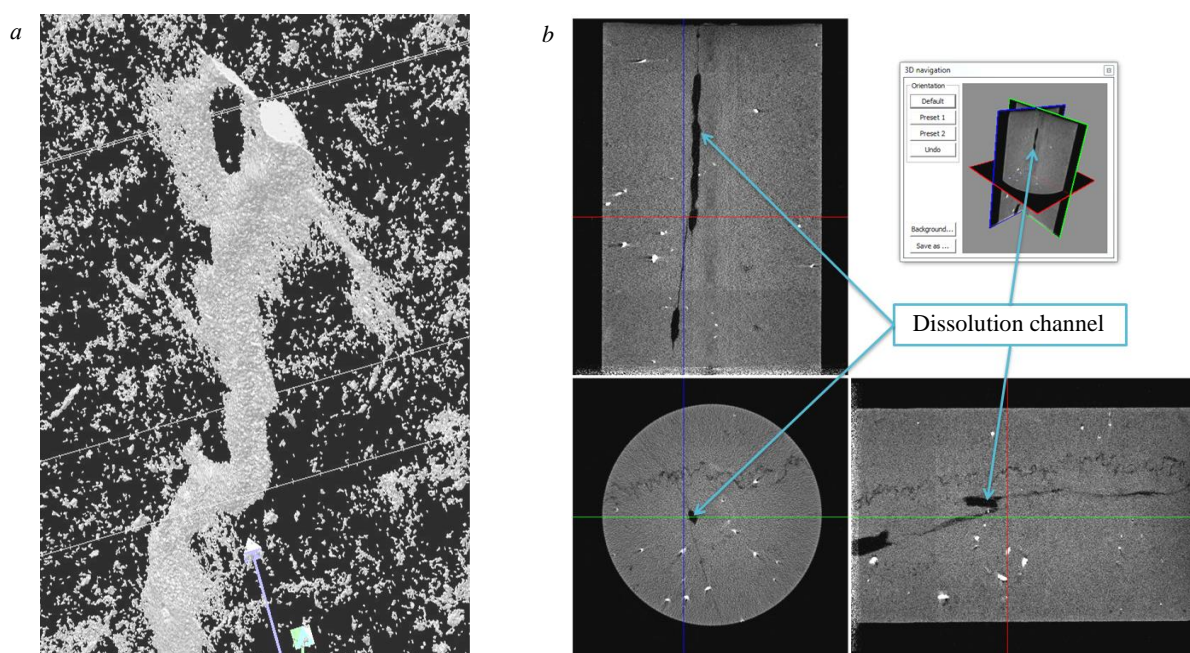


Fig.6. Internal volume of dissolution channels: *a* – 3D system and its view on X-ray tomographic slices; *b* – 2D system



Summary of petrophysical properties of acid solution impact zones on pore-cavern (sample KP-01) and fracture (sample T-02) reservoirs

Parameter	KP-01						T-02					
	Zone I		Zone II		Zone III		Zone I		Zone II		Zone III	
	Before	After	Before	After	Before	After	Before	After	Before	After	Before	After
h , mm	–	0.53	–	7.4	–	38.6	–	0.34	–	4.4	–	41
V_p , cm ³	–	0.28	–	0.29	–	0.44	–	0.09	–	0.013	–	0.12
N_p , number	–		10593	17231	15891	21975	–		791	2828	670	2203
K_p , %	–		1	6.53	1.3	2.9	–		0.04	0.45	0.04	0.45
Md_p , μm	–		21.9	25	21.2	22.8	–		21.2	19.4	17.7	18.2
Pd_p , units/mm ³	–		233	379	349	483	–		18	65	16	51
S_p , mm ² /mm ³	–		62.4	225.5	87	162.7	–		2.9	17.4	2.6	14.4
			Dissolution channel						Dissolution channel			
N_c , number	–			1			–			2		
d_c , mm	–			1.9 × 2.8 ÷ 1.3 × 1.4			–			–		
l , mm	–			99			–			83		
T_c , u.f.	–			4.3			–			3		
V , mm ³	–			368			–			92.3		
S_c , mm ² /mm ³	–			262.1			–			794.3		
$v_{c,d}$, mm/min	–			1.5			–			4.9		

Notes: h – thickness of the HAT impact zone; V_p and V – dissolution and object volumes; N_c – number of dissolution channels; d_c – diameter of dissolution channels at the inlet and outlet faces; l – length of continuous dissolution channels; $v_{c,d}$ – dissolution channel dissolution rate.

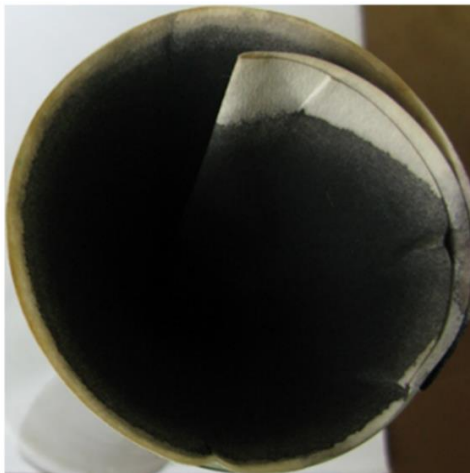


Fig.7. External appearance of asphaltene-resin-paraffin deposits on the filter

Thus, the pore transformation rates and dissolution channel development in the pore-cavern type reservoir are 1.5 mm/min, while in the fracture type reservoir they are 4.9 mm/min. The dissolution channel tortuosity in the first sample is 4.3 u.f., while in the second sample it is 3 u.f. The permeability of the rock changes from 0.8 to 5900 mD for the first type and from 0.2 to 5930 mD for the second type.

In addition to the dissolution of carbonate material and the formation of channels, the release of heavy hydrocarbons is observed in the samples. Fig.7 shows a photograph of the insoluble component (asphaltene, resin, and paraffin compounds, ARPC) on a paper filter. The movement of ARPC within the pore space can lead to their “smearing” along the walls of newly formed voids, potentially degrading the hydrodynamic connection between the dissolution channels and voids in the rock matrix – resulting in the process of clogging.

Conclusion

The results of filtration and digital X-ray tomography studies of core samples aimed at investigating the formation process of a high-conductivity channel (wormhole) in rock samples with a complex pore space structure are presented. The X-ray computed tomography method enabled a detailed examination of the rocks in both two-dimensional and three-dimensional spaces. It provided a comprehensive characterization of the pore space at the micro-level before and after acid treatment:

1. Under the specified acid solution injection regimes, highly permeable channels are formed, indicating that the injection regime was properly selected.

2. As a result of the study, the behavior of an acid solution commonly used in HAT in specific complex reservoirs of the oil rim of Orenburg oil and gas condensate field was identified. During the process, three zones of physicochemical impact were formed within the rock:



- zone of constant contact between carbonate minerals and the acid solution;
- zone of structural transformation of the pore space of reservoirs, with the formation of caverns and short channels;

- zone of development of a continuous extended dissolution channel.

3. The geometry of dissolution channels formed in various complex reservoirs with different pore space types, namely fracture-type and pore-cavern type, was determined. Under the influence of hydrochloric acid, the fracture-type reservoir sample developed a conical channel with low branching, while the pore-cavern type reservoir sample formed a branched channel. Several practical conclusions can be drawn for the fracture-type reservoir:

- repeated acid treatment: since reservoirs undergo multiple acid treatments, the experiment showed that during subsequent treatments, the acid would follow the same dissolution channel without forming additional branches. To enhance channel branching at the micro-level, the use of diversion technologies is recommended to redirect the acid into the low-permeability rock matrix in wells subjected to repeated HAT;

- handling large fractures: in cases where the well intersects large extended fractures, the worm-hole will also propagate along them. To ensure adequate stimulation of all zones near the wellbore, particularly the reservoir matrix, it is necessary to seal extended fractures before injecting acid into the formation. This can be achieved using plugging materials or suspensions.

4. In carbonate formations, the two studied types of complex reservoirs typically coexist. Since the rate of development of high-conductivity channels differs, it is recommended to use a chemical reagent that reduces filtration during acid treatment to equalize the acid treatment front. Additionally, dispersed systems such as emulsions and thickened solutions can be used.

5. Hydrocarbon compounds ARPC released during acid treatment can isolate dissolution channels from the voids in the rock matrix. This highlights the necessity of using a chemical reagent in the acid solution that dissolves ARPC or combining the chemical acid treatment method with thermal treatment methods. Based on the results of this study, thermo-acid treatment was conducted in several wells in the field, and on average, its effectiveness was higher (a 70 % increase in flow rate) compared to conventional acid treatment (a 40 % increase in flow rate).

REFERENCES

1. Ramazanov R.R., Kharlamov K.A., Letko I.I., Martsenyuk R.A. Efficiency analysis of geological and technical measures. *Oil Industry Journal*. 2019. N 6, p. 62-65 (in Russian). DOI: [10.24887/0028-2448-2019-6-62-65](https://doi.org/10.24887/0028-2448-2019-6-62-65)
2. Iktissanov V.A., Sakhabutdinov R.Z. Evaluation of effectiveness of EOR and bottomhole treatment technologies using rate transient analysis. *Oil Industry Journal*. 2019. N 5, p. 72-76 (in Russian). DOI: [10.24887/0028-2448-2019-5-72-76](https://doi.org/10.24887/0028-2448-2019-5-72-76)
3. Borkhovich S.Yu., Pchelnikov I.V., Natarov A.L. Developing criteria of wells selection for geological and engineering operations. *Oil Industry Journal*. 2018. N 4, p. 80-83 (in Russian). DOI: [10.24887/0028-2448-2018-4-80-83](https://doi.org/10.24887/0028-2448-2018-4-80-83)
4. Frasch H. Patent N US 556669. Increasing the flow of oil wells. Publ. 17.03.1896.
5. Akhmerova E.E., Shafikova E.A., Apkarimova G.I. et al. Selection of effective acid compound for carbonate collector treatment. *Bashkir chemistry journal*. 2018. Vol. 25. N 3, p. 86-92 (in Russian). DOI: [10.17122/bcj-2018-3-86-92](https://doi.org/10.17122/bcj-2018-3-86-92)
6. Shumakher M.Yu., Kononov V.V., Khafizov V.M. The study of the main technological properties of hydrochloric acid compositions of different types and their comparative assessment. *Exposition Oil Gas*. 2020. Iss. 5, p. 44-48 (in Russian). DOI: [10.24411/2076-6785-2020-10101](https://doi.org/10.24411/2076-6785-2020-10101)
7. Novikov V.A., Martyushev D.A. Experience in acid treatments in carbonate deposits of Perm Region fields. *Perm Journal of Petroleum and Mining Engineering*. 2020. Vol. 20. N 1, p. 72-87. DOI: [10.15593/2224-9923/2020.1.7](https://doi.org/10.15593/2224-9923/2020.1.7)
8. Brikov A.V., Markin A.N., Andreev A.B., Kulaev E.G. Technologies for mineral scale removal from well equipment with hydrochloric acid. *Oilfield engineering*. 2019. N 6 (606), p. 65-71 (in Russian). DOI: [10.30713/0207-2351-2019-6\(606\)-65-71](https://doi.org/10.30713/0207-2351-2019-6(606)-65-71)
9. Kalinin V. Criteria for choosing the optimal technology to increase well productivity by physical and chemical methods in carbonate reservoirs. *Nedra Povolzhya i Prikaspiya*. 2022. Iss. 105, p. 4-42 (in Russian). DOI: [10.24412/1997-8316-2022-105-4-42](https://doi.org/10.24412/1997-8316-2022-105-4-42)



10. Ravelev K.A. Technical and economic substantiation of the choice of technologies for hydrochloric acid treatment at the deposit of the Perm Krai. *Moscow Economic Journal*. 2020. N 7, p. 34-44 (in Russian). DOI: [10.24411/2413-046X-2020-10512](https://doi.org/10.24411/2413-046X-2020-10512)
11. Lufeng Zhang, Jiayuan He, Haibo Wang et al. Experimental investigation on wormhole propagation during foamed-VES acidizing. *Journal of Petroleum Science and Engineering*. 2021. Vol. 198. N 108139. DOI: [10.1016/J.PETROL.2020.108139](https://doi.org/10.1016/J.PETROL.2020.108139)
12. Dawei Zhu, Yunjin Wang, Mingyue Cui et al. Effects of spent viscoelastic-surfactant acid flow on wormholes propagation and diverting performance in heterogeneous carbonate reservoir. *Energy Reports*. 2022. Vol. 8, p. 8321-8332. DOI: [10.1016/j.egyr.2022.06.056](https://doi.org/10.1016/j.egyr.2022.06.056)
13. Alarji H., Clark S., Regenauer-Lieb K. Wormholes effect in carbonate acid enhanced oil recovery methods. *Advances in Geo-Energy Research*. 2022. Vol. 6. N 6, p. 492-501. DOI: [10.46690/ager.2022.06.06](https://doi.org/10.46690/ager.2022.06.06)
14. Alarji H., Alazman A., Regenauer-Lieb K. The impact of effective tortuosity on carbonate acidizing and the validation of Damköhler and Péclet dimensionless phase space. *Journal of Petroleum Science and Engineering*. 2022. Vol. 212. N 110313. DOI: [10.1016/j.petrol.2022.110313](https://doi.org/10.1016/j.petrol.2022.110313)
15. Kiani S., Jafari S., Apourvari S.N., Mehrjoo H. Simulation study of wormhole formation and propagation during matrix acidizing of carbonate reservoirs using a novel in-situ generated hydrochloric acid. *Advances in Geo-Energy Research*. 2021. Vol. 5. N 1, p. 64-74. DOI: [10.46690/ager.2021.01.07](https://doi.org/10.46690/ager.2021.01.07)
16. Mazaev V.V., Tomchuk N.N., Shabalovskaya E.A., Shakhmatov I.S. Laboratory studies of acid impact efficiency on rocks of low-permeable terrigenous collectors. *Oilfield engineering*. 2020. N 2 (614), p. 41-47 (in Russian). DOI: [10.30713/0207-2351-2020-2\(614\)-41-47](https://doi.org/10.30713/0207-2351-2020-2(614)-41-47)
17. Tomchuk N.N., Filatova E.A., Mazaev V.V. Optimization of acid compositions for the bottomhole zone treatment of oil reservoirs in Middle Jurassic deposits in Western Siberia. *Neft. Gas. Novicii*. 2022. N 1 (254), p. 75-80 (in Russian).
18. Karimi M., Shirazi M.M., Ayatollahi S. Investigating the effects of rock and fluid properties in Iranian carbonate matrix acidizing during pre-flush stage. *Journal of Petroleum Science and Engineering*. 2018. Vol. 166, p. 121-130. DOI: [10.1016/j.petrol.2018.03.002](https://doi.org/10.1016/j.petrol.2018.03.002)
19. Ivanov E., Korobkov D., Varfolomeev I. et al. Digital Core Analysis as an Efficient Tool for Acid Treatment Optimization. *E3S Web of Conferences*. 2023. Vol. 366. N 01002. DOI: [10.1051/e3sconf/202336601002](https://doi.org/10.1051/e3sconf/202336601002)
20. Piyang Liu, Chaoping Huang, Lijing Jia et al. Numerical Simulation of the Wormhole Propagation in Fractured Carbonate Rocks during Acidization Using a Thermal-Hydrologic-Mechanics-Chemical Coupled Model. *Water*. 2022. Vol. 14. Iss. 24. N 4117. DOI: [10.3390/w14244117](https://doi.org/10.3390/w14244117)
21. Gaofan Yue, Xi Zhu, Guiling Wang, Feng Ma. Mineral Reaction Kinetics during Acidizing of the Gaoyuzhuang Carbonate Geothermal Reservoir in the Xiong'an New Area, Northern China. *Water*. 2022. Vol. 14. Iss. 19. N 3160. DOI: [10.3390/w14193160](https://doi.org/10.3390/w14193160)
22. Khasanov M.M., Maltcev A.A. Modeling the acid treatment of a polymictic reservoir. *Journal of Mining Institute*. 2021. Vol. 251, p. 678-687. DOI: [10.31897/PMI.2021.5.7](https://doi.org/10.31897/PMI.2021.5.7)
23. Burnashev V.F., Khuzhayorov B.H. Mathematical modeling of acid injection into near-wellbore zone of gas reservoirs with carbonate fractured collectors. *Problems of Computational and Applied Mathematics*. 2017. N 4 (10), p. 10-18 (in Russian).
24. Khuzin R.A., Khizhnyak G.P. Modeling of Multiple Acid Treatments of Carbonate Reservoirs Considering the Complex Structure of the Near-Wellbore Zone. *Perspektivnye napravleniya razvitiya sovremennoi nauki: Sbornik nauchnykh rabot 61-i Mezhdunarodnoi nauchnoi konferentsii Evraziiskogo Nauchnogo Obiedineniya*, mart 2020. Evraziiskoe Nauchnoe Obiedinenie, 2020, p. 421-426.
25. Dorfman M.B., Sentemov A.A. Modeling acidizing of carbonate formations with different reservoir properties. *Minerals and Mining Engineering*. 2021. N 4, p. 24-30. DOI: [10.21440/0536-1028-2021-4-24-30](https://doi.org/10.21440/0536-1028-2021-4-24-30)
26. Nugroho A., Amanah N.L., Kamal H.P., Angkasa S. Acid Treatment on Carbonate Rock: An Effect of HCL Concentration on Rock Properties and Fluid Flowrates. *Journal of Emerging Supply Chain, Clean Energy, and Process Engineering*. 2022. Vol. 1. N 1, p. 7-18. DOI: [10.57102/jescee.v1i1.2](https://doi.org/10.57102/jescee.v1i1.2)
27. Mannanov I.I., Taipov K.S., Gilya-Zetinov A.G., Ganiev D.I. Optimizing approach to selecting acid systems and injection conditions based on core acidizing experiments. *Neftyanaya provintsia*. 2022. N 1 (29), p. 223-237 (in Russian). DOI: [10.25689/NP.2022.1.223-237](https://doi.org/10.25689/NP.2022.1.223-237)
28. Xiangdong Qiu, Aidagulov G., Ghommam M. et al. Towards a better understanding of wormhole propagation in carbonate rocks: Linear vs. radial acid injection. *Journal of Petroleum Science and Engineering*. 2018. Vol. 171, p. 570-583. DOI: [10.1016/j.petrol.2018.07.075](https://doi.org/10.1016/j.petrol.2018.07.075)
29. Al-Arji H., Al-Azman A., Le-Hussain F., Regenauer-Lieb K. Acid stimulation in carbonates: A laboratory test of a wormhole model based on Damköhler and Péclet numbers. *Journal of Petroleum Science and Engineering*. 2021. Vol. 203. N 108593. DOI: [10.1016/j.petrol.2021.108593](https://doi.org/10.1016/j.petrol.2021.108593)
30. Hyunsang Yoo, Youngmin Kim, Wonsuk Lee, Jeonghwan Lee. An experimental study on acid-rock reaction kinetics using dolomite in carbonate acidizing. *Journal of Petroleum Science and Engineering*. 2018. Vol. 168, p. 478-494. DOI: [10.1016/j.petrol.2018.05.041](https://doi.org/10.1016/j.petrol.2018.05.041)
31. Abrosimov A.A. X-ray tomography for study of oil and gas reservoir systems. *Proceedings of Gubkin University*. 2015. N 4 (281), p. 5-15 (in Russian).
32. Reedy C.L., Reedy C.L. High-resolution micro-CT with 3D image analysis for porosity characterization of historic bricks. *Heritage Science*. 2022. Vol. 10. N 83. DOI: [10.1186/s40494-022-00723-4](https://doi.org/10.1186/s40494-022-00723-4)
33. Yazynina I.V., Shelyago E.V., Abrosimov A.A., Yakushev V.S. New Method of Oil Reservoir Rock Heterogeneity Quantitative Estimation from X-ray MCT Data. *Energies*. 2021. Vol. 14. Iss. 16. N 5103. DOI: [10.3390/en14165103](https://doi.org/10.3390/en14165103)



34. Abrosimov A.A., Shelyago E.V., Yazynina I.V. Justification of Representative Data Volume of Porosity and Permeability Properties for Obtaining Statistically Reliable Petrophysical Connections. *Journal of Mining Institute*. 2018. Vol. 233, p. 487-491. DOI: [10.31897/PMI.2018.5.487](https://doi.org/10.31897/PMI.2018.5.487)
35. Saxena N., Hows A., Hofmann R. et al. Estimating Pore Volume of Rocks from Pore-Scale Imaging. *Transport in Porous Media*. 2019. Vol. 129. Iss. 1, p. 403-412. DOI: [10.1007/s11242-019-01295-x](https://doi.org/10.1007/s11242-019-01295-x)
36. Bembel S.R., Aleksandrov V.M., Ponomarev A.A. et al. Evaluation of filtration-capacitive properties of complex reservoir rocks using the results of core microtomography. *Oil Industry Journal*. 2019. N 8, p. 86-88 (in Russian). DOI: [10.24887/0028-2448-2019-8-86-88](https://doi.org/10.24887/0028-2448-2019-8-86-88)

Author Andrei A. Abrosimov, Corresponding Member of RANS, Candidate of Engineering Sciences, Engineer, abrosimov.aa@inbox.ru, <https://orcid.org/0000-0001-7120-8405> (National University of Oil and Gas "Gubkin University", Moscow, Russia).

The author declares no conflict of interests.



Study of the pore structure in granite and gabbrodolerite crushed stone grains of various sizes

Elena E. Kameneva¹✉, Viktoriya S. Nikiforova²

¹ Petrozavodsk State University, Petrozavodsk, Russia

² Empress Catherine II Saint Petersburg Mining University, Saint Petersburg, Russia

How to cite this article: Kameneva E.E., Nikiforova V.S. Study of the pore structure in granite and gabbrodolerite crushed stone grains of various sizes. *Journal of Mining Institute*. 2025. Vol. 271. N 16276, p. 74-83.

Abstract

The results of a study on the pore structure of crushed stone grains of various sizes, obtained through staged disintegration of gabbrodolerite and microcline granite – rocks differing in texture, structure, and mineral composition – are presented. Research conducted using X-ray computed microtomography revealed that disintegration leads to changes in the pore structure of the rocks. The increase in overall porosity and pore concentration in the crushed stone grains is associated with the formation of newly developed pores of various sizes and sphericity. A clear relationship between the porosity of the crushed stone grains and their size is absent, which is due to the textural and structural characteristics as well as the mineral composition of the original rocks. The scale factor is evident only in the case of gabbrodolerite, which is characterized by a fine-grained structure, massive texture, and stable mineral composition. Fine gabbrodolerite grains exhibit lower pore concentration compared to larger grains, which aligns with the statistical theory of rock strength, according to which the probability of defects (pores and microcracks) decreases as the sample size diminishes – the smaller the grain size, the higher its strength. In contrast, for porphyritic granites with an uneven grain size, the trend is reversed – smaller grains are more porous. A study of the porosity of individual rock-forming minerals in granite showed that pores are unevenly distributed in the granite crushed stone grains. The highest concentration of pores is typical for microcline. The presence of brittle and porous microcline inclusions in the granite crushed stone grains leads to the formation of new pores and microcracks, whose number increases with the repeated application of load during staged disintegration.

Keywords

granite; gabbrodolerite; scale factor; pore structure; X-ray computed microtomography

Received: 04.07.2023

Accepted: 02.05.2024

Online: 02.10.2024

Published: 25.02.2025

Introduction

The physical and mechanical properties of rock are determined by its mineral composition, texture, and the characteristics of its pore space – specifically, the size, shape, and spatial orientation of the pores. Virtually all studies on the deformation and destruction of rocks provide data indicating that when a load is applied, a deformation field is created within the rock volume, leading to changes in the structure of the pore space – its size, shape, and the number of defects, such as microcracks and pores [1-3]. In relation to the task of disintegration of construction rocks, this information is fundamental. This is because, unlike ore materials, where effective mineral separation and weakening are important during crushing and grinding for subsequent enrichment, in the disintegration of construction rocks, the goal is to preserve the strength of the crushed stone.

When discussing the strength of crushed stone, it is important to highlight the scale factor – the size of its grains. According to the statistical theory of strength, the larger the volume of a rock sample, the more defects it contains, and therefore, the lower its strength. At the same time, the statistical nature of strength and the number of defects are not the only reasons for the manifestation of the scale



factor. In the work by A.F.Ioffe and co-authors [4], it was established that the scale effect is observed during the deformation of materials prone to brittle fracture and is less pronounced in ductile materials. Modern studies on the influence of sample size on the strength properties of rocks have shown that the relationship between strength and sample size is ambiguous. It is necessary to take into account the heterogeneity of the rock's mineral composition, the characteristics of the pore structure, and the sample's history [5-7]. The latter is of particular importance when interpreting the strength of crushed stone, which has been subjected to blasting operations and staged crushing.

Numerous results from testing commercially produced crushed stone at crushing and screening plants in Karelia indicate the inconsistency of strength across different grain size fractions. In some cases, smaller fractions exhibit greater strength, while in others, the opposite trend is observed. Therefore, in this study, we set a specific task: to examine the influence of the scale factor – the size of the crushed stone grains – on its strength. To a large extent, variations in the strength of different size fractions of crushed stone produced at the same facility can be explained by the varying degree of grain flakiness – when there is a high content of flat and elongated grains, the strength of the crushed stone decreases [8, 9]. However, the increase in flaky grain content is not the only reason for reduced strength. Research [10, 11] has shown that newly formed (secondary) microcracks and pores appear in crushed stone grains, which a priori reduce their strength characteristics. At the same time, the volume of voids does not significantly depend on the grain size of the crushed stone [10]. In study [11], a decrease in crushed stone strength as the grain size decreases was noted, which the authors attributed to an increase in microdamage due to additional loads on smaller fractions during staged crushing. These conclusions were based on microscopic analysis of thin sections [10], and in [11], the strength reduction was inferred through water absorption measurements, which indirectly relate to the material's porosity and strength. An informative characteristic linking rock strength to its structural defects is porosity, which encompasses all voids within the rock, including pores, pore channels, and microcracks [12-14]. The physical or overall porosity of rock, calculated from known mineral and bulk density values, provides only indirect insights into the transformation of the microstructure during rock destruction. To obtain objective data, it is essential to consider the specific characteristics of the pore structure – such as pore size, shape, and spatial orientation [15-17].

The aim of this study is to investigate the pore structure of crushed stone grains of various sizes, obtained through staged disintegration of rocks differing in texture, structure, and mineral composition.

Methods

The primary methods used for studying and describing the structures and textures, as well as various morphometric characteristics of rocks, are mineralogical-petrographic analysis techniques. Descriptions of thin sections provide only qualitative information about rocks and are limited in terms of obtaining quantitative and volumetric structural-textural characteristics, which can affect the quality of research result interpretations. The advent of new non-destructive methods for studying materials allows for an expanded understanding of the structural-textural characteristics of rocks and complements traditional optical-petrographic studies with quantitative data on structural defects.

To obtain a reliable picture of the three-dimensional distribution of defects, their sizes, shapes, and spatial orientations, methods such as X-ray computed microtomography (X-ray micro-CT), neutron computed tomography, contact laser ultrasonic structuroscopy, transmission electron microscopy, and acoustic spectroscopy are used [18-20]. The research method should provide data characterizing the pore structure of rocks, including total porosity, pore concentration, sizes, and geometrical shapes of pores and microcracks, as well as enable the visualization of the microstructure of the samples to identify potential heterogeneity in pore distribution [21-23]. Furthermore, the method's sensitivity must be commensurate with the sizes of the structural objects (pores, mineral grains). Among these methods, X-ray computed microtomography (X-ray micro-CT) is the most suitable [24-26].



X-ray computed microtomography is a non-destructive method for studying the internal structure of solid materials, based on the dependence of the linear attenuation coefficient of X-ray radiation on the chemical composition and density of the material. Computer processing of a set of shadow projections obtained by X-ray scanning of samples allows for the visualization of the internal three-dimensional structure of the sample and provides a detailed analysis of morphometric and density characteristics both on individual sections and throughout the entire volume of the studied sample. The promise of this method for solving practical tasks related to rock disintegration lies in its ability to obtain quantitative characteristics of the pore space structure [27-29].

The method is successfully applied to assess changes in the void structure during the disintegration of ores in crushing machines [30], and in the study of the deformation and destruction processes of rocks [31, 32]. Despite significant scientific advances, several questions related to changes in rock strength during disintegration remain unresolved. Almost all studies in this field have been conducted on samples of regular shape under static or dynamic loading conditions [33-35]. The products formed as a result of sample destruction are generally not examined by the authors.

For microtomographic research, samples of crushed stone grains from microcline granite of the Kirjavahti deposit and gabbrodolerite of the Chevzhavara deposit (Republic of Karelia) were selected. The samples were extracted from crushed stone fractions of 5-20 mm and 20-40 mm, produced under industrial conditions at crushing and screening plants. The 20-40 mm fraction was obtained after the second stage of crushing, while the 5-20 mm fraction was obtained after the third stage. For comparative data on the pore structure of crushed stone grains and the original rock, hand specimens were selected, from which cubic samples with an edge length of 4.0 cm were prepared. The compressive strength limit was determined on similar cubic samples using a standard methodology. The average value of this indicator, calculated from five tested samples, was 121 MPa for granite and 192 MPa for gabbrodolerite.

The structure of the microcline granite samples (Fig.1, *a*) is uneven-grained, with a porphyritic texture. The main rock-forming minerals are microcline, plagioclase, and quartz. Their content percentages are as follows: microcline – 35-47 %, plagioclase – 25-35 %, and quartz – 20-26 %. Secondary minerals include biotite (1-5 %) and accessory minerals (apatite, titanite) up to 1 %. According to the petrographic description of thin sections, the grain sizes of microcline range from 1.0 to 5.0 mm, plagioclase – from 1.0 to 2.0 mm. Quartz is present as xenomorphic grains up to 1 mm in size, while biotite appears as small scattered flakes (0.1-0.3 mm) in association with titanite. Apatite forms individual rounded grains up to 0.1 mm in size.

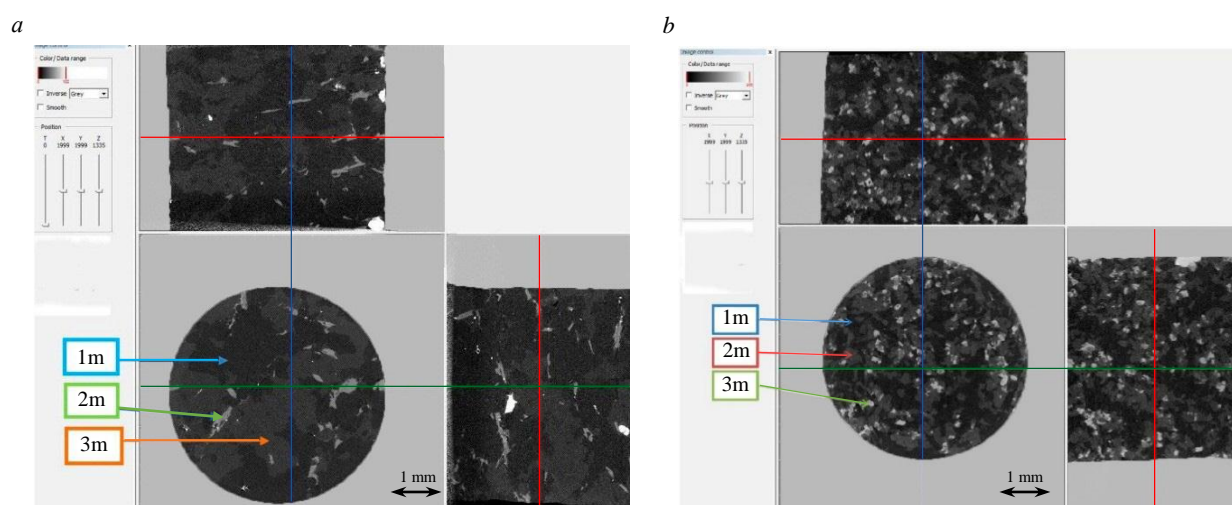


Fig.1. Microtomographic slices of granite (*a*) and gabbrodolerite (*b*) samples along three mutually perpendicular planes:
a – 1m – microcline, 2m – plagioclase + quartz, 3m – biotite;
b – 1m – plagioclase + quartz, 2m – pyroxene, 3m – titanite



The structure of the gabbrodolerite samples (Fig.1, *b*) is fine-grained, with a massive texture. The primary rock-forming minerals are plagioclase (45-50 %) and pyroxene (47-51 %). The content of quartz is 2-4 %, biotite up to 1 %, and ore minerals (titanite) up to 1 %. Pyroxene is present in the form of prismatic grains ranging in size from 0.1 to 0.8 mm, while plagioclase forms elongated crystals of 0.1-1.0 mm in size.

The main physical and mechanical properties of the crushed stone samples were determined using standard methods as outlined in GOST 8269.0-97 "Crushed stone and gravel from dense rocks for construction works. Methods of physical and mechanical testing" (Table 1). To eliminate the influence of grain shape on the strength (crushability) of the crushed stone, only isometric (cuboidal) grains were selected for testing.

Table 1

Physical and mechanical properties of the crushed stone					
Crushing stage	Fraction size, mm	Crushability (strength)		Bulk density, g/cm³	Porosity, %
		Mass loss after testing, %	Crushed stone grade by crushability		
Crushed stone from granite					
II	20-40	12.6	1,200	2.68	2.2
III	5-20	16.2	1,000	2.60	2.8
Crushed stone from gabbrodolerite					
II	20-40	5.4	1,400	2.96	0.68
III	5-20	4.8	1,400	2.98	0.60

The microstructure of the crushed stone grains was studied using a SkyScan1173 microtomograph (Belgium) with resolutions ranging from 0.5 to 15 μm . The scanning mode was set to a current of 130 mA, a voltage of 61 kV, and X-ray power of 90 W. Scanning was performed with a copper filter 0.1 mm thick and with the averaging of three images. The pixel size at maximum magnification (default resolution) was 0.5 μm , allowing for the identification of pores sized 5 μm and larger. The sample stage rotated 360° with a step of 0.2°. The number of shadow images taken ranged from 2,000 to 2,100. Subsequent reconstruction was performed using the NRecon, CTAn, and CTVol software. To speed up image processing, binarization was carried out, enabling a more detailed examination of the internal void space of the studied samples [36-38]. During the research, pore space parameters were determined, including total porosity (the volume of pores within the sample volume) and pore concentration (the number of pores per unit volume of the sample) (Table 2).

Table 2

Morphometric parameters of initial samples and crushed stone grains from granite and gabbrodolerite based on microtomographic studies

Sample number	Granite			Gabbrodolerite		
	Sample volume, mm ³	Porosity, %	Pore concentration, mm ⁻³	Grain volume, mm ³	Porosity, %	Pore concentration, mm ⁻³
Initial rock samples						
1	64,312	0.66	0.22	64,462	0.37	0.20
2	64,163	0.58	0.21	64,753	0.38	0.20
3	63,954	0.54	0.19	63,556	0.38	0.21
4	64,065	0.71	0.20	64,003	0.37	0.20
5	64,052	0.75	0.21	63,652	0.35	0.20
Average	64,109	0.65	0.21	64,085	0.37	0.20
Crushed stone grains 20-40 mm						
1	61,479	2.05	0.59	63,314	0.60	0.26
2	51,733	1.98	0.36	41,226	0.59	0.24
3	61,669	2.21	0.83	43,658	0.62	0.26



End of Table 2

Sample number	Granite			Gabbrodolerite		
	Sample volume, mm ³	Porosity, %	Pore concentration, mm ⁻³	Grain volume, mm ³	Porosity, %	Pore concentration, mm ⁻³
4	42,281	2.42	0.93	51,254	0.62	0.28
5	54,908	1.85	0.56	31,006	0.60	0.28
Average	54,414	2.10	0.65		0.60	0.26
Crushed stone grains 5-20 mm						
1	3,453	3.30	2.31	3,168	0.50	0.27
2	4,379	2.45	1.12	3,212	0.57	0.21
3	3,848	2.31	1.95	4,203	0.52	0.24
4	3,953	3.20	2.08	4,185	0.55	0.26
5	4,162	2.40	2.08	3,247	0.53	0.24
Average	3,959	2.73	1.74	–	0.53	0.24

Note. Scanning resolution is 0.5 μm.

Discussion

The analysis of the obtained data shows that the porosity of the original samples, which were not subjected to mechanical stress during blasting and disintegration in crushing machines, is lower than that of the crushed stone grains. This is consistent with conclusions drawn in studies [10, 11]. The increase in porosity of the crushed stone grains is accompanied by the appearance of newly formed defects (pores and microcracks), as evidenced by the growth in their concentration within the volume of the studied grains. This pattern is most pronounced in granite, where porosity increases on average by 3.2-4.2 times (from 0.64 to 2.1-2.73 %), and pore concentration increases by 3.1-8.3 times (from 0.21 to 0.65-1.74 mm⁻³). The effect is less noticeable in gabbrodolerite, where porosity increases on average by 1.5 times, and pore concentration increases by 1.25 times.

There is no clear dependence of porosity on grain size. In larger granite grains, taken from the 20-40 mm fraction, the average porosity is 2.1 %, while in smaller grains (from the 5-20 mm fraction), this figure is higher, at 2.73 %. In gabbrodolerite grains, the opposite trend is observed, with larger grains being more porous, although the difference in porosity values is less significant – 0.53 and 0.6 %, respectively (Table 2). The increase in porosity in smaller granite grains is associated with a higher pore concentration (an average of 1.74 mm⁻³ compared to 0.65 mm⁻³ in larger grains). The pore concentration in gabbrodolerite crushed stone grains is similar between large and small grains – 0.26 mm⁻³ and 0.24 mm⁻³, respectively.

In the structure of all the studied crushed stone grains, pores of fine capillary size, up to 40 μm, predominate in quantity (Fig.1, b). The sphericity (the ratio of the shortest to the longest axis) of these pores is high – 0.8-0.9. In small granite grains, the largest pore size is 120 μm, while in gabbrodolerite, it is 60 μm. Larger grains contain supercapillary-sized voids – up to 240 μm in granite and no more than 160 μm in gabbrodolerite (Fig.2), with only 1-3 such voids per grain. The sphericity of

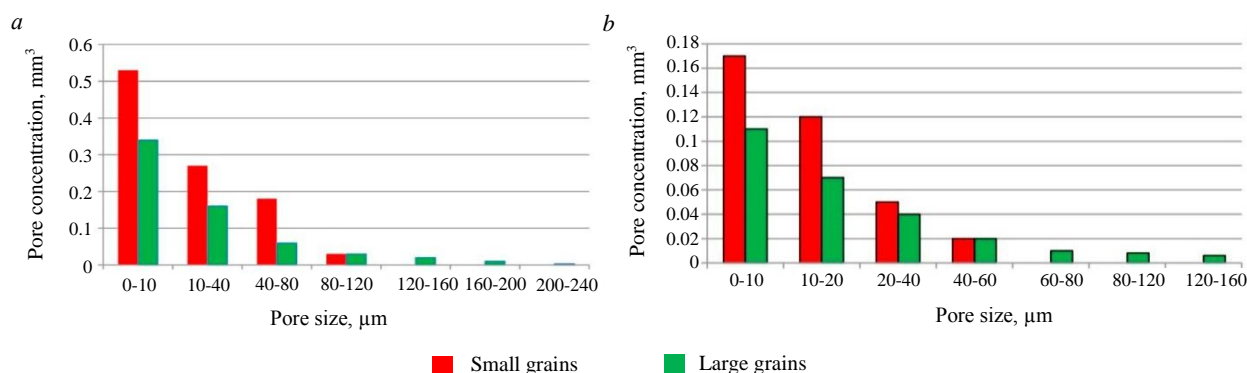


Fig.2. Pore size distribution in granite (a) and gabbrodolerite (b) grains (average values)

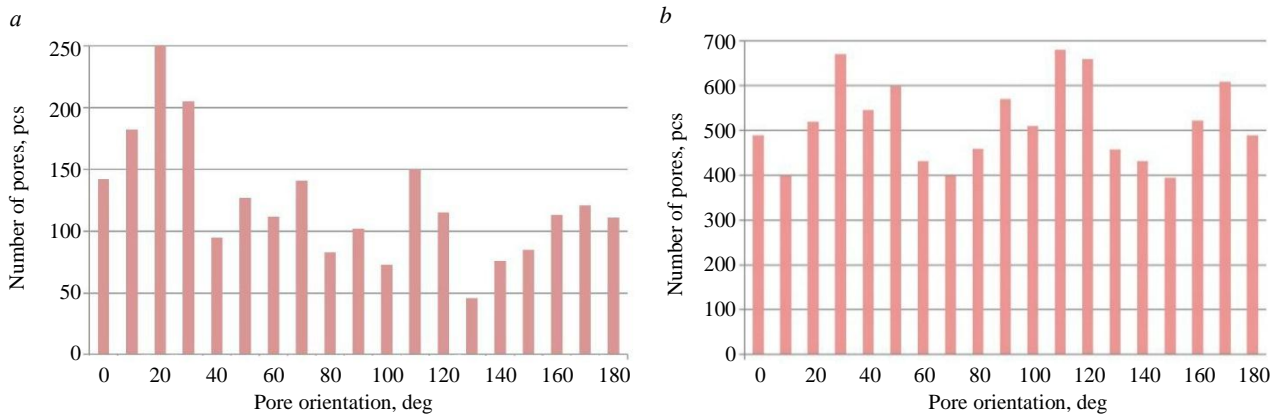


Fig.3. Pore orientation distribution along the longest axis:
grain 4 from the 5-20 mm fraction of gabbrodolerite (a), granite (b)

these pores is low – 0.1-0.3. There is no clear orientation of the pores in any specific direction (Fig.3). This feature is typical for all the studied gabbrodolerite crushed stone grains, where porosity ranges from 0.59-0.62 % in large grains and 0.5-0.57 % in small grains, while granite grains are heterogeneous. Their porosity varies from 1.85-2.42 % in large grains and 2.31-3.3 % in small grains, respectively (Table 2).

The development of microdamage in rocks depends on the strength properties of the individual rock-forming minerals [39, 40]. Given that some varieties of granite are characterized by wide variations in pore size, shape, and content, which are unevenly distributed throughout its volume [41-43], it is crucial to study the specific features of the pore structure of the minerals that constitute it. Microtomography revealed that pores in the structure of the studied crushed granite grains are unevenly distributed. The highest concentration of pores is found in large microcline grains, where porosity is 1.5 to 2 times higher than the overall porosity of the grains. The pores in microcline are distributed chaotically and have sizes up to 40 μm . The porosity of plagioclase and quartz aggregates is significantly lower. The wide variations in microcline content, ranging from 35.34 to 47.22 %, explain the instability of the porosity in the studied granite grains (Table 3).

Table 3

Characteristics of the main rock-forming minerals
in original samples and crushed stone grains from granite, %

Grains number	Microcline		Plagioclase + quartz	
	Content	Porosity	Content	Porosity
Initial granite samples				
Average	39.82	1.2	55.31	0.3
Crushed stone grains 20-40 mm				
1	35.34	4.1	63.00	0.90
2	40.34	3.9	57.68	0.63
3	42.34	4.1	55.91	0.78
4	47.22	3.3	50.38	0.66
5	35.50	3.8	61.71	0.73
Average	40.15	3.8	57.73	0.74
Crushed stone grains 5-20 mm				
1	39.69	4.31	58.61	0.93
2	47.09	4.12	50.71	0.90
3	39.65	4.25	55.95	0.94
4	46.96	6.41	50.54	0.95
5	35.29	4.48	60.89	0.96
Average	41.74	4.71	55.34	0.94

Note. The volumetric content of minerals and their porosity were determined using X-ray computed microtomography.

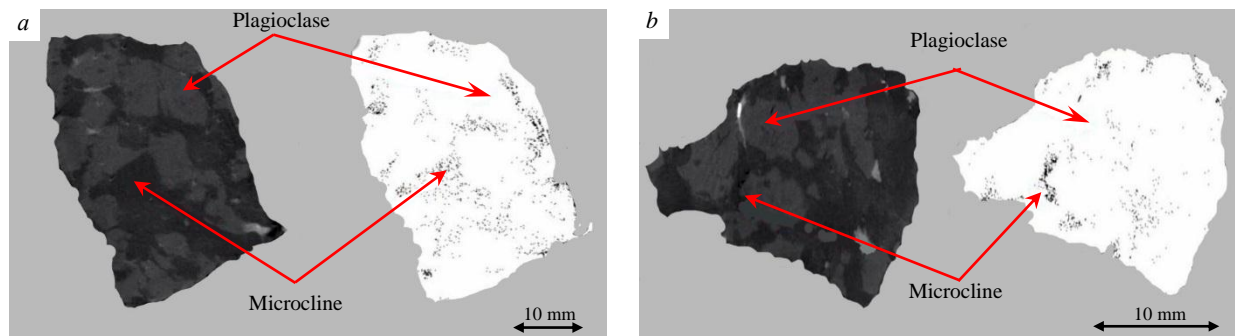


Fig.4. Single sections of granite crushed stone grains obtained through microtomographic scanning of grains from the 20-40 mm (a) and 5-20 mm (b) fractions

A comparison of tomographic slices of crushed granite grains of different sizes (Fig.4) shows that the porosity of microcline inclusions in larger grains is higher than in smaller ones. In large granite grains, the porosity of microcline averages 3.8 %, while in smaller grains this figure is higher – 4.71 %. The porosity of plagioclase and quartz in smaller grains is also higher – 0.74 % and 0.94 %, respectively (Table 3). Figure 4 presents the visualization of the sections of the studied samples, while Fig.5 shows the microtomographic slices after binarization for enhanced contrast detailing of the grains. It is logical to assume that the increased porosity of small granite grains is related to additional mechanical stresses on the smaller fractions of crushed stone, which were obtained during the third stage of crushing. The strength of a sample is determined by the strength of its weakest section [44]. Destruction begins at the most brittle areas, which in granite crushed stone grains are the microcline inclusions. Irreversible plastic deformations lead to the formation of newly developed defects, the number of which increases with repeated loading.

The studied samples of granite crushed stone contain quartz in the amount of 20-26 %. In [45], it was noted that the presence of quartz in rock composition significantly influences the formation of microcracks. When subjected to mechanical stresses, brittle and elastic quartz crystals fracture, forming intragranular microcracks [46, 47].

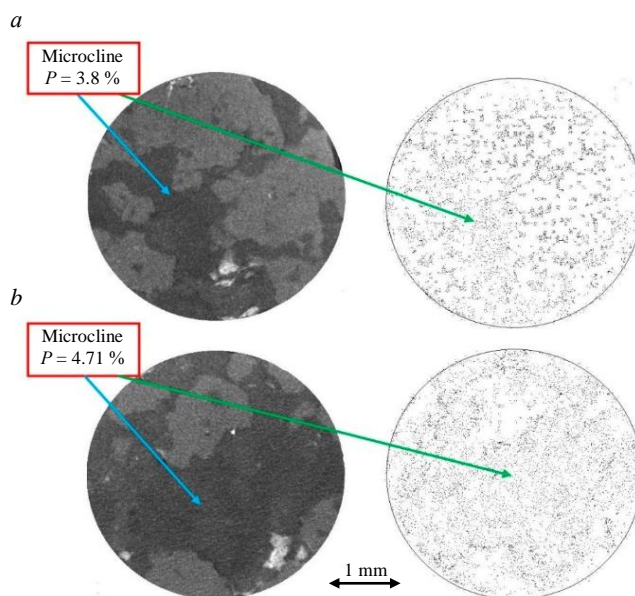


Fig.5. Single sections of granite crushed stone grains, obtained as a result of microtomographic scanning after grain binarization from the fraction 20-40 mm (a), 5-20 mm (b)

The studied gabbrodolerite crushed stone samples are homogeneous in mineral composition. The content of pyroxene ranges from 46.7 to 50.0 %, and the content of plagioclase and quartz ranges from 47.3 to 50.2 %. Pores are fairly evenly distributed within the aggregates of the main rock-forming minerals – pyroxene and plagioclase – with a slight predominance in plagioclase. In smaller grains, a slight decrease in plagioclase porosity is observed, from 0.69 % in larger grains to 0.62 % in smaller ones. The porosity of pyroxene remains almost identical for both small and large grains, at 0.46 and 0.44 %, respectively (Table 4). The reduction in the overall porosity of gabbrodolerite grains as their size decreases aligns with the statistical theory of rock strength, which posits that the likelihood of defects decreases as sample size reduces – the smaller the grain size, the higher its strength.



Table 4

**Characteristics of the main rock-forming minerals
in original samples and crushed stone grains from gabbrodolerite, %**

Grain number	Plagioclase + quartz		Plagioclase	
	Content	Porosity	Content	Porosity
Initial gabbrodolerite samples				
Average	50.6	0.44	46.1	0.2
Crushed stone grains 20-40 mm				
1	50.2	0.64	46.7	0.56
2	47.9	0.68	48.3	0.30
3	49.0	0.70	47.1	0.53
4	49.4	0.81	48.8	0.43
5	46.8	0.63	48.3	0.57
Average	48.1	0.69	48.2	0.44
Crushed stone grains 5-20 mm				
1	49.1	0.68	46.9	0.45
2	48.6	0.56	49.1	0.58
3	48.1	0.65	48.4	0.40
4	49.7	0.63	47.5	0.39
5	47.3	0.58	50.0	0.48
Average	49.0	0.62	48.2	0.46

Note. The volumetric content of minerals and their total porosity were determined using X-ray computed microtomography. Scanning resolution is 0.5 μm .

Conclusion

Thus, during disintegration, the pore structure of the rock undergoes changes. The total porosity of the crushed stone grains increases due to the formation of newly developed pores. This pattern is most pronounced in granite and less noticeable in gabbrodolerite.

Large and small crushed stone grains differ in terms of total porosity, pore size, and pore concentration. There is no clear relationship between the porosity of the crushed stone grains and their size, which is due to the textural and structural characteristics as well as the mineral composition of the original rocks.

Granite crushed stone grains are heterogeneous in mineral composition, resulting in uneven pore distribution. The presence of brittle and porous microcline inclusions in granite crushed stone grains leads to the formation of new pores and microcracks, whose number increases with repeated loading. Therefore, large crushed stone grains from the 20-40 mm fraction, obtained after the second stage of crushing, are characterized by lower porosity and pore concentration compared to smaller grains from the 5-20 mm fraction, which were crushed during the third stage.

The scale effect is evident only in gabbrodolerite, which has a fine-grained structure and massive texture – where a reduction in the size of the crushed stone grains leads to a decrease in pore size and total porosity.

REFERENCES

1. Viktorov S.D., Kochanov A.N. Some aspects of rock destruction from the standpoint of strength physics and crack mechanics. Aktualnye problemy prochnosti: Materialy 60-i Mezhdunarodnoi konferentsii, 14-18 maya 2018, Vitebsk, Belarus. Vitebsk: Vitebskii gosudarstvennyi tekhnologicheskii universitet, 2018, p. 340-342.
2. Quansheng Liu, Qi Liu, Yucong Pan et al. Microcracking Mechanism Analysis of Rock Failure in Diametral Compression Tests. *Journal of Materials in Civil Engineering*. 2018. Vol. 30. Iss. 6. N 04018082-1. DOI: [10.1061/\(ASCE\)MT.1943-5533.0002251](https://doi.org/10.1061/(ASCE)MT.1943-5533.0002251)
3. Wen-Ling Tian, Sheng-Qi Yang, Li-Xiang Xie, Zhi-Liang Wang. Cracking behavior of three types granite with different grain size containing two non-coplanar fissures under uniaxial compression. *Archives of Civil and Mechanical Engineering*. 2018. Vol. 18. Iss. 4, p. 1580-1596. DOI: [10.1016/j.acme.2018.06.001](https://doi.org/10.1016/j.acme.2018.06.001)



4. Ioffe A.F., Kirpicheva M.V., Levitskaya A.I. Deformation and strength of crystals. *Zhurnal russkogo fiziko-khimicheskogo obshchestva*. 1924. Vol. 56. N 5-6, p. 489-504.
5. Usoltseva O.M., Tsoi P.A., Semenov V.N. Sample size influence on stress-strain properties of rocks. *Fundamental and applied issues of mining*. 2020. Vol. 7. N 2, p. 53-59 (in Russian). DOI: [10.15372/FPVGN2020070209](https://doi.org/10.15372/FPVGN2020070209)
6. Zaytsev D.V., Kochanov A.N., Pantelev I.A., Panfilov P.Y. Influence of the Scale Effect in Testing the Strength of Rock Samples. *Bulletin of the RAS: Physics*. 2017. Vol. 81. N 3, p. 337-340. DOI: [10.3103/S1062873817030406](https://doi.org/10.3103/S1062873817030406)
7. Latyshev O.G., Prishchepa D.V. Accounting for the scale effect in designing parameters of mining technology. *News of the Ural State Mining University*. 2017. Iss. 1 (45), p. 59-61 (in Russian). DOI: [10.21440/2307-2091-348-2017-1-59-61](https://doi.org/10.21440/2307-2091-348-2017-1-59-61)
8. Vaysberg L.A., Kameneva E.E., Aminov V.N. Assessment of Technological Capabilities of Control over Crushed Stone Quality in the Course of Disintegration of Building Rocks. *Stroitelnye materialy*. 2013. N 11, p. 30-34 (in Russian).
9. Kolotushkin D.M., Algebraistova N.K. Properties of nonmetallic materials and their effect on the quality of end products. *Journal of Construction and Architecture*. 2016. N 6, p. 226-233 (in Russian).
10. Burtan S.T., Mustafin S.K. Composition and properties of the mineral framework in connection with the problem of asphalt concrete quality management. *Dorozhnaya derzhava*. 2010. N 10, p. 20-27.
11. Myasnikova O.V., Schekov V.A. The influence of the natural and the technogenic microjointing on the rock endurance. *Mining Informational and Analytical Bulletin*. 2009. N 8, p. 321-326 (in Russian).
12. Staněk M., Géraud Y. Granite microporosity changes due to fracturing and alteration: secondary mineral phases as proxies for porosity and permeability estimation. *Solid Earth*. 2019. Vol. 10. Iss. 1, p. 251-274. DOI: [10.5194/se-10-251-2019](https://doi.org/10.5194/se-10-251-2019)
13. Brigadnov I.A. Direct Methods for Solving the Variation Problem for Multicriteria Estimation of the Bearing Capacity of Geomaterials. *Journal of Mining Institute*. 2018. Vol. 232, p. 368-374. DOI: [10.31897/PMI.2018.4.368](https://doi.org/10.31897/PMI.2018.4.368)
14. Gospodarikov A.P., Trofimov A.V., Kirkin A.P. Evaluation of deformation characteristics of brittle rocks beyond the limit of strength in the mode of uniaxial servohydraulic loading. *Journal of Mining Institute*. 2022. Vol. 256, p. 539-548. DOI: [10.31897/PMI.2022.87](https://doi.org/10.31897/PMI.2022.87)
15. Zhukov V.S., Kuzmin Yu.O., Tikhotsky S.A. et al. Changes in fracture porosity during the preparation of rock destruction. Physical-chemical and petrophysical researches in the Earth's sciences: Proceedings of the twenty-second international conference, 27-29 September 2021, Moscow, Russia. Moscow: Institute of Geology of Ore Deposits, Petrography, Mineralogy and Geochemistry of the RAS, 2021, p. 106-109 (in Russian).
16. Rui Song, Lifu Zheng, Yao Wang, Jianjun Liu. Effects of Pore Structure on Sandstone Mechanical Properties Based on Micro-CT Reconstruction Model. *Advances in Civil Engineering*. 2020. Vol. 2020. Iss. 1. N 9085045. DOI: [10.1155/2020/9085045](https://doi.org/10.1155/2020/9085045)
17. Cheng Z.L., Sui W.B., Ning Z.F. Microstructure characteristics and its effects on mechanical properties of digital core. *Chinese Journal of Rock Mechanics and Engineering*. 2018. Vol. 37. N 2, p. 449-460. DOI: [10.13722/j.cnki.jrme.2017.1122](https://doi.org/10.13722/j.cnki.jrme.2017.1122)
18. Karch J., Dudák J., Žemlička J. et al. X-ray micro-CT and neutron CT as complementary imaging tools for non-destructive 3D imaging of rare silicified fossil plants. *Journal of Instrumentation*. 2017. Vol. 12. N 12004. DOI: [10.1088/1748-0221/12/12/C12004](https://doi.org/10.1088/1748-0221/12/12/C12004)
19. Kravcov A., Franek O., Morozov N. et al. Laser ultrasonic measurement of mechanical decay in limestone caused by freeze-thaw cycles. *Acta Polytechnica*. 2020. Vol. 60. N 5, p. 410-414. DOI: [10.14311/AP.2020.60.0410](https://doi.org/10.14311/AP.2020.60.0410)
20. Karabutov A.A., Cherepetskaya E.B., Kravcov A.N., Arrigoni M. Methods of studying structure and properties of rocks using samples (short review). *Mining Science and Technology (Russia)*. 2018. N 4, p. 10-20 (in Russian). DOI: [10.17073/2500-0632-2018-4-10-20](https://doi.org/10.17073/2500-0632-2018-4-10-20)
21. Guntoro P.I., Ghorbani Y., Koch P.-H., Rosenkranz J. X-ray Microcomputed Tomography (μCT) for Mineral Characterization: A Review of Data Analysis Methods. *Minerals*. 2019. Vol. 9. Iss. 3. N 183. DOI: [10.3390/min9030183](https://doi.org/10.3390/min9030183)
22. Bam L.C., Miller J.A., Becker M., Basson I.J. X-ray computed tomography: Practical evaluation of beam hardening in iron ore samples. *Minerals Engineering*. 2019. Vol. 131, p. 206-215. DOI: [10.1016/j.mineng.2018.11.010](https://doi.org/10.1016/j.mineng.2018.11.010)
23. Withers P.J., Bouman C., Carmignato S. et al. X-ray computed tomography. *Nature Reviews Methods Primers*. 2021. Vol. 1. N 18. DOI: [10.1038/s43586-021-00015-4](https://doi.org/10.1038/s43586-021-00015-4)
24. Rui Song, Yao Wang, Jianjun Liu et al. Comparative analysis on pore-scale permeability prediction on micro-CT images of rock using numerical and empirical approaches. *Energy Science & Engineering*. 2019. Vol. 7. Iss. 6, p. 2842-2854. DOI: [10.1002/ese3.465](https://doi.org/10.1002/ese3.465)
25. Yakushina O.A., Khozyainov M.S. Geomaterials study by X-ray computed tomography. Physical-chemical and petrophysical researches in the Earth's sciences: Proceedings of the twenty-second international conference, 27-29 September 2021, Moscow, Russia. Moscow: Institute of Geology of Ore Deposits, Petrography, Mineralogy and Geochemistry of the RAS, 2021, p. 302-305 (in Russian).
26. Pini R., Madonna C. Moving across scales: a quantitative assessment of X-ray CT to measure the porosity of rocks. *Journal of Porous Materials*. 2016. Vol. 23. Iss. 2, p. 325-338. DOI: [10.1007/s10934-015-0085-8](https://doi.org/10.1007/s10934-015-0085-8)
27. Jarzyna J.A., Krakowska P.I., Puskarczyk E. et al. X-ray computed microtomography – a useful tool for petrophysical properties determination. *Computational Geosciences*. 2016. Vol. 20. Iss. 5, p. 1155-1167. DOI: [10.1007/s10596-016-9582-3](https://doi.org/10.1007/s10596-016-9582-3)
28. Godinho J.R.A., Hassanzadeh A., Heinig T. 3D Quantitative Mineral Characterization of Particles Using X-ray Computed Tomography. *Natural Resources Research*. 2023. Vol. 32. Iss. 2, p. 479-499. DOI: [10.1007/s11053-023-10169-5](https://doi.org/10.1007/s11053-023-10169-5)
29. Callow B., Falkon-Suarez I., Marin-Moreno N. et al. Optimal X-ray micro-CT image based methods for porosity and permeability quantification in heterogeneous sandstones. *Geophysical Journal International*. 2020. Vol. 223. Iss. 2, p. 1210-1229. DOI: [10.1093/gji/ggaa321](https://doi.org/10.1093/gji/ggaa321)
30. Lau S.H., Miller J.D., Lin C.-L. 3D mineralogy, texture and damage analysis of multiphase mineral particles with a high contrast, submicron resolution X-ray tomography system. Conference Proceedings of the XXVI International Mineral Processing Congress (IMPC 2012), 24-28 September 2012, New Delhi, India. N 1022.
31. Willson C.S., Ning Lu, Likos W.J. Quantification of Grain, Pore, and Fluid Microstructure of Unsaturated Sand from X-Ray Computed Tomography Images. *Geotechnical Testing Journal*. 2012. Vol. 35. Iss. 6, p. 13. DOI: [10.1520/GTJ20120075](https://doi.org/10.1520/GTJ20120075)
32. De Kock T., Boone M.A., De Schryver T. et al. A Pore-Scale Study of Fracture Dynamics in Rock Using X-ray Micro-CT Under Ambient Freeze – Thaw Cycling. *Environmental Science & Technology*. 2015. Vol. 49. Iss. 5, p. 2867-2874. DOI: [10.1021/es505738d](https://doi.org/10.1021/es505738d)
33. Merzlikin A.V., Zakharova L.N. Peculiarities of Kinematics of Rock Mass Shear During Development of Subseismic-scale Faults. *Journal of Mining Institute*. 2018. Vol. 231, p. 235-238. DOI: [10.25515/PMI.2018.3.235](https://doi.org/10.25515/PMI.2018.3.235)



34. Reyes F., Lin Q., Cilliers J.J., Neethling S.J. Quantifying mineral liberation by particle grade and surface exposure using X-ray microCT. *Minerals Engineering*. 2018. Vol. 125, p. 75-82. DOI: [10.1016/j.mineng.2018.05.028](https://doi.org/10.1016/j.mineng.2018.05.028)
35. Van Geet M., Swennen R., Wevers M. Quantitative analysis of reservoir rocks by microfocus X-ray computerised tomography. *Sedimentary Geology*. 2000. Vol. 132. Iss. 1-2, p. 25-36. DOI: [10.1016/S0037-0738\(99\)00127-X](https://doi.org/10.1016/S0037-0738(99)00127-X)
36. Jardine M.A., Miller J.A., Becker M. Coupled X-ray computed tomography and grey level co-occurrence matrices as a method for quantification of mineralogy and texture in 3D. *Computers & Geosciences*. 2018. Vol. 111, p. 105-117. DOI: [10.1016/j.cageo.2017.11.005](https://doi.org/10.1016/j.cageo.2017.11.005)
37. Lin Qingyang, Andrew M., Thompson W. et al. Optimization of image quality and acquisition time for lab-based X-ray microtomography using an iterative reconstruction algorithm. *Advances in Water Resources*. 2018. Vol. 115, p. 112-124. DOI: [10.1016/j.advwatres.2018.03.007](https://doi.org/10.1016/j.advwatres.2018.03.007)
38. Van Offenwert S., Cnudde V., Bultreys T. Pore-Scale Visualization and Quantification of Transient Solute Transport Using Fast Microcomputed Tomography. *Water Resources Research*. 2019. Vol. 55. Iss. 11, p. 9279-9291. DOI: [10.1029/2019WR025880](https://doi.org/10.1029/2019WR025880)
39. Golovin Y.I., Tyurin A.I., Victorov S.D. et al. Size Effects and Charting the Physical and Mechanical Properties of Individual Phases and Interphases in Polycrystalline Materials. *Bulletin of the RAS: Physics*. 2018. Vol. 82. N 7, p. 856-859. DOI: [10.3103/S1062873818070201](https://doi.org/10.3103/S1062873818070201)
40. Latyshev O.G., Kazak O.O. The influence of the geological material disturbance on its properties and condition. *News of the Ural State Mining University*. 2017. Iss. 4 (48), p. 62-65 (in Russian). DOI: [10.21440/2307-2091-2017-4-62-65](https://doi.org/10.21440/2307-2091-2017-4-62-65)
41. Dajun Zhao, Shulei Zhang, Meiyan Wang. Microcrack Growth Properties of Granite under Ultrasonic High-Frequency Excitation. *Advances in Civil Engineering*. 2019. Vol. 2019. Iss. 1. N 069029. DOI: [10.1155/2019/3069029](https://doi.org/10.1155/2019/3069029)
42. Myasnikova O.V., Trishina O.M., Kovalevskii M.V. et al. Structure and properties of granites from deposits of non-metallic building materials. *Trudy Fersmanovskoi nauchnoi sessii Gornogo instituta KNTs RAS*. 2009. N 6, p. 226-230.
43. Vaisberg L.A., Kameneva E.E., Nikiforova V.S. Microtomographic studies of rock pore space as the basis for rock disintegration technology improvements. *Obogashchenie rud*. 2018. N 3, p. 51-55 (in Russian). DOI: [10.17580/or.2018.03.09](https://doi.org/10.17580/or.2018.03.09)
44. Zaytsev D.V., Kochanov A.N., Toktogulov Sh.Zh. et al. Influence of scale effect and heterogeneity of rocks to determine their strength properties. *Mining Informational and Analytical Bulletin*. 2016. N 11, p. 208-215 (in Russian).
45. Kochanov A.N. Cracks in a solid for example rocks. *Mining Informational and Analytical Bulletin*. 2015. N 7, p. 221-225 (in Russian).
46. Kuksenko V.S., Makhmudov Kh.F., Mansurov V.A. et al. Changes in structure of natural heterogeneous materials under deformation. *Journal of Mining Science*. 2009. Vol. 45. N 4, p. 355-358. DOI: [10.1007/s10913-009-0044-3](https://doi.org/10.1007/s10913-009-0044-3)
47. Menzhulin M.G., Makhmudov Kh.F., Kuksenko V.S., Sultonov U. Formation and development of focus destruction of natural strain heterogeneous materials. *Tambov University Reports. Series Natural and Technical Sciences*. 2013. Vol. 18. Iss. 4-2, p. 1667-1668 (in Russian).

Authors: **Elena E. Kameneva**, Candidate of Engineering Sciences, Head of Department, Elena.kameneva@mail.ru, <https://orcid.org/0000-0001-6767-1536> (Petrozavodsk State University, Petrozavodsk, Russia), **Viktoriya S. Nikiforova**, Candidate of Geological and Mineralogical Sciences, Senior Lecturer, <https://orcid.org/0000-0003-1278-5290> (Empress Catherine II Saint Petersburg Mining University, Saint Petersburg, Russia).

The authors declare no conflict of interests.



Environmental assessment of biochar application for remediation of oil-contaminated soils under various economic uses

Tatiana V. Minnikova✉, Sergey I. Kolesnikov

Southern Federal University, Rostov-on-Don, Russia

How to cite this article: Minnikova T.V., Kolesnikov S.I. Environmental assessment of biochar application for remediation of oil-contaminated soils under various economic uses. *Journal of Mining Institute*. 2025. Vol. 271. N 16293, p. 84-94.

Abstract

Remediation is an important area of oil-contaminated soil restoration in Russia, since oil refining industry is the major one for Russia and neighbouring countries, and the issues of environmentally effective and economically profitable remediation of oil contamination have not yet been solved. Soils under various economic uses have different surface areas and degrees of soil particles envelopment with oil due to the presence or absence of cultivation, the amount of precipitation and plant litter. The introduction of various substances for remediation into oil-contaminated soils of steppes (arable land), forests, and semi-deserts, considering their differences, gives different results. Biochar is coal obtained by pyrolysis at high temperatures and in the absence of oxygen. The uniqueness of this coal lies in the combination of biostimulating and adsorbing properties. The purpose of the study is to conduct an environmental assessment of biochar application for remediation of oil-contaminated soils under various economic uses. The article compares the environmental assessments of biochar application in oil-contaminated soils with different particle size fraction. The following indicators of soil bioactivity were determined: enzymes, indicators of initial growth and development intensity of radish, microbiological indicators. We found that the most informative bioindicator correlating with residual oil content is the total bacteria count, and the most sensitive ones are the roots length (ordinary chernozem and brown forest soil) and the shoots length (brown semi-desert soil). The use of biochar on arable land and in forest soil (ordinary chernozem and brown forest soil) is less environmentally efficient than in semi-desert soil (brown semi-desert soil). The study results can serve to develop measures and managerial and technical solutions for remediation of oil-contaminated soils under various economic uses.

Keywords

soil contamination; oil; ordinary chernozem; brown forest soil; brown semi-desert soil; residual oil content; integral indicator of biological state

Funding

The study was conducted with the financial support of the project of the Strategic Academic Leadership Program of the Southern Federal University (Priority 2030) N SP-12-23-01; the Ministry of Science and Higher Education of the Russian Federation in the Soil Health laboratory of the Southern Federal University, agreement N 075-15-2022-1122; the project of the Ministry of Science and Higher Education of the Russian Federation and the support of the youth laboratory under the Interregional Scientific and Educational Centre of the South of Russia, N FENW-2024-0001.

Received: 31.07.2023

Accepted: 07.11.2024

Online: 05.02.2025

Published: 25.02.2025

Introduction

Oil is the most common raw material for fuel production in the world [1]. Despite modern protection systems for tankers and pipelines during oil transportation, the number of accidents has increased significantly over the past couple of years both abroad^{1,2} and in Russia³. In addition, clean

¹ Пять крупных экологических аварий 2022 года. URL: <https://www.angi.ru/news/2904237-Пять%20крупных%20экологических%20аварий%202022%20года/> (accessed 31.07.2023).

² 800 tons of fuel oil spilled into the sea after oil tanker MT Princess Empress sank in the Philippines. URL: <https://eco-sphere.press/2023/03/09/800-tonn-mazuta-okazalis-v-more-posle-krusheniya-neftyanogo-tankera-mt-princess-empress-na-filippinah> (accessed 31.07.2023).

³ Oil spill in Russian region. URL: <https://lenta.ru/news/2023/01/30/razliv/> (accessed 31.07.2023).



soils without an external source of contamination also contain hydrocarbons, which are mainly of autochthonous natural origin [2]. As a result of contamination with oil and oil products, the biological condition of soils deteriorates due to the disruption of environmental and agricultural functions [3]. There are two directions for reducing the level of soil contamination with oil and oil products: 1) contamination prevention; 2) elimination of the contamination consequences with minimal damage to the environment [4-6].

In the Perm Region, monitoring of various sources of environmental pollution with oil and oil products is conducted using unmanned aerial vehicles [7]. For soil cleaning, radical sanitation methods such as removal of the contaminated layer is unacceptable, since it leads to degradation of the topsoil and its alienation. Phytoremediation is one of poorly effective but very gentle methods of restoring the soil condition [8]. The effectiveness of phytoremediation is limited by the high concentration of oil (no more than 1.5 %), soil hydrophobicity, and the need to select plants for each contamination situation [9, 10]. High soil hydrophobicity causes a decrease in plant growth and development due to disruption of water exchange in the cells of both the photosynthetic apparatus and in the stems and root system [11, 12]. Therefore, it is recommended to combine phytoremediation with other types of remediation, such as the introduction of calcium oxide or carbonate encapsulation [13].

It is necessary to evaluate the modern methods of bioremediation of oil-contaminated soils without expensive removal of the upper fertile layer or the use of ineffective phytoremediants [14, 15]. Bioremediation methods involve the use of biostimulants and bioaugmenters, which reduce the oil content and return the soil to an environmental state close to that of before contamination. One of the substances often used for bioremediation of soil contaminated with oil and oil products, heavy metals is biochar [16, 17]. Biochar is mainly produced from agricultural waste (rice and wheat straw, corn and cotton stalks, other remains of grass vegetation), forest waste (wood of various tree species), livestock waste (pig, cow manure), and municipal wastewater sludge. The use of rice husk biochar together with bacterial preparations (BP) in oil-contaminated soil regulates the microbial community succession and increases the number of microorganisms associated with oil degradation at the genus level [18]. Rice husk biochar also contributes to an increase in the number of soil fungi [19]. The application of biochar with compost together with a decrease in the oil content increases the growth and development of wheat (*Triticum aestivum* L.), corn (*Zea mays* L.), white clover (*Trifolium repens* L.), alfalfa (*Medicago sativa* L.), and ryegrass (*Lolium multiflorum* Lam.) [20]. Biochar introduced together with mycorrhiza into contaminated soil had a beneficial effect on the growth and development of clover (*Trifolium arvense* L.) and mallow (*Malva sylvestris* L.) as well as contributed to oil degradation [21]. Biochar obtained from corn was selected as a carrier to immobilize oil-degrading microorganisms: the best particle size fraction was 0.08 mm, and the best immobilization time was 18 h [22]. The application of biochar and rhamnolipid into oil-contaminated swampy soil in Louisiana wetlands (USA) allowed to increase the algae biomass, led to the growth of gram-positive bacteria, actinomycetes, arbuscular mycorrhizal fungi and to a decrease in oil concentration [23]. Despite the advantages of biochar over other substances, its application in remediation of soil contaminated with oil and oil products is not always environmentally rational [24-26]. In remediation with biochar, the soil type and the substance concentration play an important role [27-29]. The application of biochar can both promote remediation and have a toxic effect on soil biota and cause soil alienation [30-32].

The objective is to conduct an environmental assessment of biochar application for remediation of oil-contaminated soils under various economic uses. The following tasks were set: to assess the residual oil content in soils under various economic uses (arable land, forest, and semi-desert) after introducing biochar; to analyse the change in bioindicators of soil condition; to assess the environmental efficiency of biochar in soils after oil contamination.

Methods

To study the biochar efficiency in remediation of oil-contaminated soils under various economic uses (arable land, forest, and semi-desert), the following were considered: ordinary chernozem (Haplic Chernozem Loamic), brown forest (Haplic Cambisols), and brown semi-desert soils (Endosalic Calcisols Yermic) [33] (Table 1). The choice of soil types was due to the fact that in the Rostov Region (ordinary chernozem), in the beech-hornbeam forest of the Republic of Adygeya (brown forest soil), and in the steppes of the Republic of Kalmykiya (brown semi-desert soil) oil and oil products are extracted, processed, or transported [34, 35]. Soil types differ in the land type, vegetation types, particle size fraction, soil reaction (pH), cation exchange capacity (CEC), and organic matter content (C_{org}).

Air-dry soil of each type was sifted through a 2 mm sieve and moistened, and then oil was added to the vegetation vessel at a concentration of 5 % of the soil mass. After the soil was contaminated, biochar was added to it in three concentrations: recommended – 5 %; half the recommended – 2.5 %; twice the recommended – 10 % of the soil mass.

Table 1

Sampling locations and characteristics of uncontaminated soils

Soil type	Coordinates	Sampling location	Land type	pH	C_{org} , %	CEC, mEq/100 g [36]	Particle size fraction
Ordinary chernozem	47°14'17.54"N; 39°38'33.22"E	Rostov Region, Rostov-on-Don, Botanical Garden of the Southern Federal University	Arable land	7.3	7.6	33.6	Heavy loam
Brown forest	44°10'39.76"N; 40° 9'27.47"E	Republic of Adygeya, Maikop district, Nikel village	Beech-horn- beam forest	5.3	1.3	24.3	Heavy loam
Brown semi-desert	46°17'48.65"N; 46°41'40.06"E	Republic of Kalmykiya, Narimanovskii district, Drofinyi village	Semi-desert	6.7	1.0	6.5	Light loam

After incubation of contaminated soils, the residual content of oil and oil products was analysed by infrared spectroscopy using carbon tetrachloride as an extractant (PND F 16.1: 2.2.22-98).

To assess the environmental efficiency of biochar application, the residual content of oil and bioindicators characterizing the environmental state of the soil were studied (Table 2).

Table 2

Methods for assessing the environmental state of oil-contaminated soils after remediation

Bioindicator	Measurement method	Source
Catalase activity (H_2O_2 : H_2O_2 – oxidoreductase, EC 1.11.1.6)	Volumetric, assessing the volume of water displaced by oxygen as a result of hydrogen peroxide decomposition upon contact with soil, ml O_2 /1 g of soil in 1 min	[37]
Dehydrogenase activity (substrate: NAD(P) – oxidoreductase, EC 1.1.1.1)	Reduction of triphenyltetrazolium chloride (TTC) to triphenylformazans (TPF) under anaerobic conditions with spectrophotometric termination, mg TPF/10 g of soil in 24 h	[38]
Total bacteria count	Fluorescence microscopy using acridine orange dye at $\times 40$ magnification. Bacterial count, billion bacteria/1 g of soil	[39]
Radish shoots length	After 7 days from the start of the phytotoxic experiment, radish (<i>Raphanus sativus</i> L.) shoots length was measured, mm	[40]
Radish roots length	After 7 days from the start of the phytotoxic experiment, radish (<i>Raphanus sativus</i> L.) roots length was measured, mm	[40]
Radish germination	Evaluation of radish (<i>Raphanus sativus</i> L.) germination after 7 days of the experiment, %	[40]



Based on the results of bioindicator determination, the integral indicator of the biological state of soils (IIBS) was estimated [41]. For the IIBS of ordinary chernozem, the relative values of each indicator were estimated in comparison with uncontaminated soil (control – 100 %). Relative values of this indicator for other experimental variants:

$$B_1 = \frac{B_x}{B_{\max}} \cdot 100 \%,$$

where B_1 is the relative score of the indicator; B_x is the actual value of the bioindicator; B_{\max} is the maximum value of the indicator in the control.

The next stage of estimating the IIBS is summing up the relative values of bioindicators and estimating the average scores:

$$B_{\text{avg}} = \frac{B_1 + B_2 + \dots + B_n}{N},$$

where B_{avg} is the average assessment score of the indicators; N is the number of indicators.

Final stage of estimation:

$$\text{IIBS} = \frac{B_{\text{avg}}}{B_{\text{ref}}} \cdot 100 \%,$$

where B_{ref} is the control value averaged over all biological indicators.

Statistical processing of the results was performed in the Statistica 12.0 software. Mean values and variance were determined using variance analysis (Student's t-test).

Discussion of results

The residual oil content (Fig.1) after 30 days of the experiment and biochar application decreased by 10-27 % (ordinary chernozem), 7-24 % (brown forest), and 7-27 % (brown semi-desert). The higher the dose of biochar, the more effective the oil decomposition in the soil.

According to the regression equations and determination coefficients, the closest relationship between oil decomposition and the effect of biochar in different doses corresponds to brown forest soil ($R^2 = 0.9985$), the least close to brown semi-desert ($R^2 = 0.9423$), and ordinary chernozem corresponds to an intermediate value ($R^2 = 0.9735$). The difference in oil decomposition in soils is associated

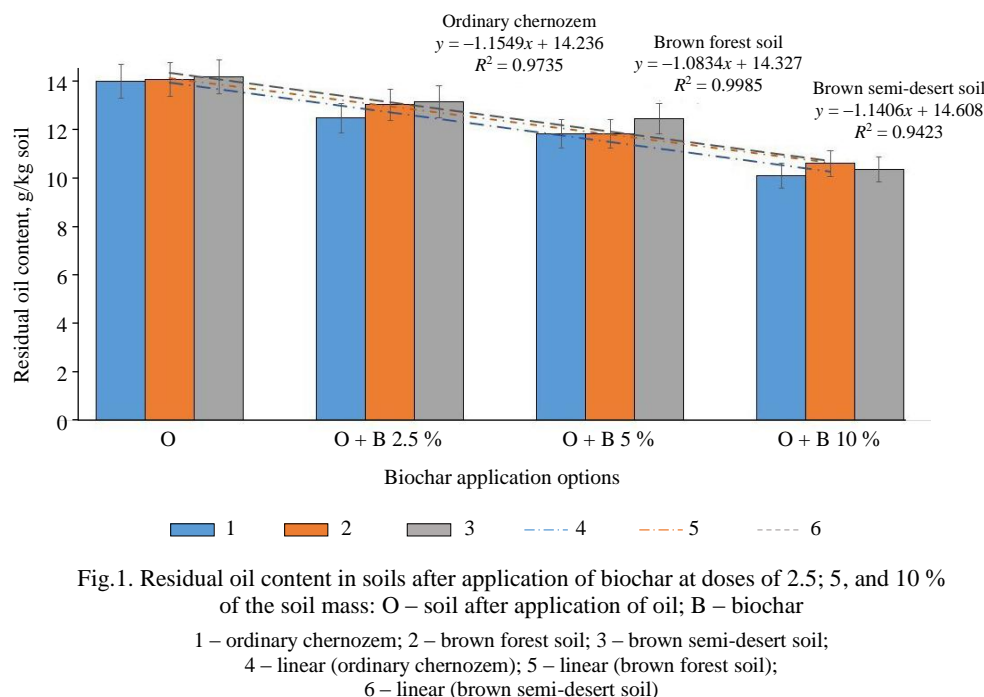


Fig.1. Residual oil content in soils after application of biochar at doses of 2.5; 5, and 10 % of the soil mass: O – soil after application of oil; B – biochar
1 – ordinary chernozem; 2 – brown forest soil; 3 – brown semi-desert soil;
4 – linear (ordinary chernozem); 5 – linear (brown forest soil);
6 – linear (brown semi-desert soil)

with the particle size fraction, organic matter content, and reaction of the soil environment [32]. In heavy loamy soils, such as brown forest soil and ordinary chernozem, the biochar application reduces the oil content to a greater extent than in brown semi-desert soil, which has a sandy loam particle size fraction. Thus, the series of biochar efficiency for oil decomposition in soils is as follows: brown forest soil > ordinary chernozem > brown semi-desert soil.

The biological parameters of the studied soils after the biochar application are given in Table 3. After the introduction of oil into ordinary chernozem, the decrease in biological parameters relative to the control was from 34 % (catalase activity) to 99 % (radish shoots and roots length). During the remediation of oil-contaminated brown forest soil, the bioactivity varied from 12 % (dehydrogenase activity) to 74 and 87 % (shoots length and roots length, respectively) relative to the control. In brown semi-desert soil, oil inhibited bioactivity in the range from 11 % (dehydrogenase activity) to 44 % (shoots length). The difference in the bioindicator sensitivity is due to the soil structure: in heavy loamy soils, a significant decrease in the radish shoots and roots length was observed, while in light loamy soil, a decrease was found in the bacteria count and the radish shoots length.

When adding biochar at 2.5, 5 and 10 % of the ordinary chernozem mass, it was noted that with an increase in the biochar concentration, bioactivity increases: catalase activity by 5-19 %; dehydrogenase activity by 0.5-9 %; total bacteria count by 17-50 %; germination by 33-600 %; shoots length by 2-39 times; roots length by 2-54 times compared to the oil-contaminated background.

In brown forest soil, biochar, just like in chernozem, stimulated biological parameters with concentration increase: catalase activity by 8-20 %; dehydrogenase activity by 10-203 %; total bacteria count by 84-133 %; radish germination by 72-105 %; shoots length by 43-156 %; roots length by 73-274 % compared to oil-polluted background. In brown semi-desert soil, biochar stimulated catalase activity by 7-31 %; dehydrogenase activity by 3-8 %; total bacteria count by 11-18 %; germination by 15-28 %; shoots length by 20-31 %; roots length by 5-18 % compared to oil-polluted background.

Table 3

Change in biological parameters after adding biochar, abs. units

Variants	Catalase activity, ml O ₂ /1 g per 1 min	Dehydrogenase activity, mg TPP/10 g per 24 h	Radish (<i>Raphanus sativus</i> L.) germination, %	Radish (<i>Raphanus sativus</i> L.) shoots length, mm	Radish (<i>Raphanus sativus</i> L.) roots length, mm	Total bacteria count, billion/1 g of soil
Ordinary chernozem						
Control	7.4	29.9	84	24.7	50.7	1.60
O	4.9	18.6	6	0.2	0.3	0.60
O + B 2.5 %	5.1	18.7	8	0.5	0.9	0.70
O + B 5 %	5.6	20.1	12	1.5	1.4	0.75
O + B 10 %	5.8	20.3	42	8.2	16.6	0.90
Brown forest soil						
Control	6.4	9.8	90	27.1	44.2	1.20
O	3.8	8.7	36	7.0	5.8	0.48
O + B 2.5 %	4.1	9.6	62	10.1	10.2	0.89
O + B 5 %	4.3	10.7	70	13.1	13.8	1.08
O + B 10 %	4.6	26.5	74	18.1	21.9	1.13
Brown semi-desert soil						
Control	2.1	18.9	86	25.0	27.4	1.00
O	1.3	16.9	66	14.0	24.2	0.62
O + B 2.5 %	1.4	17.4	76	16.8	25.4	0.69
O + B 5 %	1.52	17.8	78	18.3	26.9	0.70
O + B 10 %	1.77	18.3	85	18.4	28.5	0.73

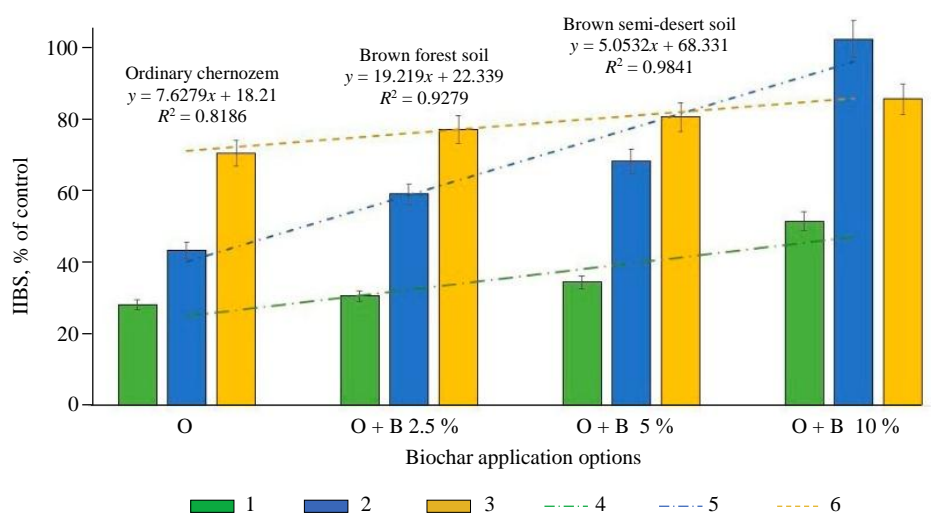


Fig.2. Change in the integral indicator of the biological state of soils after the biochar application in different doses

1 – ordinary chernozem; 2 – brown forest soil; 3 – brown semi-desert soil;
4 – linear (ordinary chernozem); 5 – linear (brown forest soil);
6 – linear (brown semi-desert soil)

During remediation of ordinary chernozem and brown forest soil, a decrease in soil phytotoxicity was observed due to an increase in the length of radish shoots and roots by 15-399 and 27-543 times, respectively, compared to the oil-contaminated background. This effect is probably due to the porous structure of biochar, which allows partial adsorption of oil and stimulation of its decomposition, as well as improvement of the soil structure, which is important for the growth and development of the root system of plants [17, 31]. However, stimulation of phytotoxic indicators relative to oil-contaminated soils did not allow achieving the control level, which is an indicator of the state of soils with a heavy loamy composition under oil contamination. In brown semi-desert soil, control values were achieved already at a biochar dose of 5 % for germination and roots length of radish.

According to Table 3, the integral indicator of the biological state was determined for each soil type after biochar application (Fig.2). According to estimations, in the soil without remediants, the IIBS of ordinary chernozem, brown forest, and brown semi-desert soils is 70, 55 and 27 % relative to the control. With the application of 2.5, 5, and 10 % biochar, the IIBS of ordinary chernozem changed by 46-68 % relative to the control. After applying biochar, the IIBS value of chernozem close to the control was not observed. The IIBS of brown forest soil increased at biochar doses of 2.5 and 5 % by 16 and 25 % relative to the oil-contaminated background (39 and 29 % lower than the control, respectively). At a biochar dose of 10 %, the IIBS of brown forest soil reached the control. In brown semi-desert soil, the IIBS value increased proportionally to the increase in the biochar dose of 2.5, 5, and 10 % by 20, 16, and 11 % below the control, respectively.

According to the regression equations presented in Fig.2, it is obvious that the change in the IIBS of each soil after remediation correlated differently with the oil content: from the highest correlation degree for brown semi-desert soil ($R^2 = -0.98$) to the lowest one among the three soils for ordinary chernozem ($R^2 = -0.82$). According to the efficiency of biochar application taken from the IIBS value, a series of soils was compiled: brown semi-desert soil > brown forest soil > ordinary chernozem.

The information content of each indicator and each soil type was assessed based on the strength of the correlation between the residual oil content and the value of all bioindicators (Table 4).

All bioindicators in the remediation of ordinary chernozem are informative ($r > 0.90$), but the most informative is the total bacteria count ($r = -1.00$). In the remediation of brown forest soil, the most informative indicator is the catalase activity ($r = -1.00$), and the least informative is the dehydrogenases activity ($r = 0.04$). For brown semi-desert soil, the most informative bioindicator is the total bacteria count ($r = -0.99$), and the least informative is the radish roots length ($r = -0.51$).



Table 4

Coefficient r of correlation between the bioindicator value and the residual oil content

Catalase activity	Dehydrogenase activity	Radish germination	Radish shoots length	Radish roots length	Total bacteria count
Ordinary chernozem					
−0.98**	−0.99**	−0.97**	−0.99**	−0.99**	−1.00**
Brown forest soil					
−1.00**	0.04	−0.80*	−0.95**	−0.98**	−0.64*
Brown semi-desert soil					
−0.96**	−0.88**	−0.72*	−0.96**	−0.51	−0.99**

Notes:

Significance of difference from control: * $p < 0.05$; ** $p < 0.001$.

The most informative indicator.

The least informative indicator.

For remediation of oil-contaminated ordinary chernozem and brown semi-desert soil with biochar, the most informative indicator is the total bacteria count, and for brown forest soil, the most informative indicator is catalase activity. Differences in the informativeness of the indicators for each soil type are due not only to their structure, but also to the content of organic matter and the soil environment reaction [42]. Among the studied samples, only in brown forest soil the soil environment reaction is acid ($\text{pH} = 5.7$), while in brown semi-desert soil ($\text{pH} = 6.7$) and ordinary chernozem ($\text{pH} = 7.3$) it is alkaline (see Table 1). The soil bacteria count is an informative bioindicator of oil-contaminated soil remediation [43].

The sensitivity of bioindicators was assessed by the difference with the control: the higher the value is than the control, the more sensitive the soil is to remediation (Table 5). The greater the difference from oil-contaminated soil without remediants, the more sensitive the indicator. Thus, for remediation of ordinary chernozem and brown forest soil with biochar, the most sensitive bioindicator is the roots length, and the least sensitive is the dehydrogenases and catalase activity.

Table 5

Relative values of bioindicators for each soil type (averaged by biochar doses), % of oil-contaminated soil without remediants

Catalase activity	Dehydrogenase activity	Radish germination	Radish shoots length	Radish roots length	Total bacteria count
Ordinary chernozem					
113	106	344	1,697	2,104	131
Brown forest soil					
113	179	191	195	261	214
Brown semi-desert soil					
117	106	121	127	111	114

Notes:

The most informative indicator.

The least informative indicator.

For remediation of brown semi-desert soil, the most sensitive bioindicator is shoots length, and the least sensitive is dehydrogenase activity. Brown semi-desert soil of the Chernozemel'skii district of the Republic of Kalmykiya, when contaminated with fuel oil and kerosene at a rate of 2.5 % of the soil mass, stimulated the growth of radish shoots and roots [44]. It was also previously determined that the combined treatment with biochar and rhamnolipid has the lowest ecotoxicity for plants and algae when used for remediation of oil-polluted wetlands [23].



The most sensitive indicator in the remediation of oil-contaminated ordinary chernozem (arable land, steppe soil) and brown forest soil (forest soil) with biochar is the radish roots length, and in brown semi-desert soil (semi-desert) – the radish shoots length.

The study results are important since thousands of hectares of soil are contaminated with oil and oil products every year due to various economic uses. The application of a single concentration of biochar for all types of soil is environmentally ineffective. The use of biochar for cleaning oil-contaminated soil depends on the soil type, the natural material from which the biochar is made, and the contamination level [45]. When remediating oil-contaminated soils with biochar, in addition to oil concentration, it is necessary to consider the agroclimatic (air temperature, amount of precipitation, wind speed), agrochemical (N content), and physicochemical parameters of the soil (humus, pH, particle size fraction, BOD, COD, easily soluble salt content). Biochar, due to the adsorbent properties, can be used in any climatic zone, since the adsorption rate does not depend on the temperature and moisture content of the soil [46-48]. Biochar as a biostimulant is more effective in soils formed in climatic conditions with a sufficient number of sunny days and precipitation, such as in soils of the steppe and forest zones.

The use of biochar is inextricably linked with the soil type (ordinary chernozem, brown forest, chestnut, brown semi-desert, solonchak, etc.) and the type of agricultural use (steppe, forest, and semi-desert). In the steppe zone of Russia (for example, in the Rostov Region and Krasnodar Territory), arable and virgin soils predominate, represented by various chernozems and chestnut soil subtypes, with a heavy loamy particle size fraction, high and medium humus and nitrogen content in the soil, and high soil buffering. As a result, in case of oil contamination of such soils, biochar application is effective, and the efficiency increases in combination with microbial preparations and humic substances [49-53]. The degradation of petroleum hydrocarbons in forest soils is influenced by the carbon and nitrogen ratio, which promotes the development of native microbiota, including oil-degrading bacteria [54-56]. The use of biochar for the remediation of forests and forest-steppes, as in the Republic of Adygeya, allows stimulating native microbiota due to the carbon introduced into the soil. The application of biochar in semi-desert soils, for example, in the Republic of Kalmykiya and the Astrakhan Region, is less effective, since it is directly related to the light particle size fraction of the soils, the virtual absence of vegetation in the soil cover, and the low content of humus and nitrogen. Therefore, the most sensitive bioindicator in the remediation of brown semi-desert soil is not the roots length, as in steppe and forest soils, but the radish shoots length. The greater sensitivity of shoots length is associated with the greater number of sunny days in the region. Thus, the application of biochar for oil contamination remediation and environmental restoration of the soil helps to reduce the pollutant concentration and is of great importance for the sustainable development of plants.

The informativeness of the bioindicator in case of contamination by oil and oil products is important first of all, since the connection between the amount of decomposed oil and the response of the bioindicator is considered [53, 57, 58]. The activity of microorganisms (fungi and bacteria) is one of the most informative, but not the most sensitive indicators [59]. The bioindicator sensitivity is determined by the indicator stimulation relative to the control. In case of oil contamination, the sensitivity is judged by the ratio of the bioindicator and the oil-polluted background, as well as the control. The use of microbiological preparations containing bacteria, fungi, and algae, i.e. microbial consortia, is most effective [60]. In case of oil contamination of sod-podzolic, light-gray, sod-carbonate, dark-gray, and floodplain soils, phytotesting methods (garden cress (*Lepidium sativum* L.), soft wheat (*Triticum aestivum* L.), Siberian spruce (*Picea obovata* Ledeb.), and Scots pine (*Pinus sylvestris* L.) observed the greatest resistance to oil contamination in floodplain soil, and the greatest vulnerability in sod-carbonate and light-gray soils [61]. In some cases, despite the set of measures such as collection and removal of spilled oil, the use of specialized oil extraction units, the application of nitrogen fertilizers, loosening and phytoremediation, the oil content in peat-gley soil is not reduced sufficiently and is dangerous for the surrounding ecosystem [62]. The application of biochar inoculated with



Bacillus and *Paenibacillus* microorganisms is also effective with preliminary BP inoculation in biochar – stimulation of dehydrogenase activity by 27 % of the background value. The most informative bioindicators of the soil are obtained when biochar is applied with *Bacillus* and *Paenibacillus*. Their application stimulates catalase activity, the total bacteria count in oil-contaminated chernozem, and increases the barley roots length, showing the greatest sensitivity [63].

Conclusion

The application of biochar for remediation of oil contaminated soils under various economic uses has different environmental efficiency. The oil content after biochar application decreases in all soils, regardless of the type of economic use. The most sensitive bioindicators for biochar remediation of arable land and forest soil are the roots length, and for semi-deserts, the shoots length. The most informative indicators for biochar remediation of oil-contaminated ordinary chernozem and brown semi-desert soil are the total bacteria count, and for brown forest soil, the catalase activity. From the point of view of environmental efficiency assessed by the integral indicator of the biological state of soils, the application of biochar on arable land and in forest soil (ordinary chernozem and brown forest soil) is less environmentally efficient than in semi-deserts (brown semi-desert soil). The obtained results serve to develop measures and managerial and technical solutions for the remediation of oil-contaminated soils under various economic uses.

The authors thank Postgraduate Student A.S.Ruseva and Master's Student S.Yu.Revina for their assistance in laboratory and analytical studies.

REFERENCES

1. Vasileva G.K., Strizhakova E.R., Bocharnikova E.A. et al. Oil and oil products as soil pollutants. Technology of combined physical and biological decontamination of soils. *Rossiiskii khimicheskii zhurnal*. 2013. Vol. 57. N 1, p. 79-104.
2. Pikovskii Yu.I., Smirnova M.A., Gennadiev A.N. et al. Parameters of the Native Hydrocarbon Status of Soils in Different Bioclimatic Zones. *Eurasian Soil Science*. 2019. Vol. 52. N 11, p. 1333-1346. DOI: [10.1134/S1064229319110085](https://doi.org/10.1134/S1064229319110085)
3. Vodyanitskii Yu.N., Shoba S.A. Biogeochemical barriers for soil and groundwater bioremediation. *Lomonosov Soil Science Journal*. 2016. N 3, p. 3-15 (in Russian).
4. Bykova M.V., Pashkevich M.A. Assessment of oil pollution of soils of production facilities of different soil and climatic zones of the Russian Federation. *News of the Tula state university. Sciences of Earth*. 2020. N 1, p. 46-59 (in Russian). DOI: [10.46689/2218-5194-2020-1-1-46-59](https://doi.org/10.46689/2218-5194-2020-1-1-46-59)
5. Polyakov R.Yu., Khotnikov E.L., Mozgovoi N.V., Bokadarov S.A. Modern means and technologies for eliminating the consequences of soil contamination by oil and oil products. *Pozharnaya bezopasnost: problemy i perspektivy*. 2013. N 1 (4), p. 343-345.
6. Shuguang Wang, Yan Xu, Zhaofeng Lin et al. The harm of petroleum-polluted soil and its remediation research. *AIP Conference Proceedings*. 2017. Vol. 1864. Iss. 1. N 020222. DOI: [10.1063/1.4993039](https://doi.org/10.1063/1.4993039)
7. Buzmakov S.A., Sannikov P.Yu., Kuchin L.S. et al. The use of unmanned aerial photography for interpreting the technogenic transformation of the natural environment during the oilfield operation. *Journal of Mining Institute*. 2023. Vol. 260, p. 180-193. DOI: [10.31897/PMI.2023.22](https://doi.org/10.31897/PMI.2023.22)
8. Ahmad A.A., Muhammad I., Shah T. et al. Remediation Methods of Crude Oil Contaminated Soil. *World Journal of Agriculture and Soil Science*. 2020. Vol. 4. Iss. 4. N WJASS.MS.ID.000595. DOI: [10.33552/WJASS.2020.04.000595](https://doi.org/10.33552/WJASS.2020.04.000595)
9. Okoye P.C., Ikhajagbe B., Obayuwana H.O., Ehiarinmwian R.I. Plant-assisted remediation of oil-polluted soil by five commonly cultivated local edible shrubs. *Nigerian Journal of Scientific Research*. 2018. Vol. 17 (1), p. 55-63.
10. Telysheva G., Jashina L., Lebedeva G. et al. Use of Plants to Remediate Soil Polluted With Oil. Environment. Technology. Resources. Proceedings of the 8th International Scientific and Practical Conference, 20-22 June 2011, Rēzekne, Latvia. Rēzekne, 2011. Vol. 1, p. 38-45. DOI: [10.17770/ETR2011VOL1.925](https://doi.org/10.17770/ETR2011VOL1.925)
11. Vysotskaya L.B., Arkhipova T.N., Kuzina E.V. et al. Comparison of responses of different plant species to oil pollution. *Biomics*. 2019. Vol. 11. N 1, p. 86-100. DOI: [10.31301/2221-6197.bmcs.2019-06](https://doi.org/10.31301/2221-6197.bmcs.2019-06)
12. Tang K.H.D., Angela J. Phytoremediation of crude oil-contaminated soil with local plant species. *IOP Conference Series: Materials Science and Engineering*. 2019. Vol. 495. N 012054. DOI: [10.1088/1757-899X/495/1/012054](https://doi.org/10.1088/1757-899X/495/1/012054)
13. Pashayan A.A., Nesterov A.V., Shchetinskaya O.S., Melnikova E.A. Recultivation of Oil-Contaminated Soils by Reagent Encapsulation with their Subsequent Phytoremediation. *Ecology and Industry of Russia*. 2022. Vol. 26. N 9, p. 20-25 (in Russian). DOI: [10.18412/1816-0395-2022-9-20-25](https://doi.org/10.18412/1816-0395-2022-9-20-25)
14. Slusarevsky A.V., Zinnatshina L.V., Vasilyeva G.K. Comparative Environmental and Economic Analysis of Methods for the Remediation of Oil-Contaminated Soils by in situ Bioremediation and Mechanical Soil Replacement. *Ecology and Industry of Russia*. 2018. Vol. 22. N 11, p. 40-45 (in Russian). DOI: [10.18412/1816-0395-2018-11-40-45](https://doi.org/10.18412/1816-0395-2018-11-40-45)



15. Kuzina E.V., Rafikova G.F., Stolyarova E.A., Loginov O.N. Efficiency of Associations of Legume Plants and Growth-Stimulating Bacteria for Restoration of Oil-Contaminated Soils. *Agrohimia*. 2021. N 4, p. 87-96 (in Russian). DOI: [10.31857/S0002188121040074](https://doi.org/10.31857/S0002188121040074)
16. Anae J., Ahmad N., Kumar V. et al. Recent advances in biochar engineering for soil contaminated with complex chemical mixtures: Remediation strategies and future perspectives. *Science of the Total Environment*. 2021. Vol. 767. N 144351. DOI: [10.1016/j.scitotenv.2020.144351](https://doi.org/10.1016/j.scitotenv.2020.144351)
17. Zahed M.A., Salehi S., Madadi R., Hejabi F. Biochar as a sustainable product for remediation of petroleum contaminated soil. *Current Research in Green and Sustainable Chemistry*. 2021. Vol. 4. N 100055. DOI: [10.1016/j.crgsc.2021.100055](https://doi.org/10.1016/j.crgsc.2021.100055)
18. Yuanfei Lv, Jianfeng Bao, Dongyang Liu et al. Synergistic effects of rice husk biochar and aerobic composting for heavy oil-contaminated soil remediation and microbial community succession evaluation. *Journal of Hazardous Materials*. 2023. Vol. 448. N 130929. DOI: [10.1016/j.jhazmat.2023.130929](https://doi.org/10.1016/j.jhazmat.2023.130929)
19. Chuan Yin, Huan Yan, Yuancheng Cao, Huanfang Gao. Enhanced bioremediation performance of diesel-contaminated soil by immobilized composite fungi on rice husk biochar. *Environmental Research*. 2023. Vol. 226. N 115663. DOI: [10.1016/j.envres.2023.115663](https://doi.org/10.1016/j.envres.2023.115663)
20. Yousaf U., Khan A.H.A., Farooqi A. et al. Interactive effect of biochar and compost with Poaceae and Fabaceae plants on remediation of total petroleum hydrocarbons in crude oil contaminated soil. *Chemosphere*. 2022. Vol. 286. Part 2. N 131782. DOI: [10.1016/j.chemosphere.2021.131782](https://doi.org/10.1016/j.chemosphere.2021.131782)
21. Abbaspour A., Zohrabi F., Dorostkar V. et al. Remediation of an oil-contaminated soil by two native plants treated with biochar and mycorrhizae. *Journal of Environmental Management*. 2020. Vol. 254. N 109755. DOI: [10.1016/j.jenvman.2019.109755](https://doi.org/10.1016/j.jenvman.2019.109755)
22. Hongyang Ren, Yuanpeng Deng, Liang Ma et al. Enhanced biodegradation of oil-contaminated soil oil in shale gas exploitation by biochar immobilization. *Biodegradation*. 2022. Vol. 33. Iss. 6, p. 621-639. DOI: [10.1007/s10532-022-09999-6](https://doi.org/10.1007/s10532-022-09999-6)
23. Zhuo Wei, Jim J. Wang, Yili Meng et al. Potential use of biochar and rhamnolipid biosurfactant for remediation of crude oil-contaminated coastal wetland soil: Ecotoxicity assessment. *Chemosphere*. 2020. Vol. 253. N 126617. DOI: [10.1016/j.chemosphere.2020.126617](https://doi.org/10.1016/j.chemosphere.2020.126617)
24. Smirnova E.V., Okunev R.V., Giniyatullin K.G. Influence of carbon sorbents on the potential ability of soils to self-cleaning from petroleum pollution. *Georesources*. 2022. Vol. 24. N 3, p. 210-218 (in Russian). DOI: [10.18599/grs.2022.3.18](https://doi.org/10.18599/grs.2022.3.18)
25. Dike C.C., Shahsavari E., Surapaneni A. et al. Can biochar be an effective and reliable biostimulating agent for the remediation of hydrocarbon-contaminated soils? *Environment International*. 2021. Vol. 154. N 106553. DOI: [10.1016/j.envint.2021.106553](https://doi.org/10.1016/j.envint.2021.106553)
26. Dike C.C., Hakeem I.G., Rani A. et al. The co-application of biochar with bioremediation for the removal of petroleum hydrocarbons from contaminated soil. *Science of the Total Environment*. 2022. Vol. 849. N 157753. DOI: [10.1016/j.scitotenv.2022.157753](https://doi.org/10.1016/j.scitotenv.2022.157753)
27. Gorovtsov A.V., Minkina T.M., Mandzhieva S.S. et al. The mechanisms of biochar interactions with microorganisms in soil. *Environmental Geochemistry and Health*. 2020. Vol. 42. Iss. 8, p. 2495-2518. DOI: [10.1007/s10653-019-00412-5](https://doi.org/10.1007/s10653-019-00412-5)
28. Hongyang Lin, Yang Yang, Zhenxiao Shang et al. Study on the Enhanced Remediation of Petroleum-Contaminated Soil by Biochar/g-C₃N₄ Composites. *International Journal of Environmental Research and Public Health*. 2022. Vol. 19. Iss. 14. N 8290. DOI: [10.3390/ijerph19148290](https://doi.org/10.3390/ijerph19148290)
29. Minnikova T., Ruseva A., Kolesnikov S. Assessment of Ecological State of Soils Contaminated by Petroleum Hydrocarbons after Bioremediation. *Environmental Processes*. 2022. Vol. 9. Iss. 3. N 49. DOI: [10.1007/s40710-022-00604-9](https://doi.org/10.1007/s40710-022-00604-9)
30. Haider F.U., Xiukang Wang, Zulfikar U. et al. Biochar application for remediation of organic toxic pollutants in contaminated soils; An update. *Ecotoxicology and Environmental Safety*. 2022. Vol. 248. N 114322. DOI: [10.1016/j.ecoenv.2022.114322](https://doi.org/10.1016/j.ecoenv.2022.114322)
31. Murtaza G., Ahmed Z., Eldin S.M. et al. Biochar as a Green Sorbent for Remediation of Polluted Soils and Associated Toxicity Risks: A Critical Review. *Separations*. 2023. Vol. 10. Iss. 3. N 197. DOI: [10.3390/separations10030197](https://doi.org/10.3390/separations10030197)
32. Xin Sui, Xuemei Wang, Yuhuan Li, Hongbing Ji. Remediation of Petroleum-Contaminated Soils with Microbial and Microbial Combined Methods: Advances, Mechanisms, and Challenges. *Sustainability*. 2021. Vol. 13. Iss. 16. N 9267. DOI: [10.3390/su13169267](https://doi.org/10.3390/su13169267)
33. World Reference Base for Soil Resources. International soil classification system for naming soils and creating legends for soil maps. Vienna: International Union of Soil Sciences, 2022. 236 p. URL: https://www.isric.org/sites/default/files/WRB_fourth_edition_2022-12-18.pdf
34. Daud R.M., Kolesnikov S.I., Minnikova T.V. et al. Biodiagnostics of arid soils resistance in the South of Russia to contamination by heavy metals, petroleum hydrocarbons, and biocides. Rostov-on-Don: Izd-vo Yuzhnogo federalnogo universiteta, 2021, p. 217.
35. Sangadzhieva L.Ch., Davaeva Ts.D., Buluktaev A.A. Influence of oil pollution on phytotoxicity of light brown soils of Kalmykia. *Bulletin of Kalmyk university*. 2013. N 1 (17), p. 44-47 (in Russian).
36. Valkov V.F., Kazeev K.Sh., Kolesnikov S.I. Soils of the South of Russia. Rostov-na-Donu: Everest, 2008, p. 276.
37. Baikhamurova M.O., Yuldashbek D.H., Sainova G.A., Anarbekova G.D. Change of catalase and urease activity at high content of heavy metals (Pb, Zn, Cd) in serozem. *European Journal of Natural History*. 2020. N 3, p. 70-73.
38. Małachowska-Jutysz A., Matyja K. Discussion on methods of soil dehydrogenase determination. *International Journal of Environmental Science and Technology*. 2019. Vol. 16. Iss. 12, p. 7777-7790. DOI: [10.1007/s13762-019-02375-7](https://doi.org/10.1007/s13762-019-02375-7)
39. Polyanskaya L.M., Pinchuk I.P., Stepanov A.L. Comparative Analysis of the Luminescence Microscopy and Cascade Filtration Methods for Estimating Bacterial Abundance and Biomass in the Soil: Role of Soil Suspension Dilution. *Eurasian Soil Science*. 2017. Vol. 50. N 10, p. 1173-1176. DOI: [10.1134/S1064229317100088](https://doi.org/10.1134/S1064229317100088)
40. Quintela-Sabaris C., Marchand L., Kidd P.S. et al. Assessing phytotoxicity of trace element-contaminated soils phytomanaged with gentle remediation options at ten European field trials. *Science of the Total Environment*. 2017. Vol. 599-600, p. 1388-1398. DOI: [10.1016/j.scitotenv.2017.04.187](https://doi.org/10.1016/j.scitotenv.2017.04.187)
41. Kolesnikov S.I., Kazeev K.S., Akimenko Y.V. Development of regional standards for pollutants in the soil using biological parameters. *Environmental Monitoring and Assessment*. 2019. Vol. 191. Iss. 9. N 544. DOI: [10.1007/s10661-019-7718-3](https://doi.org/10.1007/s10661-019-7718-3)
42. Tunç E., Şahin E.Z., Demir M. et al. Investigation of Factors Affecting Catalase Enzyme Activity In Different Agricultural Soils. 1st International Congress on Sustainable Agriculture and Technology, 1-3 April 2019, Gaziantep, Turkey. Gaziantep University, 2019, p. 103-116.
43. Bakaeva M.D., Kuzina E.V., Rafikova G.F. et al. Application of auxin producing bacteria in phytoremediation of oil-contaminated soil. *Theoretical and Applied Ecology*. 2020. N 1, p. 144-150 (in Russian). DOI: [10.25750/1995-4301-2020-1-144-150](https://doi.org/10.25750/1995-4301-2020-1-144-150)



44. Buluktaev A.A. Phytotoxicity of oil-polluted soils in arid territories: analyzing results of simulation experiments. *Russian Journal of Ecosystem Ecology*. 2019. Vol. 4 (3), p. 10 (in Russian). DOI: [10.21685/2500-0578-2019-3-5](https://doi.org/10.21685/2500-0578-2019-3-5)
45. Xue Yang, Shiqiu Zhang, Meiting Ju, Le Liu. Preparation and Modification of Biochar Materials and their Application in Soil Remediation. *Applied Sciences*. 2019. Vol. 9. Iss. 7. N 1365. DOI: [10.3390/app9071365](https://doi.org/10.3390/app9071365)
46. Masiello C.A., Dugan B., Brewer C.E. et al. Biochar effects on soil hydrology. *Biochar for Environmental Management. Science, Technology and Implementation*. Routledge. 2015, p. 543-562. DOI: [10.4324/9780203762264](https://doi.org/10.4324/9780203762264)
47. Kinney T.J., Masiello C.A., Dugan B. et al. Hydrologic properties of biochars produced at different temperatures. *Biomass and Bioenergy*. 2012. Vol. 41, p. 34-43. DOI: [10.1016/j.biombioe.2012.01.033](https://doi.org/10.1016/j.biombioe.2012.01.033)
48. Van Gestel M., Ladd J.N., Amato M. Microbial biomass responses to seasonal change and imposed drying regimes at increasing depths of undisturbed topsoil profiles. *Soil Biology and Biochemistry*. 1992. Vol. 24. Iss. 2, p. 103-111. DOI: [10.1016/0038-0717\(92\)90265-Y](https://doi.org/10.1016/0038-0717(92)90265-Y)
49. Muratova A.Yu., Panchenko L.V., Dubrovskaya E.V. et al. Bioremediation Potential of Biochar-Immobilized Cells of *Azospirillum brasilense*. *Microbiology*. 2022. Vol. 91. N 5, p. 514-522. DOI: [10.1134/S0026261722601336](https://doi.org/10.1134/S0026261722601336)
50. Minnikova T.V., Kolesnikov S.I., Minin N.S. Evaluation of dehydrogenases and invertase activity in petroleum-hydrocarbon-contaminated haplic chernozem during remediation with biochar and bacterial preparation. *Biosphere*. 2024. Vol. 16. N 1, p. 36-44 (in Russian). DOI: [10.24855/biosfera.v16i1.891](https://doi.org/10.24855/biosfera.v16i1.891)
51. Minnikova T., Kolesnikov S., Minkina T., Mandzhieva S. Assessment of Ecological Condition of Haplic Chernozem Calcic Contaminated with Petroleum Hydrocarbons during Application of Bioremediation Agents of Various Natures. *Land*. 2021. Vol. 10. Iss. 2. N 169. DOI: [10.3390/land10020169](https://doi.org/10.3390/land10020169)
52. Minnikova T., Kolesnikov S., Minin N. et al. The Influence of Remediation with *Bacillus* and *Paenibacillus* Strains and Biochar on the Biological Activity of Petroleum-Hydrocarbon-Contaminated Haplic Chernozem. *Agriculture*. 2023. Vol. 13. Iss. 3. N 719. DOI: [10.3390/agriculture13030719](https://doi.org/10.3390/agriculture13030719)
53. Ruseva A., Minnikova T., Kolesnikov S. et al. Assessment of the ecological state of haplic chernozem contaminated by oil, fuel oil and gasoline after remediation. *Petroleum Research*. 2024. Vol. 9. Iss. 1, p. 155-164. DOI: [10.1016/j.ptlrs.2023.03.002](https://doi.org/10.1016/j.ptlrs.2023.03.002)
54. Kudryarov V.N. The agrobiogeochemical cycles of carbon and nitrogen of Russian croplands. *Agrohimia*. 2019. N 12, p. 3-15 (in Russian). DOI: [10.1134/S000218811912007X](https://doi.org/10.1134/S000218811912007X)
55. Uligova T.S., Tsepikova N.L., Rapoport I.B. et al. Forest Biogeocoenoses in the Area of Brown Forest Soils of the Western Caucasus. *Biology Bulletin*. 2023. Vol. 50. N 1, p. 70-84. DOI: [10.1134/S1062359023010132](https://doi.org/10.1134/S1062359023010132)
56. Ryzhova I.M., Podvezennaya M.A., Kirillova N.P. Analysis of the effect of moisture content on the spatial variability of carbon stock in forest soil of European Russia using databases. *Lomonosov Soil Science Journal*. 2022. N 2, p. 20-27 (in Russian).
57. Lukoshkova A.A., Popova L.F. Microbiological activity of soils contaminated with oil products. Nauchnye mezhdistsiplinarnye issledovaniya. Sbornik statei VI Mezhdunarodnoi nauchno-prakticheskoi konferentsii, 25 oktyabrya 2020, Saratov, Russia. Saratov: Nauchno-obrazovatel'naya organizatsiya "Tsifrovaya nauka", 2020, p. 11-15 (in Russian). DOI: [10.24412/cl-36007-2020-6-11-15](https://doi.org/10.24412/cl-36007-2020-6-11-15)
58. Morachevskaya E.V., Voronina L.P. Bioassay as a method of integral assessment for remediation of oil-contaminated ecosystems. *Theoretical and Applied Ecology*. 2022. N 1, p. 34-43. DOI: [10.25750/1995-4301-2022-1-034-043](https://doi.org/10.25750/1995-4301-2022-1-034-043)
59. Usacheva Yu.N. Methods of bioindication in assessment of oil-contaminated soils under recultivation work. *Ecology and Industry of Russia*. 2012. N 11, p. 40-43 (in Russian). DOI: [10.18412/1816-0395-2012-11-40-43](https://doi.org/10.18412/1816-0395-2012-11-40-43)
60. Sozina I.D., Danilov A.S. Microbiological remediation of oil-contaminated soils. *Journal of Mining Institute*. 2023. Vol. 260, p. 297-312. DOI: [10.31897/PMI.2023.8](https://doi.org/10.31897/PMI.2023.8)
61. Buzmakov S.A., Andreev D.N., Nazarov A.V. et al. Responses of Different Test Objects to Experimental Soil Contamination with Crude Oil. *Russian Journal of Ecology*. 2021. Vol. 52. N 4, p. 267-274. DOI: [10.1134/S1067413621040056](https://doi.org/10.1134/S1067413621040056)
62. Maslov M.N., Maslova O.A., Ezhelev Z.S. Microbiological Transformation of Organic Matter in Oil-Polluted Tundra Soils after Their Reclamation. *Eurasian Soil Science*. 2019. Vol. 52. N 1, p. 58-65. DOI: [10.1134/S1064229319010101](https://doi.org/10.1134/S1064229319010101)
63. Minnikova T., Kolesnikov S., Revina S. et al. Enzymatic Assessment of the State of Oil-Contaminated Soils in the South of Russia after Bioremediation. *Toxics*. 2023. Vol. 11. Iss. 4. N 355. DOI: [10.3390/toxics11040355](https://doi.org/10.3390/toxics11040355)

Authors: **Tatiana V. Minnikova**, Candidate of Biological Sciences, Leading Researcher, loko261008@yandex.ru, <https://orcid.org/0000-0002-9453-7137> (Southern Federal University, Rostov-on-Don, Russia), **Sergey I. Kolesnikov**, Doctor of Agricultural Sciences, Head of Department, <https://orcid.org/0000-0001-5860-8420> (Southern Federal University, Rostov-on-Don, Russia).

The authors declare no conflict of interests.



Investigation of the accuracy of constructing digital elevation models of technogenic massifs based on satellite coordinate determinations

Mikhail Ya. Bryn¹, Murat G. Mustafin², Dinara R. Bashirova³, Bogdan Yu. Vasilev²✉

¹ Emperor Alexander I St. Petersburg State Transport University, Saint Petersburg, Russia

² Empress Catherine II Saint Petersburg Mining University, Saint Petersburg, Russia

³ AO "Gazprom Diagnostika", Saint Petersburg, Russia

How to cite this article: Bryn M.Ya., Mustafin M.G., Bashirova D.R., Vasilev B.Yu. Investigation of the accuracy of constructing digital elevation models of technogenic massifs based on satellite coordinate determinations. *Journal of Mining Institute*. 2025. Vol. 271. N 16310, p. 95-107.

Abstract

At all stages of the life cycle of buildings and structures, geodetic support is provided by electronic measuring instruments – a laser scanning system, unmanned aerial vehicles, and satellite equipment. In this context, a set of geospatial data is obtained that can be presented as a digital model. The relevance of this work is practical recommendations for constructing a local quasigeoid model and a digital elevation model (DEM) of a certain accuracy. A local quasigeoid model and a DEM were selected as the study objects. It is noted that a DEM is often produced for vast areas, and, therefore, it is necessary to build a local quasigeoid model for such models. The task of assessing the accuracy of constructing such models is considered; its solution will allow obtaining a better approximation to real data on preassigned sets of field materials. A general algorithm for creating both DEM and local quasigeoid models in the Golden Software Surfer is presented. The constructions were accomplished using spatial interpolation methods. When building a local quasigeoid model for an area project, the following methods were used: triangulation with linear interpolation (the least value of the root mean square error (RMSE) of interpolation was 0.003 m) and kriging (0.003 m). The least RMSE value for determining the heights by control points for an area project was obtained using the natural neighbour (0.004 m) and kriging (0.004 m) methods. To construct a local quasigeoid model for a linear project, the following methods were applied: kriging (0.006 m) and triangulation with linear interpolation (0.006 m). Construction of the digital elevation model resulted in the least aggregate value of the estimated parameters: on a flat plot of the earth's surface – the natural neighbour method, for a mountainous plot with anthropogenic topography – the quadric kriging method, for a mountainous plot – quadric kriging.

Keywords

digital elevation model; point cloud; spatial interpolation methods; quasigeoid; normal height; geodetic height; root mean square error; kriging; triangulation; natural neighbour

Received: 05.09.2023

Accepted: 07.11.2024

Online: 18.12.2024

Published: 25.02.2025

Introduction

Geodetic support, which includes engineering and geodetic survey, siting work, and pre-construction survey, is an important aspect of ensuring the design, construction and operation of buildings and structures, including projects in the mineral resources sector. During operation, monitoring of the facility deformations can be carried out [1]. At all life cycle stages of mineral resource sector projects it is possible to use the advanced technologies: information [2, 3], numerical [4-6] and simulation modelling [7] as well as neural networks [8, 9]. In this case, it is possible to monitor the main characteristics of the investigated project in a safe manner and in great detail, which leads to quality improvement of the handed-over field materials and an expansion of the information set regarding the research object. In respect of geodetic support of the work, the use of advanced technologies allows combining geospatial data into a single set of reliable information used for taking engineering decisions and creating integrated models for safe operation of engineering constructions [10-12]. Non-contact methods of terrain surveying, such as laser scanning [13] and photogrammetric methods [14] including unmanned aerial vehicles [15-17] are actively applied. It should be noted that



lately the observation methods with a satellite navigation system (GNSS) were applied to determine the altitude position of structural elements [18] for the efficient use of which it is necessary to have a quasigeoid height model or a height anomaly model for the construction site. It should be emphasized that in the process of designing and constructing the projects as well as in various urban development works, including land development, generation of a digital elevation model (DEM) based on the obtained data is an important stage for obtaining spatial information about the work site. Assessment of the accuracy and automation of DEM creation is a relevant task, since the quality and speed of construction allow increasing the productivity of all the related processes. Thus, the task of studying the accuracy of producing a local quasigeoid model and DEM arises in the absence of general recommendations for their construction [19, 20] and accuracy assessment [21, 22]. For example, articles [23-25] contain recommendations on the use of spatial interpolation methods [26, 27] for producing mathematical elevation models.

It should be noted that the construction of DEM is possible both with and without using a local quasigeoid model. However, this can lead to distortion of the information on topography [19, 25]. To provide the results of geodetic support, the normal height system is used [18, 28, 29]. In case of obtaining geodetic heights, the question of switching to it arises. Then, a local quasigeoid model is needed [30-32] for the creation of which it is important to have combined points [33, 34] (with known geodetic heights from the GNSS definitions and normal or orthometric heights from geometric levelling). Modelling of the surface of height anomalies [34] was caused primarily by land planning in Poland [28], Slovenia [31], coastal cities of the Red Sea [20], and Ethiopia [34].

The authors of [21, 35] noted that the production of such models in hard-to-reach mountainous areas is an important stage in accurate determination of heights using the GNSS equipment. Article [28] indicates that an accuracy of 5 mm was attained when creating a local model for the territory of Krakow. The production of such models is important for development of the regions [33]. Often, the problem of modelling the surface of height anomalies for an area project is solved. However, there are no studies aimed at creating a local quasigeoid model for an extensive linear project. No recommendations were drawn up concerning the required number of points or the method for assigning a sufficient number of points to create a model in which the accuracy of determining the heights would correspond to the accuracy indicated in work specifications at each stage of construction.

When determining the corrections to geodetic heights for further construction of DEM, it is necessary to choose the spatial interpolation method that will be used to construct a mathematical model of height anomalies [36]. DEM construction from data obtained by different survey methods [37] is actively investigated [35]. In this case, the results can be used as a spatial grid with regular spacing (GRID) or a point cloud [38]. Choice of the spatial interpolation method has a direct impact on the final accuracy of constructing the mathematical elevation model [39]. The most common method is the triangulation irregular network (TIN) [25]. However, in [40-42] the advisability of using other spatial interpolation methods is mentioned:

- The kriging method is used for constructing the topography of both the earth's, and the underwater surface [43, 44] with a correct definition of the variogram [45, 46] forming the spatial dependence.
- Radial basis function. The data on topography obtained by airborne laser scanning (ALS) are characterized by outliers which have a negative impact on the accuracy of digital elevation models. However, experimental results in the study [47] showed that the use of spline functions provides a more accurate model based on natural, rather than synthetically created data.

The obtained accuracy of constructions is affected by the density of the source geospatial data [48, 49] and the source of information [50]. The aim of the work is to assess the accuracy of creating mathematical elevation models and a quasigeoid based on spatial interpolation methods as well as to develop the initial provisions of the general methodology for creating a local quasigeoid model and a digital elevation model.



Methods

Source data. *Construction of a local quasigeoid model.* Source data for the area project were 300 combined geodetic points at which geodetic and normal heights were determined. Of the total number of points at approximately the same spacing in different parts of the project, 10 % (30 points) were used as controls and did not participate in creation of the model. Root mean square errors (RMSE) of determining the normal heights of points did not exceed 3 mm. The area of the study project was 776.39 km².

When creating a local quasigeoid model for constructing a motorway in flat terrain, 28 points lying at different sides and at equal distances from the axis of the designed project in its different parts were selected from the total number of combined geodetic points. The limitation in the number of points is due to the existing plan-elevation datum. Similarly, to control the quality of construction, a part of points (10 %) was excluded from the process of creating models, which contradicted the principle of a uniform distribution of data and could also lead to collisions in the interpretation of the results of accuracy assessment due to local instability.

Construction of DEM. Source data were the results of airborne laser scanning of three large areas on the earth's surface with different types of topography (Table 1). Using the TerraScan software by Terrasolid Company and a point cloud macro, two point clouds were automatically classified, containing:

- key points used to construct the DEM;
- points on the earth's surface that are not mandatory (key) for construction. At the same time, they contain spatial information about the earth's surface, which can be used to assess the accuracy.

Then, the areas were visually assessed for the presence of points with non-characteristic deviations, which indicate an erroneous classification of individual points of the earth's surface.

Table 1

Brief characteristic of plots

Plot	Average inclination angle, deg	Minimum height, m	Maximum height, m	Area, m ²
A	0.5	8.0	35.40	53,423
B	29.3	194.95	918.07	10,872
C	25.6	460.63	1,726.00	32,541

Plot A is a flat area (Fig.1, *a*) with minor local changes in surface curvature. Plot B (Fig.1, *b*) is a mountainous region with significant elevation differences and areas with major changes in surface curvature. Plot C is a mountainous area (Fig.1, *c*) with pronounced anthropogenic topography. Surface shows of disturbances and edges and slopes typical of open-pit mining are visible.

General description of the methodology for constructing models. Six methods of spatial interpolation were used. Constructions were performed in the Golden Software Surfer. It is proposed to create a local quasigeoid model:

- import of a set of geospatial data into the software;
- transition from a point cloud to GRID (spatial grid with regular spacing);
- construction of mathematical models by selected methods of spatial interpolation using different parameters;
- calculation of metrics for assessing the accuracy of constructions using control points;
- comparative analysis of metrics characterizing the accuracy of construction of mathematical models obtained using selected methods of spatial interpolation;
- definition of spatial interpolation method based on the values of selected metrics for constructing the mathematical model of similar plots.

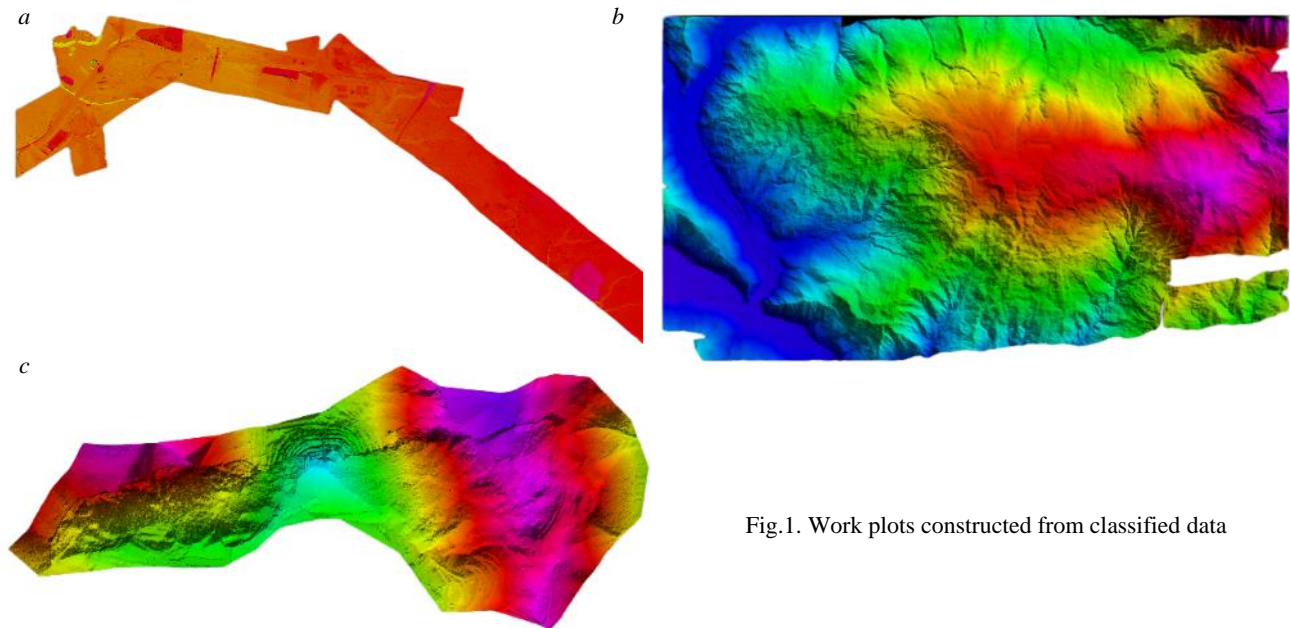


Fig.1. Work plots constructed from classified data

Creation of DEM:

- transformation of geodetic heights to normal ones in case of a large extent of the project site or according to the task set using the produced local quasigeoid model;
- division of a large area project into fragments 1,000×1,000 m;
- selection of a characteristic plot based on general morphometric characteristics from a set of obtained fragments;
- construction of DEM on a characteristic plot and drawing-up of practical recommendations for choosing the spatial interpolation method based on the accuracy assessment for the entire project site;
- creation of DEM for the entire project site using the selected spatial interpolation method.

Analysis of methods for constructing models. *Triangulation with linear interpolation.* In the Surfer program, a triangulation surface is constructed on the source data set. When a point with an unknown Z coordinate falls into the constructed plane limited by three points and determined by the equation

$$aX + bY + cZ + d = 0,$$

the coefficients are determined by expressions:

$$a = Y_1(Z_2 - Z_3) + Y_2(Z_3 - Z_1) + Y_3(Z_1 - Z_2);$$

$$b = Z_1(X_2 - X_3) + Z_2(X_3 - X_1) + Z_3(X_1 - X_2);$$

$$c = X_1(Y_2 - Y_3) + X_2(Y_3 - Y_1) + X_3(Y_1 - Y_2);$$

$$d = X_1(Y_2Z_3 - Y_3Z_2) + X_2(Y_3Z_1 - Y_1Z_3) + X_3(Y_1Z_2 - Y_2Z_1).$$

The unknown Z coordinate for a new point inserted into the surface is calculated from the formula

$$\hat{Z}_0 = \frac{-aX - bY - d}{c}.$$

Minimum curvature method. Using the least squares method, a mathematical surface is calculated that includes all the source data:

$$Z(X,Y) = a + bX + cY.$$



Difference between the resulting construction values and points with the known coordinates is determined by the formula

$$e_i = (a + bX_i + cY_i) - Z_i.$$

At the next stage, the values of heights at nodes of the regular grid are calculated. The problem of solving a modified differential equation arises

$$(1 - T_i) \nabla^2 (\nabla^2 e) - (T_i) \nabla^2 e = 0,$$

where T_i is the tension coefficient.

It is necessary to take the boundary conditions into account:

$$(1 - T_b) \frac{\partial^2 e}{\partial n^2} + (T_b) \frac{\partial e}{\partial n} = 0, \quad \frac{\partial (\nabla^2 e)}{\partial n} = 0, \quad \frac{\partial^2 e}{\partial X \partial Y} = 0,$$

where ∇^2 is the Laplace operator; n – boundary normal; T_b – boundary tension parameter.

Then, the final estimate of Z is determined by expression

$$\hat{Z}(X, Y) = a + bX + cY + \hat{e}(X, Y).$$

Using the minimum curvature method, surfaces are constructed with a change in two parameters: The Internal Tension (deflection amount) and The Boundary Tension (deflection value at edges). The higher the values of these parameters, the less pronounced the bending.

Nearest neighbour method. To determine the value of a new point added to the surface, the value of the nearest sample point is used

$$\hat{Z}_0 = Z_i,$$

where Z_i is the value of the nearest sample point.

In the process of creating models, different options for the search area of values were used in order to identify the impact of changes in the area on the accuracy of the digital model.

Natural neighbour. Definition of weights for calculating the values of coordinates at nodes of the regular grid is accomplished on the basis of proportional areas [40]:

$$\hat{Z}_0 = \sum_{i=1}^N w_{i0} Z_i,$$

where w_{i0} is the weight of the i -th point (calculated using Voronoi diagrams).

When using such method, the heights of interpolated points will not go beyond the range of heights of the source data [41].

Radial basis function. To calculate the Z coordinate for the inserted point, the following expression is used

$$\hat{Z}_0 = \sum_{i=1}^n \lambda_i B(d_{i0}),$$

where d_{i0} is distance between the determined point and the known i -th point; λ , coefficient of the i -th point with known coordinates; B , radial basis function whose argument is d_{i0} distance.

The functions available in the Surfer were used as the compute core for the method in the investigation:

- Multiquadric

$$B(d) = \sqrt{d^2 + R^2};$$



- Inverse Multiquadric

$$B(d) = \frac{1}{\sqrt{d^2 + R^2}};$$

- Miltilog

$$B(d) = \log(d^2 + R^2);$$

- Thin Plate Spline

$$B(d) = (d^2 + R^2) \log(d^2 + R^2);$$

- Natural Cubic Spline

$$B(d) = (d^2 + R^2)^{3/2},$$

where d is distance from the point with an unknown Z value to the point with known spatial coordinates; R^2 , smoothing parameter.

Kriging. The advantage of such method is the use of statistical models, which, among other things, allow making a forecast with an assessment of its accuracy. An important factor influencing the correlation coefficient is the distance between the initial points.

Z coordinate for a point added to the mathematical surface is determined from the formula

$$\hat{Z}_0 = \sum_{i=1}^n \lambda_i Z_i,$$

where n weights of λ_i is the solution of the kriging system

$$\sum_{i=1}^n \lambda_i C_{ij} = C_{oj}, \quad j = 1, \dots, n.$$

The choice of spatial interpolation methods is determined by national and foreign experience of using them to construct digital elevation models and quasigeoids. In addition, the developers of the Surfer software indicate such methods for construction of digital elevation models.

Discussion of results

Construction of a local quasigeoid model of an area project. After the stage of model construction was completed, a comparison of methods was made on the basis of analysing the RMSE values of spatial interpolation and the RMSE of determining the height anomalies by control points (Table 2). It should be noted that the Gauss formula was used to calculate the RMSE of determining the height anomaly by control points. In the analytical examination of the assessment of the accuracy of constructions, the following features are highlighted:

- the least value of the interpolation RMSE was attained using the methods of triangulation with linear interpolation (0.003 m) and kriging (0.003 m);
- the least RMSE value for determining the heights by control points was obtained using the natural neighbour (0.004 m) and kriging (0.004 m) methods.

Table 2

Assessment of the accuracy of constructing a local quasigeoid model of an area project

Method	Number of points to create a model	Number of test points	RMSE of interpolation, m	RMSE of determining height anomalies from control points, m
Triangulation with linear interpretation	268	30	0.003	0.008
Minimum curvature	269	30	0.010	0.006
Nearest neighbour	265	30	0.014	0.006
Natural neighbour	265	30	0.007	0.004
Radial basis function (cubic spline)	263	30	0.007	0.006
Kriging	270	30	0.003	0.004

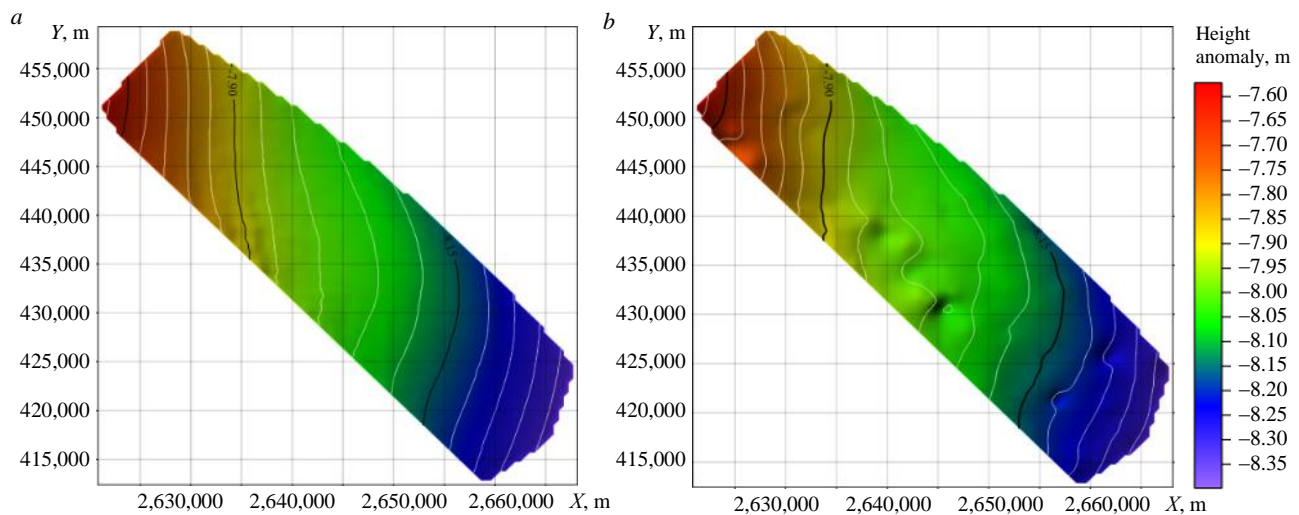


Fig.2. Local quasigeoid model constructed by triangulation methods with linear interpolation (a); kriging (b)

Figure 2 shows the results of constructing local quasigeoid models a using triangulation with linear interpolation and kriging methods.

Construction of a local quasigeoid model of a linear project. To construct the model, data on geodetic and normal heights of points lying along the projected route were used. Similar constructions were made (Table 3). The least RMSE value for determining the heights from the model was obtained by kriging (0.006 m) and triangulation with linear interpolation (0.006 m). When assessing the accuracy of constructing a model based on control points, the least RMSE value for determining the heights was obtained using the kriging method (0.007 m). The kriging method on the estimated parameters is preferable for both projects. When determining the optimal number of initial points required constructing a local quasigeoid model, the points were equidistant from each other. Spacing between the neighbouring points was 5-6 km, and they lay on the same line. To assess the required number of points, it was decided to successively exclude the initial points and assess the accuracy of constructing the model based on control points. To build a model of 27 points, it was decided to leave 10 points, provided that they were uniformly distributed. The model was built using the kriging method, the RMSE of determining the heights of the model using the Gauss formula was 4 mm. The RMSE of building the model by this method was 7 mm. With further exclusion of points and building the model (with a 10 km spacing between points), the RMSE was 26 cm, which does not satisfy the required accuracy of construction. Thus, when designing the required number of points in a given area, the recommended spacing between the combined points is 5 km.

Table 3

Assessment of the accuracy of constructing a local quasigeoid model of a linear project

Method	Number of points to create a model	Number of test points	RMSE of interpolation, m	RMSE of determining height from control points, m
Triangulation with linear interpolation	27	10	0.006	0.009
Minimum curvature	28	9	0.01	0.009
Nearest neighbour	27	9	0.021	0.016
Natural neighbour	26	9	0.011	0.008
Radial basis function (cubic spline)	26	10	0.015	0.009
Kriging	28	10	0.006	0.007

Construction of DEM based on airborne laser scanning results. Subdivision of areas into fragments. Classified airborne laser scanning data were divided into fragments measuring 1,000×1,000 m. After this, the fragments that best characterize each plot were selected based on inclination angle and visual assessment.

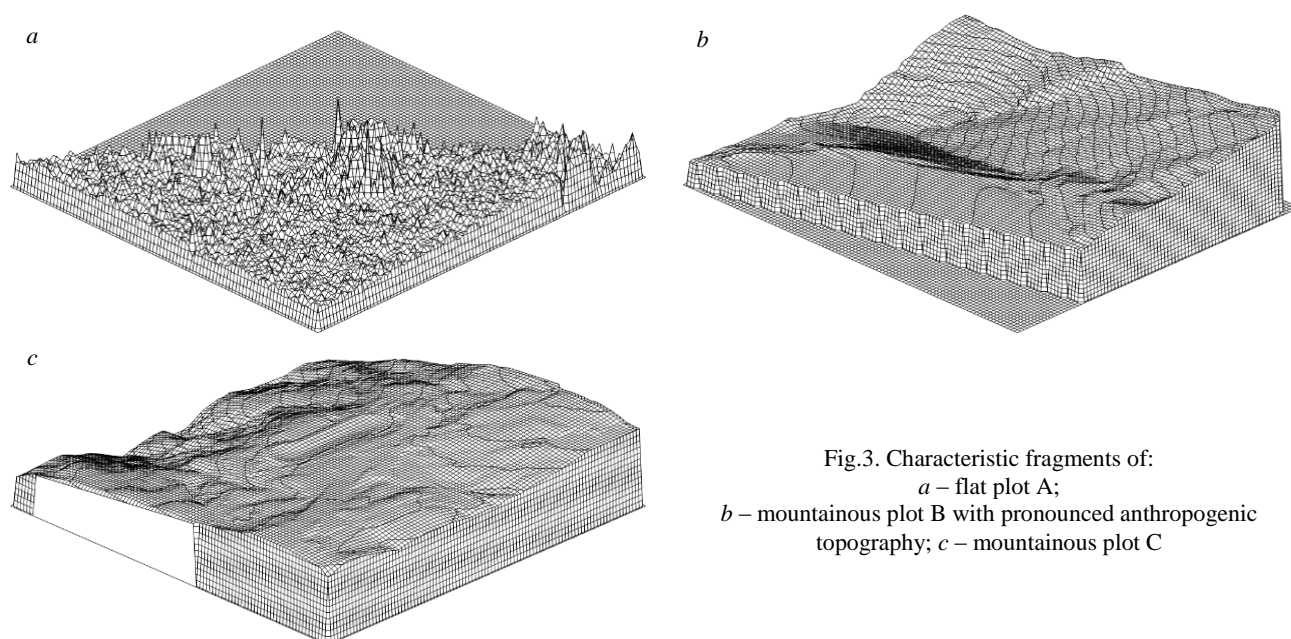


Fig.3. Characteristic fragments of:
a – flat plot A;
b – mountainous plot B with pronounced anthropogenic topography; c – mountainous plot C

Assessment of the accuracy of constructed models based on characteristic fragments using different spatial interpolation methods. To evaluate the accuracy, DEM were constructed using six spatial interpolation methods in the Surfer software. In total, 180 DEM were used, 60 models for each of three plots (Fig.3). This approach increases the speed of DEM construction for the entire project, since in the analysis of spatial interpolation methods on one characteristic fragment out of N fragments, the time for assessing the accuracy of model construction by the above methods decreases N fold provided that the hypothesis is true.

To analyse the spatial interpolation methods for accuracy, the deviation of a point on the earth's surface was calculated (two data sets), which can be considered as redundant measurements, since they were not involved in building digital elevation models. The choice of parameters “Percentage of points deviating by more than 0.33 m”, “Percentage of points deviating by more than 1 m” is determined by the adopted contour interval for plots with flat topography. The first parameter is the percentage of points with deviation from the constructed surface exceeding 1/3 of contour interval; the second parameter is with deviation from the constructed topographic surface of at least the contour interval. Contour interval for the flat fragment *a* and plot A is taken to be 1 m (Table 4). Thus, the least value of parameters “RMSE of height determination” and “Percentage of points deviating by more than 0.33 m” was obtained using the methods of natural neighbour (0.06 m, 1.13 %), triangulation with linear interpolation (0.07 m, 1.50 %), and ordinary kriging with Power variogram (0.07 m, 1.82 %).

Table 4

Assessment of the accuracy of constructed models on flat fragment *a*

Method	Parameters	RMSE of height determination, m	Percentage of points deviating by more than 0.33 m	Percentage of points deviating by more than 1 m
Natural neighbour	Standard	0.06	1.13	0.00
Triangulation with linear interpolation	Standard	0.07	1.50	0.00
Kriging	Ordinary type Power variogram	0.07	1.82	0.04
Minimum curvature	Internal Tension: 0.75 Boundary Tension: 0.75	0.07	1.95	0.02
Radial basis function	Multilog function	0.07	2.18	0.05
Nearest neighbour	Standard	0.09	2.58	0.08



DEM was constructed for a mountainous fragment with a pronounced anthropogenic factor. The choice of parameters “Percentage of points deviating by more than 1.66 m”, “Percentage of points deviating by more than 5 m” is due to the adopted contour interval for the mountainous plot with anthropogenic topography. The first parameter is the percentage of points with deviation from the constructed surface exceeding 1/3 of contour interval; the second parameter is with deviation from the constructed DEM of at least the contour interval. In the study, the contour interval for the mountainous plot with anthropogenic topography is assumed to be 5 m (Table 5).

Table 5

Assessment of the accuracy of constructed DEM on a mountainous fragment with anthropogenic topography *b*

Method	Parameters	RMSE of height determination, m	Percentage of points deviating by more than 1.66 m	Percentage of points deviating by more than 5 m
Natural neighbour	Standard	0.88	14.24	1.59
Kriging	Quadric type Variogram for Gaussian (normal) distribution	0.89	15.21	1.64
Triangulation with linear interpolation	Standard	0.94	15.31	2.12
Radial basis function	Multiquadric function	0.92	16.06	1.92
Nearest neighbour	Standard	0.95	16.13	1.81
Minimum curvature	Internal Tension: 0.75 Boundary Tension: 0.75	1.21	22.60	3.20

The least values of the RMSE and the parameter “Percentage of points deviating by more than 1.66 m” were obtained using the natural neighbour method (0.88 m, 14.24 %), quadric kriging with a variogram component according to the Gaussian (normal) distribution (0.89 m, 15.21 %), and triangulation with linear interpolation (0.94 m, 15.31 %).

DEM was constructed on a mountainous plot. The choice of parameters “Percentage of points deviating by more than 1.66 m”, “Percentage of points deviating by more than 5 m” is due to the adopted contour interval for the mountainous plot and is similar to fragment *b*. The accuracy assessment results for the mountainous fragment *c* are given in Table 6.

Table 6

Assessment of the accuracy of constructed digital models on mountainous fragment *c*

Method	Parameters	RMSE of height determination, m	Percentage of points deviating by more than 1.66 m	Percentage of points deviating by more than 5 m
Kriging	Quadric type Variogram with a spherical component	0.30	1.04	0.00
Natural neighbour	Standard	0.31	1.28	0.00
Radial basis function	Multiquadric function	0.32	1.29	0.00
Minimum curvature	Internal Tension: 0.75 Boundary Tension: 0.75	0.39	1.34	0.00
Nearest neighbour	Standard	0.35	1.47	0.00
Triangulation with linear interpolation	Standard	0.33	1.74	0.18

Based on a comprehensive assessment of the RMSE parameters for determining the height and parameter “Percentage of points deviating by more than 1.66 m”, it is possible to distinguish the quadric kriging method with a spherical component of variogram (0.30 m, 1.04 %).

Checking the accuracy of DEM constructed using spatial interpolation methods for the entire project. Construction and accuracy assessment of digital elevation models created for the entire area of plots A, B and C were accomplished. Thus, the results obtained at the previous stage are aimed at getting

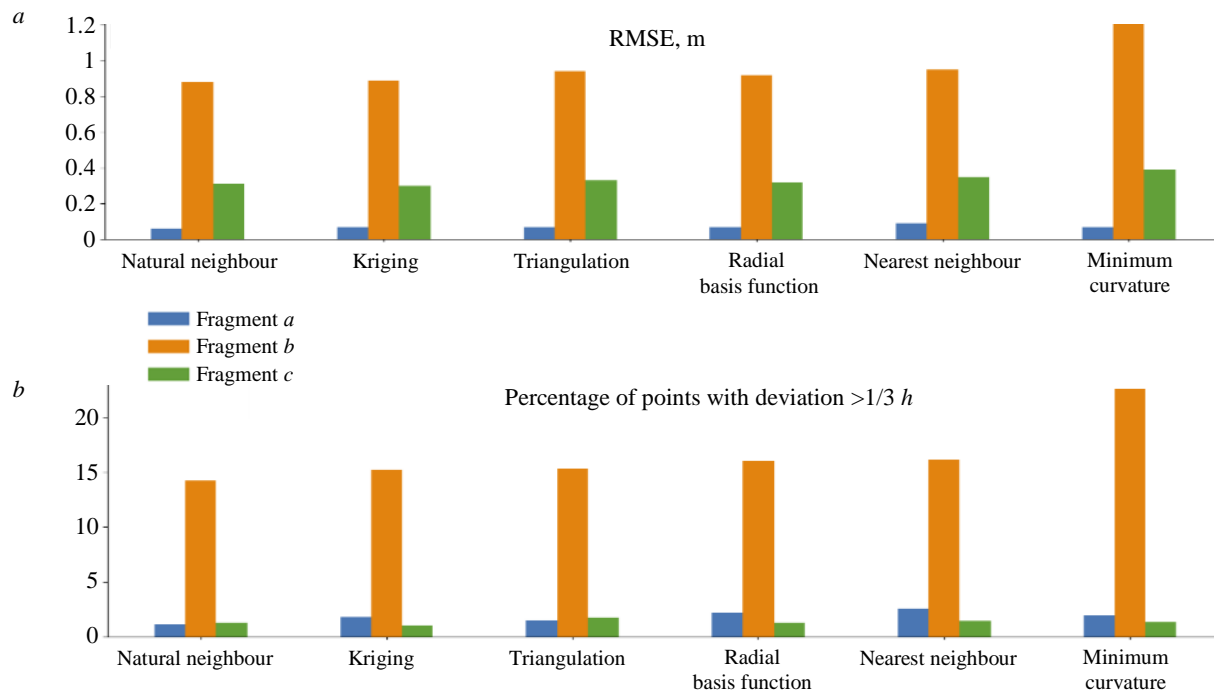


Fig.4. Assessment of the accuracy of methods for constructing DEM on the assigned fragments

a preliminary idea of the accuracy of DEM produced for each plot of the earth's surface, since differences in topography types clearly indicate the need to use a differentiated approach. Histogram with estimated parameters for fragments *a*, *b* and *c* is shown in Fig.4. A comprehensive assessment of the accuracy of constructed models for plots A, B and C is given in Table 7.

Table 7

Assessment of the accuracy of digital elevation models

Method	RMSE of height determination, m	Number of points	Percentage of points deviating by more than $1/3 h$ (m)	Percentage of points deviating by more than h (m)
Flat plot A				
Natural neighbour	0.11	53,288,238	5.84	0.84
Kriging	0.12	53,288,238	6.78	1.06
Triangulation with linear interpolation	0.12	53,288,238	6.93	1.09
Mountainous plot B with anthropogenic topography				
Kriging	0.55	4,556,172	6.63	0.77
Natural neighbour	0.57	4,556,172	7.17	0.80
Radial basis function	0.57	4,556,172	7.08	0.95
Mountainous plot C				
Kriging	0.29	17,476,315	0.83	0.01
Natural neighbour	0.29	17,476,315	0.91	0.01
Radial basis function	0.29	17,476,315	0.94	0.01

Methods of spatial interpolation according to the considered plots should be noted:

- Natural neighbour for plot A. Consistent with assessment of the accuracy of the characteristic fragment.
- Quadric kriging with a variogram component according to the Gaussian (normal) distribution and a natural neighbour for plot B. Partially consistent with assessment of the accuracy of the characteristic fragment. Differences in the comprehensive assessment appeared to be negligible, since the natural neighbour method showed greater resistance to the formation of outliers in the topographic



surface. The kriging method slightly surpassed the natural neighbour method by other estimated parameters.

- Quadric kriging with a spherical variogram component for plot C. Consistent with a comprehensive assessment of the accuracy of the characteristic fragment.

Conclusion

In hard-to-reach regions, development or assessment of the integrity of the existing elevation datum is problematic. Creation of digital models will significantly reduce the production costs for repeated measurements of the investigated plots and search for the most productive solutions on choosing an algorithm for constructing a mathematical analogue with pre-assigned accuracy. Reducing the costs of constructing digital models will increase the availability of a single set of reliable geo-spatial information, which is used in designing, construction and further monitoring of buildings and engineering structures, in assessing the risk of landslides, flood monitoring and is the basis for research in Earth sciences based on background information.

Investigation of the accuracy of the local quasigeoid model showed:

- The least RMSE interpolation value for an area project was attained using triangulation with linear interpolation (0.003 m) and kriging (0.003 m). The least RMSE value for determining the heights by control points for an area project was obtained using the natural neighbour (0.004 m) and kriging (0.004 m) methods.

- The least RMSE for determining the heights from the model was shown by kriging (0.006 m) and triangulation with linear interpolation (0.006 m). When assessing the accuracy of constructing a model on control points, the least RMSE value for determining the heights was obtained using the kriging method (0.007 m).

- When constructing quasigeoid models, it is necessary to determine the number of starting points in the work area, which depends on anomaly of the region. When designing the required number of points in a given area, the recommended spacing between combined points is 5 km.

Investigation of DEM construction accuracy showed:

- Construction of a digital elevation model applying the natural neighbour method on flat plot A of the earth's surface led to the least aggregate value of the estimated parameters: RMSE, "Percentage of points deviating by more than 0.33 m", and "Percentage of points deviating by more than 5 m".

- For DEM construction on mountainous plot B on the earth's surface with pronounced anthropogenic topography, the authors proposed the quadric kriging method with a variogram component according to the Gaussian (normal) distribution.

- For mountainous plot C, the authors identified the quadric kriging method with a spherical variogram component based on the least values of the estimated parameters.

- The approach to assessing the accuracy of construction based on the characteristic flat and mountainous fragments turned out to be efficient, since it was confirmed when constructing a DEM for the entire flat and mountainous project site. This is due to similar morphometric characteristics. On the mountainous fragment with anthropogenic topography such approach requires additional control by two spatial interpolation methods that are close to the optimal one in terms of the estimated parameters, which is accounted for by areas with a marked change in surface curvature.

All spatial interpolation methods resulted in deviations above the permissible ones for topographic surfaces on flat, mountainous plots with anthropogenic topography, and mountainous plots of the earth's surface with the least percentage deviations of 5.84, 6.63, and 0.83 %, respectively.

REFERENCES

1. Ponomarenko M.R., Kutepov Yu.I., Shabarov A.N. Open pit mining monitoring support with information and analysis using web mapping technologies. *Mining Informational and Analytical Bulletin*. 2022. N 8, p. 56-70 (in Russian). DOI: [10.25018/0236_1493_2022_8_0_56](https://doi.org/10.25018/0236_1493_2022_8_0_56)
2. Raguzin I.I., Bykova E.N., Lepikhina O.Yu. Polygonal Metric Grid Method for Estimating the Cadastral Value of Land Plots. *Lomonosov Geography Journal*. 2023. Vol. 78. N 3, p. 92-103 (in Russian). DOI: [10.55959/MSU0579-9414.5.78.3.8](https://doi.org/10.55959/MSU0579-9414.5.78.3.8)



3. Bykova E., Skachkova M., Raguzin I. et al. Automation of Negative Infrastructural Externalities Assessment Methods to Determine the Cost of Land Resources Based on the Development of a “Thin Client” Model. *Sustainability*. 2022. Vol. 14. Iss. 15. N 9383. DOI: [10.3390/su14159383](https://doi.org/10.3390/su14159383)
4. Bazhin V.Yu., Masko O.N., Martynov S.A. Automatic burden balance monitoring and control in the production of metallurgical silicon. *Tsvetnyye metally*. 2023. N 4, p. 53-60 (in Russian). DOI: [10.17580/tsm.2023.04.07](https://doi.org/10.17580/tsm.2023.04.07)
5. Bazhin V.Yu., Masko O.N., Huy H. Nguyen. Increasing the speed of information transfer and operational decision-making in metallurgical industry through an industrial bot. *Non-ferrous Metals*. 2023. N 1, p. 62-67. DOI: [10.17580/nfm.2023.01.10](https://doi.org/10.17580/nfm.2023.01.10)
6. Gendler S.G., Kryukova M.S. Thermal management of metro lines, including double-track and single-track tunnels. *Mining Informational and Analytical Bulletin*. 2023. N 9-1, p. 248-269 (in Russian). DOI: [10.25018/0236_1493_2023_91_0_248](https://doi.org/10.25018/0236_1493_2023_91_0_248)
7. Karasev M.A., Posphehov G.B., Astapenko T.S., Shishkina V.S. Stress-strain behavior prediction models for weak manmade soil. *Mining Informational and Analytical Bulletin*. 2023. N 11, p. 49-69 (in Russian). DOI: [10.25018/0236_1493_2023_11_0_49](https://doi.org/10.25018/0236_1493_2023_11_0_49)
8. Kulchitskiy A.A., Mansurova O.K., Nikolaev M.Yu. Recognition of defects in hoisting ropes of metallurgical equipment by an optical method using neural networks. *Chernyye metally*. 2023. N 3, p. 81-88 (in Russian). DOI: [10.17580/chm.2023.03.13](https://doi.org/10.17580/chm.2023.03.13)
9. Petrov P.A., Shestakov A.K., Nikolaev M.Yu. Use of multifunctional crust breaker and machine vision system for acquisition and processing of aluminium reduction cell data. *Tsvetnyye metally*. 2023. N 4, p. 45-53 (in Russian). DOI: [10.17580/tsm.2023.04.06](https://doi.org/10.17580/tsm.2023.04.06)
10. Petrova T.A., Astapenko T.S., Kalahryuka A.A., Yesman M.M. Reducing the geo-environmental impact of halite waste storage. *Mining Informational and Analytical Bulletin*. 2022. N 10-1, p. 155-162. DOI: [10.25018/0236_1493_2022_101_0_155](https://doi.org/10.25018/0236_1493_2022_101_0_155)
11. Belikov A.A., Belyakov N.A. Method of predicting the stress-strain state of interchamber pillars lined with a compliant rope fastener. *Mining Informational and Analytical Bulletin*. 2023. N 4, p. 20-34 (in Russian). DOI: [10.25018/0236_1493_2023_4_0_20](https://doi.org/10.25018/0236_1493_2023_4_0_20)
12. Belyakov N.A., Belikov A.A. Prediction of the integrity of the water-protective stratum at the Verkhnekamskoye potash ore deposit. *Mining Informational and Analytical Bulletin*. 2022. N 6-2, p. 33-46 (in Russian). DOI: [10.25018/0236_1493_2022_62_0_33](https://doi.org/10.25018/0236_1493_2022_62_0_33)
13. Huxiong Li, Weiya Ye, Jun Liu et al. High-Resolution Terrain Modeling Using Airborne LiDAR Data with Transfer Learning. *Remote Sensing*. 2021. Vol. 13. Iss. 17. N 3448. DOI: [10.3390/rs13173448](https://doi.org/10.3390/rs13173448)
14. Hashemi-Beni L., Jones J., Thompson G. et al. Challenges and Opportunities for UAV-Based Digital Elevation Model Generation for Flood-Risk Management: A Case of Princeville, North Carolina. *Sensors*. 2018. Vol. 18. Iss. 11. N 3843. DOI: [10.3390/s18113843](https://doi.org/10.3390/s18113843)
15. Gusev V.N., Blishchenko A.A., Sannikova A.P. Study of a set of factors influencing the error of surveying mine facilities using a geodetic quadcopter. *Journal of Mining Institute*. 2022. Vol. 254, p. 173-179. DOI: [10.31897/PMI.2022.35](https://doi.org/10.31897/PMI.2022.35)
16. Kremcheev E.A., Danilov A.S., Smirnov Yu.D. Metrological Support of Monitoring Systems Based on Unmanned Aerial Vehicles. *Journal of Mining Institute*. 2019. Vol. 235, p. 96-105. DOI: [10.31897/PMI.2019.1.96](https://doi.org/10.31897/PMI.2019.1.96)
17. Menshikov S.N., Dzhajabov A.A., Vasilev G.G. et al. Spatial Models Developed Using Laser Scanning at Gas Condensate Fields in the Northern Construction-Climatic Zone. *Journal of Mining Institute*. 2019. Vol. 238, p. 430-437. DOI: [10.31897/PMI.2019.4.430](https://doi.org/10.31897/PMI.2019.4.430)
18. Luethje F., Tiede D., Eisank C. Terrain Extraction in Built-Up Areas from Satellite Stereo-Imagery-Derived Surface Models: A Stratified Object-Based Approach. *ISPRS International Journal of Geo-Information*. 2017. Vol. 6. Iss. 1. N 9. DOI: [10.3390/ijgi6010009](https://doi.org/10.3390/ijgi6010009)
19. Das R.K., Samanta S., Jana S.K., Rosa R. Polynomial interpolation methods in development of local geoid model. *The Egyptian Journal of Remote Sensing and Space Science*. 2018. Vol. 21. Iss. 3, p. 265-271. DOI: [10.1016/j.ejrs.2017.03.002](https://doi.org/10.1016/j.ejrs.2017.03.002)
20. Ahmed H.M., Mohamed E.A., Bahaa S.A. Evaluating two numerical methods for developing a local geoid model and a local digital elevation model for the Red Sea Coast, Egypt. *Journal of King Saud University – Engineering Sciences*. 2023. Vol. 35. Iss. 6, p. 384-392. DOI: [10.1016/j.jksues.2021.04.004](https://doi.org/10.1016/j.jksues.2021.04.004)
21. Banasik P., Bujakowski K. The Use of Quasigeoid in Leveling Through Terrain Obstacles. *Reports on Geodesy and Geoinformatics*. 2017. Vol. 104. Iss. 1, p. 57-64. DOI: [10.1515/rgg-2017-0015](https://doi.org/10.1515/rgg-2017-0015)
22. Borowski Ł., Banaś M. The Best Robust Estimation Method to Determine Local Surface. *Baltic Journal of Modern Computing*. 2019. Vol. 7. N 4, p. 525-540. DOI: [10.22364/bjmc.2019.7.4.06](https://doi.org/10.22364/bjmc.2019.7.4.06)
23. Habib M., Alzubi Y., Malkawi A., Awwad M. Impact of interpolation techniques on the accuracy of large-scale digital elevation model. *Open Geosciences*. 2020. Vol. 12. Iss. 1, p. 190-202. DOI: [10.1515/geo-2020-0012](https://doi.org/10.1515/geo-2020-0012)
24. Amodio A.M., Aucelli P.P.C., Garfi V., Rosskopf C.M. Digital photogrammetric analysis approaches for the realization of detailed terrain models. *Rendiconti Online della Società Geologica Italiana*. 2020. Vol. 52, p. 69-75. DOI: [10.3301/ROL.2020.21](https://doi.org/10.3301/ROL.2020.21)
25. Bui L.K., Glennie C.L., Hartzell P.J. Rigorous Propagation of LiDAR Point Cloud Uncertainties to Spatially Regular Grids by a TIN Linear Interpolation. *IEEE Geoscience and Remote Sensing Letters*. 2022. Vol. 19. N 7003105. DOI: [10.1109/LGRS.2021.3134587](https://doi.org/10.1109/LGRS.2021.3134587)
26. Boreggio M., Bernard M., Gregoretti C. Evaluating the Differences of Gridding Techniques for Digital Elevation Models Generation and Their Influence on the Modeling of Stony Debris Flows Routing: A Case Study From Rovina di Cancia Basin (North-Eastern Italian Alps). *Frontiers in Earth Science*. 2018. Vol. 6. N 89. DOI: [10.3389/feart.2018.00089](https://doi.org/10.3389/feart.2018.00089)
27. Fazilova D., Magdiiev H. Comparative Study of Interpolation Methods in Development of Local Geoid. *International Journal of Geoinformatics*. 2018. Vol. 14. N 1, p. 29-33.
28. Banasik P., Bujakowski K., Kudrys J. et al. Development of a precise local quasigeoid model for the city of Krakow – QuasigeoidKR2019. *Reports on Geodesy and Geoinformatics*. 2020. Vol. 109. Iss. 1, p. 25-31. DOI: [10.2478/rgg-2020-0004](https://doi.org/10.2478/rgg-2020-0004)
29. Mysen E. On the uncertainty of height anomaly differences predicted by least-squares collocation. *Journal of Geodetic Science*. 2020. Vol. 10. Iss. 1, p. 53-61. DOI: [10.1515/jogs-2020-0111](https://doi.org/10.1515/jogs-2020-0111)
30. Hosseini-Asl M., Amiri-Simkooei A.R., Safari A. Establishment of a corrective geoid surface by spline approximation of Iranian GNSS/levelling network. *Measurement*. 2022. Vol. 197. N 111341. DOI: [10.1016/j.measurement.2022.111341](https://doi.org/10.1016/j.measurement.2022.111341)
31. Medved K., Kuhar M., Koler B. Regional gravimetric survey of central Slovenia. *Measurement*. 2019. Vol. 136, p. 395-404. DOI: [10.1016/j.measurement.2018.12.065](https://doi.org/10.1016/j.measurement.2018.12.065)



32. Chymyrov A. Comparison of different DEMs for hydrological studies in the mountainous areas. *The Egyptian Journal of Remote Sensing and Space Science*. 2021. Vol. 24. Iss. 3. Part 2, p. 587-594. DOI: [10.1016/j.ejrs.2021.08.001](https://doi.org/10.1016/j.ejrs.2021.08.001)
33. Mahbuby H., Safari A., Foroughi I. Local gravity field modeling using spherical radial basis functions and a genetic algorithm. *Comptes Rendus Geoscience*. 2017. Vol. 349. N 3, p. 106-113. DOI: [10.1016/j.crte.2017.03.001](https://doi.org/10.1016/j.crte.2017.03.001)
34. Belay E.Y., Godah W., Szelachowska M., Tenzer R. ETH-GQS: An estimation of geoid-to-quasigeoid separation over Ethiopia. *Geodesy and Geodynamics*. 2022. Vol. 13. Iss. 1, p. 31-37. DOI: [10.1016/j.geog.2021.09.006](https://doi.org/10.1016/j.geog.2021.09.006)
35. Qingwang Liu, Liyong Fu, Qiao Chen et al. Analysis of the Spatial Differences in Canopy Height Models from UAV LiDAR and Photogrammetry. *Remote Sensing*. 2020. Vol. 12. Iss. 18. № 2884. DOI: [10.3390/rs12182884](https://doi.org/10.3390/rs12182884)
36. Mustafin M.G., Balandin V.N., Bryn M.Ja. et al. Topographic-geodetic and Cartographic Support of the Arctic Zone of the Russian Federation. *Journal of Mining Institute*. 2018. Vol. 232, p. 375-382. DOI: [10.31897/PMI.2018.4.375](https://doi.org/10.31897/PMI.2018.4.375)
37. Mustafin M.G., Valkov V.A., Kazantsev A.I. Monitoring of Deformation Processes in Buildings and Structures in Metropolises. *Procedia Engineering*. 2017. Vol. 189, p. 729-736. DOI: [10.1016/j.proeng.2017.05.115](https://doi.org/10.1016/j.proeng.2017.05.115)
38. Rusli N., Majid M.R., Nur Fakihin Auni A. Razali, Nur Fatma Fadilah Yaacob. Accuracy Assessment of DEM from UAV and TanDEM-X Imagery. 2019 IEEE 15th International Colloquium on Signal Processing & Its Applications, 8-9 March 2019, Penang, Malaysia. IEEE Xplore, 2019, p. 127-131. DOI: [10.1109/CSPA.2019.8696088](https://doi.org/10.1109/CSPA.2019.8696088)
39. Habib M. Evaluation of DEM interpolation techniques for characterizing terrain roughness. *Catena*. 2021. Vol. 198. N 105072. DOI: [10.1016/j.catena.2020.105072](https://doi.org/10.1016/j.catena.2020.105072)
40. Li L., Nearing M.A., Nichols M.H. et al. The effects of DEM interpolation on quantifying soil surface roughness using terrestrial LiDAR. *Soil and Tillage Research*. 2020. Vol. 198. N 104520. DOI: [10.1016/j.still.2019.104520](https://doi.org/10.1016/j.still.2019.104520)
41. Chuanfa Chen, Yixuan Bei, Yanyan Li, Weiwei Zhou. Effect of interpolation methods on quantifying terrain surface roughness under different data densities. *Geomorphology*. 2022. Vol. 417. N 108448. DOI: [10.1016/j.geomorph.2022.108448](https://doi.org/10.1016/j.geomorph.2022.108448)
42. Căteanu M., Ciubotaru A. Accuracy of Ground Surface Interpolation from Airborne Laser Scanning (ALS) Data in Dense Forest Cover. *ISPRS International Journal of Geo-Information*. 2020. Vol. 9. Iss. 4. N 224. DOI: [10.3390/ijgi9040224](https://doi.org/10.3390/ijgi9040224)
43. Tao Zhang, Xiaosu Xu, Shengbao Xu. Method of establishing an underwater digital elevation terrain based on kriging interpolation. *Measurement*. 2015. Vol. 63, p. 287-298. DOI: [10.1016/j.measurement.2014.12.025](https://doi.org/10.1016/j.measurement.2014.12.025)
44. Ikechukwu M.N., Ebinne E., Idorenyin U., Raphael N.I. Accuracy Assessment and Comparative Analysis of IDW, Spline and Kriging in Spatial Interpolation of Landform (Topography): An Experimental Study. *Journal of Geographic Information System*. 2017. Vol. 9. N 3, p. 354-371. DOI: [10.4236/jgis.2017.93022](https://doi.org/10.4236/jgis.2017.93022)
45. Pavlova A.I. Analysis of elevation interpolation methods for creating digital elevation models. *Optoelectronics, Instrumentation and Data Processing*. 2017. Vol. 53. N 2, p. 171-177. DOI: [10.3103/S8756699017020108](https://doi.org/10.3103/S8756699017020108)
46. Helwig Z.D., Guggenberger J., Elmore A.C., Uetrecht R. Development of a variogram procedure to identify spatial outliers using a supplemental digital elevation model. *Journal of Hydrology X*. 2019. Vol. 3. N 100029. DOI: [10.1016/j.hydroa.2019.100029](https://doi.org/10.1016/j.hydroa.2019.100029)
47. Arun P.V. A comparative analysis of different DEM interpolation methods. *The Egyptian Journal of Remote Sensing and Space Science*. 2013. Vol. 16. Iss. 2, p. 133-139. DOI: [10.1016/j.ejrs.2013.09.001](https://doi.org/10.1016/j.ejrs.2013.09.001)
48. Bui L.K., Glennie C.L. Estimation of lidar-based gridded DEM uncertainty with varying terrain roughness and point density. *ISPRS Open Journal of Photogrammetry and Remote Sensing*. 2023. Vol. 7. N 100028. DOI: [10.1016/j.ophoto.2022.100028](https://doi.org/10.1016/j.ophoto.2022.100028)
49. Agüera-Vega F., Agüera-Puntas M., Martínez-Carricondo P. et al. Effects of point cloud density, interpolation method and grid size on derived Digital Terrain Model accuracy at micro topography level. *International Journal of Remote Sensing*. 2020. Vol. 41. Iss. 21, p. 8281-8299. DOI: [10.1080/01431161.2020.1771788](https://doi.org/10.1080/01431161.2020.1771788)
50. McRoberts R.E., Domke G.M., Qi Chen et al. Using genetic algorithms to optimize k-Nearest Neighbors configurations for use with airborne laser scanning data. *Remote Sensing of Environment*. 2016. Vol. 184, p. 387-395. DOI: [10.1016/j.rse.2016.07.007](https://doi.org/10.1016/j.rse.2016.07.007)

Authors: **Mikhail Ya. Bryn**, Doctor of Engineering Sciences, Professor, <https://orcid.org/0000-0002-4722-9289> (Emperor Alexander I St. Petersburg State Transport University, Saint Petersburg, Russia), **Murat G. Mustafin**, Doctor of Engineering Sciences, Head of Department, <https://orcid.org/0000-0001-9416-2358> (Empress Catherine II Saint Petersburg Mining University, Saint Petersburg, Russia), **Dinara R. Bashirova**, Candidate of Engineering Sciences, Principal Discipline Engineer, <https://orcid.org/0000-0002-8005-6340> (AO "Gazprom Diagnostika", Saint Petersburg, Russia), **Bogdan Yu. Vasilev**, Candidate of Engineering Sciences, Leading Engineer, Vasilev_BYu2@pers.spmi.ru, <https://orcid.org/0000-0003-4119-4051> (Empress Catherine II Saint Petersburg Mining University, Saint Petersburg, Russia).

The authors declare no conflict of interests.



Investigation of the effectiveness of the use of various substances for dust suppression during the transshipment of granular sulfur

Viktoriya V. Lisai¹, Yurii D. Smirnov², Andrei V. Ivanov²✉, Gabriel Borowski³

¹ Stevedoring and Shipping Company Limited, Saint Petersburg, Russia

² Empress Catherine II Saint Petersburg Mining University, Saint Petersburg, Russia

³ Lublin University of Technology, Lublin, Poland

How to cite this article: Lisai V.V., Smirnov Yu.D., Ivanov A.V., Borowski G. Investigation of the effectiveness of the use of various substances for dust suppression during the transshipment of granular sulfur. Journal of Mining Institute. 2025. Vol. 271. N 16323, p. 108-119.

Abstract

The article is devoted to the problem of dusting during the transshipment of granular sulfur and existing methods of dust suppression. The analysis of various methods for reducing dust emission at granulated sulfur storage and transportation facilities is presented. The necessity of using special reagents to increase the efficiency of dust suppression and re-granulation of sulfur crushed by abrasion is noted. The sulfur dust obtained from the port terminal during the transshipment of technical sulfur was analyzed for granulometric composition. The results of experimental studies of the effectiveness of the use of various substances for sulfur dust suppression (alkyl polyglycosides, sodium silicate, starch) are presented. The laboratory installation was a hopper, inside which a test sample of dusty material was placed. The sample was subjected to an aerodynamic effect by an air flow at a given speed. The concentrations of suspended solids were measured with a dust meter-nephelometer with a sampling tube placed in the geometric center of the hopper. The effectiveness of dust suppression agents was determined based on a comparison of the concentration values obtained on dry and treated samples. For dust suppression at granulated sulfur treatment facilities, it is proposed to use a composition based on nonionic surfactants represented by a mixture of C12-14-alkylglycosides oligomers (1-1.5 %), additionally containing a mixture of amylose and amylopectin polysaccharides in the form of soluble starch (1-2.5 %) and water. The dust suppressor showed consistently high dust suppression efficiency both when measured immediately after irrigation (98.3 %) and after the expected time (99.7 %). The developed composition provides an increase in the dust-suppressing ability of the solution and the elimination of the possibility of repeated dusting due to the formation of a polymer film on the surface, as well as the regranulation of the product crushed by abrasion.

Keywords

sulfur; granular sulfur; dust; transportation; pouring; dust emission; dust suppression

Funding

The work was carried out within the framework of the State assignment of the Ministry of Science and Higher Education of the Russian Federation (FSRW-2024-0005).

Received: 03.10.2023

Accepted: 07.11.2024

Online: 02.12.2024

Published: 25.02.2025

Introduction

Sulfur is one of the main resources of the chemical industry and is extracted in large quantities as a by-product during the purification of oil and natural gas. Sulfur compounds present in significant amounts in hydrocarbon raw materials cause a wide range of negative consequences, for example, lead to a decrease in engine efficiency and corrosion of pipelines. To improve the quality of the product and reduce the risk of emergencies, desulfurization or removal of sulfur from the produced fuel is carried out [1-3]. Applications of sulfur are the production of mineral fertilizers (simple superphosphate, ammonium sulfate, ammonium-sodium sulfate, potassium sulfate, kalimagnesium, magnesium sulfate, nitrosulfate, sulfoammophos, etc.) [4, 5], sulfuric acid [6], oil production (dilution of drilling and oil solutions) [7], production of explosives [8]. Work on flowability modeling is in demand and requires the use of modern software [9-11].



Technical sulfur is produced in three commercial forms: liquid, block, and granular. Granular sulfur is especially common because of its properties and uniform granulometric composition [12]. Emissions and losses of sulfur are a factor in the deterioration of the components of the natural environment [13], the processes of storage, transportation and transshipment of granular sulfur are accompanied by intense dusting, which can negatively affect both the health of workers and the state of the environment. Currently existing measures to reduce dust emission show low efficiency [14, 15]. The clean water irrigation systems most often used in enterprises are simple and economical to implement [16], but have an efficiency of less than 50 % due to the strong hydrophobicity of dust and high surface tension of water [17].

To improve the wettability of solutions, research is being conducted on dust suppression technologies using surfactants, which are able to form an insulating layer between the surface of the solution and the air [18-20]. Surfactants are a class of chemicals whose concentration in solution is higher on the surface than in the volume of a liquid. This means that the surfactant concentrates on the surface where it should function, which makes it very economical to use, since in this way it is possible to preserve most of the properties of water and improve wetting at low cost. This phenomenon is known as adsorption and occurs at the liquid – solid, liquid – liquid and liquid – air interfaces [21].

At the micro level, the characteristics of dust suppression foam are closely related to morphology, which can be characterized by the size of foam droplets and their distribution. As a rule, smaller and more homogeneous foam bubbles are more suitable for dust suppression, since they allow for stable dust suppression [22]. In fact, when foam hits a dust source and captures its particles, the number, average size, distribution and uniformity of bubbles in a large area foam will greatly affect the effectiveness of dust suppression by foam. If the size of the foam bubbles is too large or their distribution is uneven, the dust suppression stability is low. The size of the bubbles and their distribution depend to a certain extent on the properties of the foaming agent solution system, such as viscosity, surface tension, etc. [23]. Thus, in order to improve the morphology of foam and increase the efficiency of dust suppression, it is possible to change the properties of solutions of foaming agents [24].

In addition to surfactants, various wetting reagents can be used to increase the efficiency of dust suppression, which are fatty alcohols with the addition of sodium hydroxide, calcium chloride, ethyl alcohol, bischofite, sodium chloride, and water [25]. However, most wetting reagents have such disadvantages – unsanitary and unhygienic properties, strong corrosive effects on equipment, complex preparation methods, high cost, uncertainty about human health effects and low biodegradability, therefore their use may be limited [26].

The article analyzes the scientific literature on existing and developing dust suppression formulations that could be used to reduce dusting during the transshipment of technical sulfur. One such means of dust suppression is a composition for coating elemental sulfur in order to protect against atmospheric exposure [27], which is a mixture of silicone and an aqueous solution of sodium silicate. The composition in question is prepared with a ratio of silicone and sodium silicate from 25:75 to 75:25 wt.% and may additionally contain a coloring additive. The composition may also differ in that the sodium silicate is in water. The composition has high heat and frost resistance, adheres well to sulfur, is resistant to penetration of water and sulfur bacteria, is fire-resistant and relatively inexpensive. Sodium silicate is a highly effective sealant. There is a low efficiency of dust suppression of previously settled dust, which, when blown up, becomes a source of secondary air pollution by dust.

The composition [28] is known, which is a mixture of polysaccharide and boric acid, which, when mixed, turn into a gel with the formation of a stable elastic crust when applied to the surface. The resulting coating increases the stability of the substrate and prevents the loss of solid particles, i.e. dust formation. The first main component of the stabilizing composition is a mixture containing from 0.5 to 5 % polysaccharide, for example, starch. As soon as the two components combine to form



a stabilizing compound, polysaccharide molecules, especially glucose molecules, begin to bind to borate at a controlled speed. This process, called complexation, forms weak covalent bonds comparable to weak cross-bonds in a polymer inside a polysaccharide matrix. The use of this composition may be limited, since boric acid has a negative impact on the environment and human health.

The use of polysaccharides as dust suppressants is also noted in the article [29] describing the use of a composition based on organic and rapidly decomposing substances with a ratio of the constituent components (water and a mixture of flax and starch) 98:2, which has a high adhesive ability.

There are known studies of compositions for suppressing dust formation using aqueous solutions of higher alkylglycosides [30-32]. Compositions of higher alkylglycosides are well-known materials with surface-active properties. Alkylglycosides are usually present in an aqueous solution to about 1 % by weight of an aqueous solution. With the help of such compositions, a long-lasting dust suppression effect is achieved. In addition, the composition is completely biodegradable and is not harmful to humans or the environment.

Alkylglycosides ($R-(O-C_6H_{10}O_5)_nH$) belong to the class of nonionic surfactants and are obtained from a reaction occurring in the presence of sulfonic acids and glucose at temperatures up to 140 °C or from butyl esters followed by interesterification. Nonionic surfactants are highly resistant to alkalis, acids and salts. Aqueous solutions of alkyl polyglycosides have the highest wetting ability compared to other surfactants and wetting agents [33].

Methods

The sulfur dust collected at the terminal for the transshipment of granular sulfur from railway wagons in a commercial seaport was studied. The granulometric composition of the dust under study was carried out using the HORIBA LA-950 particle size analyzer.

The effectiveness of reducing dust emission during irrigation of sulfur with various reagents was determined at a laboratory installation designed by St. Petersburg Mining University, which is a dust suppression hopper BPP 001 and a dust meter-nephelometer DustTrak 8533 (Fig.1).

The DustTrak DRX Model 8533 dust meter is a desktop analyzer with interchangeable impactors for measuring the mass concentration and fractional composition of dust in real time. This model of dust meter has an external pump that allows continuous monitoring of the concentration of suspended particles. The DustTrak dust analyzer measures the fractions PM₁₀, PM₄, PM_{2.5} and PM₁ set by the standards, as well as the total dust content simultaneously, by combining an optical meter



Fig.1. Laboratory dust suppression unit in the laboratory of the Mining University



and a nephelometer in one housing. The measurement range of the aerosol mass concentration is 0.1-150 mg/m³.

Before conducting the experiment in the dust suppression hopper, the main meteorological characteristics were measured using the MES-200A meteorometer: air temperature, relative humidity and air flow speed.

The method [34] for determining the effectiveness of dust suppression was implemented as follows:

1. For testing in BPP 001, the optimal weight of the suspension of the studied sulfur dust was determined – 15 g. Such a mass was selected by performing preparatory experiments taking into account the current aerodynamic conditions formed in the dust suppression hopper of dust concentrations and the measurement limits and errors of the dust meter.

2. Prior to testing with dusty samples, the dust suppression hopper was disassembled and vacuumed. The use of wet cleaning was limited in order to prevent changes in the formed experimental conditions, in particular, air humidity.

3. A compressor nozzle was installed and fixed in the front part of the hopper and the air supply was started. At the location of the dust samples at the bottom of the dust suppression hopper, the air speed was measured and adjusted. After setting the desired wind speed (in the ongoing work, the wind speed in the surface layer of the considered area of the Ust-Luga MTP is 7 m/s), the air blower nozzle was turned off.

4. The installation was completely assembled. A holder with an air intake tube was inserted into a special hole on the lid of the hopper, the opposite end of which was connected to the DustTrak 8533 dust meter. In order to prevent the accumulation of static electricity, the hopper was grounded with a special wire.

5. At the same time, the air supply to the hopper was turned on at a fixed speed and the measurement of dust concentrations was started using a dust meter. The duration of measurements in the work carried out was 2 min, which is due to the unevenness of the dust concentrations created at the point where the concentrations were recorded by the dust meter. As a result of this test, the background dust concentration was obtained before placing dusty samples in the hopper.

6. Next, all devices and grounding were disconnected, the air intake tube was dismantled, and the hopper was completely disassembled. An oval mold with an area of 110 cm² was placed at the bottom of the hopper in a specially marked place in the center. The test sample of sulfur dust was poured into a mold and evenly distributed over the surface using a spatula. Thus, an ellipse-shaped dust sample was formed at the bottom of the hopper.

7. The hopper was completely assembled in the same way as paragraph 4.

8. With the launch of the air blower and the dust meter-nephelometer, dust concentrations in the dust suppression hopper were measured. In addition to the background concentration, dust particles were thrown up from the surface of the sample placed at the bottom of the hopper. The duration of the measurements was 2 min.

9. The hopper was disassembled again and vacuumed. The remains of the analyzed dust sample were removed using a vacuum cleaner.

Discussion of the results

According to the obtained results of granulometric analysis on the HORIBA LA-950V2 device (Fig.2) it was found that the average size of dust particles collected at the sulfur processing unit is 101 microns. At the same time, the highest content in the sample (about 13 %) falls on particles with a diameter of 88 microns, and the proportion of particles of the dusty fraction (less than 10 microns), which is of the greatest interest, is about 0.2 %.

Based on the results of the analysis of scientific publications on the development of compositions for suppressing dust during the transshipment of bulk materials, the following chemicals were selected for research:

- a mixture of oligomers of C12-14-alkyl polyglycosides (APG);
- sodium silicic acid meta 5-aqueous Na₂SiO₃·5H₂O (sodium silicate);
- soluble starch (C₆H₁₀O₆)_n.

Aqueous solutions with three different concentrations wt.% were prepared with these substances:

- alkyl polyglycosides 0.5/1/1.5 %;
- sodium silicate 0.5/1/1.5 %;
- starch 1/2.5/5 %.

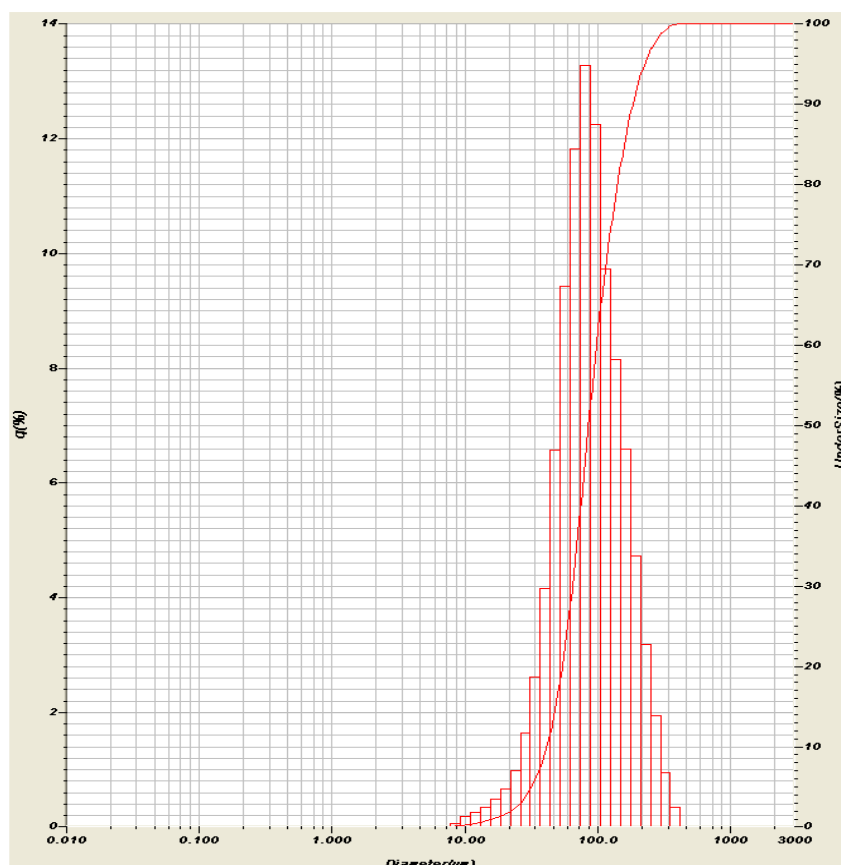


Fig.2. Histogram of the particle size distribution of dust taken at the enterprise

A visual experiment was conducted with the obtained aqueous solutions to determine the possibility of these substances to contribute to the granulation of sulfur dust particles to ensure the prevention of further dusting. Sulfur samples of 15 g were scattered on paper, the studied solutions were sprayed onto dust samples using a spray gun in an amount of about 3.6 g and mixed.

Photos of sulfur before irrigation, as well as after irrigation with clean water are shown in Fig.3 (1, 2).

Fig.3 (3-5, 9-11, 15-17) shows dust samples after irrigation with aqueous solutions of alkyl polyglycosides, sodium silicate, and starch. The observations show that nonionic surfactants and starch solution contribute to the greatest granulation of sulfur.

Fig.3 (6-8, 12-14, 18-20) shows the results of a visual experiment to determine the properties of granulation of the studied substances 1 h after irrigation. It can be seen that the granulation of sulfur particles under the influence of solutions of alkyl polyglycosides and starch decreases, but remains quite high compared with a solution of sodium silicate and pure water.

In addition to single-component aqueous solutions, binary compositions from mixtures of the substances in question were tested in the following ratios, wt.%:

- composition A – alkyl polyglycosides 1 %, sodium silicate 1 %;
- composition B – alkyl polyglycosides 1 %, starch 2.5 %;
- composition C – sodium silicate 1 %, starch 2.5 %.

The results are shown in Fig.3 (21-26). The greatest effect of granulation is shown by compositions A and B.

Tests were carried out in the dust suppression hopper to determine the effectiveness of irrigation of sulfur with water and various substances. Sulfur was treated with dust suppression agents by surface spraying with a spray gun. 1.8 g of water or an aqueous solution of a dust suppressor was applied to the dry sample. A series of three experiments was carried out with each reagent under consideration, in which the concentration of dust particles was measured instantly. In addition, three experiments were conducted with measuring the dust concentration after 20 min.

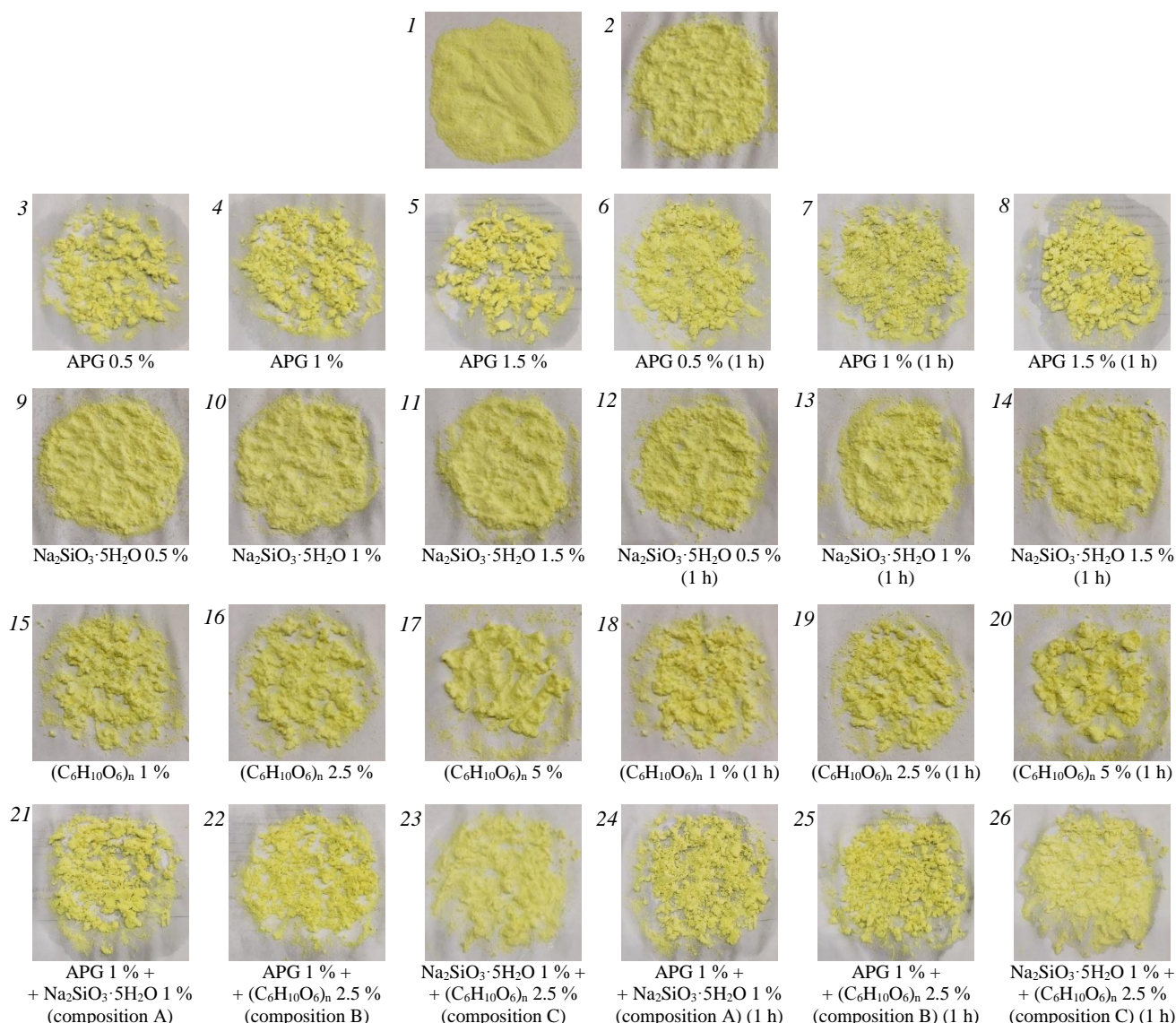


Fig.3. Visual determination of sulfur samples granulation: 1 – without dust suppression in air-dry condition; 2 – after water irrigation; 3 – when treated with an aqueous 0.5 % solution of alkyl polyglycosides; 4 – by 1 % solution; 5 – by 1.5 % solution; 6 – by 0.5 % solution after 1 h; 7 – by 1 % solution after 1 h; 8 – by 1.5 % solution after 1 h; 9 – when treated with an aqueous 0.5 % sodium silicate solution; 10 – by 1 % solution; 11 – by 1.5 % solution; 12 – by 0.5 % solution after 1 h; 13 – by 1 % solution after 1 h; 14 – by 1.5 % solution after 1 h; 15 – when treated with an aqueous 1 % starch solution; 16 – by 2.5 % solution; 17 – by 5 % solution; 18 – by 1 % solution after 1 h; 19 – by 2.5 % solution after 1 h; 20 – by 5 % solution after 1 h; 21 – when treated with a water-based formulation containing 1 % alkyl polyglycosides and 1 % sodium silicate (composition A); 22 – composition with 1 % alkyl polyglycosides and 2.5 % starch (composition B); 23 – composition with 1 % sodium silicate and 2.5 % starch (composition C); 24 – by composition A after 1 h; 25 – by composition B after 1 h; 26 – by composition C after 1 h

Tests in the dust suppression hopper were carried out with aqueous solutions of the following concentrations, wt. %: alkyl polyglycosides – 1 %, sodium silicate – 1 %, starch – 2.5 %, compositions A, B, and C.

The effectiveness of reducing dust emission was estimated by the formula:

$$\eta = \frac{\sum_{i=1}^n \left(1 - \frac{C_{li}}{C_{0i}} \right)}{n},$$

where C_{0i} – concentration without dust suppression, mg/m^3 ; C_{li} – concentration when using dust suppression agents, mg/m^3 ; n – number of measurements.

Graphs of the dependence of dust concentrations on time are shown in Fig.4. The results of calculating the dust suppression efficiency are presented in Table 1.

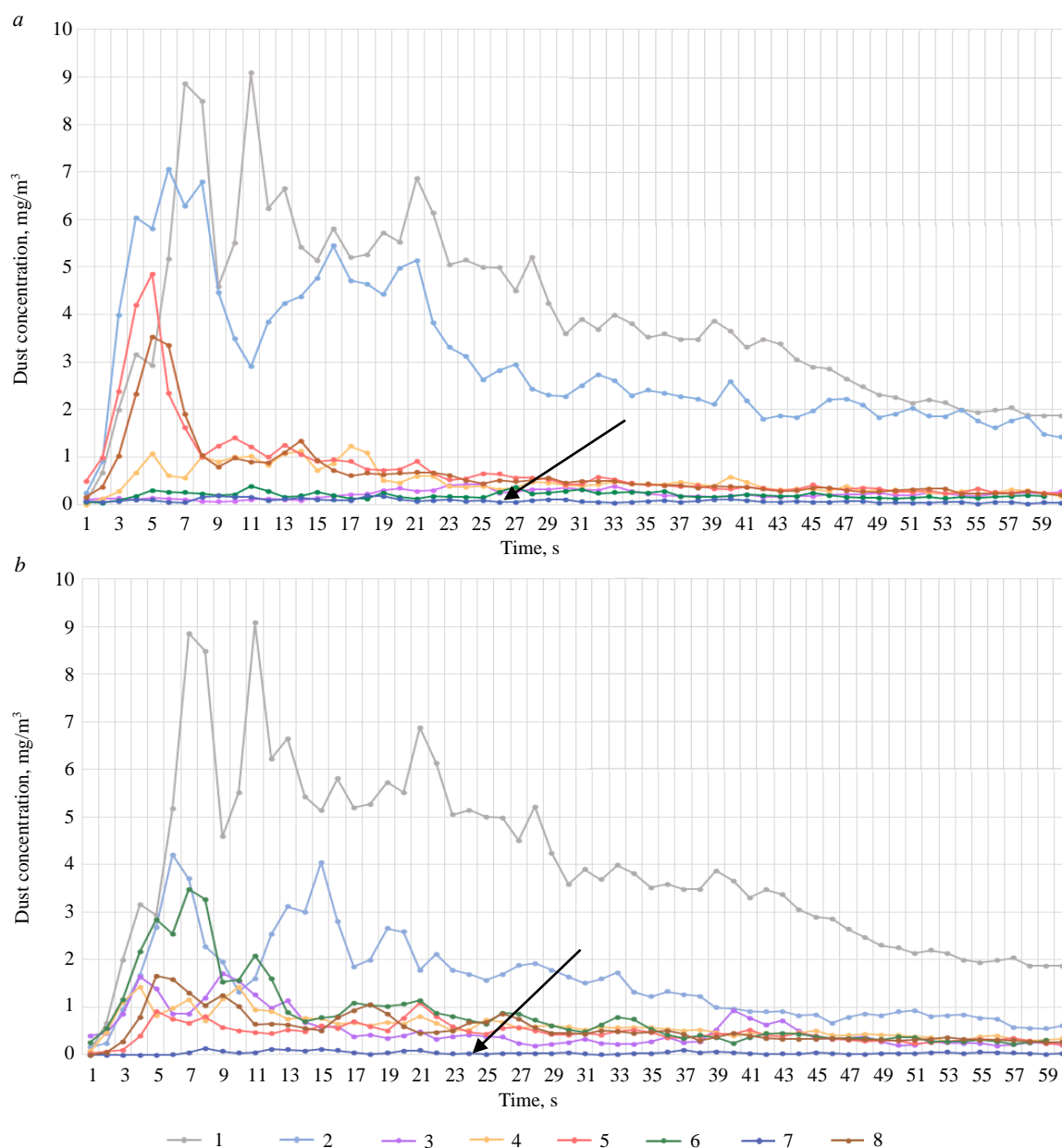


Fig.4. Graph of the dependence of the total concentration of dust particles on time during instantaneous measurement (a) and 20 min later (b) after irrigation of sulfur with water and other substances

1 – without dust suppression; 2 – water; 3 – alkyl polyglycosides;
4 – sodium silicate; 5 – starch; 6 – composition A; 7 – composition B; 8 – composition C

Table 1

The results of measuring the dust concentration using various means of dust suppression

Dust suppression agent	Average concentration at a time, mg/m ³				Air temperature, °C	Air humidity, %	Average dust suppression efficiency, %
	10 s	30 s	75 s	120 s			
Without dust suppression	9.085	3.594	1.409	0.557	18.1	29	–
Water	3.487	2.273	1.226	0.471	17.9	31	30.5
Water after 20 min	1.322	1.648	0.529	0.124	18.4	33	64.4
Alkyl polyglycosides	0.075	0.357	0.198	0.124	18.0	28	87.4
Alkyl polyglycosides after 20 min	1.548	0.268	0.148	0.083	17.7	25	86.2
Sodium silicate	0.999	0.999	0.213	0.099	18.0	28	86.2
Sodium silicate after 20 min	1.432	0.590	0.217	0.077	18.4	28	83.6
Starch	1.402	0.420	0.206	0.061	17.5	26	83.9



End of Table 1

Dust suppression agent	Average concentration at a time, mg/m ³				Air temperature, °C	Air humidity, %	Average dust suppression efficiency, %
	10 s	30 s	75 s	120 s			
Starch after 20 min	0.515	0.425	0.142	0.059	17.5	26	87.3
Composition A	0.207	0.282	0.087	0.029	18.0	28	93.2
Composition A after 20 min	1.575	0.525	0.196	0.083	18.0	28	82.6
Composition B	0.165	0.100	0.021	0.023	17.5	28	97.5
Composition B after 20 min	0.039	0.044	0.013	0.006	17.5	28	98.9
Composition C	0.979	0.457	0.196	0.062	17.7	33	85.0
Composition C after 20 min	1.024	0.452	0.149	0.061	17.7	33	86.6

The results show that composition B, which is a mixture of alkyl polyglycosides and starch, is the most effective. The dust suppression efficiency is 97.5 % with instantaneous measurement and reaches 98.9 % after 20 min, which indicates a decrease in the possibility of repeated dusting of the material.

To clarify the concentrations of the components of the developed composition, additional experiments were conducted to evaluate the effectiveness of dust suppression of a composition based on nonionic surfactants and starch with the following component ratios, wt.%:

- composition 1 – alkyl polyglycosides 0.5 %, starch 2.5 %;
- composition 2 – alkyl polyglycosides 1.5 %, starch 1 %;
- composition 3 – alkyl polyglycosides 1.5 %, starch 2.5 %;
- composition 4 – alkyl polyglycosides 0.5 %, starch 1 %;
- composition 5 – alkyl polyglycosides 1 %, starch 1 %;
- composition 6 – alkyl polyglycosides 1 %, starch 2.5 %.

The use of starch in a concentration of 5 % was excluded based on the results of a visual experiment for determining granulation due to the high content of the substance in question and the possibility of its negative effect on the physico-chemical properties of the product.

Dust concentrations were measured for all experiments at a temperature of 19.6 °C and an air humidity of 41 %. The results of calculating the efficiency of dust suppression using different compositions of alkyl polyglycosides and starch are presented in Table 2. Graphs of the dependence of sulfur dust concentrations on time are shown in Fig.5.

The experiments show that the proposed composition achieves the highest efficiency of sulfur dust suppression with the following content of components in an aqueous solution: a mixture of C12-14-alkyl polyglycosides oligomers – 1-1.5; soluble starch – 1-2.5 wt.%.

Table 2

The results of measuring the dust concentration using different compositions of alkyl polyglycosides and starch

Dust suppression agent	Average concentration at a time, mg/m ³				Average dust suppression efficiency, %	Efficiency compared to water, %
	10 s	30 s	75 s	120 s		
Composition 1	2.211	1.212	0.383	0.131	86.5	68.2
Composition 1 after 20 min	0.142	0.045	0.023	0.012	97.1	96.8
Composition 2	0.056	0.021	0.024	0.004	98.1	97.2
Composition 2 after 20 min	0.124	0.019	0.013	0.009	99.7	96.1
Composition 3	0.019	0.023	0.002	0.003	98.3	98.6
Composition 3 after 20 min	0.008	0.013	0.001	0.005	99.7	99.3
Composition 4	2.707	1.290	0.436	0.165	66.3	56.5
Composition 4 after 20 min	2.219	1.492	0.380	0.177	63.2	38.2
Composition 5	0.385	0.366	0.184	0.029	88.3	86.7
Composition 5 after 20 min	1.353	0.651	0.288	0.062	81.5	64.8
Composition 6	0.165	0.100	0.021	0.023	97.1	97.2
Composition 6 after 20 min	0.039	0.044	0.013	0.006	98.9	97.1

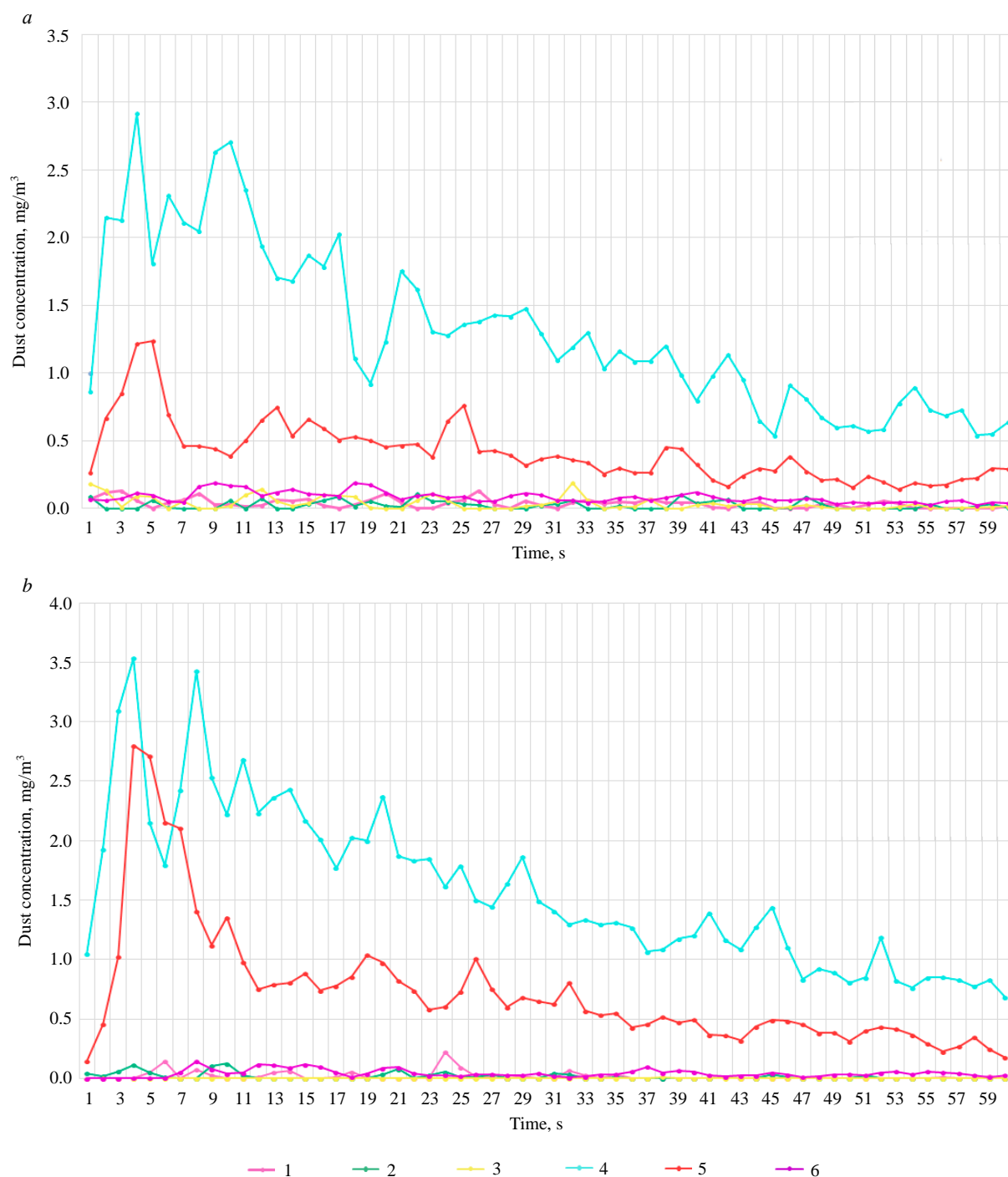


Fig.5. Graphs of the dependence of the total concentration of dust particles on time during instantaneous measurement (a) and 20 min (b) after irrigation of sulfur with the tested compounds 1-6

The proposed composition can be used in existing water aerosol dust suppression systems at sulfur transportation facilities. In seaports and railway terminals, the first transshipment operation is the transshipment of sulfur from a gondola car to a conveyor belt by means of a car dump device located in an isolated room. As a rule, at this stage of transshipment, the first stage of the dust suppression system is implemented – a network of nozzles oriented to the pouring front. Repeated dust suppression (subsequent stages) is carried out by nozzle networks in closed transfer hoppers between conveyor sections. The operation of such a system using the proposed composition will allow granulation to reduce dust emission during all further sulfur transshipment operations, this is provided in two ways:



humidification, coagulation, precipitation of blown sulfur dust in the air and humidification of the surface of the transported sulfur containing dusty fractions. The proposed composition can be used for spraying with different types of nozzles, and the conditions created in the BPP 001 dust suppression hopper are similar to those created in isolated rooms and closed overflow hoppers.

Conclusion

An experimental assessment of the effectiveness of various dust suppression methods conducted in the laboratories of Saint Petersburg Mining University has allowed to establish that the use of clean water as a working medium for the dust suppression process at granulated sulfur treatment facilities really shows low efficiency (30.5 %), which can lead to contamination of territories with sulfur dust formed as a result of transshipment.

As is known, sulfur is hydrophobic, i.e. it is not wetted with water. Surfactant molecules, having a diphilic nature, are adsorbed on the water – sulfur interface, which leads to a decrease in the surface tension of water. Nonionic surfactants, represented by alkyl polyglucosides, added to water to increase the wettability of the processed material, are characterized not only by high efficiency, but also by good biodegradability. Alkyl polyglycosides are characterized by the highest emulsifying ability among industrial surfactants, which effectively reduces their consumption when used as a working medium for dust suppression [35, 36].

Polysaccharides are one of the most affordable and cheap resources, whose reserves are continuously replenished due to photosynthesis in plants. Starch is a high molecular weight organic compound represented by a mixture of amylose and amylopectin. Starch macromolecules are elongated and branched chains consisting of D-glucose residues in amylosis, interconnected by glycoside bonds. In addition to carbohydrates, starch contains a certain amount of fatty acids, which determine its ability to form a number of esters and ethers [37].

Starch hydrogels (paste) are widely used in various industries. There are known studies [38] confirming the ability of amylose in starch to form non-stoichiometric compounds with alcohols and other hydrocarbons. The reason for the steady thickening and increase in viscosity of starch hydrogels is the formation of complexes between starch amylose and highly mobile surfactant molecules.

For dust suppression at granulated sulfur treatment facilities, it is proposed to use a composition based on nonionic surfactants represented by a mixture of C12-14-alkylglycosides oligomers, additionally containing a mixture of amylose and amylopectin polysaccharides in the form of soluble starch and water in the following component ratio, wt.%: a mixture of C12-14-alkylpolyglycosides oligomers – 1-1.5; soluble starch – 1-2.5.

The proposed highly dispersed sulfur dust suppressor showed consistently high dust suppression efficiency both when measured immediately after irrigation (98.3 %) and after the expected time (99.7 %). The developed composition provides an increase in the dust-suppressing ability of the solution and the elimination of the possibility of repeated dusting due to the formation of a polymer film on the surface, as well as the regranulation of the product crushed by abrasion. The treatment of highly dispersed sulfur with this dust suppressor guarantees an effective reduction in the surface tension of water at such concentrations of the components used that eliminate negative effects on other physical-chemical properties of the finished product, such as flowability, hygroscopicity and caking.

REFERENCES

1. Saleh T.A. Characterization, determination and elimination technologies for sulfur from petroleum: Toward cleaner fuel and a safe environment. *Trends in Environmental Analytical Chemistry*. 2020. Vol. 25. N e00080. DOI: [10.1016/j.teac.2020.e00080](https://doi.org/10.1016/j.teac.2020.e00080)
2. Rongrong Yang, Zhirong Wang, Juncheng Jiang et al. Cause analysis and prevention measures of fire and explosion caused by sulfur corrosion. *Engineering Failure Analysis*. 2020. Vol. 108. N 104342. DOI: [10.1016/j.engfailanal.2019.104342](https://doi.org/10.1016/j.engfailanal.2019.104342)
3. Naiyan Zhang, Zhi Zhang, Zhenhua Rui et al. Comprehensive risk assessment of high sulfur-containing gas well. *Journal of Petroleum Science and Engineering*. 2018. Vol. 170, p. 888-897. DOI: [10.1016/j.petrol.2018.07.016](https://doi.org/10.1016/j.petrol.2018.07.016)
4. Shakhparonova T., Sobianina D., Karapetyan K. Development of a dissolution model of a vitreous phosphorus-containing fertilizer concerning interdiffusion applied for calculation of fertilizer doses. *Research on Crops*. 2021. Vol. 22. Iss. 2, p. 279-284. DOI: [10.31830/2348-7542.2021.069](https://doi.org/10.31830/2348-7542.2021.069)



5. Kameshkov A.V., Kondrasheva N.K., Gabdulkhakov R.R., Rudko V.A. Comparison of coking additives obtained from different types of oil stock. *Tsvetnye metally*. 2020. N 10, p. 35-42 (in Russian). DOI: [10.17580/tsm.2020.10.05](https://doi.org/10.17580/tsm.2020.10.05)
6. Rodionov V.A., Karpov G.N., Leisle A.V. Methodological approach to the need to assess the explosion and fire hazard properties of sulfide-containing polymetallic ores. *Mining Informational and Analytical Bulletin*. 2022. Iss. 6-1, p. 198-213 (in Russian). DOI: [10.25018/0236_1493_2022_61_0_198](https://doi.org/10.25018/0236_1493_2022_61_0_198)
7. Dvoynikov M.V., Nutskova M.V., Blinov P.A. Developments Made in the Field of Drilling Fluids by Saint Petersburg Mining University. *International Journal of Engineering*. 2020. Vol. 33. Iss. 4, p. 702-711. DOI: [10.5829/IJE.2020.33.04A.22](https://doi.org/10.5829/IJE.2020.33.04A.22)
8. Kovalevsky V.N., Myslin A.V. Performance of tubular elastic charges in natural stone production. *Mining Informational and Analytical Bulletin*. 2023. N 1, p. 20-34 (in Russian). DOI: [10.25018/0236_1493_2023_1_0_20](https://doi.org/10.25018/0236_1493_2023_1_0_20)
9. Zhukovskiy Y.L., Batueva D.E., Buldysko A.D. et al. Fossil Energy in the Framework of Sustainable Development: Analysis of Prospects and Development of Forecast Scenarios. *Energies*. 2021. Vol. 14. Iss. 17. N 5268. DOI: [10.3390/en14175268](https://doi.org/10.3390/en14175268)
10. Boikov A., Savelev R., Payor V., Potapov A. Universal Approach for DEM Parameters Calibration of Bulk Materials. *Symmetry*. 2021. Vol. 13. Iss. 6. N 1088. DOI: [10.3390/sym13061088](https://doi.org/10.3390/sym13061088)
11. Kanyukov R.R., Zapevalov D.N., Vagapov R.K. Analysis of the application and impact of carbon dioxide media on the corrosion state of oil and gas facilities. *Journal of Mining Institute*. 2021. Vol. 250, p. 578-856. DOI: [10.31897/PMI.2021.4.11](https://doi.org/10.31897/PMI.2021.4.11)
12. Khuzhakulov A.Kh. The use of sulfur in agriculture in Uzbekistan and training in safety requirements. *Problemy nauki*. 2021. N 6 (65), p. 96-102. DOI: [10.24411/2413-2101-2021-10601](https://doi.org/10.24411/2413-2101-2021-10601)
13. Ivanov A.V., Smirnov Y.D., Lisai V.V., Borowski G. Issues of the Impact of Granulated Sulfur Transportation on the Environmental Components. *Journal of Ecological Engineering*. 2023. Vol. 24. Iss. 6, p. 86-97. DOI: [10.12911/22998993/162558](https://doi.org/10.12911/22998993/162558)
14. Bazhin V., Masko O. Monitoring of the Behaviour and State of Nanoscale Particles in a Gas Cleaning System of an Ore-Thermal Furnace. *Symmetry*. 2022. Vol. 14. Iss. 5. N 923. DOI: [10.3390/sym14050923](https://doi.org/10.3390/sym14050923)
15. Zyryanova O.V., Kireeva E.V., Abramova A.E. Development of Dust-suppressing Compositions to Ensure Environmental Safety in Open-pit Mining. *Ecology and Industry of Russia*. 2022. Vol. 26. N 10, p. 22-28 (in Russian). DOI: [10.18412/1816-0395-2022-10-22-28](https://doi.org/10.18412/1816-0395-2022-10-22-28)
16. Cong Zhang, Shuo Yuan, Ningning Zhang et al. Dust-suppression and cooling effects of spray system installed between hydraulic supports in fully mechanized coal-mining face. *Building and Environment*. 2021. Vol. 204. N 108106. DOI: [10.1016/j.buildenv.2021.108106](https://doi.org/10.1016/j.buildenv.2021.108106)
17. Qun Zhou, Botao Qin. Coal dust suppression based on water mediums: A review of technologies and influencing factors. *Fuel*. 2021. Vol. 302. N 121196. DOI: [10.1016/j.fuel.2021.121196](https://doi.org/10.1016/j.fuel.2021.121196)
18. Chaohang Xu, Hetang Wang, Deming Wang et al. Improvement of Foaming Ability of Surfactant Solutions by Water-Soluble Polymers: Experiment and Molecular Dynamics Simulation. *Polymers*. 2020. Vol. 12. Iss. 3. N 571. DOI: [10.3390/polym12030571](https://doi.org/10.3390/polym12030571)
19. Hetang Wang, Xiaobin Wei, Yunhe Du, Deming Wang. Effect of water-soluble polymers on the performance of dust-suppression foams: Wettability, surface viscosity and stability. *Colloids and Surfaces A: Physicochemical and Engineering Aspects*. 2019. Vol. 568, p. 92-98. DOI: [10.1016/j.colsurfa.2019.01.062](https://doi.org/10.1016/j.colsurfa.2019.01.062)
20. Smirnyakov V.V., Rodionov V.A., Smirnyakova V.V., Orlov F.A. The influence of the shape and size of dust fractions on their distribution and accumulation in mine workings when changing the structure of air flow. *Journal of Mining Institute*. 2022. Vol. 253, p. 71-81. DOI: [10.31897/PMI.2022.12](https://doi.org/10.31897/PMI.2022.12)
21. Guang Xu, Yinping Chen, Jacques Eksteen, Jialin Xu. Surfactant-aided coal dust suppression: A review of evaluation methods and influencing factors. *Science of the Total Environment*. 2018. Vol. 639, p. 1060-1076. DOI: [10.1016/j.scitotenv.2018.05.182](https://doi.org/10.1016/j.scitotenv.2018.05.182)
22. Xiaobin Wei, Hetang Wang, Ying Xie, Yunhe Du. An experimental investigation on the effect of carboxymethyl cellulose on morphological characteristics of dust-suppression foam and its mechanism exploration. *Process Safety and Environmental Protection*. 2020. Vol. 135, p. 126-134. DOI: [10.1016/j.psep.2019.12.009](https://doi.org/10.1016/j.psep.2019.12.009)
23. Zidong Zhao, Ping Chang, Guang Xu et al. Comparison of the coal dust suppression performance of surfactants using static test and dynamic test. *Journal of Cleaner Production*. 2021. Vol. 328. N 129633. DOI: [10.1016/j.jclepro.2021.129633](https://doi.org/10.1016/j.jclepro.2021.129633)
24. Ping Chang, Zidong Zhao, Guang Xu et al. Evaluation of the coal dust suppression efficiency of different surfactants: A factorial experiment. *Colloids and Surfaces A: Physicochemical and Engineering Aspects*. 2020. Vol. 595. N 124686. DOI: [10.1016/j.colsurfa.2020.124686](https://doi.org/10.1016/j.colsurfa.2020.124686)
25. Yen-Yi Lee, Chung-Shin Yuan, Po-Hsuan Yen et al. Suppression Efficiency for Dust from an Iron Ore Pile Using a Conventional Sprinkler and a Water Mist Generator. *Aerosol and Air Quality Research*. 2022. Vol. 22. Iss. 2. N 210320. DOI: [10.4209/aaqr.210320](https://doi.org/10.4209/aaqr.210320)
26. Huitian Peng, Wen Nie, Peng Cai et al. Development of a novel wind-assisted centralized spraying dedusting device for dust suppression in a fully mechanized mining face. *Environmental Science and Pollution Research*. 2019. Vol. 26. Iss. 4, p. 3292-3307. DOI: [10.1007/s11356-018-3264-8](https://doi.org/10.1007/s11356-018-3264-8)
27. Friesen D.E., Radok A. Patent N CA 2640857 A1. Methods and compositions for coating sulfur blocks. Publ. 10.04.2009.
28. Weagle G., Horvath T. Patent N CA 2645851 A1. Method and composition to form a flexible crust on a substrate. Publ. 04.06.2010.
29. Katsubin A.V., Kovshov S.V., Ilyashenko I.S., Marinina V.M. Study of Organic Compounds for Reduction of the Aero-technogenic Load from the Coal Mines Highways. *Occupational Safety in Industry*. 2020. N 1, p. 63-67 (in Russian). DOI: [10.24000/0409-2961-2020-1-63-67](https://doi.org/10.24000/0409-2961-2020-1-63-67)
30. Winstanley R.A., Swartzlander M.W., Cooke T.W. Patent N US 5223165 A. Use of alkyl glycosides for dust suppression. Publ. 29.06.1993.
31. van der Galiën M. Patent N NL 2011049 C2. Dust-suppressing composition and method there for. Publ. 05.01.2015.
32. Beeksmma W.J. Patent N NL 1027690 C2. Antidusting composition for treating dust-producing materials comprises alkyl glucoside, nonionic surfactant and water. Publ. 01.08.2006.
33. Korneva M.V. Development and justification of measures to reduce the concentration of fine fractions in the dust aerosol of coal mines: Avtoref. dis. ... kand. tekhn. nauk. Saint Petersburg: Saint Petersburg Mining University, 2020, p. 20.



34. Ivanov A.V., Smirnov Yu.D., Chupin S.A. Development of the concept of an innovative laboratory installation for the study of dust-forming surfaces. *Journal of Mining Institute.* 2021. Vol. 251, p. 757-766. DOI: [10.31897/PMI.2021.5.15](https://doi.org/10.31897/PMI.2021.5.15)
35. Skorobogatko D.S., Golovkov A.N., Kudinov I.I., Kulichkova S.I. Revisiting the ecotoxicity and efficiency of different classes of industrial nonionic surfaces used for cleaning metal surfaces in the process of capillary control of details of the aviation technology (review). *Aviation Materials and Technologies.* 2021. N 4 (65), p. 98-106 (in Russian). DOI: [10.18577/2713-0193-2021-0-4-98-106](https://doi.org/10.18577/2713-0193-2021-0-4-98-106)
36. Nureev R.R., Pashkevich M.A., Kharko P.A. Assessment of the impact of copper ore processing waste on surface and ground-water. *Geology and Geophysics of Russian South.* 2022. Vol. 12. N 4, p. 169-179 (in Russian). DOI: [10.46698/VNC.2022.37.95.013](https://doi.org/10.46698/VNC.2022.37.95.013)
37. Mozheyko F.F., Shevchuk V.V., Potkina T.N., Voytenko A.I. Using mixtures of non-ionic surfactants and polyvalent metal salts use for sylvinit ore flotation. *Proceedings of the National Academy of Sciences of Belarus, Chemical Series.* 2014. N 1, p. 113-117 (in Russian).
38. Yusova A.A., Lipatova I.M., Moryganov A.P. Influence of Surfactants on the State of Starch Hydrogels under High Shear Stresses. *Russian Journal of Applied Chemistry.* 2003. Vol. 76. N 3, p. 434-438. DOI: [10.1023/A:1025609003041](https://doi.org/10.1023/A:1025609003041)

Authors: **Viktoriya V. Lisai**, Labor Protection and Environmental Specialist, <https://orcid.org/0000-0002-8164-0119> (Stevedoring and Shipping Company Limited, Saint Petersburg, Russia), **Yurii D. Smirnov**, Candidate of Engineering Sciences, Associate Professor, <https://orcid.org/0000-0002-2631-6674> (Empress Catherine II Saint Petersburg Mining University, Saint Petersburg, Russia), **Andrei V. Ivanov**, Candidate of Engineering Sciences, Associate Professor, ivanov_av4@pers.spmi.ru, <https://orcid.org/0000-0003-1045-5052> (Empress Catherine II Saint Petersburg Mining University, Saint Petersburg, Russia), **Gabriel Borowski**, Doctor of Engineering Sciences, Professor, <https://orcid.org/0000-0001-6971-5395> (Lublin University of Technology, Lublin, Poland).

The authors declare no conflict of interests.



Crustal movement model in the ITRF2020 – a case study in Northern Vietnam

Bui Thi Hong Tham, Phi Truong Thanh✉

Hanoi University of Natural Resources and Environment, Hanoi, Vietnam

How to cite this article: Bui Thi Hong Tham, Phi Truong Thanh. Crustal movement model in the ITRF2020 – a case study in Northern Vietnam. Journal of Mining Institute. 2025. Vol. 271. N 16324, p. 120-130.

Abstract

In the North area of Vietnam, the crustal movement velocity of 38 GNSS points belonging to different international Earth reference frames (ITRF2000, ITRF2005, ITRF2008) is adjusted to the international Earth reference frame ITRF2020. This is the latest frame up to now. Since then, the picture of crustal movement in the North area of Vietnam has been unified in a dynamic coordinate system. In the study area, the rate of crustal movement is about 35 mm/year, and the direction of displacement is from northwest to southeast. To build a model of the crustal movement of the Earth in the northern area of Vietnam, the movement velocity data of 38 stations in ITRF2020 is evaluated with high accuracy. All points are also satisfactory. And then, the crustal movement velocity model is built by using the collocation method in the form of the 3-order Markov function. Within 38 stations, 34 stations are used to build the model and 4 remaining stations are used as checked stations. The obtained results show that the Earth's crust movement velocity model has an accuracy of about 2 mm/year for movement velocity and 2 deg for movement direction. This is the first model of Earth's crust movement in the North of Vietnam that has been built in the latest dynamic coordinate system ITRF2020. These results have important significance in the research and practical application of the movement of the Earth's crust. The steps of building the movement velocity model in this study can be applied to other experimental areas in the territory of Vietnam.

Keywords

movement velocity; Northern Vietnam; ITRF; ITRF2020; collocation; crustal movement

Received: 04.10.2023

Accepted: 24.09.2024

Online: 24.12.2024

Published: 25.02.2025

Introduction

The Global Navigation Satellite System (GNSS) is being widely used in the world to monitor the deformation of the Earth's crust [1-3] and has supported forecasting and warning earthquakes [4-6] tectonic movement [7-9]. During the processing of GNSS station location time series, the time series of GNSS coordinates is used to model the movement of the Earth's crust [10-12]. The use of time series in determining the Earth's crust movement through continuous GNSS measurements was conducted [13-15]. Similarly, the determination of horizontal movement in the Northwest area of Vietnam's Earth's crust is also accomplished through periodic GPS measurements [16, 17].

From the 1990s to the present, GNSS technology has been used in Vietnam to study the movement of the Earth's crust. The movement velocity values at the stations defined in the dynamic coordinate systems (ITRF94, ITRF2000, ITRF2005, ITRF2008, ITRF2014) are different and inconsistent, making it difficult to build a movement velocity model. To build the movement model of the Earth's crust, we transfer the movement velocities of the GNSS stations to the same coordinate system and model them. There are two methods for transforming: collect and reprocess all data in a single ITRF; collect velocities of the stations, along with corrections. The first way, the collecting, and processing of data are very complicated and time-consuming [18-20]; the second way, the data processing is fast and more accurate [21-23]. In this paper, we use the second one to correct the movement velocities of the GNSS stations into one dynamic coordinate system ITRF2020 – the latest version of ITRF, which is more accurate than the previous versions [24-26]. The ITRF2020 released in 2021. Transformation parameters between ITRF2020 and other ITRFs can be found on the website*. And the least-squares collocation

* International Terrestrial Reference Frame (ITRF). URL: <https://itrf.ign.fr/en/solutions/transformations> (accessed 04.10.2023).



method is used to model the movement velocity of the Earth's crust [27-29]. This is a mathematical function with high accuracy and reliability.

The GNSS stations of various ITRFs in the North area of Vietnam are chosen in this case:

- the movement velocity in ITRF2000 of GNSS stations which supports studying the Red River fault systems, Dien Bien Phu fault, Song Da River fault [30];
- the movement velocity in ITRF2005 of GNSS stations in Vietnam that participated in the Asia-Pacific network (PCGIAP) [31];
- the movement velocity in ITRF2005 of the DGNSS/CORS station that belongs to the military coordinate network [32];
- the movement velocity in ITRF2008 of GNSS stations belong to the geodynamic network on the fault zones in the northwestern area of Vietnam, which supported for forecasting of natural hazards.

Methodology

The methodology for presenting the construction of the Earth's crustal velocity model within a single international Earth reference frame is outlined as follows: the crustal velocity in various Earth reference frames is standardized to a single reference frame; they are examined and, these crustal velocity values are mathematically modelled using a mathematical function.

Velocity transfer between Earth's frame of reference. The formula to transfer the coordinate in the reference system (I) to the reference system (II) at time t has a form as follows [23, 24]:

$$X(t)_{(II)} = X(t)_{(I)} + T(t) + D(t)X(t)_{(I)} + R(t)^T X(t)_{(I)};$$

$$R^T = R_1^T (R_1) R_2^T (R_2) R_3^T (R_3) = \begin{pmatrix} 1 & -R_3 & R_2 \\ R_3 & 1 & -R_1 \\ -R_2 & R_1 & 1 \end{pmatrix},$$

where $X_{(II)}$ is the coordinate vector of the site in the frame of reference, $X_{(II)} = [X; Y; Z]_{(II)}^T$; $X_{(I)}$ is the corresponding coordinate vector of that station in the old frame of reference, $X_{(I)} = [X; Y; Z]_{(I)}^T$; T is the translation or displacement vector among frames, $T = [T_1; T_2; T_3]^T$; D is a different scale; R^T is the coordinate axis rotation matrix between the two frames of reference; R_1, R_2 , and R_3 – are the small rotation angles.

From the dynamic point of view, $T_1, T_2, T_3, R_1, R_2, R_3$, and D are considered as functions of time and expressed in the linear form. The common symbol of the parameters from $i = 1$ to 7 first-order derivative of β_i under time

$$\beta_i(t) = \beta_i(t_0) + \dot{\beta}_i(t - t_0),$$

where $\beta_i(t_0)$ is the value of β_i at time t_0 .

The formula to calculate the transformation velocity between frames of reference is:

$$V_{(II)} = V_{(I)} + \dot{T} + \dot{D}X(t)_{(I)} + \dot{R}^T X(t)_{(I)};$$

$$V(t) = \begin{bmatrix} V_X(t) \\ V_Y(t) \\ V_Z(t) \end{bmatrix},$$

where $V(t)$ is the coordinate movement velocity vector.

The matrix of movement velocity converts from V_X, V_Y, V_Z into V_E, V_N, V_U [33]

$$\begin{pmatrix} V_E \\ V_N \\ V_U \end{pmatrix} = \begin{pmatrix} -\sin \lambda & \cos \lambda & 0 \\ -\cos \lambda \sin \varphi & -\sin \lambda \sin \varphi & \cos \varphi \\ \cos \lambda \cos \varphi & \sin \lambda \cos \varphi & \sin \varphi \end{pmatrix} \begin{pmatrix} V_X \\ V_Y \\ V_Z \end{pmatrix},$$

where V_E, V_N, V_U are velocities to the east, north and vertical, respectively; φ, λ – are the longitude and latitude, respectively.



The horizontal movement velocity of a point and azimuth angle is calculated by the formulas:

$$V = \sqrt{V_E^2 + V_N^2};$$

$$Az = \arctan \frac{V_E}{V_N}.$$

Evaluation of the range of measurement values. A set of n observed data values V_1, V_2, \dots, V_n . The average of the observed data is calculated by the formula

$$V_{av} = \sum_{i=1}^n V_i / n; \quad (1)$$

the correction number of the observed i value is calculated by the following formula

$$v_i = V_{av} - V_i; \quad (2)$$

the variance is calculated following formula

$$\sigma^2 = \frac{\sum_{i=1}^n v_i^2}{n-1}. \quad (3)$$

Standard deviation σ is the square root of the variance. The standard deviation is used to evaluate the quality of the observed data. The value is frequently chosen to evaluate the quality of the data series to be 3σ , which corresponds to the probability of occurrence of the measured series of ~99.73 %.

Model of movement velocity. Assume that there are two sets of random variables:

- the set of measurement values l_1, l_2, \dots, l_q is represented by a q -dimensional vector

$$l = [l_1 \quad l_2 \quad \dots \quad l_q]^T;$$

- the set of signals that needs to determine to be S_1, S_2, \dots, S_m , represented by the m -dimensional vector

$$S = [S_1 \quad S_2 \quad \dots \quad S_m]^T.$$

The best linear estimator of the vector S :

$$\hat{S} = C_{Sl} C_{ll}^{-1} l. \quad (4)$$

The equation (4) is called least squares interpolation or least-squares collocation interpolation. To calculate according to this equation, it is necessary to determine the covariance matrices C_{ll} and C_{Sl} . To determine the parameters of the theoretical covariance function, firstly must calculate the experimental covariance values. Call l_i is the value of point i .

The experimental covariance follows the distance of k pairs of points P, Q is calculated by the equation:

$$C_s = \text{cov}(dl_i, dl_Q) = \frac{1}{k} \sum_{i=1}^k dl_i^P dl_i^Q;$$

$$dl_i = l_i - \frac{1}{n} \sum_{i=1}^n l_i.$$

The theoretical covariance function must be chosen from the law of variation of the experimental covariance values and the parameters of the theoretical covariance function must be determined using the function approximation method.

In this study, the 3rd-order Markov function is used to establish the movement velocity model in the experimental part and its direction [34, 35]



$$C_s = C_0 e^{-\frac{s}{L}} \left(1 + \frac{s}{L} + \frac{s^2}{3L^2} \right),$$

where C_0 is the parameter of the theoretical covariance function; L is the relation distance.

The standard deviation between the theoretical covariance function and experimental covariance is calculated in formula

$$\mu = \sqrt{\frac{\sum_{i=1}^k \varepsilon_i^2}{k-2}}, \quad (5)$$

where ε_i is the deviation between theoretical covariance function and experimental covariance of the i -th point; k is the number of experimental covariance values following distance.

The root mean square error of the covariance function at the checked points is calculated according to the formula

$$\text{RMS} = \sqrt{\frac{\sum_{i=1}^m d_i^2}{m}},$$

where d_i is the deviation of the measured value and interpolated value for i -th checked point; m is the number of checked points.

The data in this paper is a dataset of Earth's crustal movement velocity vectors of 38 GNSS stations in the North area of Vietnam which is chosen from the following statistics:

- the movement velocity in ITRF2000 of 22 GNSS stations which support studying the Red River fault systems, Dien Bien Phu fault, Song Da River fault;
- the movement velocity in ITRF2005 of four GNSS stations in Vietnam which were a part of the Asia-Pacific network (PCGIAP);
- the movement velocity in ITRF2005 of 1 DGNSS/CORS station belongs to the military coordinate network;
- the movement velocity in ITRF2008 of 11 GNSS stations that are part of the Ministry of Natural Resources and Environment's project in Vietnam, which aims to establish a seismic geodetic network in the faulted areas of Northern Vietnam to support natural disaster prediction.

Results

The building of the absolute movement velocity model of the earth's crust is implemented according to the steps follows.

Step 1 – unify the movement velocity of the Earth's crust in the North area of Vietnam in ITRF2020. To build a model of the movement velocity of the GNSS stations in different ITRFs in Table 1, the velocities must be unified into one ITRF and are calculated in Table 2.

Table 1

Coordinates and movement velocity of GNSS stations in the North area of Vietnam

Station	φ , deg	λ , deg	V_E , mm/year	V_N , mm/year	V_U , mm/year	ITRF
CAM1	20.999	107.313	34.60	-13.41	32.95	ITRF2000
SOC1	21.308	105.826	32.88	-11.94	-1.84	ITRF2000
XUY0	21.849	105.738	34.95	-12.46	0.53	ITRF2000
TAM2	21.455	105.638	32.42	-12.24	-0.60	ITRF2000
BAV1	21.097	105.373	32.14	-11.08	-1.28	ITRF2000
OAN0	21.853	105.336	33.49	-11.85	-14.02	ITRF2000



End of Table 1

Station	φ , deg	λ , deg	V_E , mm/year	V_N , mm/year	V_U , mm/year	ITRF
HUN1	21.361	105.330	33.14	-11.69	-5.24	ITRF2000
DOI0	21.677	105.202	33.66	-11.83	-10.47	ITRF2000
NTH0	21.475	105.186	33.27	-12.23	-10.70	ITRF2000
SON1	21.191	105.181	32.80	-12.13	-3.73	ITRF2000
HOA1	20.864	105.178	33.90	-11.34	-2.75	ITRF2000
LAP1	21.384	105.033	32.92	-12.47	-4.99	ITRF2000
NAM0	21.691	104.458	35.09	-12.04	3.23	ITRF2000
MON1	21.189	104.245	32.43	-13.44	-1.05	ITRF2000
NOI1	21.131	104.172	33.03	-12.08	-4.40	ITRF2000
NAD2	20.984	104.167	32.36	-12.13	-10.19	ITRF2000
LOT1	21.203	104.064	33.45	-13.56	-6.17	ITRF2000
QTA2	21.306	103.943	33.91	-12.52	-9.63	ITRF2000
NGA1	22.268	103.242	39.12	-9.74	12.09	ITRF2000
HAM1	21.931	103.236	32.87	-10.47	15.33	ITRF2000
DON1	22.131	103.051	35.17	-12.10	15.17	ITRF2000
LEM1	21.792	103.029	34.83	-11.12	11.92	ITRF2000
DIEB	21.428	103.005	26.98	-9.60	3.92	ITRF2005
DOSN	20.694	106.795	27.35	-7.99	16.64	ITRF2005
NT01	20.668	106.814	36.00	-11.72	7.54	ITRF2005
QT01	21.403	103.029	29.92	-10.32	-19.98	ITRF2005
MCRS	21.526	107.968	30.80	-7.80	-1.80	ITRF2005
C004	21.926	103.238	37.58	-12.34	-14.60	ITRF2008
C014	20.147	105.136	35.94	-11.75	-9.85	ITRF2008
C022	21.029	104.312	30.04	-10.72	-7.04	ITRF2008
C033	21.549	104.036	34.70	-10.05	-15.56	ITRF2008
C045	21.119	104.982	31.79	-9.92	-29.24	ITRF2008
C049	22.225	104.445	39.34	-12.15	-26.71	ITRF2008
C052	21.636	104.787	34.08	-13.86	-30.45	ITRF2008
C056	20.880	105.497	31.55	-11.38	15.31	ITRF2008
C065	21.810	105.438	36.46	-13.50	-18.32	ITRF2008
C070	21.930	106.794	31.40	-12.91	8.97	ITRF2008
C075	20.988	106.816	34.68	-13.68	7.82	ITRF2008

Table 2

Movement velocity of GNSS stations in ITRF2020

Station	V_E , mm/year	V_N , mm/year	V_U , mm/year	V , mm/year	Az , deg
CAM1	34.70	-11.83	32.89	36.66	108.8
SOC1	32.98	-10.36	-1.90	34.57	107.4
XUY0	35.05	-10.89	0.49	36.70	107.3
TAM2	32.52	-10.67	-0.65	34.22	108.2
BAV1	32.24	-9.50	-1.34	33.61	106.4
OAN0	33.59	-10.28	-14.06	35.12	107.0
HUN1	33.24	-10.11	-5.30	34.74	106.9
DOI0	33.76	-10.26	-10.52	35.28	106.9
NTH0	33.37	-10.66	-10.75	35.03	107.7
SON1	32.90	-10.55	-3.79	34.55	107.8



End of Table 2

Station	V_E , mm/year	V_N , mm/year	V_U , mm/year	V , mm/year	Az , deg
HOA1	34.00	-9.72	-2.99	35.36	106.0
LAP1	33.02	-10.89	-5.05	34.77	108.3
NAM0	35.19	-10.47	3.18	36.71	106.6
MON1	32.53	-11.86	-1.11	34.62	110.0
NOI1	33.13	-10.50	-4.47	34.75	107.6
NAD2	32.46	-10.55	-10.26	34.13	108.0
LOT1	33.55	-11.98	-6.23	35.62	109.7
QTA2	34.01	-10.94	-9.69	35.72	107.8
NGA1	39.22	-8.17	12.05	40.06	101.8
HAM1	32.97	-8.90	15.28	34.15	105.1
DON1	35.27	-10.53	15.13	36.81	106.6
LEM1	34.93	-9.55	11.87	36.21	105.3
DIEB	27.25	-9.75	3.85	28.94	109.7
DOSN	27.61	-8.15	16.58	28.79	106.4
NT01	36.26	-11.87	7.49	38.15	108.1
QT01	30.18	-10.47	-20.06	31.95	109.1
MCRS	31.00	-7.93	-1.89	32.00	104.3
C004	37.55	-12.47	-14.74	39.57	108.4
C014	35.92	-11.88	-9.98	37.83	108.3
C022	30.01	-10.84	-7.18	31.91	109.9
C033	34.68	-10.18	-15.69	36.14	106.4
C045	31.76	-10.05	-29.37	33.31	107.6
C049	39.31	-12.28	-26.85	41.18	107.3
C052	34.05	-13.99	-30.58	36.81	112.3
C056	31.53	-11.51	15.17	33.56	110.1
C065	36.43	-13.63	-18.46	38.90	110.5
C070	31.37	-13.04	8.83	33.98	112.6
C075	34.65	-13.81	7.69	37.30	111.7

The calculated results in Table 2 show that the magnitude values and azimuth of the horizontal movement velocity vectors of the GNSS stations are quite uniform. These vectors tend to move in the northwest – southeast direction (Fig.1). This is a necessary condition to calculate the experimental covariance at different distances for applying the least-squares collocation method.

Step 2 – evaluate V and Az . The data in Table 2 shows that some stations which have different movement velocities from the general trend of stations in the experimental area need to be evaluated before using them to build a velocity model of the absolute movement of the Earth's crust.

The average velocity and of the GNSS stations from formula (1) is:

$$V_{av} = \sum_{i=1}^{38} V_i / 38 = 35.26 \text{ mm/year};$$

$$Az_{av} = \sum_{i=1}^{38} Az_i / 38 = 107.9 \text{ deg.}$$

Call v_i , v_{Az_i} to be the correction for the i -th velocity and azimuth. These values are calculated according to formula (2) and presented in Table 3.

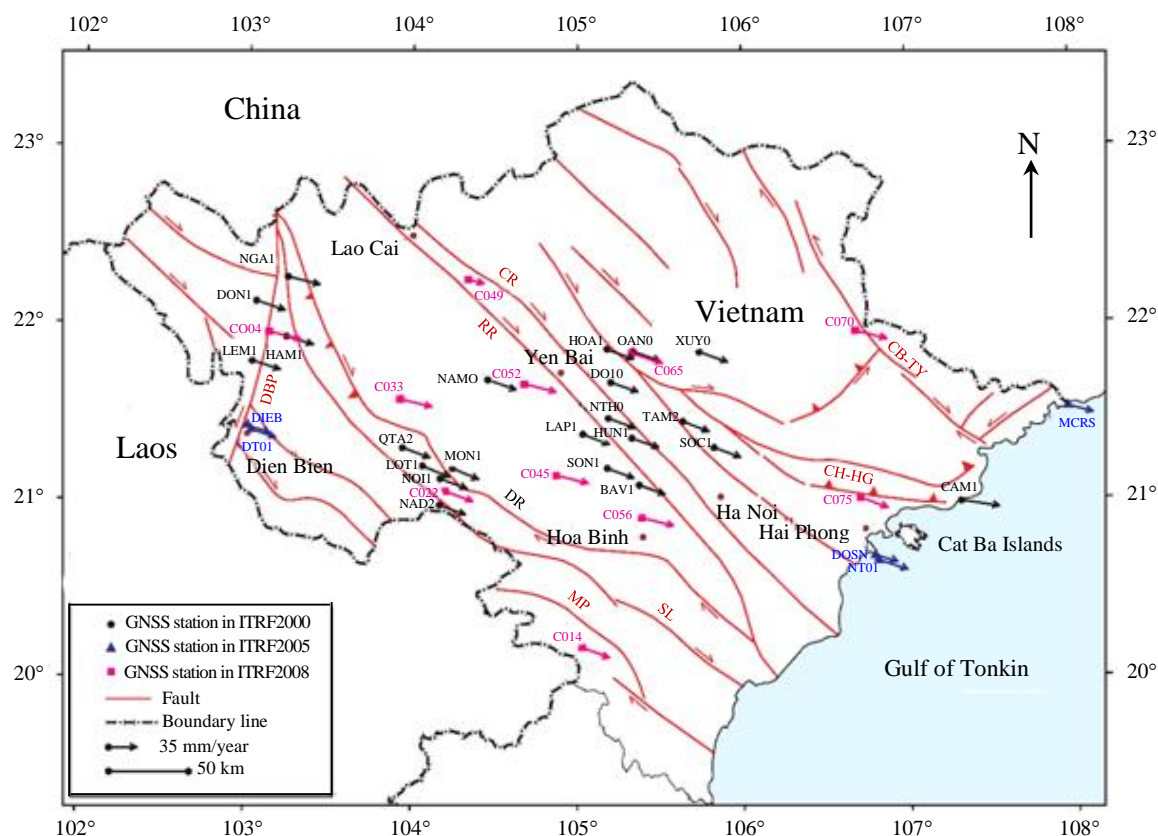


Fig.1. Map of Earth's crustal movement velocity of GNSS stations in northern area of Vietnam in ITRF2020 (the GNSS stations is located at the positions belong to stable geological block along the fault zone)

Table 3

Deviation of velocity and azimuth at stations with their corresponding average values

Station	v_i , mm/year	v_{Az_i} , deg	Station	v_i , mm/year	v_{Az_i} , deg
CAM1	-1.40	-0.9	HAM1	1.11	2.8
SOC1	0.69	0.5	DON1	-1.55	1.3
XUY0	-1.44	0.6	LEM1	-0.95	2.6
TAM2	1.04	-0.3	DIEB	6.32	-1.8
BAV1	1.65	1.5	DOSN	6.47	1.5
OAN0	0.14	0.9	NT01	-2.89	-0.2
HUN1	0.52	1.0	QT01	3.31	-1.2
DOI0	-0.02	1.0	MCRS	3.26	3.6
NTH0	0.23	0.2	C004	-4.31	-0.5
SON1	0.71	0.1	C014	-2.57	-0.4
HOA1	-0.10	1.9	C022	3.35	-2.0
LAP1	0.49	-0.4	C033	-0.88	1.5
NAM0	-1.45	1.3	C045	1.95	0.3
MON1	0.64	-2.1	C049	-5.92	0.6
NOI1	0.51	0.3	C052	-1.55	-4.4
NAD2	1.13	-0.1	C056	1.70	-2.2
LOT1	-0.36	-1.8	C065	-3.64	-2.6
QTA2	-0.46	0.1	C070	1.28	-4.7
NGA1	-4.80	6.1	C075	-2.04	-3.8



The standard deviation of the observed data series is calculated from the formula (3):

$$\sigma_V = \sqrt{\sum_{i=1}^{38} v_i^2 / 37} = \pm 2.62 \text{ mm/year};$$

$$\sigma_{Az} = \sqrt{\sum_{i=1}^{38} v_{Az_i}^2 / 37} = \pm 2.1 \text{ deg}.$$

Thus, the probability of occurrence of movement velocity value of GNSS stations in the range of $(35.26 - 3\sigma)$ and $(35.26 + 3\sigma)$, respectively from 27.40 mm/year to 43.12 mm/year, and their movement directions at GNSS stations are in the range of $(107.9 - 3\sigma)$ and $(107.9 + 3\sigma)$, respectively from 101.6 deg to 114.2 deg is 99.73 %. When processing data in the next steps, the GNSS station's movement velocity will be eliminated if it is outside the range of values mentioned above.

The analytical results show that all stations are in the range of values mentioned above, so it is used in the next steps.

Step 3 – build an absolute movement velocity model. In the study area, the 38 GNSS stations are used for experimental calculations. Among these stations, 04 stations OAN0, LOT1, C075, and QT01 are used to test the accuracy of the model but they are not used to build the model. The modeling of movement velocity of GNSS stations is implemented by the least-squares collocation method of the 3rd-order Markov function. During the data processing, the characteristic parameters of the function are determined. The model of movement velocity of the northern area of Vietnam is expressed under a 3rd-order Markov function:

$$C_{S_V} = -3.7513e^{-\frac{S}{4.2143}} \left(1 - \frac{S}{4.2143} + \frac{S^2}{53.2810} \right); \quad (6)$$

$$C_{S_{Az}} = 10.7777e^{-\frac{S}{3.1549}} \left(1 + \frac{S}{3.1549} + \frac{S^2}{29.86018} \right). \quad (7)$$

The standard deviation between the theoretical covariance function and the experimental covariance of the movement velocity value and their movement direction calculated according to formula (5) is $\pm 0.44 \text{ mm}^2$ and $\pm 0.9 \text{ deg}^2$, respectively. The graphs of Fig.2 show that the value and direction of the movement velocity calculated by the theoretical covariance function match the experimental covariance function.

The value of movement velocity of the tested stations in the study area is interpolated. The comparison of these values with their respective values in Table 2 will be obtained from the deviations in Table 4.

The information in Table 4 provides details about the values of velocity deviation for the checked GNSS stations. The highest deviation is 1.94 mm per year, the lowest is 0.17 mm per year. These deviation values are quite small when compared to the average movement velocity of about 35 mm per year in the studied region.

In Table 4, the results show that the deviation of the azimuth of measured values and interpolated values at checked GNSS stations is not large.

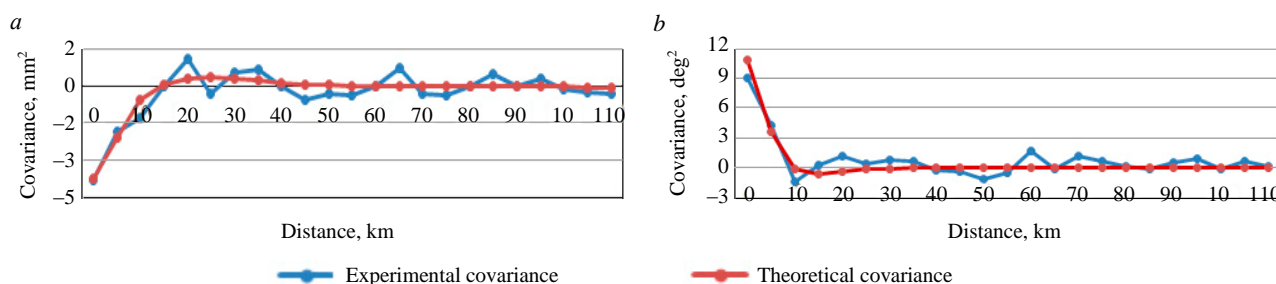


Fig.2. Graph of 3rd-order Markov function of the movement velocity (a) and movement direction (b)



Table 4

The determined value of movement velocity and value of azimuth of tested GNSS stations

Station	Value of movement velocity, mm/year			Value of azimuth, deg		
	V	V_m^*	Deviation	Az	Az_m^*	Deviation
OAN0	35.12	35.29	-0.17	107.0	107.5	-0.5
LOT1	35.62	35.41	0.21	109.7	108.7	1.0
C075	37.30	35.36	1.94	111.7	109.8	1.9
QT01	31.95	31.20	0.75	109.1	108.5	0.6

* Movement velocity calculated from the model.

From Table 4, the mean square error of velocity and their movement direction at the checked stations are ± 1.05 mm/year and ± 1.1 deg, respectively. This comparison indicates that the movement velocity model and their direction are established for the northern area of Vietnam, using the 3rd-order Markov function as described in formulas (6) and (7).

Discussions

The northern part of Vietnam has a complex tectonic setting, dominated by active faults such as the Red River fault, Chay River fault, Lo River fault – all of them belong to the Red River fault system, Dien Bien Phu fault, Da River fault, and Son La fault. The Red River fault plays the most important role in this area, as it divides the study area into two tectonic structures: the Northwestern and Northeastern. Up to now, the Earth's crustal movement in the northern part of Vietnam has been measured using GPS technology along active fault zones [16, 36].

The results of monitoring using GPS stations on the territory of Vietnam and adjacent areas have shown the movement of these stations in the northwest – southeast direction [16, 31]. The decrease in movement velocity from west to east of the northern GPS stations (Lang, Bach Long Vi, and Hai Nam) has indicated that the gulf of Tonkin area is currently compressed in the sub-latitude direction or East-Southeast direction. This stress field is unfavourable for the active extension fault system in the sub-meridian, as well as the strike-slip fault in the northwest – southeast.

In 2013, the movement velocity of the Red River fault was determined to be 34.5 ± 1 mm/year to the east and 12 ± 1 mm/year to the south through the analysis of GPS data. This data was obtained from 27 stations in the northern region of Vietnam between 1994 and 2007 using the GAMIT/GLOBK software [30]. At the same time, the horizontal movement velocity of 22 GPS stations in the northwest area of Vietnam, in the ITRF2008 coordinate system, from 2001 to 2012 was determined using Bernese version 5.0 software, and it was found to be 34.3 ± 0.7 mm/year [16].

In 2016, the absolute movement in the southern area of the Red River fault zone (Viet Tri – Hanoi) was calculated using data from Thac Ba stations, Tam Dao – Ba Vi, as well as measurements taken in the years 2013 and 2015. This analysis was conducted using Bernese 5.0 software, and the average value was approximately 34 mm/year [17].

In 2020, the velocity of Earth's crust movement at 06 stations (MTEV, MLAY, DBIV, TGIV, SMAV, SLAV) in the northwest area of Vietnam, as well as at 01 PHUT station (Hanoi), was calculated using GAMIT/GLOBK [36]. The determined Earth's crust movement velocities for these stations are as follows: 34.10 ± 0.71 mm/year (DBIV), 34.31 ± 0.65 mm/year (PHUT), 34.51 ± 0.75 mm/year (SMAV), 34.55 ± 0.80 mm/year (MLAY), 34.80 ± 0.72 mm/year (TGIV), 34.93 ± 0.99 mm/year (SLAV), and 35.59 ± 0.73 mm/year (MTEV). These results are consistent with the current tectonic setting in Southeast Asia, which is moving southeastward due to the collision of the Indian subcontinent into the Eurasian plate.

In 2022, the stations within the VNGEONET network have been determined for their absolute velocity of displacement on the Earth's crust using the GAMIT/GLOBK software. In general, these stations all tend to move in the southeast direction, with respective absolute displacement velocities: MCAI = 34.42 mm/year, SDON = 36.09 mm/year, HYEN = 32.87 mm/year, CPHU = 32.98 mm/year, TQUA = 33.95 mm/year, and MGTE = 34.46 mm/year [37].



The Earth's crustal movements of GNSS stations in the North area of Vietnam are corrected using the least-squares collocation method with a 3rd order Markov function, achieving an accuracy of about 2 mm/year in ITRF2020 for movement velocity and about 2 deg for movement direction. The determination of data in one dynamic coordinate system has formed a comprehensive picture of the Earth's crustal movement in the North area of Vietnam within a uniform framework. The movement velocity of the Earth's crust is ~35 mm/year in the northwest-southeast direction, which coincides with previous research results in the northern area of Vietnam, confirming the accuracy of the data correction from ITRF2000, ITRF2005, and ITRF2008 to ITRF2020.

Conclusions

The study involved the transformation of movement velocity data from 38 GNSS stations across various dynamic coordinate systems, namely ITRF2000, ITRF2005, and ITRF2008, into a single unified coordinate system known as ITRF2020. This transformation was achieved using parameters provided by the ITRF.

The analysis revealed that the movement velocity of these stations exhibited a change of ~35 mm/year, primarily in a direction from the northwest to the southeast. Among these stations, 34 were utilized to construct models for the movement of the Earth's crust, while the remaining four stations – OAN0, LOT1, C075, and QT01 – were reserved for testing and evaluating the accuracy of the models.

The research employed the least-squares collocation method to establish a model for the movement of the Earth's crust in the northern region of Vietnam. This model exhibited a high accuracy level, with a precision of about 2 mm/year.

This study marked the first time that a highly accurate Earth's crust movement velocity model was developed in Northern Vietnam using the latest dynamic coordinate system. The methodology employed in creating this precise crustal movement model holds potential applicability to other research domains with similar data sets. This achievement bears great importance in advancing the understanding and practical applications of modern Earth's crust movement. The outcomes of this research serve as a crucial data source that contributes to the establishment and utilization of the dynamic coordinate system within Vietnam.

The authors would like to thank the Vietnam Institute of Surveying and Mapping, Ministry of Natural Resources and Environment (MONRE), Vietnam, for providing the data from the project “Establishing a seismic geodetic network in the faulted areas of Northern Vietnam to support natural disaster prediction”.

REFERENCES

1. Altamimi Z., Rebischung P., Métivier L., Collilieux X. ITRF2014: A new release of the International Terrestrial Reference Frame modeling nonlinear station motions. *Journal of Geophysical Research: Solid Earth*. 2016. Vol. 121. Iss. 8, p. 6109-6131. DOI: [10.1002/2016JB013098](https://doi.org/10.1002/2016JB013098)
2. Amagua C.G.P., Euriques J.F., Alves S. da C., Krueger C.P. Analysis of local surface displacement using repeated GPS measurements: a case study of the Guabirotuba area, Curitiba, Brazil. *Bulletin of Geodetic Sciences*. 2022. Vol. 28. Iss. 1. N e2022005. DOI: [10.1590/s1982-21702022000100005](https://doi.org/10.1590/s1982-21702022000100005)
3. Araszkievicz A. Integration of Distributed Dense Polish GNSS Data for Monitoring the Low Deformation Rates of Earth's Crust. *Remote Sensing*. 2023. Vol. 15. Iss. 6. N 1504. DOI: [10.3390/rs15061504](https://doi.org/10.3390/rs15061504)
4. Bevis M., Bedford J., Caccamise II D.J. The Art and Science of Trajectory Modelling. *Geodetic Time Series Analysis in Earth Sciences*. Springer, 2020, p. 1-27. DOI: [10.1007/978-3-030-21718-1_1](https://doi.org/10.1007/978-3-030-21718-1_1)
5. Bilgen B., Inal C. An open-source software for geodetic deformation analysis in GNSS networks. *Earth Science Informatics*. 2022. Vol. 15. Iss. 3. P. 2051-2062. DOI: [10.1007/s12145-022-00844-1](https://doi.org/10.1007/s12145-022-00844-1)
6. Bui T.H.T. Transformation coordinates between international terrestrial reference frames. *Journal of Mining and Earth Sciences*. 2013. Vol. 41. N 1, p. 53-57 (in Vietnamese).
7. Bui T.H.T. Research on the theoretic basis for the modernization of the national geodetic control network in Vietnam by global navigation satellite system GNSS: Specialty Geodesy and Mapping Ph.D. thesis, Hanoi University of Mining and Geology, Hanoi, Vietnam (2014), p. 142.
8. Bui T.H.T. Determination of absolute crustal movements of Việt Nam territory from data of Differential Global Navigation Satellite System (DGNSS). *Journal of Geology. Series A*. 2014. Vol. 340 (1-2), p. 46-52.
9. Butwong K., Thongtan T., Boonterm K. Precision coordinate transformations for Thai national geodetic infrastructure. 20th International Conference on Electrical Engineering/Electronics, Computer, Telecommunications and Information Technology (ECTI-CON), 9-12 May 2023, Nakhon Phanom, Thailand. IEEE, 2023, p. 4. DOI: [10.1109/ECTI-CON58255.2023.10153290](https://doi.org/10.1109/ECTI-CON58255.2023.10153290)
10. Gang Chen, Anmin Zeng, Feng Ming, Yifan Jing. Multi-quadratic collocation model of horizontal crustal movement. *Solid Earth*. 2015. Vol. 7. Iss. 3, p. 817-825. DOI: [10.5194/se-7-817-2016](https://doi.org/10.5194/se-7-817-2016)



11. Pengfei Cheng, Yingyan Cheng, Xiaoming Wang, Yantian Xu. Update China geodetic coordinate frame considering plate motion. *Satellite Navigation*. 2021. Vol. 2. N 2. DOI: [10.1186/s43020-020-00032-w](https://doi.org/10.1186/s43020-020-00032-w)
12. Gill J., Shariff N.S., Omar K., Amin Z.M. Tectonic motion of Malaysia: analysis from years 2001 to 2013. ISPRS Annals of the Photogrammetry, Remote Sensing and Spatial Information Sciences: Joint International Geoinformation Conference, 28-30 October 2015, Kuala Lumpur, Malaysia. Copernicus Publications, 2015. Vol. II-2/W2, p. 199-206. DOI: [10.5194/isprsannals-II-2-W2-199-2015](https://doi.org/10.5194/isprsannals-II-2-W2-199-2015)
13. Guohua Gu, Wuxing Wang. Advantages of GNSS in Monitoring Crustal Deformation for Detection of Precursors to Strong Earthquakes. *Positioning*. 2013. Vol. 4. N 1, p. 11-19. DOI: [10.4236/pos.2013.41003](https://doi.org/10.4236/pos.2013.41003)
14. Häkli P., Evers K., Jivall L. et al. NKG2020 transformation: An updated transformation between dynamic and static reference frames in the Nordic and Baltic countries. *Journal of Geodetic Science*. 2023. Vol. 13. Iss. 1. N 20220155. DOI: [10.1515/jogs-2022-0155](https://doi.org/10.1515/jogs-2022-0155)
15. Hodgkinson K.M., Mencin D.J., Feaux K. et al. Evaluation of Earthquake Magnitude Estimation and Event Detection Thresholds for Real-Time GNSS Networks: Examples from Recent Events Captured by the Network of the Americas. *Seismological Research Letters*. 2020. Vol. 91. N 3, p. 1628-1645. DOI: [10.1785/0220190269](https://doi.org/10.1785/0220190269)
16. Jagoda M., Rutkowska M. An Analysis of the Eurasian Tectonic Plate Motion Parameters Based on GNSS Stations Positions in ITRF2014. *Sensors*. 2020. Vol. 20. Iss. 21. N 6065. DOI: [10.3390/s20216065](https://doi.org/10.3390/s20216065)
17. Maciuk K., Szombara S. Annual crustal deformation based on GNSS observations between 1996 and 2016. *Arabian Journal of Geosciences*. 2018. Vol. 11. Iss. 21. N 667. DOI: [10.1007/s12517-018-4022-4](https://doi.org/10.1007/s12517-018-4022-4)
18. Kuncoro H., Meilano I., Susilo S. Sunda and Sumatra Block Motion in ITRF2008. International Symposium on Global Navigation Satellite System 2018, 21-23 November 2018, Bali, Indonesia. E3S Web of Conferences. 2019. Vol. 94. N 04006. DOI: [10.1051/e3sconf/20199404006](https://doi.org/10.1051/e3sconf/20199404006)
19. Minh L.H., Masson R., Bourdillon A. et al. Recent crustal motion in Vietnam and in the Southeast Asia region by continuous GPS data. *Vietnam Journal of Earth Sciences*. 2014. Vol. 36. N 1, p. 1-13 (in Vietnamese). DOI: [10.15625/0866-7187/36/1/4132](https://doi.org/10.15625/0866-7187/36/1/4132)
20. Minh L.H., Hung V.T., Hu J.-C. et al. Contemporary movement of the Earth's crust in the Northwestern Vietnam by continuous GPS data. *Vietnam Journal of Earth Sciences*. 2020. Vol. 42. N 4, p. 334-350. DOI: [10.15625/0866-7187/42/4/15282](https://doi.org/10.15625/0866-7187/42/4/15282)
21. Azhari M., Altamimi Z., Azman G. et al. Semi-kinematic geodetic reference frame based on the ITRF2014 for Malaysia. *Journal of Geodetic Science*. 2020. Vol. 10. Iss. 1, p. 91-109. DOI: [10.1515/jogs-2020-0108](https://doi.org/10.1515/jogs-2020-0108)
22. Mattioli G., Mencin D., Hodgkinson K. et al. The EarthScope Plate Boundary Observatory and allied networks, the makings of nascent Earthquake and Tsunami Early Warning System in Western North America. European Geosciences Union General Assembly, 23-28 April 2017, Vienna, Austria. Geophysical Research Abstracts. 2016. Vol. 18. N EGU2016-10953.
23. Duong N., Sagiya T., Kimata F. et al. Contemporary horizontal crustal movement estimation for northwestern Vietnam inferred from repeated GPS measurements. *Earth, Planets and Space*. 2013. Vol. 65. Iss. 12, p. 1399-1410. DOI: [10.5047/eps.2013.09.010](https://doi.org/10.5047/eps.2013.09.010)
24. Trọng N.G., Nghĩa N.V., Khải P.C. et al. Determination of tectonic velocities in Vietnam territory based on data of CORS stations of VNGEONET network. *Journal of Hydro-Meteorology*. 2022. Vol. 739, p. 59-66 (in Vietnamese). DOI: [10.36335/VNJHM.2022\(739\).59-66](https://doi.org/10.36335/VNJHM.2022(739).59-66)
25. Ohta Y., Ohzono M. Potential for crustal deformation monitoring using a dense cell phone carrier Global Navigation Satellite System network. *Earth, Planets and Space*. 2022. Vol. 74. Iss. 1. N 25. DOI: [10.1186/s40623-022-01585-7](https://doi.org/10.1186/s40623-022-01585-7)
26. Wei Qu, Hailu Chen, Shichuan Liang et al. Adaptive Least-Squares Collocation Algorithm Considering Distance Scale Factor for GPS Crustal Velocity Field Fitting and Estimation. *Remote Sensing*. 2019. Vol. 11. Iss. 22. N 2692. DOI: [10.3390/rs11222692](https://doi.org/10.3390/rs11222692)
27. Rabah M., Shaker A., Farhan M. Towards a Semi-Kinematic Datum for Egypt. *Positioning*. 2015. Vol. 6. N 3, p. 49-60. DOI: [10.4236/pos.2015.63006](https://doi.org/10.4236/pos.2015.63006)
28. Rudenko S., Esselborn S., Schöne T., Dettmering D. Impact of terrestrial reference frame realizations on altimetry satellite orbit quality and global and regional sea level trends: a switch from ITRF2008 to ITRF2014. *Solid Earth*. 2019. Vol. 10. Iss. 1, p. 293-305. DOI: [10.5194/se-10-293-2019](https://doi.org/10.5194/se-10-293-2019)
29. Steffen R., Legrand J., Ågren J. et al. HV-LSC-ex²: velocity field interpolation using extended least-squares collocation. *Journal of Geodesy*. 2022. Vol. 96. Iss. 3. N 15. DOI: [10.1007/s00190-022-01601-4](https://doi.org/10.1007/s00190-022-01601-4)
30. Tamay J., Galindo-Zaldivar J., Soto J., Gil A.J. GNSS Constraints to Active Tectonic Deformations of the South American Continental Margin in Ecuador. *Sensors*. 2021. Vol. 21. Iss. 12. N 4003. DOI: [10.3390/s21124003](https://doi.org/10.3390/s21124003)
31. Tran D.T., Nguyen Q.L., Nguyen D.H. General Geometric Model of GNSS Position Time Series for Crustal Deformation Studies – A Case Study of CORS Stations in Vietnam. *Journal of the Polish Mineral Engineering Society*. 2021. Vol. 1. N 2, p. 183-198. DOI: [10.29227/JM-2021-02-16](https://doi.org/10.29227/JM-2021-02-16)
32. Trần Đ.T., Nguyễn T.Y., Dương C.C. et al. Recent crustal movements of northern Vietnam from GPS data. *Journal of Geodynamics*. 2013. Vol. 69, p. 5-10. DOI: [10.1016/j.jog.2012.02.009](https://doi.org/10.1016/j.jog.2012.02.009)
33. Tucikešić S., Milinković A., Božić B. et al. GNSS Time Series as a Tool for Seismic Activity Analysis Related to Infrastructure Utilities. *Contributions to International Conferences on Engineering Surveying*. Cham: Springer, 2021, p. 246-256. DOI: [10.1007/978-3-030-51953-7_21](https://doi.org/10.1007/978-3-030-51953-7_21)
34. Hai V.Q., Cuong T.Q., Thuan N.V. Crustal movement along the Red River Fault zone from GNSS data. *Vietnam Journal of Earth Sciences*. 2016. Vol. 38. N 1, p. 14-21 (in Vietnamese). DOI: [10.15625/0866-7187/38/1/7846](https://doi.org/10.15625/0866-7187/38/1/7846)
35. Wang Wei, Dang Ya-Min, Zhang Chuan-Yin et al. Monitoring crustal deformation and gravity change caused by the terrestrial water load in the three gorges area base on CORS network. *Chinese Journal of Geophysics*. 2017. Vol. 60. Iss. 2, p. 154-163. DOI: [10.1002/cjg2.30035](https://doi.org/10.1002/cjg2.30035)
36. Jarmołowski W. A priori noise and regularization in least squares collocation of gravity anomalies. *Geodesy and Cartography*. 2013. Vol. 62. N 2, p. 199-216. DOI: [10.2478/geocart-2013-0013](https://doi.org/10.2478/geocart-2013-0013)
37. Jarmołowski W., Bakula M. Two covariance models in Least Squares Collocation (LSC) tested in interpolation of local topography. *Contributions to Geophysics and Geodesy*. 2013. Vol. 43. N 1, p. 1-19. DOI: [10.2478/congeo-2013-0001](https://doi.org/10.2478/congeo-2013-0001)

Authors: Bui Thi Hong Tham, PhD, Dean, <https://orcid.org/0000-0002-3932-4040> (Hanoi University of Natural Resources and Environment, Hanoi, Vietnam), Phi Truong Thanh, Associate Professor, Dean, pthanhdc@hunre.edu.vn, <https://orcid.org/0000-0003-0421-6557> (Hanoi University of Natural Resources and Environment, Hanoi, Vietnam).

The authors declare no conflict of interests.



Radiation characteristics of coals at different stages of metamorphism

Nadezhda L. Aluker✉, Boris P. Aduiev, Denis R. Nurmukhametov

Federal Research Center of Coal and Coal Chemistry, Siberian Branch of the RAS, Kemerovo, Russia

How to cite this article: Aluker N.L., Aduiev B.P., Nurmukhametov D.R. Radiation characteristics of coals at different stages of metamorphism. Journal of Mining Institute. 2025. Vol. 271. N 16332, p. 131-140.

Abstract

The formation of deposits and subsequent metamorphic processes that affect concentrations of radioactive elements in coal can indicate ongoing geological activities, therefore, analyzing trends in the radiation characteristics of coal throughout the metamorphic series is highly relevant. The aim of this work is to experimentally evaluate the radiation characteristics of different coal ranks (metamorphic stages) using thermoluminescent (TL) dosimetry and beta activity measurements, and to identify correlations between these radiation characteristics and data obtained from technical, elemental, and thermogravimetric analyses, as well as mass spectrometric and electron paramagnetic resonance spectroscopy (EPR) measurements. For dosimetric measurements that indirectly characterize the content of radionuclides in coal, a modified dosimetric complex and original soil-equivalent thermoluminescent detectors based on SiO₂ were used. The analysis of the obtained results supports the use of TL studies to determine the ash content of coals at low and medium stages of metamorphism (coal rank B→G), while indicating that this method is not feasible for coals at higher stages of metamorphism. The correlation dependencies in the metamorphism series suggest abrupt change in the conditions of coal formation during the time range corresponding to transformation from high to low volatile bituminous coals (coal rank G→Zh→K). These abrupt changes in regional metamorphism conditions (time, temperature, pressure, oxidation-reduction conditions) are confined to the boundary of the Permian and Triassic periods (~250 million years ago), during which both the transformation of existing coal deposits and the formation of new deposits occurred.

Keywords

coal; metamorphism; ash content; thermoluminescence; absorbed dose; radioactivity

Funding

This work was carried out as part of the State assignment of the Institute of Coal Chemistry and Material Science, Federal Research Center for Coal and Coal Chemistry, Siberian Branch of the RAS (project 121031500513-4) using the equipment of the Shared Research Facilities of the Federal Research Center for Coal and Coal Chemistry, Siberian Branch of the RAS.

Received: 28.10.2023

Accepted: 07.11.2024

Online: 17.01.2025

Published: 25.02.2025

Introduction

The radioactivity of coal, like that of other natural objects, is determined by the content of natural uranium and thorium in equilibrium with their decay products, as well as the content of a number of beta-emitting long-lived isotopes (⁴⁰K, ⁵⁰V, ⁸⁷Rb, ¹¹⁵In, ¹²³Te, ¹³⁸La, ¹⁷⁶Lu, ¹⁸⁷Re), the main one being ⁴⁰K due to its high content [1-3].

The content of ²³⁸U and the equilibrium amount of ²²⁶Ra in solid coal matrix generally corresponds to their content in soils and is at safe concentration levels. Due to the good solubility of ²²⁶Ra, equilibrium distribution can be disrupted. The decay of ²²⁶Ra leads to the appearance of a gaseous short-lived decay product (²²²Rn), whose potential release into the inter-pore space from the solid matrix usually disrupts the natural radioactive equilibrium in the ²³⁸U series [3-5]. In equilibrium with its nearest short-lived decay products, in the absence of a new source of ²²²Rn, it rapidly decays according to an exponential law, so emanation can only be detected at the location of a constant radon source [3]. The short-lived decay products of ²²²Rn produce α-, β- and γ- radiation.



Radioactive impurities are present in both the organic and ash fractions of coal. Thorium is mainly found in phosphate minerals (monazite, apatite), while uranium is present both in mineral inclusions – uranium-thorium-containing minerals (zirconium, pyrochlore, monazite, or their own minerals) – and in the organic fraction as organometallic compounds. The organic part usually contains an order of magnitude less uranium than the inorganic part (which determines the ash content); therefore, after coal combustion, most of the uranium, thorium and their decay products are retained in solid waste (the specific concentration of radioactive elements in ash is 5-7 times higher than in the original coal) [2, 6-8]. Elevated levels of uranium and thorium in coals are often accompanied by the accumulation of rare-earth elements, zirconium, hafnium, and other rare elements [6-8].

In general, the radionuclide content in the coals of the Kuznetsk Basin is not high and is comparable to that in soils [3, 9]. The worst radiation levels in Kuzbass are found in the brown (lignite and sub-bituminous) coals of the Kansk-Achinsk Basin, mined in the Kemerovo region at the Itatsky open-pit mine [3, 6-9]. The uranium content in coals and host rocks of the Itatsky deposit is several times higher than the values typical for Kuzbass (uranium, average – 56.9 g/t, variations – 6-139 g/t) [3, 7]. The distribution of uranium across the open-pit area is localized, with areas of elevated content occupying ~20 % of the area [3, 7]. In the ash and slag material formed during the combustion of such coal, the uranium content reaches up to 900 g/t, and this material is classified according to global standards as ordinary uranium ore (uranium content range of 0.05-0.1 %) [9-11].

Since radionuclides are concentrated in 10-20 % of the mineral fraction of coal, radioactivity can reflect the mineral content of coal and correlate with the ash content of samples [12-14].

This study investigates the radiation characteristics of coals from the Kuznetsk Basin across different stages of metamorphism and correlates the obtained data with the results of technical analysis [15-17] and other physicochemical studies (elemental and thermogravimetric analyses, mass spectrometric and EPR studies) [18-21], with the aim to determine the feasibility of using the radiation characteristics of coal to assess ash content and analyze changes in radiation characteristics across the metamorphic series.

Methods

Samples and research methodology. Coals (Table 1) from the metamorphic series with particle sizes ≤ 3 mm were studied [13-15, 19]. A representative sample of coals was transferred into a plastic container (1 liter), filling it to 2/3, with thermoluminescent detectors placed inside. Thus, the detectors were surrounded on all sides by a layer of coal and were kept in the sample for 20 days.

For all selected representative samples from the metamorphic series, comprehensive information was available regarding the coal mine of provenance, technical characteristics (Table 1), and the results of extended physicochemical analyses conducted at the Shared Research Facilities of the Federal Research Center for Coal and Coal Chemistry, Siberian Branch of the RAS [13-15].

Table 1

Characteristics of coal samples

Analytical sample description	Coal rank	A_d , %	V_{daf} , %	W_a , %
N 27, open-pit mine “Kaichaksky”	B	10	53.1	11.8
N 72, open-pit mine “Kamyshansky”	D	6.2	44.5	7.6
N 64, mine “V.D.Yalevsky”, seam 52	DG	4.7	42.6	5.7
N 40, mine “S.M.Kirov”, seam Polenovskiy	G	3.3	40.4	1.2
N 15, mine “S.D.Tikhova”, seam 23	Zh	7.8	33.3	0.8
N 10, OOO “Uchastok Koksovy”, seam II internal	K	4.9	21.3	0.6
N 34, open-pit mine “Tomusinsky”	OS	6.7	19.8	0.1
N 45, open-pit mine “Bachatsky”	SS	4.7	19.0	1.3
N 81, AO “Kuznetskinveststroy”, seam 19a	T	6.2	14.4	0.5

Notes: A_d – ash content; V_{daf} – volatile matter yield; W_a – analytical moisture content.

Equipment. The study of absorbed doses accumulated in coals due to the presence of radioactive elements was conducted using the thermoluminescence dosimetry method [3, 22, 23]. A modified



dosimetric complex DTU-01M was used, providing signal registration in the temperature range up to 450 °C with the ability to change the heating rate from 1 to 20 °C/s. The DTU-01M dosimetric device was calibrated together with TLD-K detectors based on SiO₂, which were placed in the analyzed sample for a fixed exposure period, and the absorbed doses caused by the radionuclide content in the coal were calculated based on the detector readings [3, 24]. Because the effective atomic number, Z_{eff} , of the detectors closely corresponds to that of quaternary deposits, the detectors correctly measure the absorbed dose [3, 23, 24].

After exposure, the detectors were placed on the heating element of the calibrated DTU-01M complex, and the absorbed dose was measured in centigrays (cGy). To register background radiation, the detectors were also placed in a container without coal. The background radiation was subtracted to quantify the annual dose due to the content of radionuclides in coal, in excess of the background dose.

Due to the lack of hygroscopicity, TLD-K detectors can be used for dosimetry of aqueous media, i.e. for studying the characteristics of mine waters, settling ponds, discharges, and drinking surface and borehole waters [3].

To determine the beta activity of coals (Bq/kg), a KRVP-3B radiometer with a large lead chamber was used. The activity of dried potassium chloride powder, which has a standard beta activity due to its ⁴⁰K content, was measured as a reference sample.

EPR measurements were carried out using a Bruker EMX 6/1 micro spectrometer in the X-band (9.5 GHz) with the following settings:

- magnetic field sweep range $\Delta H = 1300\text{-}5600$ Gs;
- signal gain coefficient $2.24 \cdot 10^2$;
- microwave power attenuation 20 dB;
- signal conversion time 15 ms;
- signal sweep time 31 s.

Results

The results of dosimetry and determination of beta activity of coal samples are presented in Table 2. Each sample contained at least five detectors; Table 2 shows the average values and deviations for the samples. The average deviation did not exceed 3 % for any of the samples. The results indicate that specific beta activities and the absorbed doses in addition to the background are correlated, decreasing with increase in coal metamorphism from grade B to grade Zh; and highly metamorphosed coals are more radioactive than moderately metamorphosed coals.

Table 2

Results of dosimetry and determination of beta activity of coal samples

Coal rank	Dose during monitoring D , cGy	Average deviation ΔD , cGy	Annual absorbed dose, cGy/year	Annual absorbed dose minus background, cGy/year	Specific beta activity A , Bq/kg
B	0.0225	0.0005	0.411	0.081	75
D	0.0208	0.0004	0.380	0.050	46
DG	0.0202	0.0004	0.369	0.039	37
G	0.0196	0.0004	0.358	0.028	27
Zh	0.0190	0.0004	0.346	0.016	16
K	0.0221	0.0005	0.404	0.074	72
OS	0.0235	0.0007	0.428	0.098	84
SS	0.0225	0.0006	0.410	0.080	60
T	0.0241	0.0007	0.440	0.110	62

Correlation analysis of radiation characteristics of coals in the metamorphism series with other physicochemical characteristics. Figure 1 shows the dependencies of absorbed doses on moisture content and volatile matter yield, along with the correlation coefficients when approximating the data with a linear relationship.

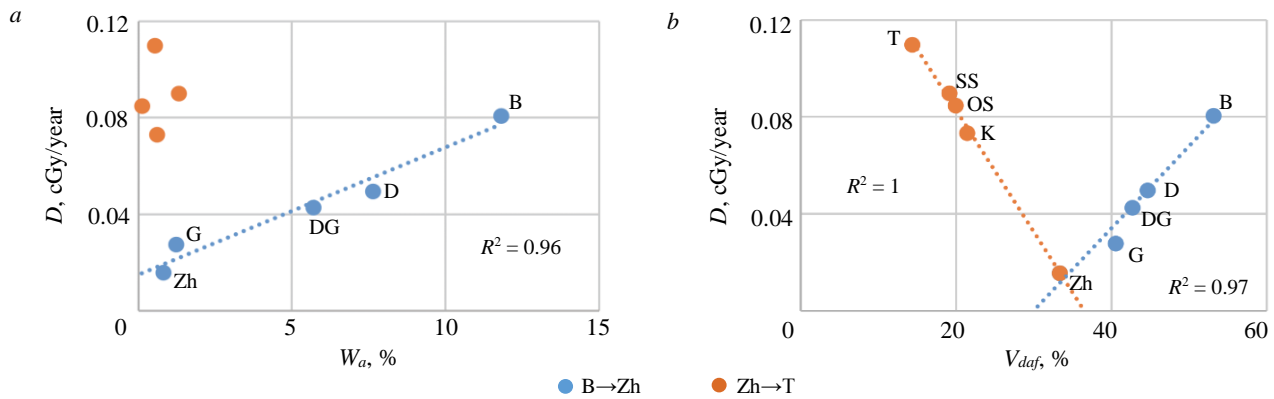


Fig.1. Dependence of the absorbed dose, formed in coals due to radioactive elements, on moisture content (a) and volatile matter yield (b)

Comparison of radiation characteristics with the results of technical analysis of coal samples in the B→T series shows:

- the dependence of the absorbed dose on the degree of coal metamorphism in the B→T series is complex. From B→Zh, radioactivity decreases to the minimum values in the Zh sample, and then, with increasing metamorphism, radioactivity increases from Zh→T (Fig.1);
- coals with higher moisture content in the Zh→B series (decreasing degree of metamorphism) are more radioactive, suggesting that some radionuclides are in water-soluble compounds;
- the radioactivity of coals increases with a volatile matter yield of more than 35 % (in the Zh→B series). For highly metamorphosed coals (in the T→Zh series), radioactivity decreases with a volatile matter yield in the range of 15 to 35 %. This trend suggests that some radionuclides are associated with the organic fraction of the coal.

Since radionuclides are mainly concentrated in the ash part of coal, let us consider the dependence of the absorbed dose D on the ash content A_d (Fig.2).

For coal samples in the G→B series, the ash content of the samples increases from 3 to 10 %, and in this series, a linear increase in absorbed doses is observed (Fig.2, a). When the ash content range is expanded to 25 % (including samples of G and D coals with high ash content from the “Zarechnaya” mine), samples with higher ash content fit well into the linear dependence of dose on ash content (Fig.2, b). This allows for a preliminary conclusion about the possibility of determining the ash content of coal samples of low and medium degrees of metamorphism based on their radiation characteristics. An additional argument confirming the possibility of using dosimetric studies of coals to determine ash content is the constancy of doses normalized to ash content in the B→G series. The slight change in absorbed doses per unit ash content in the B→G series of metamorphosed coals may contribute minimally to the error in determining ash content based on radioactivity.

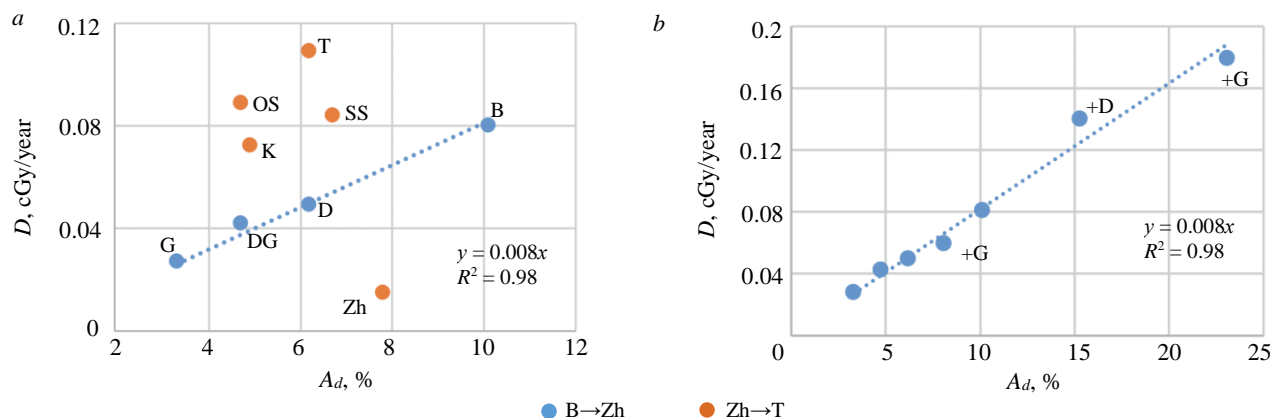


Fig.2. Dependence of the absorbed dose on the ash content of coal samples $A_d = 3-10$ % (a) and up to 25 % (b)



For samples in the Zh→T series, no dependence of the dose on the ash content is observed (Fig.2, *a*). It should be noted that the dose per unit ash content for K→T coals, with a wide range of values, is almost twice as high as for low- and medium-metamorphosed coals. This may indicate the presence of radionuclides in the organic matrix of highly metamorphosed coals. The Zh coal sample stands out with a low value of the dose normalized to ash content.

When comparing the radiation characteristics of coals in the metamorphism series with the results of elemental analysis of organic elements in coal samples in the B→Zh series, the following patterns are observed (Fig.3):

- decrease in the radioactivity of samples with an increase in the content of carbon, nitrogen, and hydrogen (increase in the degree of metamorphism);
- increase in absorbed doses with an increase in oxygen content (decrease in the degree of metamorphism);
- coals with higher degrees of metamorphism show a change in the trend and reveal different tendencies in the Zh→T series;
- with an increase in the degree of metamorphism in the Zh→T series, absorbed doses increase after passing the minimum for Zh coals.

The decrease in absorbed doses with an increase in nitrogen concentration in the B→Zh series (increase in the degree of metamorphism) changes to an increase in dose with a decrease in nitrogen content when transitioning to higher degrees of metamorphism in the Zh→T series. The turning point is the Zh coal sample.

A characteristic inflection of the characteristics when crossing the degree of metamorphism Zh is observed for oxygen content at a concentration of ~15 %, carbon at a concentration of ~78 % (Fig.3), and for volatile matter content at a concentration of ~35 % in coal samples (see Fig.1). Absorbed doses pass through a minimum at certain concentrations and then increase with the degree of metamorphism. The observed patterns likely result from sharply changing conditions of coal formation or transformation (time, temperature, pressure, etc.) during the formation of coal deposits of grades G→Zh→K.

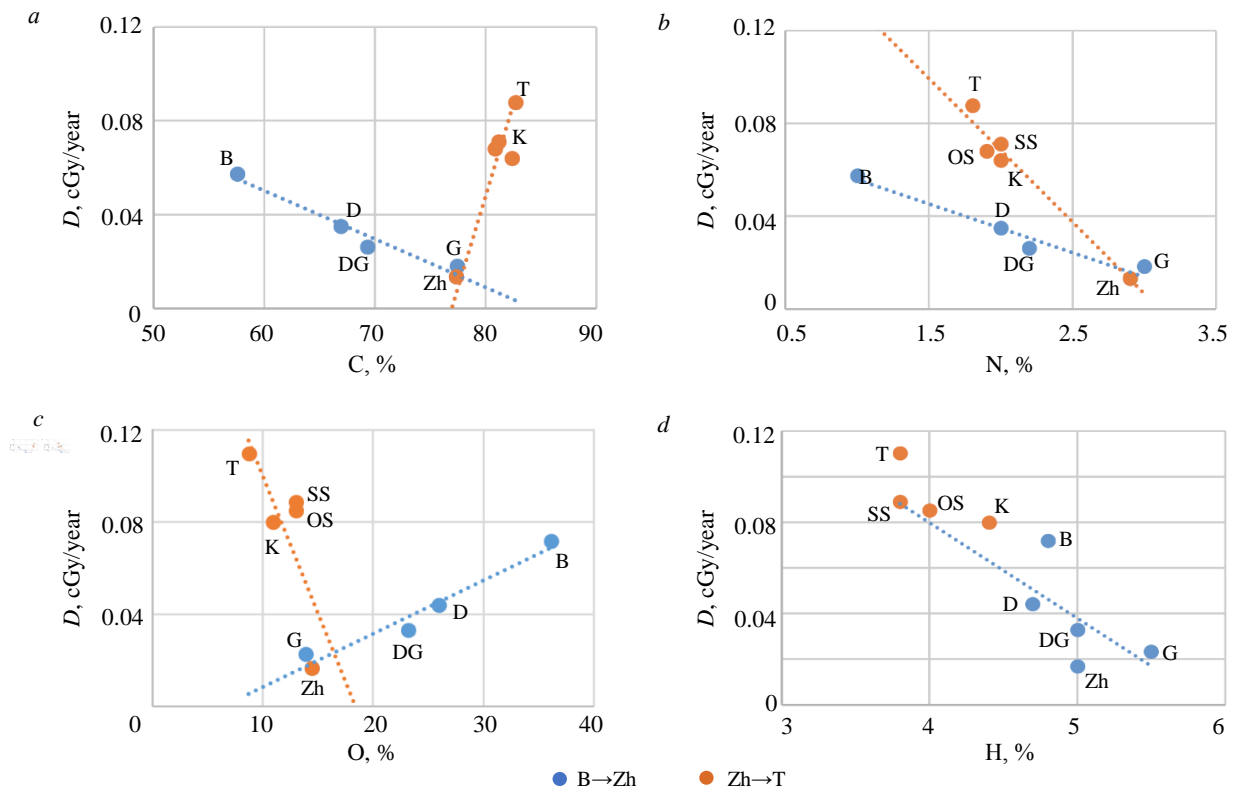


Fig.3. Dependence of the absorbed dose on the content of carbon (*a*), nitrogen (*b*), oxygen (*c*) and hydrogen (*d*) in the metamorphism series

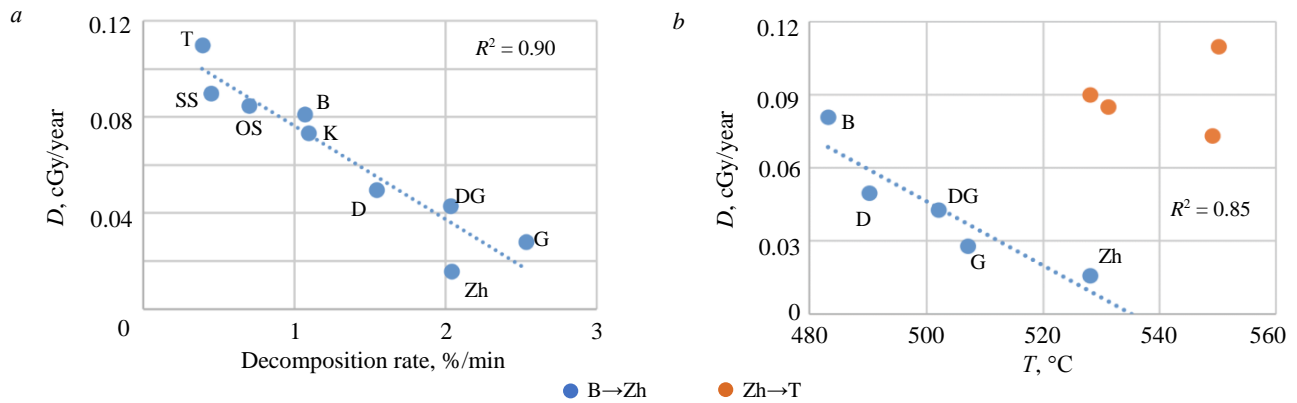


Fig.4. Correlation dependences of absorbed doses and degrees of metamorphism on the rates of coal decomposition (a) and the temperatures of maximum H_2O release in an inert environment (b)

The dependence of absorbed doses and degrees of metamorphism on the rates of coal decomposition and the temperatures of maximum H_2O release in an inert environment in Fig.4 is multidirectional. With an increase in the decomposition rate of coal samples in an inert environment, a decrease in absorbed dose is observed for T→K coals (decrease in the degree of metamorphism) and for B→Zh coals (increase in the degree of metamorphism), with minimum dose values for the metamorphism stages G and Zh (Fig.4). A similar trend is observed for the dependence of absorbed dose on hydrogen concentration (see Fig.3). The maximum temperatures of H_2O release during decomposition in an inert environment in the B→Zh series increase with a decrease in absorbed doses.

The distribution of carbon across structural fragments – carbonyl (C=O); carboxyl (COOH); aromatic carbon atoms (C_{ar}); aromatic carbon atoms bonded to oxygen atoms ($C_{ar}-O$); protonated aromatic carbon atoms ($C_{ar}-H$); methoxyl fragments (OCH₃); alkyl fragment carbon atoms (CH₂) – modeled based on NMR studies in an inert environment, shows diverse behavior of fragments depending on absorbed doses (degrees of metamorphism of samples) (Fig.5). With the increase in the

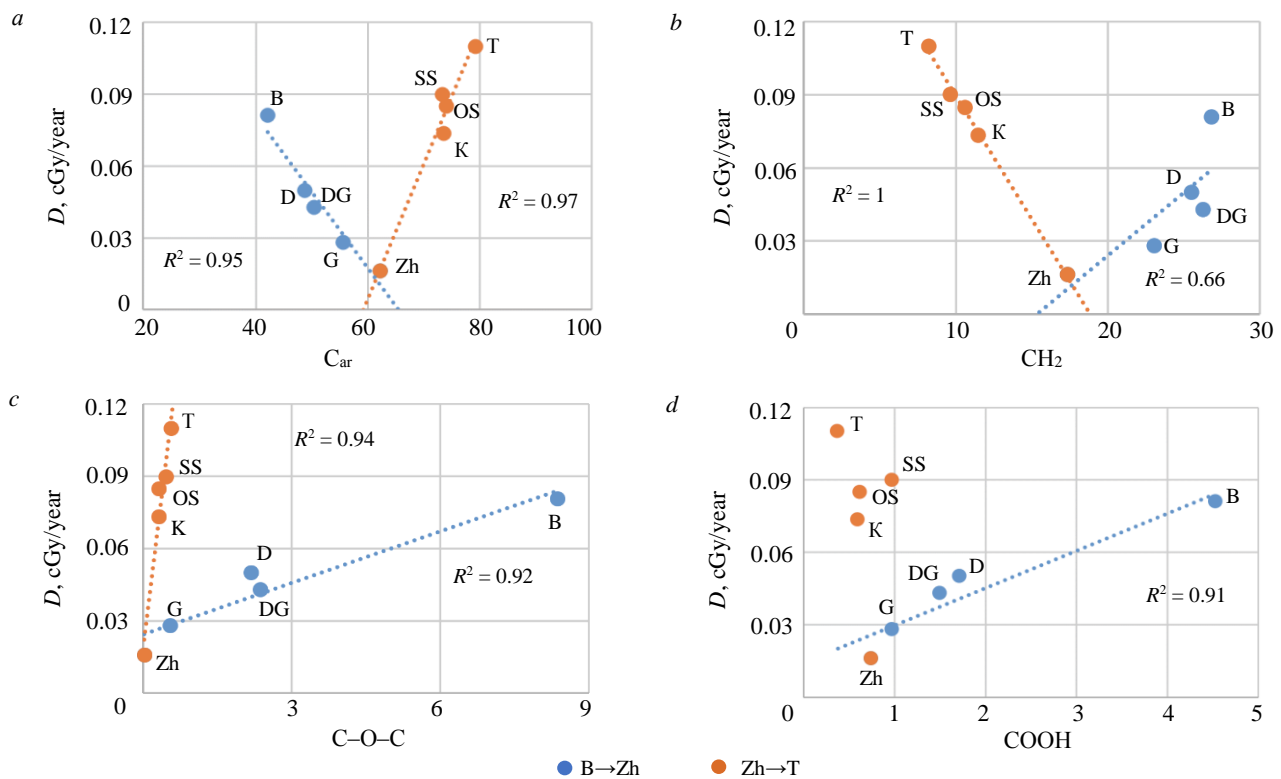


Fig.5. Correlation dependences of absorbed doses and degrees of metamorphism from structural fragments of carbon in the series B→T: C_{ar} (a); CH_2 (b); $C-O-C$ (c) and $COOH$ (d)



degree of metamorphism and the decrease in absorbed doses in the B→Zh series, there is an increase in the content of C_{ar} , as well as CH_3 and OCH_3 fragments, and a decrease in the amount of $C_{ar}-H$, $C_{ar}-O$, CH_2 fragments, $C-O-C$, $COOH$, and $C=O$. The correlation dependencies of C_{ar} , CH_2 , $C-O-C$, and $COOH$ on the absorbed dose for the entire studied metamorphism series are shown in Fig.5.

As in Fig.1 and 4, a characteristic inflection of the dependencies is observed when coals pass through the degrees of metamorphism $G \rightarrow Zh \rightarrow K$, with a turning point at the Zh stage. For coals of high metamorphism stages, an increase in dose with an increase in the degree of metamorphism is observed, along with an increase in C_{ar} and $C-O-C$ content and a decrease in CH_2 content.

Figure 6 shows the dependence of the number of paramagnetic centers on the dose normalized to ash content, i.e., the dose per unit ash content. Coals exhibit paramagnetism due to the presence of various types of paramagnetic centers (defects) [25-27]. Paramagnetic centers can accumulate in coal due to prolonged exposure to alpha-emitting radionuclides contained in them [28, 29].

With an increase in the degree of metamorphism, there is an increase in the normalized absorbed dose and the number of paramagnetic centers. Along with the radioactivity of coals, the time factor also plays a role in the observed dependence. The younger the coal, the less time it is exposed to radiation from radionuclides contained in the sample or the surrounding rocks, and the fewer paramagnetic centers it contains. The older the coal, the longer the exposure time and the higher the accumulated number of paramagnetic centers.

The Zh coal sample deviates from the dependence, as it has a high number of paramagnetic centers despite the minimum absorbed dose and average age. It can be assumed that, in addition to the considered radiation factor, more complex specific conditions of defect formation (temperature, pressure, etc.) are responsible for their creation.

Discussion of results

The changes in radioactivity in the coal metamorphism series at low and medium stages of metamorphism are generally predictable and are determined by the time frames of coal formation and the half-lives of the main present radionuclides [1-3]. The age of the oldest coals is estimated at $3.5 \cdot 10^8$ years, and the half-lives of the main radionuclides are comparable to this age (Table 3).

Table 3

Characteristics of decay and activity estimates of the main radionuclides contained in coal

Radionuclide	Half-life, coal age (years)	Specific activity, Bq/g	Radionuclide content in natural element mixture, %	Average radionuclide content in coal, g/t	Average radionuclide activity in coal, Bq/kg
^{40}K	$1.25E+09$	$2.65E+05$	0.0119	0.1	29.3
^{238}U	$4.5E+09$	$1.2E+04$	99.3	1.9	23.4
^{235}U	$7.1E+08$	$7.9E+04$	0.7	$1.2E-02$	0.96
^{234}U	$2.45E+05$	$2.3E+08$	0.0055	0.0	0.0
^{232}Th	$1.4E+10$	$3.1E+03$	100	6.9	21.4
Coal	$3.5E+08$	0.075			$\Sigma 75$

After the formation of the radionuclides in the coal, coal activity naturally decreases over time, which may explain the observed decrease in activity in the B→K series with comparable concentrations of radionuclides during formation. With an increase in the degree of metamorphism due to prolonged irradiation of the coal mass by radionuclides contained in the sample, the number of radiation

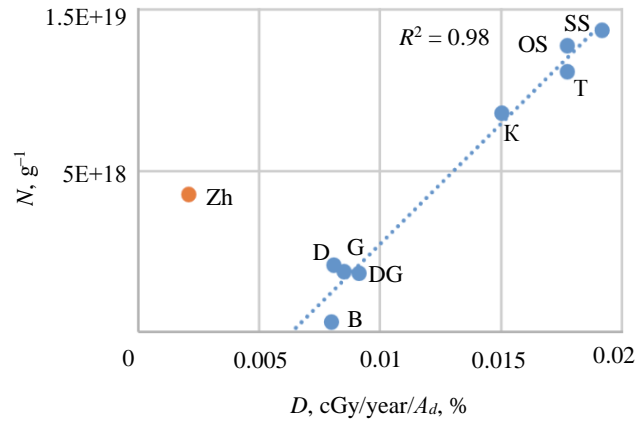


Fig.6. Dependence of the number of paramagnetic centers in a gram of coal on the absorbed dose normalized to ash content (for coal with unit ash content)



defects should increase, which is observed experimentally in EPR studies. Thus, the time factor of metamorphism explains the observed dependence of changes in the radioactivity of samples in the series of weakly metamorphosed samples. For highly metamorphosed samples, it is necessary to assume the presence of radionuclides in both the mineral and organic components of coals, with higher radionuclide content in the biosphere during their formation.

A linear dependence of radioactivity on ash content is recorded at medium and low degrees of metamorphism ($G \rightarrow B$) and can be used to determine the ash content of a sample by its radioactivity. When transitioning to higher degrees of metamorphism, the dependence becomes significantly more complex.

The dependencies of absorbed dose on volatile yield, carbon, oxygen, nitrogen concentrations, and carbon structural fragments shown in Fig.1, 3, and 5 demonstrate a sharp change in absorbed doses when transitioning from Zh coal to higher degrees of metamorphism. All dependencies undergo a sharp change in trend with a tendency for absorbed doses to increase in the $K \rightarrow T$ metamorphism series, contrary to what is observed at low degrees of metamorphism. The sharp change in the trend of dependencies can only be explained by invoking the hypothesis of significant changes in the conditions of formation or transformation of coal masses (temperature, depth, pressure, gas environment, mineralization, redox conditions) [26-29]. The change in radionuclide accumulation conditions in coals occurs during the stages of metamorphism $G \rightarrow Zh \rightarrow K$ and is likely associated with global processes during their formation period, with more intense radionuclide input into biosphere objects during the formation of highly metamorphosed coals.

Changes in the trend of dependencies at the boundary of metamorphism $G \rightarrow Zh \rightarrow K$ can be traced without involving radiation measurements if the volatile matter content in coal is taken as an indicator of the degree of metamorphism (Fig.7). A sharp change in the rates of carbon and oxygen accumulation, as well as the presence of maxima in hydrogen and nitrogen content, is observed when coals pass through the Zh metamorphism stage.

The combination of identified factors may indicate changes in both radiation conditions and redox conditions in the biosphere during the formation period of $Zh \rightarrow G$ coals [30-32].

Conclusion

The analysis of the results supports the feasibility of using thermoluminescent analyses to determine the absorbed doses formed due to the coal radionuclide content, for determining the ash content of coal with low and medium degrees of metamorphism ($B \rightarrow G$).

The observed correlations of absorbed doses with technical, elemental, and thermogravimetric analysis data, as well as EPR and mass spectrometric study results in the metamorphism series, indicate changes in coal formation (transformation) in the time range of the coals $G \rightarrow Zh \rightarrow K$, with abrupt change in conditions during this period.

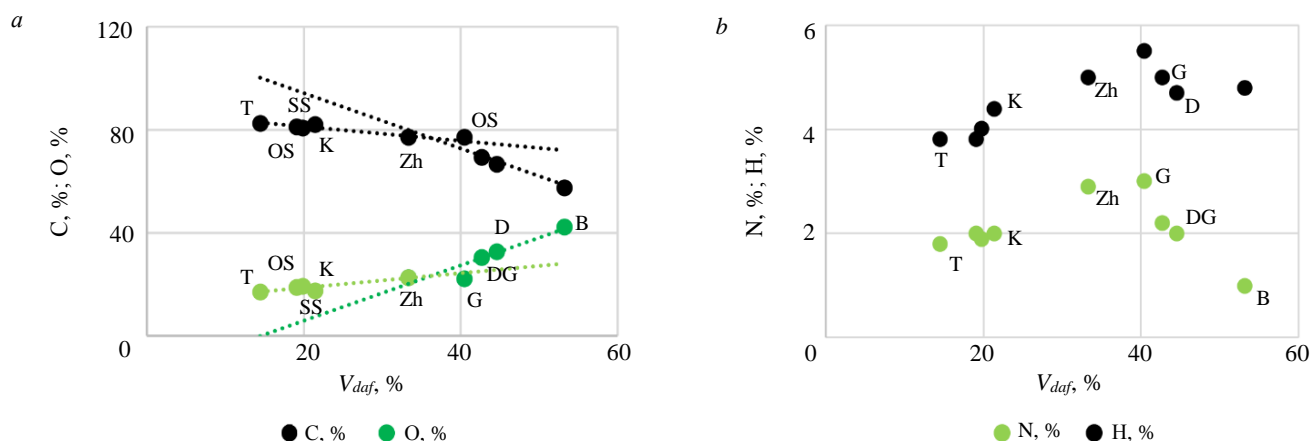


Fig.7. Dependence of concentrations of the main organic elements of coal on the content of volatile substances in coals of different stages of metamorphism: *a* – carbon, oxygen; *b* – nitrogen, hydrogen



Based on the analysis of the results, it can be assumed that the process of coal formation and metamorphism $K \rightarrow T$ spans the time range of the Carboniferous and Permian periods, while coals with lower degrees of metamorphism were formed after a major volcanic activity outbreak at the end of the Permian – early Triassic, which radically changed the structure of the Earth's biosphere. This period is characterized by the release of a large amount of “light” carbon into the atmosphere due to the combustion of surface coal deposits through which rising magma broke through [33-35].

The change in formation conditions is associated with a sharp change in regional metamorphism conditions (time, temperature, pressure, redox conditions) at the boundary of the Permian and Triassic periods (~250 million years ago). This time is characterized by volcanism, continental plate shifts, Siberian Traps eruptions, carbon release into the atmosphere, combustion processes with the deposition of a large amount of products, rapid sediment burial, and the catastrophic extinction of marine and terrestrial life forms on Earth [35-37].

REFERENCES

1. Rikhvanov L.P. Radioactivity and radioactive elements as the factor of the geological environment and his use in sciences about the earth. *Prospect and protection of mineral resources*. 2017. N 12, p. 55-61 (in Russian).
2. Pak Y.N., Pak D.Y., Ponomaryova M.V. et al. Radioactivity of Coal and Its Combustion Wastes. *Coke and Chemistry*. 2018. Vol. 61. N 5, p. 188-192. DOI: [10.3103/S1068364X1805006X](https://doi.org/10.3103/S1068364X1805006X)
3. Aluker N.L., Artamonov A.S., Herrmann M. Radiation Monitoring as a Measure to Improve the Safety of Coal Mining. *Instruments and Experimental Techniques*. 2022. Vol. 65. N 4, p. 628-635. DOI: [10.1134/s0020441222040017](https://doi.org/10.1134/s0020441222040017)
4. Kochkin B.T. Reduced-Type Alterations at Exogenic Infiltration Uranium Deposits and Their Relation to Rising Groundwater. *Geology of Ore Deposits*. 2020. Vol. 62. N 1, p. 19-30. DOI: [10.1134/S1075701520010043](https://doi.org/10.1134/S1075701520010043)
5. Chekryzhov I.Yu., Popov N.Yu., Arbuzov S.I. Uranium and thorium in the coals of the Cainozoic basins of Primorye. Radioactivity and Radioactive Elements in Environment: Proceedings of VI International Conference, 20-24 September 2021, Tomsk, Russia. In 2 volumes. Tomsk: National Research Tomsk Polytechnic University, 2021. Vol. 1, p. 600-604 (in Russian).
6. Sidorova G.P., Krylov D.A. Radiation hazard issues in the coal power generation industry. *Mining Informational and Analytical Bulletin*. 2017. N 11, p. 200-209 (in Russian). DOI: [10.25018/0236-1493-2017-11-0-200-209](https://doi.org/10.25018/0236-1493-2017-11-0-200-209)
7. Fedorin V.A., Nifantov B.F., Anikin M.V., Borisov I.L. Valuable impurity elements in Kuzbass coals. *Naukoemkie tekhnologii razrabotki i ispolzovaniya mineralnykh resursov*. 2017. N 3, p. 85-88 (in Russian).
8. Vyalov V.I., Nastavkin A.V. Concentration Levels of Industrially Valuable Trace Elements in Coals. *Solid Fuel Chemistry*. 2019. Vol. 53. N 5, p. 314-318. DOI: [10.3103/S0361521919050112](https://doi.org/10.3103/S0361521919050112)
9. Schastlivtsev E.L., Kovalev V.A., Potapov V.P. Monitoring the state of the natural environment in coal mining areas of Kuzbass. Novosibirsk: SO RAN, 2013, p. 312 (in Russian).
10. Artemev V.B., Galkin V.A., Makarov A.M. et al. Mechanism for preventing the occurrence of a hazardous production situation. *Ugol*. 2016. N 5, p. 73-77 (in Russian). DOI: [10.18796/0041-5790-2016-5-73-77](https://doi.org/10.18796/0041-5790-2016-5-73-77)
11. Cheng-lin Miao, Meng-meng Duan, Xin-xiu Sun, Xin-yu Wu. Safety management efficiency of China's coal enterprises and its influencing factors – Based on the DEA-Tobit two-stage model. *Process Safety and Environmental Protection*. 2020. Vol. 140, p. 79-85. DOI: [10.1016/j.psep.2020.04.020](https://doi.org/10.1016/j.psep.2020.04.020)
12. Legnaioli S., Campanella B., Pagnotta S. et al. Determination of Ash Content of coal by Laser-Induced Breakdown Spectroscopy. *Spectrochimica Acta Part B: Atomic Spectroscopy*. 2019. Vol. 155, p. 123-126. DOI: [10.1016/j.sab.2019.03.012](https://doi.org/10.1016/j.sab.2019.03.012)
13. Kamoza E.S., Mikhailova E.S., Ismagilov Z.R. Studying the effect the physicochemical properties of fine size raw coal organic and mineral composition have on beneficiation efficiency. *News of the Higher Institutions. Mining Journal*. 2021. N 6, p. 65-75 (in Russian). DOI: [10.21440/0536-1028-2021-6-65-75](https://doi.org/10.21440/0536-1028-2021-6-65-75)
14. Kraft Y.V., Gavriluk O.M., Ismagilov Z.R. Low-Temperature Pyrolysis of Kuznetsk Basin Coal: Composition of the Products. *Coke and Chemistry*. 2023. Vol. 66. N 1, p. 17-22. DOI: [10.3103/S1068364X23700400](https://doi.org/10.3103/S1068364X23700400)
15. Zhuravleva N.V., Khabibulina E.R., Ismagilov Z.R. et al. Studies of the interconnection of the structure of fossil coal and the concentrations of polycyclic aromatic hydrocarbons in it. *Chemistry for Sustainable Development*. 2016. Vol. 24. N 3, p. 355-361 (in Russian). DOI: [10.15372/KhUR20160310](https://doi.org/10.15372/KhUR20160310)
16. Jun Deng, Shuai-Jing Ren, Yang Xiao et al. Thermal properties of coals with different metamorphic levels in air atmosphere. *Applied Thermal Engineering*. 2018. Vol. 143, p. 542-549. DOI: [10.1016/j.applthermaleng.2018.07.117](https://doi.org/10.1016/j.applthermaleng.2018.07.117)
17. Vranjes-Wessely S., Misch D., Issa I. et al. Nanoscale pore structure of Carboniferous coals from the Ukrainian Donets Basin: A combined HRTEM and gas sorption study. *International Journal of Coal Geology*. 2020. Vol. 224. N 103484. DOI: [10.1016/j.coal.2020.103484](https://doi.org/10.1016/j.coal.2020.103484)
18. Pengxiang Wang, Mingjun Liu, Tong Pei et al. Ultraviolet Raman spectra: The reasonable method of evaluating coal pyrolysis graphitization. *AIP Advances*. 2020. Vol. 10. Iss. 11. N 115007. DOI: [10.1063/5.0018691](https://doi.org/10.1063/5.0018691)
19. Nelyubina N.V., Kraft Ya.V., Lyrshchikov S.Yu., Ismagilov Z.R. Investigation of the Correlation between the Energy Threshold of Laser Ignition of Coals and the Degree of Their Aromaticity. *Chemistry for Sustainable Development*. 2021. Vol. 29. N 5, p. 576-581. DOI: [10.15372/KhUR2021335](https://doi.org/10.15372/KhUR2021335)



20. Sheta S., Afgan M.S., Zongyu Hou et al. Coal analysis by laser-induced breakdown spectroscopy: a tutorial review. *Journal of Analytical Atomic Spectrometry*. 2019. Vol. 34. Iss. 6, p. 1047-1082. DOI: [10.1039/C9JA00016J](https://doi.org/10.1039/C9JA00016J)
21. Wenbing Li, Jidong Lu, Meirong Dong et al. Quantitative Analysis of Calorific Value of Coal Based on Spectral Preprocessing by Laser-Induced Breakdown Spectroscopy (LIBS). *Energy & Fuels*. 2018. Vol. 32. Iss. 24-32. DOI: [10.1021/acs.energyfuels.7b01718](https://doi.org/10.1021/acs.energyfuels.7b01718)
22. Sobolev I.S., Orekhov K.A., Orekhov A.N. Background and anomaly components analysis of the radioactive spatial patterns in gamma-spectrometric exploration for mineral resources. Radioactivity and Radioactive Elements in Environment: Proceedings of VI International Conference, 20-24 September 2021, Tomsk, Russia. In 2 volumes. Tomsk: National Research Tomsk Polytechnic University, 2021. Vol. 1, p. 536-541 (in Russian).
23. Aluker N.L., Suzdaltseva J.M., Herrmann M., Dulepova A.C. High-efficiency thermoluminescent detectors for measuring the absorbed ionizing radiation dose in the environment. *Instruments and Experimental Techniques*. 2016. Vol. 59. N 5, p. 733-739. DOI: [10.1134/S002044121605002X](https://doi.org/10.1134/S002044121605002X)
24. Aluker N.L., Artamonov A.S., Gimadova T.I., Zverev A.S. Thermoluminescent Dosimeters Based on Aluminum Oxide and Aluminum Nitride Ceramics. *Instruments and Experimental Techniques*. 2021. Vol. 64. N 6, p. 860-868. DOI: [10.1134/S0020441221050158](https://doi.org/10.1134/S0020441221050158)
25. Nelyubina N.V., Nikitin A.P., Valnyukova A.S., Ismagilov Z.R. Study Of Fossil Coals In The Kuznetsk Basin By Epr Spectroscopy. *Journal of Physics: Conference Series*. 2021. Vol. 1749. N 012018. DOI: [10.1088/1742-6596/1749/1/012018](https://doi.org/10.1088/1742-6596/1749/1/012018)
26. Furega R.I., Khabibulina E.R., Ismagilov Z.R. et al. EPR study of hard coals reached in Kuzbass. *Butlerov Communications*. 2017. Vol. 51. N 9, p. 149-152 (in Russian).
27. Soroka E.I., Galeev A.A., Petrova V.I. et al. Organic Matter in the Saf'yanovka Copper Massive Sulfide Deposit (Middle Urals). *Proceedings of Kazan University: Natural Sciences Series*. 2019. Vol. 161. N 2, p. 307-324 (in Russian). DOI: [10.26907/2542-064X.2019.2.307-324](https://doi.org/10.26907/2542-064X.2019.2.307-324)
28. Krasnovyid S.V., Konchits A.A., Shanina B.D. et.al. Adsorption processes on a carbonaceous surface: Electron spin resonance study. *Physica B: Condensed Matter*. 2023. Vol. 651. N 414571. DOI: [10.1016/j.physb.2022.414571](https://doi.org/10.1016/j.physb.2022.414571)
29. Konchits A.A., Shanina B.D., Valakh M.Ya. et al. Local structure, paramagnetic properties, and porosity of natural coals: Spectroscopic studies. *Journal of Applied Physics*. 2012. Vol. 112. Iss. 4. N 043504. DOI: [10.1063/1.4745015](https://doi.org/10.1063/1.4745015)
30. Burgess S.D., Bowring S.A. High-precision geochronology confirms voluminous magmatism before, during, and after Earth's most severe extinction. *Science Advances*. 2015. Vol. 1. Iss. 7. N e1500470. DOI: [10.1126/sciadv.1500470](https://doi.org/10.1126/sciadv.1500470)
31. Pavlov V.E., Fluteau F., Latyshev A.V. et al. Geomagnetic Secular Variations at the Permian-Triassic Boundary and Pulsed Magmatism During Eruption of the Siberian Traps. *Geochemistry, Geophysics, Geosystems*. 2019. Vol. 20. Iss. 2, p. 773-791. DOI: [10.1029/2018GC007950](https://doi.org/10.1029/2018GC007950)
32. Daoliang Chu, Grasby S.E., Haijun Song et al. Ecological disturbance in tropical peatlands prior to marine Permian-Triassic mass extinction. *Geology*. 2020. Vol. 48. N 3, p. 288-292. DOI: [10.1130/G46631.1](https://doi.org/10.1130/G46631.1)
33. Menghan Li, Grasby S.E., Shui-Jiong Wang et al. Nickel isotopes link Siberian Traps aerosol particles to the end-Permian mass extinction. *Nature Communications*. 2021. Vol. 12. N 2024. DOI: [10.1038/s41467-021-22066-7](https://doi.org/10.1038/s41467-021-22066-7)
34. Payne J.L., Clapham M.E. End-Permian Mass Extinction in the Oceans: An Ancient Analog for the Twenty-First Century? *Annual Review of Earth and Planetary Sciences*. 2012. Vol. 40, p. 89-111. DOI: [10.1146/annurev-earth-042711-105329](https://doi.org/10.1146/annurev-earth-042711-105329)
35. Elkins-Tanton L.T., Grasby S.E., Black B.A. et al. Field evidence for coal combustion links the 252 Ma Siberian Traps with global carbon disruption. *Geology*. 2020. Vol. 48. N 10, p. 986-991. DOI: [10.1130/G47365.1](https://doi.org/10.1130/G47365.1)
36. Valiulin S.V., Onischuk A.A., Zamashchikov V.V. et al. Influence of Organic Aerosol in Coal Mines on the Ignition Limit of Methane-Air Mixture. *Russian Journal of Physical Chemistry B*. 2021. Vol. 15. N 2, p. 291-298. DOI: [10.1134/S199079312102024X](https://doi.org/10.1134/S199079312102024X)
37. Ribeiro J., Ania C.O., Suárez-Ruiz I., Flores D. Chapter 7 – The Spontaneous Combustion of Coal-Mine Waste and Stream Effects in the El Bierzo Coalfield, Spain. *Coal and Peat Fires: A Global Perspective*. Elsevier, 2019. Vol. 5: Case Studies – Advances in Field and Laboratory Research, p. 97-124. DOI: [10.1016/B978-0-12-849885-9.00007-X](https://doi.org/10.1016/B978-0-12-849885-9.00007-X)

Authors: Nadezhda L. Aluker, Candidate of Physics and Mathematics, Leading Engineer, naluker@gmail.com, <https://orcid.org/0000-0002-6484-6617> (Federal Research Center of Coal and Coal Chemistry, Siberian Branch of the RAS, Kemerovo, Russia), Boris P. Aduiev, Doctor of Physics and Mathematics, Chief Researcher, <https://orcid.org/0000-0003-1878-1071> (Federal Research Center of Coal and Coal Chemistry, Siberian Branch of the RAS, Kemerovo, Russia), Denis R. Nurmukhametov, Doctor of Physics and Mathematics, Leading Researcher, <https://orcid.org/0000-0002-8301-9457> (Federal Research Center of Coal and Coal Chemistry, Siberian Branch of the RAS, Kemerovo, Russia).

The authors declare no conflict of interests.



Evaluation of the impact of the distance determination function on the results of optimization of the geographical placement of renewable energy sources-based generation using a metaheuristic algorithm

Andrei M. Bramm✉, Stanislav A. Eroshenko

Ural Federal University named after the first President of Russia B.N.Yeltsin, Yekaterinburg, Russia

How to cite this article: Bramm A.M., Eroshenko S.A. Evaluation of the impact of the distance determination function on the results of optimization of the geographical placement of renewable energy sources-based generation using a metaheuristic algorithm. *Journal of Mining Institute*. 2025. Vol. 271. N 16333, p. 141-153.

Abstract

Since the United Power System was created electrical supply of remote and hard-to-reach areas remains one of the topical issues for the power industry of Russia. Nowadays, usage of various renewable energy sources to supply electricity at remote areas has become feasible alternative to usage of diesel-based generation. It becomes more suitable with world decarbonization trends, the doctrine of energy security of Russia directives, and equipment cost decreasing for renewable energy sources-based power plants construction. Geological exploration is usually conducted at remote territories, where the centralized electrical supply can not be realized. Placement of large capacity renewable energy sources-based generation at the areas of geological expeditions looks perspective due to development of industrial clusters and residential consumers of electrical energy at those territories later on. Various metaheuristic methods are used to solve the task of optimal renewable energy sources-based generation geographical placement. The efficiency of metaheuristics depends on proper tuning of that methods hyperparameters, and high quality of big amount of meteorological and climatic data. The research of the effects of the calculation methods defining distance between agents of the algorithm on the optimization of renewable generation placement results is presented in this article. Two methods were studied: Euclidean distance and haversine distance. There were two cases considered to evaluate the effects of distance calculation method change. The first one was for a photovoltaic power plant with installed capacity of 45 MW placement at the Vagaitskii district of the Tyumen region. The second one was for a wind power plant with installed capacity of 25 MW at the Tungokochenskii district of the Trans-Baikal territory. The obtained results show low effects of distance calculation method change at average but the importance of its proper choose in case of wind power optimal placement, especially for local optima's identification.

Keywords

PV power plants; wind power plants; Capacity factor; swarm intelligence; artificial intelligence; forecasting

Funding

The research funding from the Ministry of Science and Higher Education of the Russian Federation (Ural Federal University named after the first President of Russia B.N.Yeltsin within the Priority-2030 Program) is gratefully acknowledged.

Received: 29.10.2023

Accepted: 08.04.2024

Online: 18.09.2024

Published: 25.02.2025

Introduction

The Russian Federation has a huge potential in terms of mineral resources and fossil fuels represented by complex of minerals distributed over a vast territory. This mineral complex consists of oil, natural gas, coal, metallic ores, raw mineral materials which are used in building industry, etc. The development of raw materials deposits and their extraction are carried out throughout the vast territory of the country from the Caucasus to the Far East. Geological exploration expeditions play an important role in confirming the mining potential of the territories. These expeditions are usually carried out in remote areas, where the centralized electrical supply can not be realized [1, 2].



Mobile generation systems, based on small-capacity diesel generators, or fast-built installations, based on one large-capacity diesel generator, are used to provide electricity in these conditions [3, 4]. The use of diesel generators is the simple way to establish a local electrical supply. However, there are some specific aspects of exploitation, related to fuel transportation and the negative ecological impact (emissions of nitrogen and carbon oxides) [5-7].

Mining and industrial clusters and working settlements are developed in the area if geological exploration succeeds. These new consumers of electricity require the construction of long overhead power transmission lines or a local power plant for electrical supply. Decreasing the share of diesel-based generation and replacing it with local energy sources-based generation is one of the keynotes of the Russian Energy Security Doctrine¹. Developing renewable energy sources-based power generation (RES) in areas of geological exploration is a major alternative for non-environmentally friendly diesel generation with low efficiency considering these keynotes.

Decarbonization trends of all sections of the economy suggest the integration of more environmentally friendly energy sources into the economy, including electrical supply to remote and hard-to-reach areas. The government's economic development plan for the Russian Federation includes programs to support decarbonization and the development of green power generation [8]. It is reasonable to evaluate the potential for locating RES-based power plants at geological exploration sites [9-11], considering both their environmental impact [12-14] and mining prospects in these territories [15]. Optimization of the geographical location of RES-based generation is essential for efficient use, particularly in large countries such as the Russian Federation, which have various climatic zones with diverse meteorological conditions. The goal of this optimization is to maximize electricity generation, represented by the capacity utilization factor (CF), of power plants. CF is one of the parameters used as indicators for new project selection within governmental support programs such as PSA RES 2.0. The minimum requirements for CF for photovoltaic power plants (PVPP) and wind power plants (WPP) in Russia are 0.14 and 0.27 p.u., respectively, according to official tender documentation.

Meteorological data, a CF forecasting system, and appropriate mathematical optimization methods capable of showing high results when working with heterogeneous, complex objective function forms are required for optimization of this type. There are many factors affecting the optimization results. One of these factors is the determination of the distance between geographical points that determine the various potential positions of the planned power generation unit. Not all methods are suitable for this task, and some show good results when dealing with uneven and complex objective functions.

Different metaheuristic [16-18] optimization methods such as the Firefly algorithm [19, 20], Grey Wolves Pack [21-23], etc. are effective tools for optimizing in complex and unique situations. Metaheuristics is based on the natural behavior of animals and insects during vital processes, such as food search and hunting. Mathematical descriptions of animal and insect behavior are used in many economic fields, including engineering, construction, logistics, and the power industry. Metaheuristic algorithms have advantages over traditional optimization methods based on gradient descent or generalized Newton's method, which are also used for technical tasks.

The main advantages of metaheuristics include:

- universality: optimization algorithms can be used for both simple single-extremum problems and unique multiple-extremums;
- smaller probability of getting stuck in a local extremum or plain space;

¹ Russian Federation Energy Security Doctrine. URL: <https://minenergo.gov.ru/ministry/energy-security-doctrine?ysclid=lsipl3svw513749979> (accessed 15.02.2024).



- smaller influence of initial evaluation on final results of the optimization (algorithm's agents first placement).

One of the main drawbacks of metaheuristic optimization algorithms is the need to tune their hyperparameters. The efficient values of these parameters may vary depending on the task being considered, the objective function, or the restriction system.

There are various factors that affect the results of RES-based power generation optimization. One of these factors is the distance calculation function used in the algorithm. Metaheuristic methods are often applied to optimization tasks involving integer-valued or discrete parameters. In these cases, the agents of the algorithm move to predefined grid nodes in the solution space, and Euclidean distance [24, 25] is typically used by default. A significant part of research focuses on accurately tuning the hyperparameters of the algorithm, while working on optimization tasks that use geographical coordinates as parameters. When working with optimization tasks where there are not only integer values but also infinite fractional values, haversine distances, which are used in transport logistics and navigation [26, 27] could be used as an alternative to Euclidean distance.

This research presents the effects of the distance function used in optimization algorithms on RES-based generation placement optimization results. The main objective is to confirm the hypothesis that selection of the distance functions affects the optimization results. Application of optimization methods based on metaheuristic algorithms for geographical placement of different types and capacities of RES-generation, and evaluation of various distance functions' influence on results represent the scientific novelty of this study.

To confirm the hypothesis, two areas were considered for geological exploration: the Urals [28-31] and the Trans-Baikal territory [32].

Methodology

The objective function of the optimization task has a unique form and contains many local maximum areas, considering the geographical placement of RES-based generation to maximize its CF. The objective function shows how CF changes depending on electrical parameters (energy source type and installed capacity), geographical parameters (location of power plant) and climatic/meteorological parameters (air temperature, humidity, wind speed, solar irradiation, albedo, etc.) This function cannot be defined using interpretable combinations of mathematical and trigonometric functions.

Models, based on artificial intelligence (AI), especially forecasting models [33-35], are widely used to evaluate the potential and efficiency of RES-based power plant placement in areas. AI-model are able to describe the correlations between stochastic climatic and meteorological parameters and electricity production of RES-based power generation. The results of these models are highly accurate compared to traditional approaches based on probability distributions [36-38].

The machine learning forecasting model for RES-based generation CF values forecasting proposed by the authors in [39] which is based on an ensemble algorithm named "random forest", was used to determine the objective function for this research. The initial data for this model include the type of energy source, installed capacity of the power plant, geographical location, and a number of meteorological variables (which may vary depending on the type of energy source).

The developed model was trained using data on the geographical positions of RES-based power plants, electricity generation throughout the year and averaged meteorological parameters for the area of the power plants for five years. The data used to train the model was extracted from certificates confirming the origin of electricity consumed for qualified RES-generation².

The adapted firefly's optimization algorithm was applied to the task of optimal RES-based geographical placement of generation. This algorithm was chosen because of its efficiency in this task,

² Renewable Energy Sources. URL: <https://www.np-sr.ru/ru/market/vie/index.htm> (accessed 29.10.2023).



which has been demonstrated in comparison with random search, particle swarm optimization, fireflies, and grey wolf pack optimization algorithms in [39].

The optimization task solution process using the proposed algorithm can be divided into four stages, as follows:

- preparation – choosing the area under consideration and forming restrictions on the power plant's placement (borders of the area);
- initial population creation – creating agents and randomly distributing them within the borders of the considered area;
- optimal placement search – an iterative process of moving agents according to their objective function values and algorithm parameters;
- final – end of optimization and creation of a report on results (statistical metrics and visualization of results).

Mathematical description of the agent's movement process:

$$x_{i+1} = x_i + \beta(x_j - x_i) + \alpha(c_{rand} - 0.5);$$

$$x_{bi+1} = x_{bi+1} + \alpha(c_{rand} - 0.5),$$

where x_i , x_j are the agent's positions (geographical latitude and longitude); x_{bi} is the position of the agent with the highest objective function score; α is the coefficient determines random move of agents; β is the agents attraction function (depends on the agent's values of the objective function and the distance between them); c_{rand} is the random value in range from zero to one.

The agent's attraction function is defined as follows:

$$\beta = \beta_0 e^{-\gamma d^2},$$

where γ is the transparency coefficient; d is the distance between two agents; β_0 – attraction force of the agent at the distance of $d = 0$.

It is required to tune the hyperparameters to provide correct work of the proposed metaheuristic algorithm:

- α is the coefficient defining the step length of the agent in the random direction (measures in p.u. according to the size of the considered optimization area). This coefficient may remain constant during the optimization process, or it may change according to the chosen pattern. The reasonable change of α is to decrease it during the optimization process to provide the convergence of the agents to one area;
- β_0 is the coefficient defining the strength of attractiveness between agents on the minimal distance. This coefficient is used to define the attractiveness function β . This could remain constant or change according to the pattern. It is necessary to use a smaller values of β_0 at the beginning, and then gradually increase β_0 till the value of 1.0 to strengthen the exploration ability at the start of the algorithm and to accelerate the convergence of the algorithm at the final iterations;
- γ is the coefficient which defines the transparency of the environment and affects the movement of the agents with the smaller values of the objective function to the agents with the higher values of the objective function. This coefficient could change in the range from zero to one. If $\gamma = 0$, then the environment is assumed as fully transparent, which leads to the algorithm transforming into a random search. If $\gamma = 1$, then the environment is assumed as fully non-transparent;
- d is a function of the distance between agents of the algorithm. The behavior of the algorithm may change if the distance function is changed. In the stated problem, the position of agents refers to



the actual values of geographical latitude and longitude, so the most suitable distance functions may be Euclidean distance and haversine distance.

Optimal values for the parameters α , β_0 и γ listed above were defined in the previous research [40]. Effects of the agent's distance function selection on the optimization results have not been studied in the previous research. Different distance functions are considered to calculate the distance between two geographical points in the frame of the current research.

Since the geographical coordinates of the potential location of power plants are used for calculations, a hypothesis about the incorrectness of using the Euclidean position as a function for calculating the distance in this formulation of the optimization problem was formulated.

It is proposed to use the haversine function, which is used in navigation calculations and has physical and geographical validity to improve the optimization results.

The Euclidean distance between two geographical points is defined as follows:

$$d_{\text{euc}} = \sqrt{(\lambda_2 - \lambda_1)^2 + (\varphi_2 - \varphi_1)^2},$$

where φ_1 , φ_2 are latitude coordinates of two points, rad; λ_1 , λ_2 are longitude coordinates of two points, rad.

The haversine distance between two geographical points is defined as follows:

$$d_{\text{hav}} = 2r \cdot \arcsin \left(\sqrt{\sin^2 \left(\frac{\varphi_2 - \varphi_1}{2} \right) + \cos(\varphi_1) \cdot \cos(\varphi_2) \cdot \sin^2 \left(\frac{\lambda_2 - \lambda_1}{2} \right)} \right),$$

where r is the major sphere's circle radius, km.

Euclidean distance is applicable to calculating the distance between two points on the same plane, and it equals the length of a straight line connecting these points. The haversine equation is rarely used trigonometric function and mainly uses in the field of navigation to calculate the shortest distance between any two route points.

The curvature of the Earth's surface can be accurately approximated by the plane when considering small distances between two points (about 1 km). The difference between Euclidean and Haversine distance functions in these cases is about 0.1 % [41]. The accuracy of the plane approximation decreases with increasing distance between the points. When the distance is near to a few geographical degrees, the difference between the two distance functions becomes noticeable. These differences are due to Mercator projection distortions. Therefore, the shortest distance between any two points on Earth's curved surface is measured by the Haversine formula, not by a straight line (Euclidean).

Results and discussion

The calculations were provided to confirm the proposed hypothesis. Two territories of the Russian Federation were chosen for these calculations. Geological exploration expeditions are actively performed in these territories in accordance with the Unified Fund of Geological Information about the Subsoil of the Russian Federation³ and Rosgeo⁴ data. The obtained results of comparison for two types of RES-based power generation were provided. Figure 1 shows the form of the objective functions for the two considered territories: Tungokochenskii district of Trans-Baikal region, where placer gold deposits are being explored, and Vagaiskii district of Tumen region where peat deposits are being investigated.

³ Unified Fund of geological information about the subsoil. Register of original and interpreted information. URL: <https://efgi.ru/> (accessed 15.02.2024).

⁴ Rosgeology news portal. URL: <https://nedra.rusgeology.ru/subdivision/nvniigg/news/> (accessed 15.02.2024).

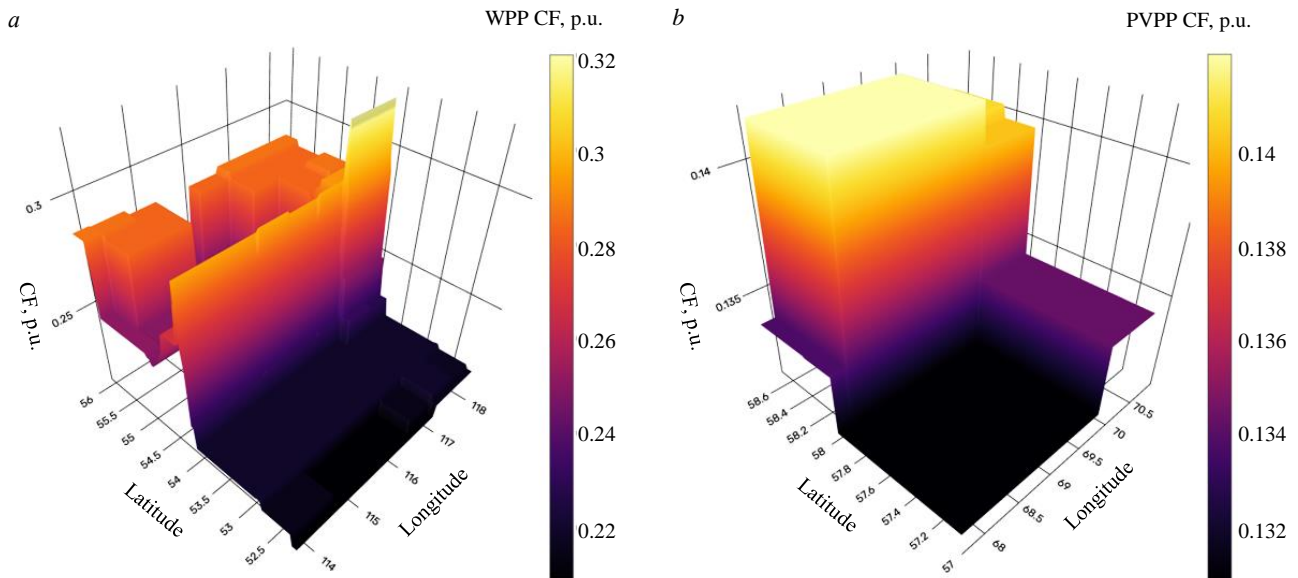


Fig.1. The objective function examples of the optimization task under study:
a – WPP placed in the Tungokochenskii district; *b* – PP placed in the Vagaishkii district

The results of the agent's placement at the initial population creation stage are presented in Fig.2. These results were used to evaluate the difference between two methods for calculating distance when the distance between two points is greater than one degree. The Table shows the absolute error of the Euclidean distance compared to the haversine:

$$E = d_{hav} - d_{euc},$$

where d_{hav} is the distance according to the haversine method, km; d_{euc} is the distance according to the Euclidean method, km.

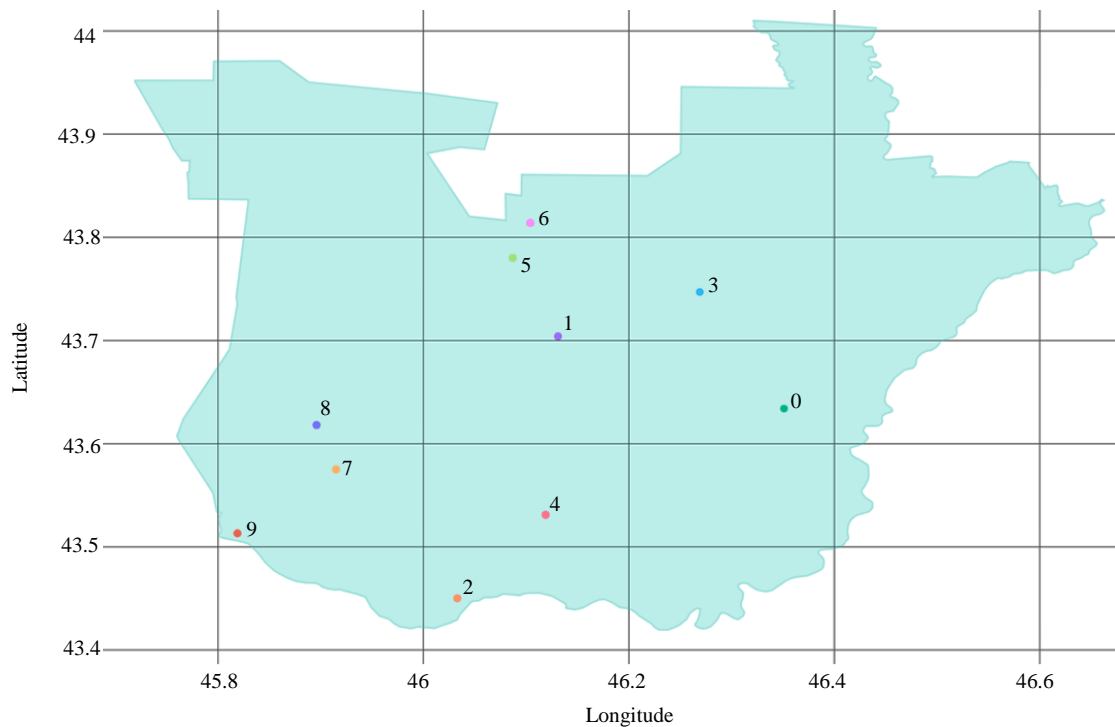


Fig.2. Initial population agent's placement



The difference of Euclidean distance and haversine for initial population agent's distance calculation, km

Agent	0	1	2	3	4	5	6	7	8	9
0	0	-6.329	-8.043	-1.333	-6.297	-6.815	-5.786	-13.186	-13.935	-15.719
1	-6.329	0	-0.945	-3.989	-0.022	-0.604	-0.172	-5.429	-6.628	-7.768
2	-8.043	-0.945	0	-4.072	-1.764	-0.231	-0.361	-2.266	-2.399	-6.162
3	-1.333	-3.989	-4.072	0	-2.357	-5.489	-4.596	-9.444	-10.619	-11.783
4	-6.298	-0.022	-1.764	-2.357	0	-0.108	-0.021	-6.042	-6.202	-9.131
5	-6.815	-0.604	-0.231	-5.489	-0.108	0	-0.207	-3.087	-4.172	-5.362
6	-5.786	-0.172	-0.361	-4.596	-0.021	-0.207	0	-3.262	-4.305	-5.515
7	-13.186	-5.429	-2.266	-9.444	-6.042	-3.087	-3.262	0	-0.207	-2.340
8	-13.935	-6.629	-2.399	-10.619	-6.202	-4.172	-4.305	-0.207	0	-1.255
9	-15.719	-7.769	-6.162	-11.783	-9.131	-5.362	-5.515	-2.340	-1.255	0

Based on the data in Table it can be concluded that the plane approximation and Euclidean distance calculations are not applicable to this task. The error distribution in distance calculation is non-linear, which could be due to the uneven curvature of the Earth's surface across latitude and longitude. Even though the error in distance calculation may be nonlinear, there is a positive correlation between the error values and the distance between two points. In the example presented, the maximum error reached 15-16 km (0.14 degrees) when the distance between the two points was 56 km (half a degree).

Such errors (see Table) are significant for the studied optimization task, considering the objective function's form (see Fig.1). A drastic change in the CF value may occur within an interval of 0.1 degrees of longitude or latitude for flat surfaces, or the optimal area may be missed for surfaces with a peaked shape. The size of a RES-based power plant is equal to 2-3 km for one of the Orenburg PVPPs or 6-8 km for Kamenskaya WPP, which is the distance between two end wind generators. An error that is 2-5 times larger than the size of the object under consideration is unacceptable, but it may be tolerable if installations of new units (capacity increase, territory expansion) for this power plant are considered later.

The comparison of the results of optimizing the placement of RES-based power plants placement using two different distance functions (Euclidean and haversine) presented below.

The 25 MW WPP placement optimization was considered for the Tungokochenskii district area. The objective function for this area (see Fig.1, *a*) is characterized by a global optimum area clearly localized at 54 degrees latitude. Figure 3 shows the results of comparing two distance functions for calculating agent distances. Figure 3, *a* shows distribution density curves of the best CF values found by the optimization algorithm after 100 iterations, and Fig.3, *b* shows the geographical location of the best results on the district map, projected onto the objective function plane. In both figures, green colors represent results obtained using the Euclidean distance function, while blue colors represent haversine results, and gray areas represent territory exploration expeditions⁵.

⁵ The State register of works on the subsoil geological exploration. URL: <https://rfgf.ru/ReestrGin/> (accessed 15.02.2024).

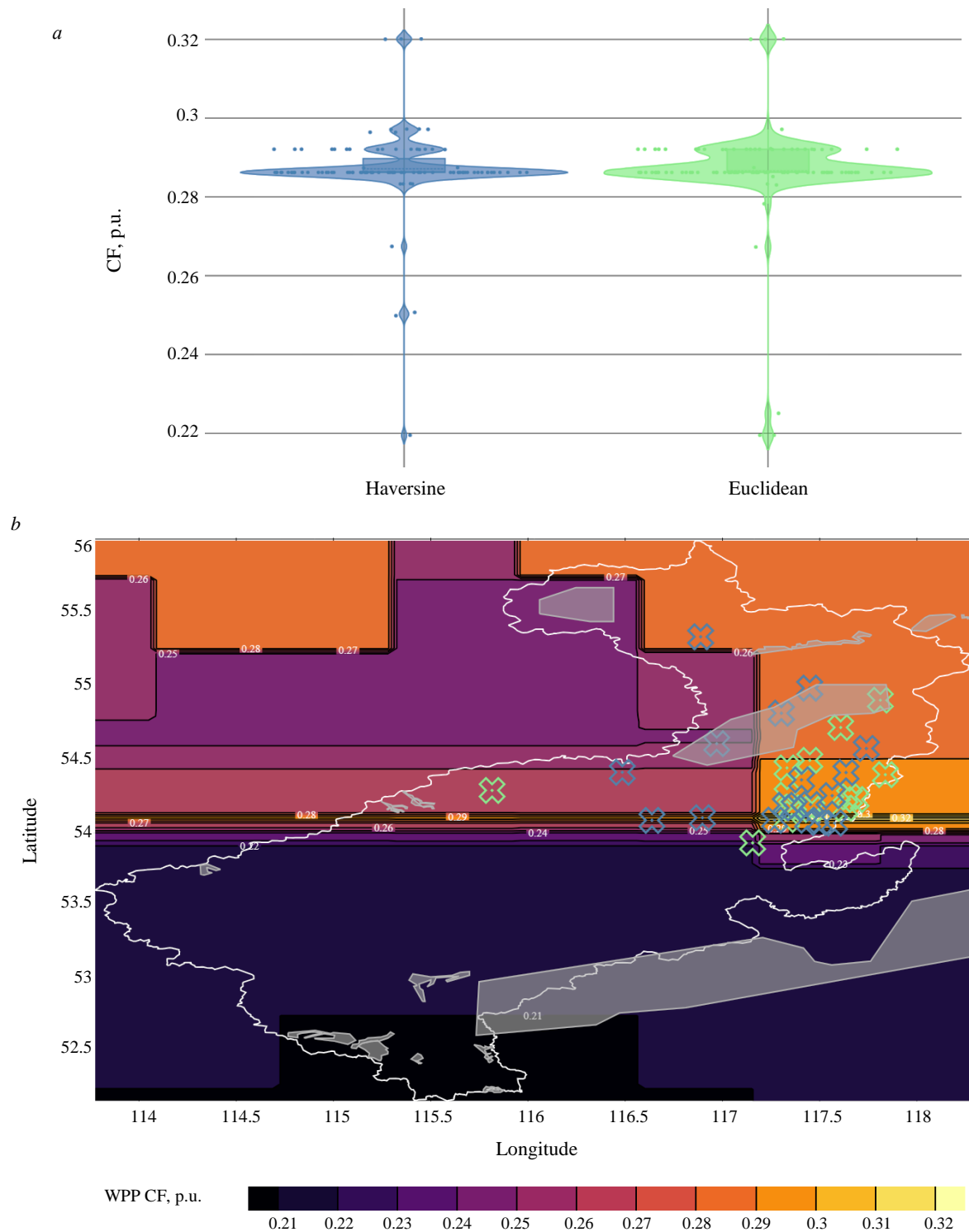


Fig.3. Distribution of the optimal CF values which were defined during the 25 MW WPP placement optimization in the Tungokochenskii district: *a* – violin plots for CF values of the optimal placement results; *b* – geographical distribution of the optimal placement results

For the convenience of perceiving the results geographical maps of the considered districts (Fig.3, *b* and 4, *b*) were combined with the objective functions (see Fig.1) in the form of a contour plots which demonstrate changes in the CF values of the power plant at the considered territories.

The following conclusions were formulated based on the obtained results for the Tungokochenskii district:



- The violin distribution plots have a similar shape for both distance functions. The haversine results distribution plot is more clearly defined than the Euclidean distance results. The optimization algorithm more accurately identifies global optimum areas when using the haversine distance function.

- The geographical distribution of the optimization results (Fig.3, *b*) shows that most of the results fall between 54th and 56th latitudes, which are the global optimum and local optimal areas, respectively.

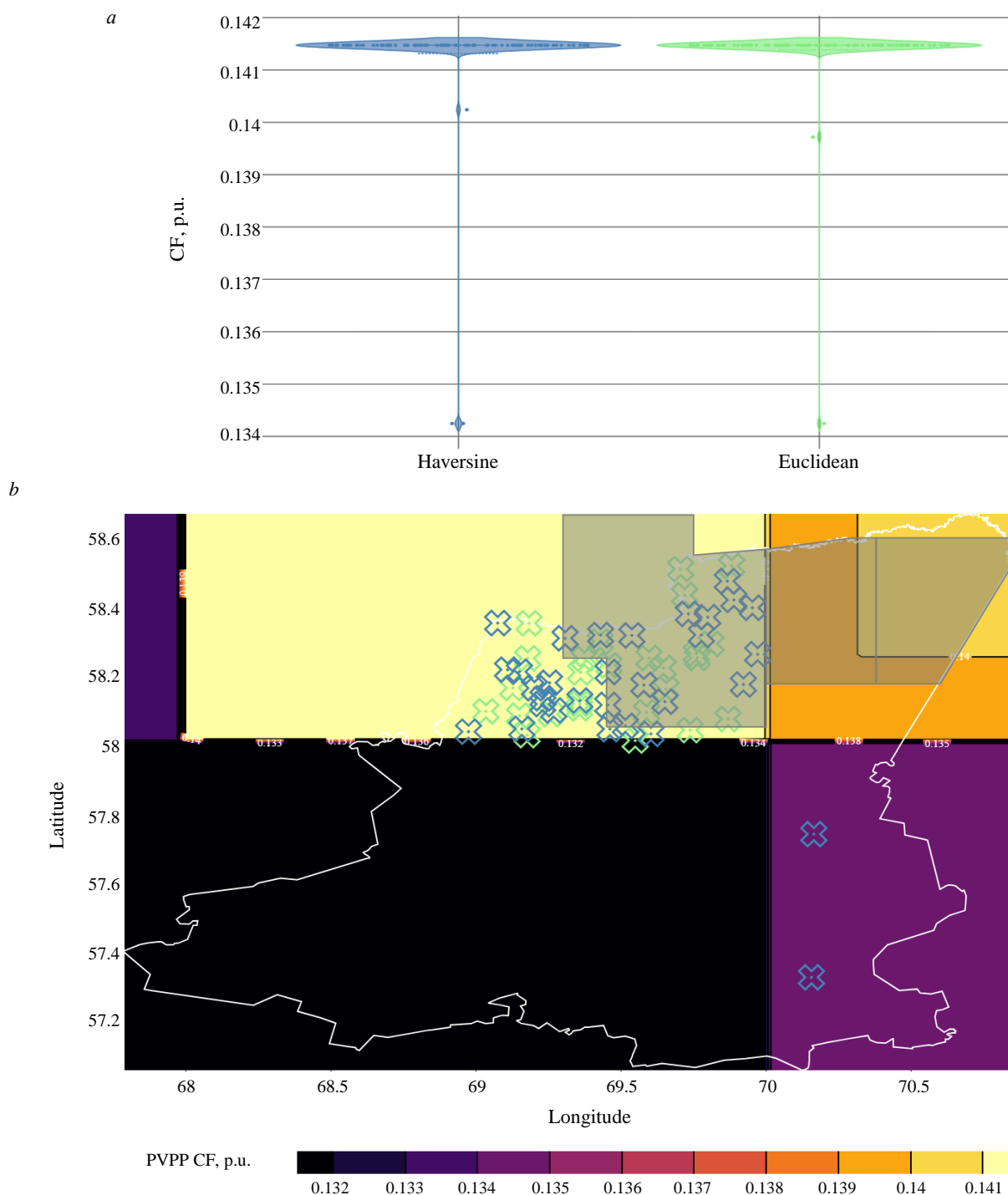


Fig.4. Distribution of the optimal CF values which were defined during the 45 MW PVPP placement optimization in the Vagaiskii district: *a* – violin plots for CF values of the optimal placement results; *b* – geographical distribution of the optimal placement results



The 45 MW PVPP placement optimization was considered for the Vagaiskii district area. The objective function for this area (see Fig.1, *b*) is flat and has a poorly expressed global optimum (the difference between the minimum and maximum values is 0.01 p.u.). Figure 4, *a* shows the distribution density curves of the best CF values found by the optimization algorithm after 100 iterations. Figure 4, *b* shows the geographical location of these results projected onto the district map in the plane of the objective function. In both figures, green represents the results obtained using the Euclidean distance function, and blue represents haversine results. Grey areas represent the territories of geological exploration expeditions⁶.

The following conclusions were formulated based on the obtained results for the Vagaiskii district:

- The majority of the solutions found are located in the same area due to the flat form of the objective function.
- More than 90 % of the results correspond to the global optimum area, due to the flat form of the objective function (the difference between minimum and maximum values of CF is 0.01 p.u.).
- Violin distribution plots are nearly identical for both distance functions used (Fig.4, *a*), with only minor deviations explained by the stochastic nature of the optimization algorithm.

The objective function of the CF values changes mainly in the latitude direction and has a flat-tened, stepwise form, which can be explained by the physics of solar irradiation spreading. This leads to the absence of a local optimal area for small territories (district, municipal district), so the choice of distance function does not affect the optimization results. However, the effect of the distance function may become noticeable when considering larger territories such as an entire region or country.

The objective function of the CF values has a more stochastic distribution than that of PVPP, and it clearly has localized sub-optimal areas. The latitude dependency plays a smaller role, and the landscape specifics are more significant. The choice of the distance function significantly affects the optimization results, considering these conditions. These effects are evident in the more distinct borders of the distribution plot (when using the haversine function), and local optimal areas are exceeded (when using Euclidean distance). However, the change in the distance function still has minor effects on the overall results.

There is an influence of the selected distance calculation function on the optimization algorithm, when considering tasks for RES-based power generation optimization in territories where geological exploration is actively conducted. This influence has a major impact on tasks where the objective function has narrow optimal and suboptimal areas (Tungokochenskii district and WPP placement). A minor impact was observed in the task with a flat objective function and one optimal area (Vagaiskii district and PVPP placement).

Conclusion

The hypothesis about selecting a function for distance calculation in the firefly's metaheuristic optimization algorithm has an impact on the results of optimization when optimizing the placement of RES-based power generation using CF values as an objective function. Two functions for calculating the distance between two geographic points were used to validate the proposed hypothesis: Euclidean distance and haversine distance. When these two functions were compared directly, the maximum error was 0.14 degrees of geography (15-16 km), and the distance between the two points corresponded to a maximum error of 0.5 degrees of geography (which corresponds to the distance of about 56 km). These comparison results confirmed the physical theory of Earth's surface geometry and the shortest path between two points on a sphere.

⁶ The State register of works on the subsoil geological exploration. URL: <https://rfgf.ru/ReestrGin/> (accessed at 15.02.2024).



It was noted that with the observed errors in calculating the distance during the implementation of the optimization algorithm, the zone of global/local optimum can be skipped for the functions of the CF change with clearly expressed local optima, and for functions of flat shapes there may be a failure to reach the global optimum zone.

The following conclusions about the initial hypothesis were formulated based on the results of the experiments on the RES-based generation placement optimization in the territories of the Tungokochenskii and Vagaiskii districts:

- The objective function (dependency of CF values from geographical coordinates) has a flat form for the tasks of PVPP placement optimization (Vagaiskii district). Changing the distance calculation function has a minor impact on the placement optimization results for 45 MW PVPP in the Vagaiskii district. The distribution of results is almost identical for both the Euclidean and haversine distances.

- The objective function has a more uneven and peaked shape with clearly defined optimal regions for WPP placement (Tungokochenskii district) optimization. Changing the calculation method for distance has a notable impact, but barely affects the reachability of the global optimum. This effect is mainly expressed in a more distinct detection of local optimal areas when using the haversine method.

The initial hypothesis was partially confirmed by the results obtained during the experiments. Also, several adjustments to the initial hypothesis were made based on the results. The selection of the distance calculation function had a limited impact on the results of RES-based geographical placement optimization to increase the CF of the power plant.

The distance function selection does not affect the optimization results when PVPP placement optimization is considered on relatively small territories. However, the distance function may lead to the skipping of important local optimal areas when considering WPP placement optimization.

The results of the research could be used to find a technically reasonable and energy-efficient location for the placement of RES-based power plants. These results also could also be useful for electricity supply in remote areas, hard-to-reach areas, or areas where geological exploration is taking place.

REFERENCES

1. Yakovleva E.V. Electrotechnical complex with photovoltaic power plant for electricity supply of the geological exploration expedition: Avtoref. dis. ... kand. tekhn. nauk. St. Petersburg: Natsionalnyi mineralno-syrevoi universitet "Gornyi", 2013, p. 22 (in Russian).
2. Yakovleva E.V. Electrosupply of Prospecting Works with Use of Hybrid Power Stations. *Mining Equipment and Electromechanics*. 2013. N 3, p. 19-22 (in Russian).
3. Limitovskiy A.M., Bashkurov A.Yu. Auxiliary power plants as an alternative energy cogeneration facilities mineral complex. *Prospect and protection of mineral resources*. 2019. N 9, p. 35-37 (in Russian).
4. Bashkurov A.Yu. Optimization of centralized and localized energy supply of mineral exploration services customers. *Mining Informational and Analytical Bulletin*. 2015. N 2, p. 386-391 (in Russian).
5. Titov S.V. Methods and techniques for reducing emissions from marine diesel power plants. Avtoref. dis. ... d-ra tekhn. nauk. Novosibirsk: Sibirskii gosudarstvennyi universitet vodnogo transporta, 2022, p. 35 (in Russian).
6. Heikkilä J., Ingo S. Izmereniya vybrosov tverdykh chastits i otdelnykh komponentov otrabotavshikh gazov – metody i zadachi na budushchee. *Dvigatelistroenie*. 2017. N 4 (270), p. 46-52 (in Russian).
7. Ntziachristos L., Saukko E., Ronkko T. et al. Vliyanie uslovii i metodiki probotoobra na rezul'taty izmerenii tverdykh chastits sudovym dizelem. *Dvigatelistroenie*. 2017. N 4 (270), p. 53-61 (in Russian).
8. Maksimov A. RES 2.0: New program for the development of "green" energy in Russia. *Energy Policy*. 2020. N 11 (153), p. 22-27 (in Russian). DOI: [10.46920/2409-5516.2020.11153.22](https://doi.org/10.46920/2409-5516.2020.11153.22)
9. Akhmetshin A.I. Ecological problems of Russian regions with oil&gas-oriented industry. Regional development management: problems, opportunities, and perspectives: Proceedings of the International scientific-practical conference with international attendance, 28 November 2018, Cheboksary, Russia. Cheboksary: Chuvashskii gosudarstvennyi pedagogicheskii universitet im. I.Ya.Yakovleva, 2018, p. 462-469 (in Russian).



10. Lipina S.A. North-Caucasian region economic integration. *Sovremennyye proizvoditelnye sily*. 2013. N 3, p. 67-75 (in Russian).
11. Senkevich V.S. Features and results of drilling deep geochemical searches on the flanks of the Mulinskaya Depression (Trans-Baikal territory). Scientific and methodological foundations of forecasting, prospecting, and evaluation of deposits of diamonds, precious and non-ferrous metals: Collection of abstracts of the IX International Scientific and Practical Conference, April 17-19, 2019, Moscow, Russia. Moscow: Tsentralnyi nauchno-issledovatel'skii geologorazvedochnyi institut tsvetnykh i blagorodnykh metallov, 2019, p. 195-196 (in Russian).
12. Zaborayeva Kh.Sh. Geoecological basis of increasing efficiency of agricultural lands use (by the example of Chechen Republic). *Theoretical and Applied Ecology*. 2012. N 2, p. 79-84 (in Russian).
13. Noskova E.V. Statistical features of wind speed dynamics in the Trans-Baikal territory. *Zapiski Zabaikalskogo otdeleniya Russkogo geograficheskogo obshchestva*. 2014. Iss. 133. Vol. 1, p. 131-138 (in Russian).
14. Erofeeva A.A. Analysis natural systems Tobolsk, Uvatsky and Vagaysky districts as the reasons for the formation socio-economic relations. *Regional Geosystems*. 2021. Vol. 45. N 3, p. 316-327 (in Russian). DOI: [10.52575/2712-7443-2021-45-3-316-327](https://doi.org/10.52575/2712-7443-2021-45-3-316-327)
15. Kosyanov V.A., Limitovsky A.M., Merkulov M.V., Golovin S.V. Increasing of effectiveness in combination energy-supply of decentralized geological objects in Arctic and utmost North environment. *Proceedings of higher educational establishments. Geology and Exploration*. 2014. N 4, p. 81-85 (in Russian).
16. Yanpu Zhao, Changsheng Huang, Mengjie Zhang, Yang Cui. AOBMOA: A Hybrid Biomimetic Optimization Algorithm for Numerical Optimization and Engineering Design Problems. *Biomimetics*. 2023. Vol. 8. Iss. 4. N 381. DOI: [10.3390/biomimetics8040381](https://doi.org/10.3390/biomimetics8040381)
17. Rahman C.M., Rashid T.A., Alsadoon A. et al. A Survey on Dragonfly Algorithm and its Applications in Engineering. *Evolutionary Intelligence*. 2023. Vol. 16. Iss. 1, p. 1-21. DOI: [10.1007/s12065-021-00659-x](https://doi.org/10.1007/s12065-021-00659-x)
18. Shukla N.K., Srivastava R., Mirjalili S. A Hybrid Dragonfly Algorithm for Efficiency Optimization of Induction Motors. *Sensors*. 2022. Vol. 22. Iss. 7. N 2594. DOI: [10.3390/s22072594](https://doi.org/10.3390/s22072594)
19. Güven A.F., Yörükören N., Tag-Eldin E., Samy M.M. Multi-Objective Optimization of an Islanded Green Energy System Utilizing Sophisticated Hybrid Metaheuristic Approach. *IEEE Access*. 2023. Vol. 11, p. 103044-103068. DOI: [10.1109/ACCESS.2023.3296589](https://doi.org/10.1109/ACCESS.2023.3296589)
20. Ali S., Rehman A.U., Wadud Z. et al. Demand Response Program for Efficient Demand-Side Management in Smart Grid Considering Renewable Energy Sources. *IEEE Access*. 2022. Vol. 10, p. 53832-53853. DOI: [10.1109/ACCESS.2022.3174586](https://doi.org/10.1109/ACCESS.2022.3174586)
21. Xingyu Jiang, Jiazhen Li, Yitao Lu, Guangdong Tia. Design of Reverse Logistics Network for Remanufacturing Waste Machine Tools Based on Multi-Objective Gray Wolf Optimization Algorithm. *IEEE Access*. 2020. Vol. 8, p. 141046-141056. DOI: [10.1109/ACCESS.2020.3011509](https://doi.org/10.1109/ACCESS.2020.3011509)
22. Wei Zhang, Sai Zhang, Fengyan Wu, Yagang Wang. Path Planning of UAV Based on Improved Adaptive Grey Wolf Optimization Algorithm. *IEEE Access*. 2021. Vol. 9, p. 89400-89411. DOI: [10.3390/s22145232](https://doi.org/10.3390/s22145232)
23. Guo M.W., Wang J.S., Zhu L.F., Guo S.S., Xie W. An Improved Grey Wolf Optimizer Based on Tracking and Seeking Modes to Solve Function Optimization Problems. *IEEE Access*. 2020. Vol. 8, p. 69861-69893. DOI: [10.1109/ACCESS.2020.2984321](https://doi.org/10.1109/ACCESS.2020.2984321)
24. Shyh-Jier Huang, Xian-Zong Liu, Wei-Fu Su, Shu-Hsuan Yang. Application of Hybrid Firefly Algorithm for Sheath Loss Reduction of Underground Transmission Systems. *IEEE Transactions on Power Delivery*. 2013. Vol. 28. N 4, p. 2085-2092. DOI: [10.1109/TPWRD.2013.2265913](https://doi.org/10.1109/TPWRD.2013.2265913)
25. Srinivasan B., Venkatesan R., Aljafari B. et al. A Novel Multicriteria Optimization Technique for VLSI Floorplanning Based on Hybridized Firefly and Ant Colony Systems. *IEEE Access*. 2023. Vol. 11, p. 14677-14692. DOI: [10.1109/ACCESS.2023.3244346](https://doi.org/10.1109/ACCESS.2023.3244346)
26. Anbalagan A., Sundarsingh E.F., Ramalingam V.S. et al. Smart Dynamic Position Tracking Wearable for Geofencing in Marine Environment. *IEEE Transactions on Instrumentation and Measurement*. 2023. Vol. 72. N 8005109. DOI: [10.1109/TIM.2023.3311076](https://doi.org/10.1109/TIM.2023.3311076)
27. Jimoh O.D., Ajao L.A., Adeleke O.O., Kolo S.S. A Vehicle Tracking System Using Greedy Forwarding Algorithms for Public Transportation in Urban Arterial. *IEEE Access*. 2020. Vol. 8, p. 191706-191725. DOI: [10.1109/ACCESS.2020.3031488](https://doi.org/10.1109/ACCESS.2020.3031488)
28. Kerimov I.A., Bachaeva T.Kh., Vismuradov A.V., Daukaev A.A. Solid non-metallic minerals spreading on the Chechen Republic territory. *Vestnik Akademii nauk Chechenskoi Respubliki*. 2015. N 3 (28), p. 103-112 (in Russian).
29. Askhabova Kh.N., Ozdykhanov M.S., Soltamuradov G.D. Evaluation of the ecological state of the environment in the territory of the Chechen Republic in 2017. *Advances in Current Natural Sciences*. 2019. N 1, p. 7-12 (in Russian).
30. Solodovnikov A.Yu. Tyumen region geography: minerals and their use. Tyumen: TyumGU-Press, 2023, p. 352 (in Russian).
31. Solodovnikov A.Yu. Mineral resources of the Vagaiskii district and their use. *Gornye vedomosti*. 2017. N 3 (151), p. 68-77 (in Russian).
32. Barabasheva E.E., Bryljova M.S. On the question of forms concentrating of gold coals for example Transbaikal coalfields. *Mining Informational and Analytical Bulletin*. 2016. N 9, p. 194-203 (in Russian).
33. Ahmed R., Sreeram V., Mishra Y., Arif M.D. A review and evaluation of the state-of-the-art in PV solar power forecasting: Techniques and optimization. *Renewable and Sustainable Energy Reviews*. 2020. Vol. 124. N 109792. DOI: [10.1016/j.rser.2020.109792](https://doi.org/10.1016/j.rser.2020.109792)
34. Sergeev N.N., Matrenin P.V. A review of international experience in forecasting renewable energy generation using machine learning methods. *iPolytech Journal*. 2023. Vol. 27. N 2, p. 354-369 (in Russian). DOI: [10.21285/1814-3520-2023-2-354-369](https://doi.org/10.21285/1814-3520-2023-2-354-369)
35. Nespoli A., Ogliairi E., Leva S. et al. Day-Ahead Photovoltaic Forecasting: A Comparison of the Most Effective Techniques. *Energies*. 2019. Vol. 12. Iss. 9. N 1621. DOI: [10.3390/en12091621](https://doi.org/10.3390/en12091621)



36. Wais P. Two and three-parameter Weibull distribution in available wind power analysis. *Renewable Energy*. 2017. Vol. 103, p. 15-29. DOI: [10.1016/j.renene.2016.10.041](https://doi.org/10.1016/j.renene.2016.10.041)
37. Wannakam K., Jiriwibhakorn S. Evaluation of Wind Energy Production Using Weibull Distribution and Artificial Neural Networks. 2018 International Conference on Engineering, Applied Sciences, and Technology, 4-7 July 2018, Phuket, Thailand. IEEE, 2018, p. 4. DOI: [10.1109/iceast.2018.8434474](https://doi.org/10.1109/iceast.2018.8434474)
38. Simeng Cheng, Yimiao Xie, Zhan Shu et al. Effect of Different Solar Irradiance Parameters on Reliability Evaluation of the Grid. *IOP Conference Series: Earth and Environmental Science*. 2019. Vol. 300. Iss. 4. N 042115. DOI: [10.1088/1755-1315/300/4/042115](https://doi.org/10.1088/1755-1315/300/4/042115)
39. Bramm A.M., Eroshenko S.A., Khalyasmaa A.I., Matrenin P.V. Grey Wolf Optimizer for RES Capacity Factor Maximization at the Placement Planning Stage. *Mathematics*. 2023. Vol. 11. Iss. 11. N 2545. DOI: [10.3390/math11112545](https://doi.org/10.3390/math11112545)
40. Bramm A.M., Mazunina M.V. Effects of the Firefly Optimization Algorithm Hyperparameters on the Optimal Placement Problem Results of Renewables-Based Power Plants. 2023 Belarusian-Ural-Siberian Smart Energy Conference, 25-29 September 2023, Ekaterinburg, Russia. IEEE, 2023, p. 48-53. DOI: [10.1109/BUSSEC59406.2023.10296466](https://doi.org/10.1109/BUSSEC59406.2023.10296466)
41. Maria E., Budiman E., Haviliddin, Taruk M. Measure distance locating nearest public facilities using Haversine and Euclidean Methods. *Journal of Physics: Conference Series*. 2020. Vol. 1450. N 012080. DOI: [10.1088/1742-6596/1450/1/012080](https://doi.org/10.1088/1742-6596/1450/1/012080)

Authors: Andrei M. Bramm, Junior Researcher, am.bramm@urfu.ru, <https://orcid.org/0000-0002-1868-4389> (Ural Federal University named after the first President of Russia B.N.Yeltsin, Yekaterinburg, Russia), Stanislav A. Eroshenko, Candidate of Technical Sciences, Associate Professor, <https://orcid.org/0000-0001-9617-2154> (Ural Federal University named after the first President of Russia B.N.Yeltsin, Yekaterinburg, Russia).

The authors declare no conflict of interests.



Enhancing the interpretability of electricity consumption forecasting models for mining enterprises using SHapley Additive exPlanations

Pavel V. Matrenin^{1,2}✉, **Alina I. Stepanova¹**

¹ Ural Federal University named after the first President of Russia B.N.Yeltsin, Yekaterinburg, Russia

² Novosibirsk State Technical University, Novosibirsk, Russia

How to cite this article: Matrenin P.V., Stepanova A.I. Enhancing the interpretability of electricity consumption forecasting models for mining enterprises using SHapley Additive exPlanations. *Journal of Mining Institute*. 2025. Vol. 271. N 16345, p. 154-167.

Abstract

The objective of this study is to enhance user trust in electricity consumption forecasting systems for mining enterprises by applying explainable artificial intelligence methods that provide not only forecasts but also their justifications. The research object comprises a complex of mines and ore processing plants of a company purchasing electricity on the wholesale electricity and power market. Hourly electricity consumption data for two years, schedules of planned repairs and equipment shutdowns, and meteorological data were utilized. Ensemble decision trees were applied for time series forecasting, and an analysis of the impact of various factors on forecasting accuracy was conducted. An algorithm for interpreting forecast results using the SHapley Additive exPlanation method was proposed. The mean absolute percentage error was 7.84 % with consideration of meteorological factors, 7.41 % with consideration of meteorological factors and a load plan formulated by an expert, and the expert's forecast error was 9.85 %. The results indicate that the increased accuracy of electricity consumption forecasting, considering additional factors, further improves when combining machine learning methods with expert evaluation. The development of such a system is only feasible using explainable artificial intelligence models.

Keywords

electricity consumption forecasting; mining enterprises; wholesale electricity and power market; explainable artificial intelligence; ensemble models; Shapley vector

Funding

The research funding from the Ministry of Science and Higher Education of the Russian Federation (Ural Federal University named after the first President of Russia B.N.Yeltsin Program of Development within the Priority-2030 Program) is gratefully acknowledged.

Received: 10.11.2023

Accepted: 03.06.2024

Online: 16.10.2024

Published: 25.02.2025

Introduction

Electricity consumption forecasting is essential for planning the operation of power systems [1, 2]. Many countries are introducing economic incentives to develop demand-responsive electricity consumption¹ [3]. One of the tools stimulating enterprises to plan their daily electricity consumption curves is the wholesale electricity and power market [4]. When connected to such market, mining enterprises can benefit from lower tariffs than when connected to the retail market, provided accurate electricity consumption forecasting is undertaken, as tariffs for electricity payment include charges for deviations between actual and planned consumption graphs. The consumption graphs of the enterprises considered often have a high aperiodic component of electrical load, which requires considering multiple production factors to account for, making the forecasting process labor-intensive [5-7]. Thus,

¹ On the technology of the community-dependent consumption. URL: <https://www.so-ups.ru/functioning/markets/dr/> (accessed 10.11.2023).



the task of electricity consumption forecasting becomes important not only for the system operator but also economically relevant for large enterprises.

Methods for short-term (1-3 days) forecasting of electricity consumption graphs can be divided into deterministic (statistical) and machine learning methods. The former include seasonal models [8] and methods based on autoregression, among which ARMA and ARIMA are most used [9, 10]. Algorithms employing various signal filtering techniques, such as the Kalman filter [11] or wavelet transformation, can also be classified under autoregression methods and are used to build forecasts.

Machine learning methods can consider many factors, including meteorological [12-14] and production-related [15] factors, as well as the dependencies between them [16]. The advantages of using machine learning methods over deterministic ones are demonstrated in works [5, 17, 18]. Typically, the best results are achieved using neural network models [19-21], including recurrent [5, 22, 23] and deep neural networks [24-26], as well as ensemble decision tree models [6, 13, 27].

Forecasting electricity consumption for industrial enterprises differs primarily from forecasting large power systems (cities or regions) due to the less pronounced periodicity of the graph and greater dispersion, which is associated with the summation of electricity consumption from many objects when dealing with large energy systems. The average error of electricity consumption forecasting for regions of Russia ranges from 1-2 %, as shown in works such as for the Ural Power Grid [27], Altai Krai [14], and Siberia [28]. For industrial enterprises, such accuracy is often unattainable due to the necessity of accurately accounting for various technological process parameters. It is demonstrated in [29] that for several enterprises, it is impossible to construct an acceptable forecast without using precise data on the plant's electricity consumption. However, not all enterprises can plan their hourly load curve with high accuracy. For example, in the coal mining industry, this is impossible due to a complex of geological and technological factors [5, 30]. A more realistic approach is to account for scheduled repairs and shutdowns of the most energy-intensive equipment [16], where the use of data on scheduled equipment repairs reduced the forecast error from 7 to 5.5 %.

Studies dedicated to short-term forecasting of electricity consumption for mining enterprises [5, 6, 30] are an order of magnitude fewer than those for large energy systems. They do not consider meteorological and production factors. In works [31, 32], the task of forecasting monthly consumption values for enterprises is considered, which significantly differs from short-term hourly planning.

A significant factor hindering the industrial adoption of machine learning, which receives insufficient attention, is the low level of trust in machine learning model results due to their lack of interpretability. Users must accept outcomes without explanation. The challenge in implementing machine learning lies in the negative impact of errors and distortions in input data on forecast accuracy, which are impossible to trace [33].

The objective of this study is to investigate and develop methods for interpreting the results of short-term electricity consumption forecasting models for a mining enterprise using explainable artificial intelligence. The tasks of the study include collecting and preprocessing data from the mining enterprise; building a short-term electricity consumption forecasting model based on machine learning; examining the influence of meteorological and production factors on forecasting accuracy; analyzing methods of explainable artificial intelligence and selecting an interpretation algorithm; applying the chosen algorithm and analyzing the results.

Methods

Initial data. The data used in this study pertains to a mining enterprise located in Yakutia. The complex includes mines, ore processing plants, and administrative buildings. The initial dataset included half-hourly electricity consumption values for two years without missing values, obtained from the enterprise's automated commercial electricity metering system (ACEMS), manually created forecasted consumption values, and data on scheduled repairs of energy-intensive equipment (or



complexes) at the enterprise. The use of data for two years is due to the availability of digitized indicators and updates to the energy-intensive equipment at the enterprise. Meteorological data, including wind speed, air temperature, atmospheric pressure, humidity, was also added from the rp5.ru website archive. Table 1 provides information on the original data and the preprocessing performed. Half-hourly electricity consumption values were summed pairwise to obtain hourly values, as it is the time series with hourly values that is submitted to the sales company or directly to the system operator as the enterprise's electricity consumption forecast curve.

Table 1

Initial data for research		
Name	Time sampling step, h	Source
Electricity consumption, MW·h	0.5	ACEMS
Manually created forecasted consumption values, MW·h	1	Chief engineer's department
Wind speed, m/s	3	rp5.ru
Air temperature, °C	3	rp5.ru
Atmospheric pressure, mm Hg	3	rp5.ru
Humidity, %	3	rp5.ru
Scheduled repairs	–	Chief engineer's department

Linear interpolation was applied to the meteorological data. In this study, actual meteorological data is used instead of forecasted data due to the lack of open access to archives of specifically forecasted weather values. This assumption is since meteorological factors are secondary rather than primary, and they are considered in the electricity consumption forecast for the enterprise, as well as the sufficiently high accuracy of weather forecasts for the next day.

The data on scheduled repairs, initially presented as a list of repair time intervals for each equipment or complex, has been generated by constructing matrix R , where element r_{ij} is equal to one if the j -th equipment is planned to be in a repair state at the i -th time moment (hour), and otherwise, the value is zero. The amount of equipment for the object is $m = 23$.

Figure 1 shows a fragment of the hourly electricity consumption graph for two months. In order to enhance visibility, the graph starts at the 100 MW·h level.

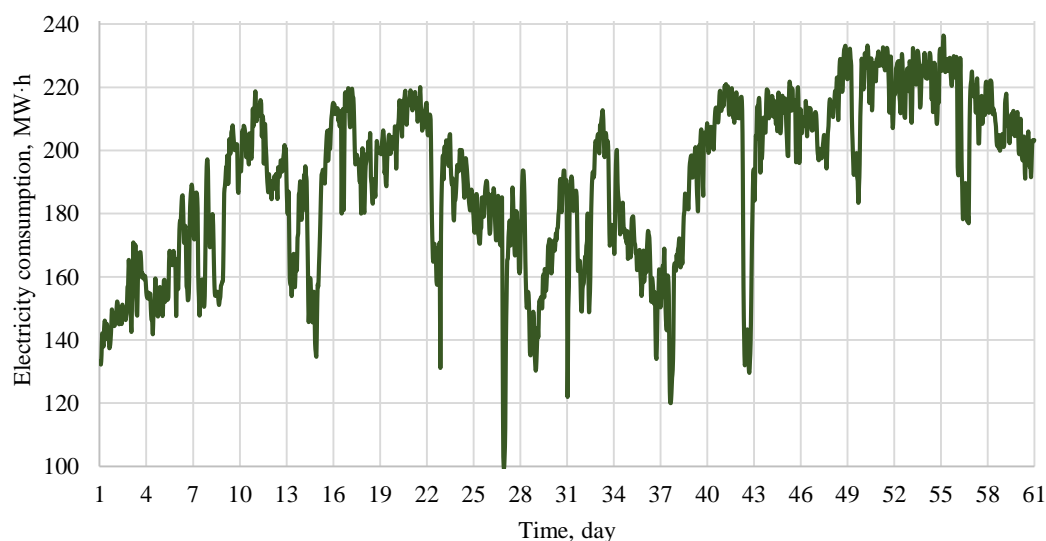


Fig.1. Fragment of the enterprise's electricity consumption graph



Dataset formation for machine learning application. Time series forecasting using machine learning models, one of the key factors affecting the result is the selection of features [14, 16, 34]. Typically, in addition to other features, electricity consumption forecasting uses previous values to predict subsequent ones:

$$y_i^* = f(g(y_{i-h}, y_{i-h-1}, \dots, y_{i-h-w}), X),$$

where y_i^* is the forecasted electricity consumption at i time; f is the forecasting model; g is a function that defines the rule for selecting retrospective actual electricity consumption values; h is the forecasting horizon; w – is the width of the retrospective data window; X are other features (e.g., hour or day of the week, meteorological factors, production factors, etc.).

When using neural network models, especially recurrent ones, it is possible to process all values of the time series $y_{i-h}, y_{i-h-1}, \dots, y_{i-h-w}$ [5, 6, 21]. However, for industrial enterprises, it is sufficient to use retrospective time series values that are offset from the forecasted hour by a multiple of 6, 12, or 24 h, which is related to production technological cycles. This allows for significantly simplifying the model and reducing the risk of overfitting due to an excessive number of features [6, 16, 35].

During preliminary correlation analysis, it was determined that for forecasting, it is sufficient to use hours with a step of 12 and a retrospective depth of three days. For example, to forecast the daily load profile component for 28.10.2023 from 19:00 to 20:00, the following data will be used: electricity consumption from 27.10.2023 from 19:00 to 20:00 and 07:00 to 08:00, from 26.10.2023 from 19:00 to 20:00, and from 25.10.2023 from 19:00 to 20:00. Thus, the expression takes the form:

$$y_i^* = f(y_{i-24}, y_{i-36}, y_{i-48}, y_{i-60}, y_{i-72}, X),$$

where X contains the following features: hour number i (from 0 to 23); day of the month for the forecast (from 1 to 31); day of the week for the forecast (1-7); month for the forecast (1-12); expert-manual load forecast y_i^e (results were obtained with and without its consideration); wind speed at hour i ; air temperature at hour i ; atmospheric pressure at hour i ; relative humidity at hour i ; scheduled repairs, vector $r_{ij}, j = 1, \dots, m$.

As a result, the full feature vector contains 37 values (5 retrospective electricity consumption values; 4 calendar features; expert-manual load forecast; 4 meteorological factors; 23 repair-related features). During the study, various combinations of features were tested to determine their impact on forecast accuracy. Data preprocessing, model building, and testing were performed in Python 3 using the open-source Pandas and Scikit-Learn libraries.

Used machine learning methods. Short-term electricity consumption forecasting for enterprises is effectively addressed using artificial neural networks and decision tree ensembles. Previous research by the authors of this article demonstrated that ensemble models of gradient and adaptive boosting, as well as random forests, achieve comparable accuracy to neural network models while offering faster training times and simpler hyperparameter tuning [6, 16, 33]. Studies [27, 29] successfully applied decision tree ensembles for forecasting electricity consumption.

Therefore, in this work, ensemble methods including random forest (Random Forest) and adaptive boosting (AdaBoost)², extreme gradient boosting (XGBoost) [36] for building ensembles of regression decision trees. A single tree can be represented as

$$y_i^* = t(Z_i),$$

where t is a hierarchical system of rules, each comparing the value of a specific feature to a threshold.

² 1.11. Ensembles: Gradient boosting, random forests, bagging, voting, stacking. URL: <https://scikit-learn.org/stable/modules/ensemble.html> (accessed 01.11.2023).



Random forest builds a regression model as an ensemble of k decision trees, each trained independently on a randomly selected subset of instances from the training dataset³:

$$y_i^* = \frac{1}{k} \sum_{j=1}^k t_j(Z_i).$$

In contrast, adaptive boosting and extreme gradient boosting build ensembles iteratively. Each subsequent model in the ensemble depends on the results of previous ones. Ultimately, the model is formed as

$$y_i^* = \sum_{j=1}^k w_j t_j(Z_i),$$

where w_j is the weight of the j -th model (in this case, a decision tree).

After adding each new model to the ensemble, adaptive boosting adjusts the weights of the training dataset instances, increasing them proportionally to the deviation of the model's output from the true value. In gradient boosting, the gradient of the error of the current ensemble serves as the optimization criterion for building each new model in the ensemble. Various implementations of gradient boosting exist, including extreme boosting [36].

Analysis of the applicability of eXplainable Artificial Intelligence. The use of systems that provide experts with decisions without explanations based on non-interpretable algorithms is limited because they lack user trust and may contain hidden risks of unforeseen critical errors. To address this issue, the field of research focusing on improving user interaction with intelligent systems through eXplainable Artificial Intelligence (XAI) methods is developing. XAI aims to create intelligent systems capable of interpreting their results and explaining them to the user [37, 38]. The XAI concept involves adhering to principles of explainability (the intelligent system must explain its results), significance (the explanation should be tailored for the user), accuracy (the explanation should truthfully describe how the model obtained the result), and limits of knowledge (the intelligent system must understand its applicability boundaries and not attempt to solve tasks beyond its capabilities).

The directions of XAI application can be divided into creating self-interpretable models and methods of a posteriori explanation of obtained results. For example, a decision tree with a small depth is an interpretable model because it represents a system of rules. For complex tasks, current methods use non-interpretable models, employing the second approach – applying a posteriori explanation method. Among such explanation methods, there is the Local Interpretable Model-Agnostic Explanations (LIME) method [39]. LIME involves building a local surrogate model that explains the workings of the explainable model in a narrow neighborhood of the considered input instance. The local surrogate model is a simple, interpretable model, such as a decision tree or linear regression, trained to predict the output of the explainable model in this neighborhood. A limitation of the method is the need to select, tune, and train the surrogate model, as well as the implicit violation of the accuracy principle, as the hypothesis that the surrogate model's explanation corresponds to the decision-making mechanism of the explainable model is an unverifiable assumption in each specific case.

For convolutional neural networks, methods based on class activation mapping (CAM), such as Grad-CAM, are used [40]. A limitation of this method is its applicability only to convolutional neural networks, as it relies on processing feature maps formed by each convolutional layer and calculating gradients derived from the model's output results with respect to the feature maps.

³ 1.11. Ensembles: Gradient boosting, random forests, bagging, voting, stacking. URL: <https://scikit-learn.org/stable/modules/ensemble.html> (accessed 01.11.2023).



If the user of an intelligent decision support system is an expert in the solved task, displaying features that influenced the decision formation along with their significance (weights) increases trust in the system and the likelihood of effective collaborative work with it. Therefore, in such areas as diagnostics, planning, or forecasting, where the model is used by an expert, the application of the additive SHAP (SHapley Additive exPlanations) method based on the Shapley vector is particularly relevant [41]. The additive SHAP explanation is based on the Shapley values algorithm from game theory. It determines the contribution of each player to the overall winnings. If players are replaced by features and winnings by the machine learning model's results, an algorithm for determining the impact of each feature on the model's result is obtained. When using the SHAP algorithm, the significance of the j -th feature for the model f when analyzing input data Z_i is calculated as:

$$\varphi_j(f, Z_i) = \sum_{S \subseteq P \setminus \{j\}} \frac{|S|!(m-|S|-1)!}{m!} [f_{S \cup \{j\}}(Z_{i, S \cup \{j\}}) - f_S(Z_{i, S})],$$

where m is the number of features; S is a subset of features; P is the set of all possible feature combinations; i is the input data instance; j is the feature index. If a feature is not used, its value is replaced with the average value. As a result, the feature's importance j is assessed by analyzing its impact on the model's results with and without it for various sets of other features.

The application of LIME and SHAP methods in power industry is still in its initial stages. In [42], both methods are applied to solar power plant generation forecasting. SHAP is used for electricity consumption forecasting in [43], but the object is a large energy system, not a specific enterprise.

In this work, for the first time, the principles of an intelligent system for short-term forecasting of electrical power consumption of a mining enterprise, considering meteorological factors and scheduled repairs, which provides the user with a forecast justification using the additive SHAP explanation were proposed and validated. The analysis of the obtained explanations and the description of the specialist's interaction with the intelligent system in load planning were presented.

Discussion

Results of electricity consumption forecast. The performance metrics of AdaBoost, XGBoost, and Random Forest methods for forecasting of electrical consumption were compared to the load forecast error manually created by an expert: mean absolute error (MAE) – 16.53 MW·h; mean absolute percentage error (MAPE) – 9.85 %; root mean square error (RMSE) – 21.18 MW·h. The dataset for model construction was divided into training and test sets with a 90:10 ratio.

Experiments to build machine learning models for forecasting the electrical consumption of a mining enterprise, considering different features were conducted.

In the first experiment, the following features were chosen:

- hour number i (from 0 to 23);
- day of the month for the forecast (from 1 to 31);
- day of the week for the forecast (1-7);
- month for the forecast (1-12);
- retrospective electricity consumption (consumption_1, consumption_2, consumption_3, consumption_4, consumption_5 – $y_{i-24}, y_{i-36}, y_{i-48}, y_{i-60}, y_{i-72}$).

Table 2 presents the forecasting results for electricity consumption using these features. Used notations are max_depth – maximum depth of decision trees in the ensemble; n_estimators – number of trees in the ensemble. The AdaBoost method achieved the best MAPE for the test set – 9.68 %. Compared to the MAPE of forecast manually created by an expert (9.85 %), the accuracy improved by 0.17 %. It can be concluded that without additional consideration of technological process parameters and metrological factors, the application of machine learning models does not enhance the accuracy of electricity consumption forecasting. However, it reduces the time



required to obtain the result. An expert takes 2-4 h to compile a consumption graph, whereas training takes up to 5 min.

Table 2

**Forecasting of electricity consumption of the enterprise
with consideration of retrospective consumption**

Method	MAE, MW·h		MAPE, %		RMSE, MW·h		max_depth	n_estimators
	Training	Test	Training	Test	Training	Test		
AdaBoost	10.28	15.80	8.88	9.68	12.51	20.96	7	200
XGBoost	9.09	18.45	8.34	11.58	12.84	23.79	3	150
Random Forest	10.60	17.07	9.96	10.89	15.30	23.56	7	7

In the second experiment, the feature vector $r_{ij}, j = 1, \dots, m$ of scheduled repairs was added to the features selected in first experiment (Table 3).

Table 3

**Forecasting of electricity consumption of the enterprise
with consideration of retrospective consumption and scheduled repairs**

Method	MAE, MW·h		MAPE, %		RMSE, MW·h		max_depth	n_estimators
	Training	Test	Training	Test	Training	Test		
AdaBoost	10.27	17.15	8.93	10.40	12.51	22.23	7	200
XGBoost	10.71	17.24	9.76	10.72	15.06	22.63	2	150
Random Forest	11.28	18.26	10.61	11.39	16.32	24.34	6	150

Similarly to the first experiment, the AdaBoost method achieved the best MAPE for the test set – 10.40 %. Incorporating the scheduled repairs factor degraded the forecast accuracy by 0.55 %, contrary to expectations of improved accuracy with additional consideration of production process factors. Further experiments with various repair grouping variants (feature aggregations) did not yield accuracy improvements. This is due to discrepancies between scheduled and actual repairs. For instance, if a repair was scheduled for 2 h from 10:00 to 12:00, it might have occurred at a different time (e.g., 14:00 to 16:00) or lasted longer (e.g., 10:00 to 17:00).

In the future, it may be beneficial to consider only repairs scheduled with high accuracy, such as those lasting several days. This would reduce the stochastic impact of short repairs on the electricity consumption graph.

In the third experiment, meteorological parameters for the i -th hour (wind speed, air temperature, atmospheric pressure, and humidity) were added to the features selected for the first experiment (Table 4).

Table 4

**Forecasting of electricity consumption of the enterprise
with consideration of retrospective consumption and meteorological factors**

Method	MAE, MW·h		MAPE, %		RMSE, MW·h		max_depth	n_estimators
	Training	Test	Training	Test	Training	Test		
AdaBoost	9.44	13.14	8.17	8.17	11.39	17.66	7	200
XGBoost	8.12	12.89	7.57	7.85	11.49	17.18	3	150
Random Forest	8.79	13.59	8.37	8.73	12.70	18.93	8	150



In the fourth experiment, both scheduled repairs and meteorological factors were considered (Table 5). The AdaBoost method achieved the best MAPE for the test set – 8.38 %. Although this represents a 1.48 % improvement over the forecast manually created by an expert, it is primarily due to the inclusion of meteorological factors. The discrepancy between actual and scheduled repairs prevents the use of repair data for model construction.

Table 5

**Forecasting of electricity consumption of the enterprise
with consideration of retrospective consumption, scheduled repairs, and meteorological factors**

Method	MAE, MW·h		MAPE, %		RMSE, MW·h		max_depth	n_estimators
	Training	Test	Training	Test	Training	Test		
AdaBoost	8.31	13.57	8.03	8.38	11.22	18.10	7	200
XGBoost	7.93	14.73	7.38	9.13	11.29	19.26	3	150
Random Forest	8.72	14.38	8.32	9.04	12.56	19.57	8	150

In the fifth experiment, retrospective consumption data, meteorological factors, and the forecast manually created by an expert were used (Table 6). Additionally, computational experiments with long short-term memory neural networks, specifically, Gated Recurrent Units (GRU), were conducted for model applicability assessment, following the architecture and hyperparameter selection approach described in [5]. The XGBoost method yielded the best MAPE for the test set – 7.41 %. This represents a 2.44 % improvement over the manually conducted expert forecast (9.85 %). In an intelligent system, integrating the expert forecast can be achieved through two methods: applying expert adjustments to the model-generated load curve; refining the expert load curve using the model.

The first method is preferable as it saves the time the expert spends on creating the planned electricity consumption load curve.

Table 6

**Forecasting of electricity consumption of the enterprise
with consideration of retrospective consumption, meteorological factors, and the forecast manually created by an expert**

Method	MAE, MW·h		MAPE, %		RMSE, MW·h		max_depth	n_estimators
	Training	Test	Training	Test	Training	Test		
AdaBoost	8.06	13.63	6.79	8.35	9.67	17.91	7	200
XGBoost	8.29	11.94	7.29	7.41	11.85	16.53	2	150
Random Forest	9.50	13.14	8.26	8.30	13.71	17.84	5	150
GRU	8.11	13.16	7.15	8.31	11.52	17.80	–	–

Figure 2 compares actual and forecasted electricity consumption. Analysis of the load curves indicates that incorporating and the forecast manually created by an expert allows the machine learning model to more accurately forecast sudden aperiodic consumption changes, highlighted by red ovals. Future research could focus on identifying and formalizing production factors related to these technological process changes, and integrating these factors as additional features into the machine learning model.

Table 7 summarizes the experimental results. Absolute and relative forecast improvements were calculated relative to the MAPE of the forecast manually created by an expert (9.85 %). Considering additional factors enhances accuracy. With retrospective consumption and meteorological data, forecast accuracy improves by 20.34 %. Including the forecast manually created by an expert, it further increases accuracy by 24.75 %.

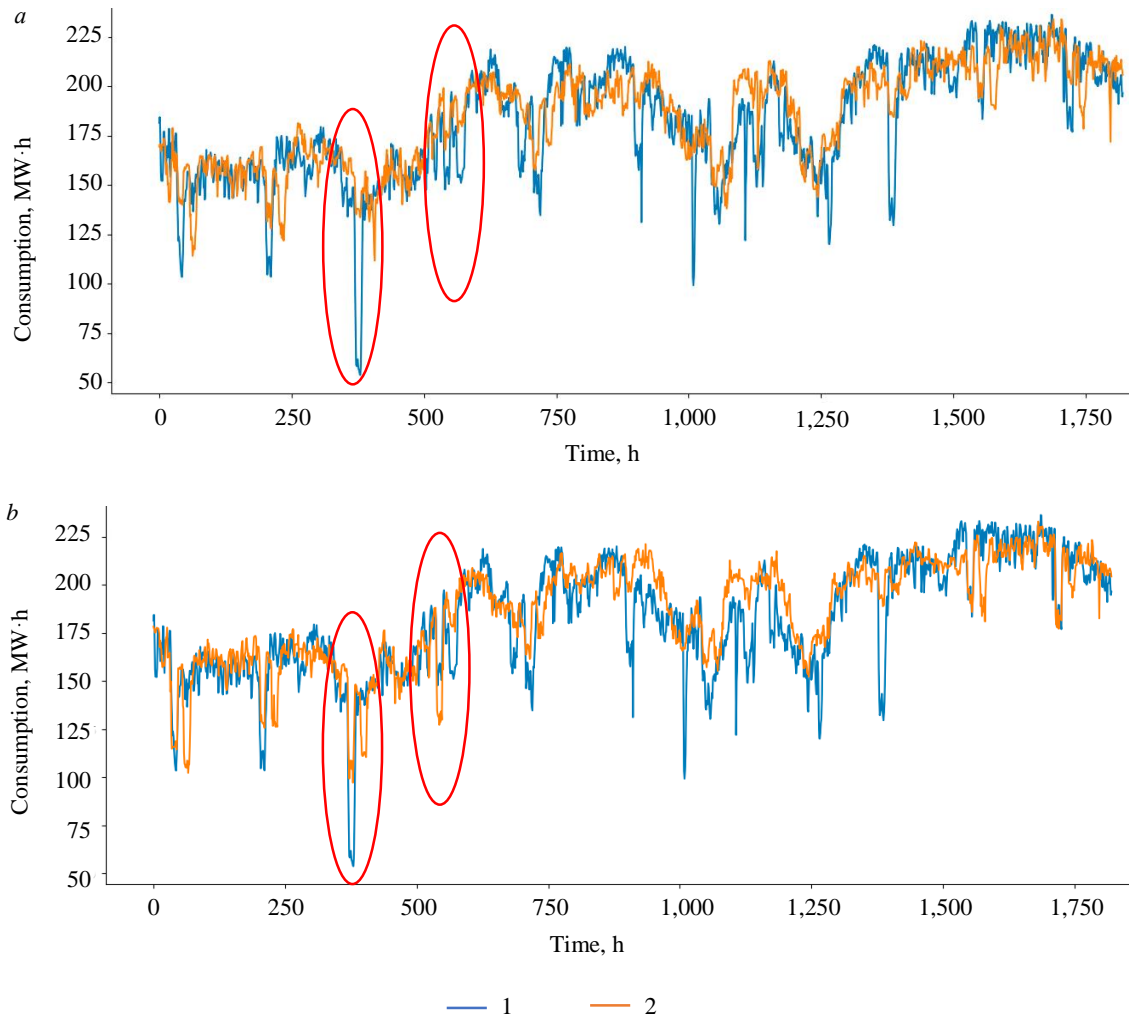


Fig.2. Comparison of actual (1) and forecasted (2) consumption considering: retrospective consumption and meteorological parameters (a); retrospective consumption, meteorological parameters, and the forecast manually created by an expert (b)

Table 7

Forecasting of electricity consumption of the enterprise with consideration of different features

Experiment	Feature under consideration	Model	MAPE, %	Absolute forecast improvement	Relative forecast improvement
1	Retrospective consumption	AdaBoost	9.68	0.17	1.70
2	Retrospective consumption, scheduled repairs	AdaBoost	10.40	−0.55	−5.54
3	Retrospective consumption, meteorological factors	XGBoost	7.85	2.00	20.34
4	Retrospective consumption, meteorological factors, and scheduled repairs	AdaBoost	8.38	1.48	14.97
5	Retrospective consumption, meteorological factors, and forecast manually created by an expert	XGBoost	7.41	2.44	24.75

Explanation of results. SHAP enables the formal mapping of features that influenced the forecast of electricity consumption for each hour, along with their significance (weights), which can be interpreted by an expert.

Figure 3 illustrates the features affecting the electricity consumption forecast for one hour during the winter period in the third experiment, which considered retrospective consumption and meteorological

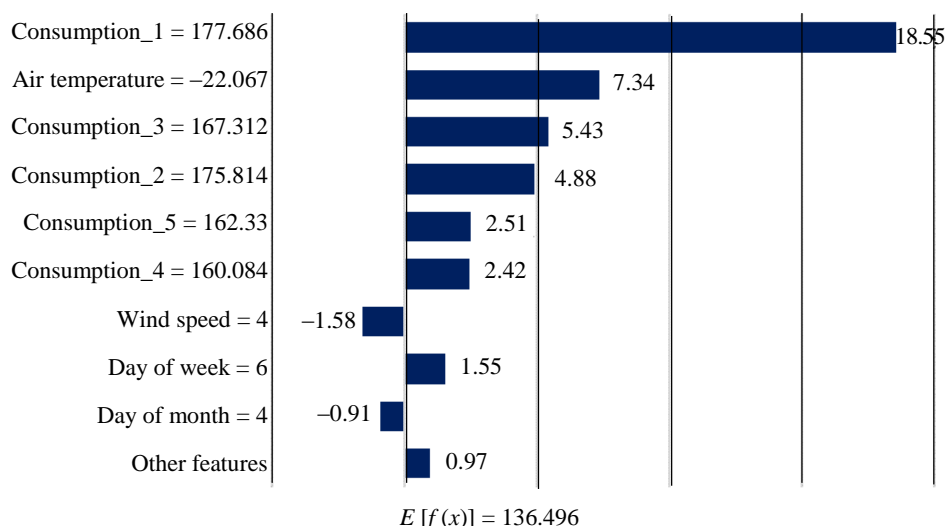


Fig.3. Visualization of features impacting the electricity consumption forecast
 $f(x) = 177.665 \text{ MW} \cdot \text{h}$

factors. Features are arranged in descending order of their impact on the deviation of the forecasted consumption $f(x)$ from the average value $E[f(x)]$. Thus, for the data in Fig.3, it can be concluded that the deviation of $f(x)$, which was $177.665 \text{ MW} \cdot \text{h}$, from the average value of $136.496 \text{ MW} \cdot \text{h}$, is justified by high consumption 24, 36, and 48 h before the forecasted hour and low air temperature.

Figure 4 shows the features affecting the electricity consumption forecast for another hour during the winter period in the same experiment. The deviation of $f(x)$, which was $213.972 \text{ MW} \cdot \text{h}$, from the average value of $136.496 \text{ MW} \cdot \text{h}$, is justified by abnormally low air temperature and high consumption 24, 36, and 72 h before the forecasted hour.

Figure 5 depicts the features affecting the electricity consumption forecast during the winter period in the same experiment with a different distribution of significance for meteorological features. The deviation of $f(x)$, which was $190.858 \text{ MW} \cdot \text{h}$, from the average value of $136.496 \text{ MW} \cdot \text{h}$, is justified by consumption 24, 36, and 72 h before the forecasted hour, air temperature, as well as wind speed and pressure values. The analysis of features obtained using the Shapley method confirms the necessity of considering meteorological factors when building a model for forecasting electricity consumption.

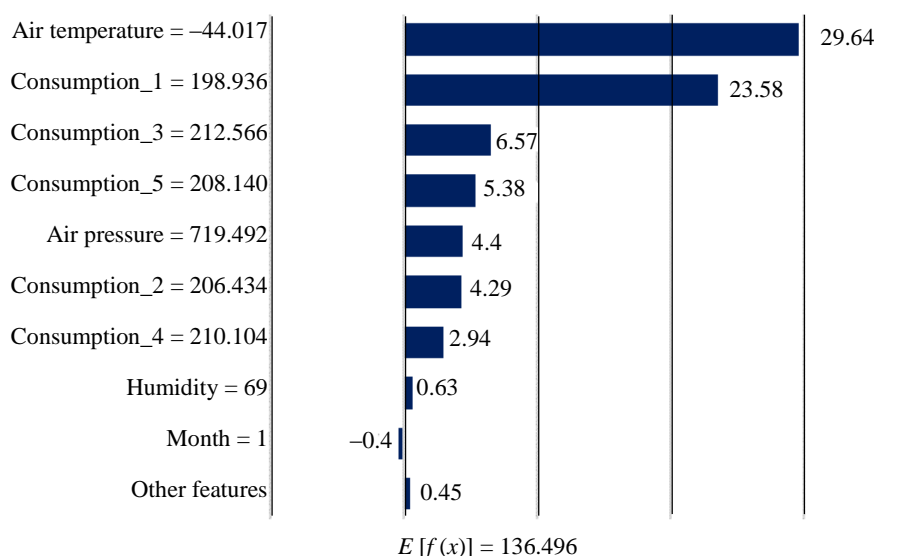


Fig.4. Visualization of features impacting the electricity consumption forecast
 $f(x) = 213.972 \text{ MW} \cdot \text{h}$

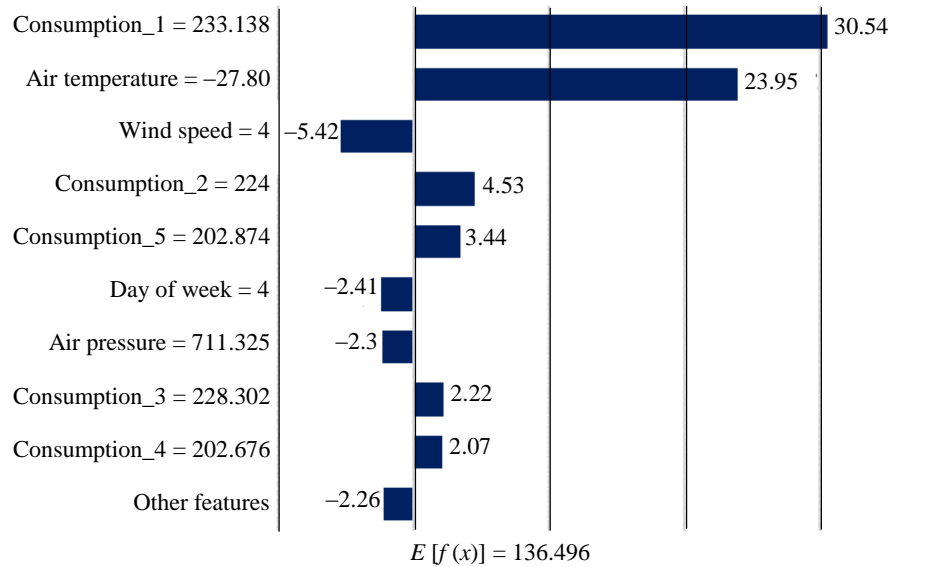


Fig.5. Visualization of features impacting the electricity consumption forecast
 $f(x) = 190.858 \text{ MW} \cdot \text{h}$

Figure 6 presents the results for the fifth experiment, where the expert-formulated consumption plan was considered for the same hour analyzed in Fig.3. The expert-formulated plan itself contributed the most to the value of $f(x)$, which was $180.863 \text{ MW} \cdot \text{h}$. However, the meteorological factors also play a crucial role even when considering the expert-formulated consumption plan, as shown in Fig.7 for the same hour analyzed in Fig.4.

The experiments conducted demonstrate that the SHapley Additive exPlanations for each output value of the machine learning model visually and comprehensibly illustrates the feature impacts, enhancing the model's interpretability for experts. It should be noted that this result does not fully meet the requirements for explainable artificial intelligence outlined above. Nonetheless, the SHapley Additive exPlanations is considered one of the most promising methods in explainable artificial intelligence, and its further development in forecasting tasks will likely increase the trust of electricity consumption experts in machine learning-based systems.

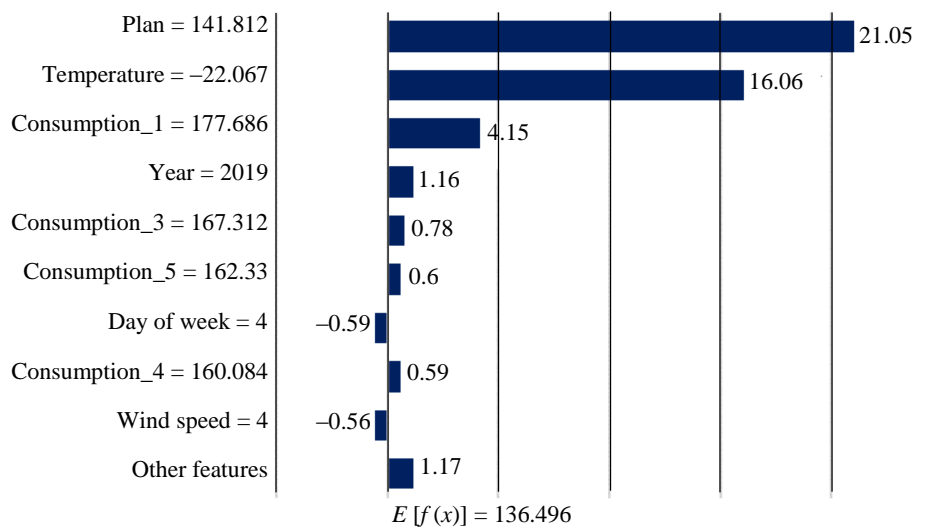


Fig.6. Visualization of features impacting the electricity consumption forecast
 $f(x) = 180.863 \text{ MW} \cdot \text{h}$

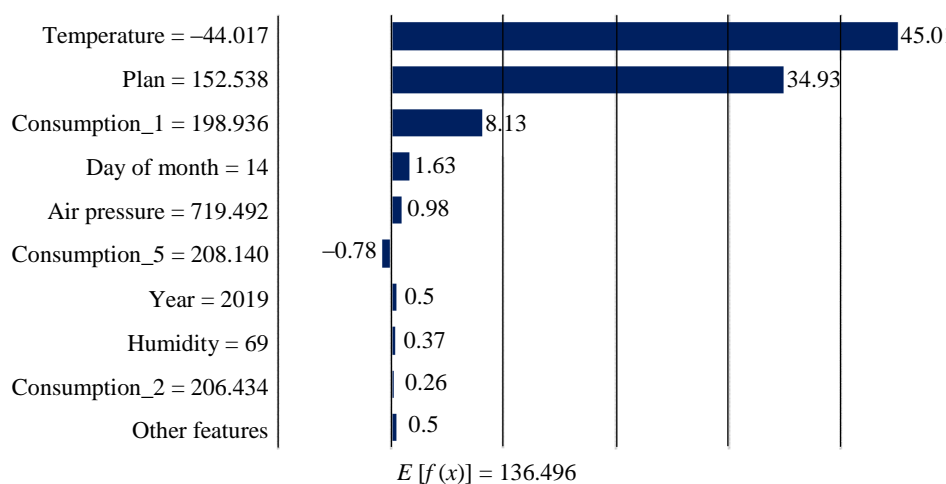


Fig.7. Visualization of features impacting the electricity consumption forecast
 $f(x) = 227.987 \text{ MW} \cdot \text{h}$

Conclusion

An approach to creating an intelligent system for short-term forecasting of electricity consumption of a mining enterprise, considering meteorological factors and scheduled repairs was proposed. Incorporating meteorological factors in addition to consumption history enhances forecast accuracy by 20.34 %.

However, due to discrepancies between actual and planned repairs, forecast accuracy decreases by 0.55 % relative to the forecast manually created by an expert when considering scheduled repairs. Future research will focus on accounting only for repairs lasting more than 12 h to minimize the impact of inaccurate repair forecasts on model training results.

Applying an expert-formulated plan along with retrospective consumption and meteorological factors increases forecast accuracy to 24.75 %. In developing an information system, this expert plan can be incorporated through expert correction functions and analysis of historical discrepancies between expert corrections and model results. Future research also aims to more precisely formalize expert experience.

The proposed approach to creating an information system includes a model that provides users with a forecast justification using SHapley Additive exPlanations. Explanation results enable experts to analyze the impact of factors on forecasting results, simplifying the introduction of expert corrections and accelerating system implementation. The practical significance of the study lies in enhancing the accuracy of short-term electricity consumption forecasting for industrial enterprises by considering equipment repairs and shutdowns and creating conditions for industry-wide adoption of machine learning-based information systems using explainable artificial intelligence algorithms, thereby increasing user trust.

The proposed system is planned to be tested using machine learning methods and explainable machine learning models on data from other industrial enterprises with larger volumes of available indicator data and deeper historical depth; to specify and formalize production factors for their inclusion as model features; modify the SHapley Additive exPlanations to improve the interpretability of its results for the considered task; and analyze the impact of electricity consumption forecast accuracy on the enterprise's electricity consumption costs.

REFERENCES

1. Park S., Ruy S., Choi Y. et al. Data-Driven Baseline Estimation of Residential Buildings for Demand Response. *Energies*. 2015. Vol. 8. Iss. 9, p. 10239-10259. DOI: [10.3390/en80910239](https://doi.org/10.3390/en80910239)
2. Almuhaini S.H., Sultana N. Forecasting Long-Term Electricity Consumption in Saudi Arabia Based on Statistical and Machine Learning Algorithms to Enhance Electric Power Supply Management. *Energies*. 2023. Vol. 16. Iss. 4. N 2035. DOI: [10.3390/en16042035](https://doi.org/10.3390/en16042035)



3. Faria P., Vale Z. Demand Response in Smart Grids. *Energies*. 2023. Vol. 16. Iss. 2. N 863. DOI: [10.3390/en16020863](https://doi.org/10.3390/en16020863)
4. Kanapelko R.A. Russian and foreign practice of interaction between corporate and government structures of the wholesale electricity and capacity market. *Journal of Economy and Business*. 2019. N 2, p. 47-51 (in Russian). DOI: [10.24411/2411-0450-2019-10364](https://doi.org/10.24411/2411-0450-2019-10364)
5. Matrenin P.V., Manusov V.Z., Khalyasmaa A.I. et al. Improving Accuracy and Generalization Performance of Small-Size Recurrent Neural Networks Applied to Short-Term Load Forecasting. *Mathematics*. 2020. Vol. 8. Iss. 12. N 2169. DOI: [10.3390/math8122169](https://doi.org/10.3390/math8122169)
6. Antonenkov D.V., Matrenin P.V. Ensemble and Neural Network Machine Learning Models for Short-Term Load Forecasting of Open Cast Mining Companies. *Electrotechnical Systems and Complexes*. 2021. N 3 (52), p. 57-65 (in Russian). DOI: [10.18503/2311-8318-2021-3\(52\)-57-65](https://doi.org/10.18503/2311-8318-2021-3(52)-57-65)
7. Nepsha F.S., Krasilnikov M.I., Perevalov K.V. Application of a digital platform to build intelligent energy management systems for mining enterprises. *Avtomatizatsiya i IT v energetike*. 2021. N 5 (142), p. 26-34. (in Russian)
8. Jianjun Fan, Xinzhong Liu, Zhimin Li et al. Power load forecasting research based on neural network and Holt-winters method. *IOP Conference Series: Earth and Environmental Science*. 2021. Vol. 692. N 022120. DOI: [10.1088/1755-1315/692/2/022120](https://doi.org/10.1088/1755-1315/692/2/022120)
9. Potapov V., Khamitov R., Makarov V. et al. Short-Term Forecast of Electricity Load for LLC “Omsk Energy Retail Company” Using Neural Network. 2018 Dynamics of Systems, Mechanisms and Machines (Dynamics), 13-15 November 2018, Omsk, Russia. IEEE, 2018. DOI: [10.1109/Dynamics.2018.8601430](https://doi.org/10.1109/Dynamics.2018.8601430)
10. Chodakowska E., Nazarko J., Nazarko L. ARIMA Models in Electrical Load Forecasting and Their Robustness to Noise. *Energies*. 2021. Vol. 14. Iss. 23. N 7952. DOI: [10.3390/en14237952](https://doi.org/10.3390/en14237952)
11. Sharma S., Majumdar A., Elvira V., Chouzenoux É. Blind Kalman Filtering for Short-Term Load Forecasting. *IEEE Transactions on Power Systems*. 2020. Vol. 35. Iss. 6, p. 4916-4919. DOI: [10.1109/TPWRS.2020.3018623](https://doi.org/10.1109/TPWRS.2020.3018623)
12. Madhukumar M., Sebastian A., Xiaodong Liang et al. Regression Model-Based Short-Term Load Forecasting for University Campus Load. *IEEE Access*. 2022. Vol. 10, p. 8891-8905. DOI: [10.1109/ACCESS.2022.3144206](https://doi.org/10.1109/ACCESS.2022.3144206)
13. Serebryakov N.A. Application of Deep Neural Network Ensemble in a Problem of Short-Term Load Forecasting Guaranteed Electricity Supplier. *Electrotechnical Systems and Complexes*. 2021. N 2 (51), p. 52-60 (in Russian). DOI: [10.18503/2311-8318-2021-2\(51\)-52-60](https://doi.org/10.18503/2311-8318-2021-2(51)-52-60)
14. Caro E., Juan J., Nouhitehrani S. Optimal Selection of Weather Stations for Electric Load Forecasting. *IEEE Access*. 2023. Vol. 11, p. 42981-42990. DOI: [10.1109/ACCESS.2023.3270933](https://doi.org/10.1109/ACCESS.2023.3270933)
15. Sergeev N., Matrenin P. Improving Accuracy of Machine Learning Based Short-Term Load Forecasting Models with Correlation Analysis and Feature Engineering. 2023 IEEE 24th International Conference of Young Professionals in Electron Devices and Materials (EDM), 29 June – 3 July 2023, Novosibirsk, Russia. IEEE, 2023, p. 1000-1004. DOI: [10.1109/EDM58354.2023.10225058](https://doi.org/10.1109/EDM58354.2023.10225058)
16. Habbak H., Mahmoud M., Metwally K. et al. Load Forecasting Techniques and Their Applications in Smart Grids. *Energies*. 2023. Vol. 16. Iss. 3. N 1480. DOI: [10.3390/en16031480](https://doi.org/10.3390/en16031480)
17. Ryu S., Noh J., Kim H. Deep Neural Network Based Demand Side Short Term Load Forecasting. *Energies*. 2017. Vol. 10. Iss. 1. N 3. DOI: [10.3390/en10010003](https://doi.org/10.3390/en10010003)
18. Szczepaniuk H., Szczepaniuk E.K. Applications of Artificial Intelligence Algorithms in the Energy Sector. *Energies*. 2023. Vol. 16. Iss. 1. N 347. DOI: [10.3390/en16010347](https://doi.org/10.3390/en16010347)
19. Lizhen Wu, Chun Kong, Xiaohong Hao, Wei Chen. A Short-Term Load Forecasting Method Based on GRU-CNN Hybrid Neural Network Model. *Mathematical Problems in Engineering*. 2020. Vol. 2020. Iss. 1. N 1428104. DOI: [10.1155/2020/1428104](https://doi.org/10.1155/2020/1428104)
20. Zhuofu Deng, Binbin Wang, Yanlu Xu et al. Multi-Scale Convolutional Neural Network With Time-Cognition for Multi-Step Short-Term Load Forecasting. *IEEE Access*. 2019. Vol. 7, p. 88058-88071. DOI: [10.1109/ACCESS.2019.2926137](https://doi.org/10.1109/ACCESS.2019.2926137)
21. Weicong Kong, Zhao Yang Dong, Youwei Jia et al. Short-Term Residential Load Forecasting Based on LSTM Recurrent Neural Network. *IEEE Transactions on Smart Grid*. 2019. Vol. 10. Iss. 1, p. 841-851. DOI: [10.1109/TSG.2017.2753802](https://doi.org/10.1109/TSG.2017.2753802)
22. Potapov V.I., Gritsay A.S., Tyunkov D.A., Sinitin G.E. Using neural network for building short-term forecast of electricity load of LLC “Omsk Energy Retail Company”. *Bulletin of the Tomsk Polytechnic University. Geo Assets Engineering*. 2016. Vol. 327. N 8, p. 44-51 (in Russian).
23. Cai M., Pipattanasomporn M., Rahman S. Day-ahead building-level load forecasts using deep learning vs. traditional time-series techniques. *Applied Energy*. 2019. Vol. 236, p. 1078-1088. DOI: [10.1016/j.apenergy.2018.12.042](https://doi.org/10.1016/j.apenergy.2018.12.042)
24. Ye Hong, Yingjie Zhou, Qibin Li et al. A Deep Learning Method for Short-Term Residential Load Forecasting in Smart Grid. *IEEE Access*. 2020. Vol. 8, p. 55785-55797. DOI: [10.1109/ACCESS.2020.2981817](https://doi.org/10.1109/ACCESS.2020.2981817)
25. Zhuofu Deng, Binbin Wang, Yanlu Xu et al. Multi-Scale Convolutional Neural Network With Time-Cognition for Multi-Step Short-Term Load Forecasting. *IEEE Access*. 2019. Vol. 7, p. 88058-88071. DOI: [10.1109/ACCESS.2019.2926137](https://doi.org/10.1109/ACCESS.2019.2926137)
26. Ahmad N., Ghadi Y., Adnan M., Ali M. Load Forecasting Techniques for Power System: Research Challenges and Survey. *IEEE Access*. 2022. Vol. 10, p. 71054-71090. DOI: [10.1109/ACCESS.2022.3187839](https://doi.org/10.1109/ACCESS.2022.3187839)
27. Klyuev R.V., Morgoeva A.D., Gavrina O.A. et al. Forecasting planned electricity consumption for the united power system using machine learning. *Journal of Mining Institute*. 2023. Vol. 261, p. 392-402.
28. Rusina A.G., Filippova T.A., Kalinin A.E., Terlyga N.S. Short-Term Electricity Consumption Forecast in Siberia IPS Using Climate Aspects. 2018 19th International Conference of Young Specialists on Micro/Nanotechnologies and Electron Devices (EDM), 29 June – 3 July 2018, Erlagol, Russia. IEEE, 2018, p. 6403-6407. DOI: [10.1109/EDM.2018.8435002](https://doi.org/10.1109/EDM.2018.8435002)
29. Morgoev I.D., Dzgoev A.E., Klyuev R.V., Morgoeva A.D. Forecasting of electricity consumption by enterprises of the public sector complex in conditions of incomplete information. *Izvestiya Kabardino-Balkarskogo nauchnogo tsentra RAS*. 2022. N 3 (107), p. 9-20 (in Russian). DOI: [10.35330/1991-6639-2022-3-107-9-20](https://doi.org/10.35330/1991-6639-2022-3-107-9-20)
30. Antonenkov D.V., Solovov D.B. Mathematic simulation of mining company’s power demand forecast (by example of “Neryungri” coal strip mine). *IOP Conference Series: Earth and Environmental Science*. 2017. Vol. 87. Iss. 3. N 032003. DOI: [10.1088/1755-1315/87/3/032003](https://doi.org/10.1088/1755-1315/87/3/032003)
31. Morgoeva A.D., Morgoev I.D., Klyuev R.V., Gavrina O.A. Forecasting of electric energy consumption by an industrial enterprise using machine learning methods. *Bulletin of the Tomsk Polytechnic University. Geo Assets Engineering*. 2022. Vol. 333. N 7, p. 115-125 (in Russian). DOI: [10.18799/24131830/2022/7/3527](https://doi.org/10.18799/24131830/2022/7/3527)



32. Vyalkova S.A., Morgoeva A.D., Gavrina O.A. Development of a hybrid model for predicting the consumption of electrical energy for a mining and metallurgical enterprise. *Sustainable Development of Mountain Territories*. 2022. Vol. 14. N 3 (53), p. 486-493 (in Russian). DOI: [10.21177/1998-4502-2022-14-3-486-493](https://doi.org/10.21177/1998-4502-2022-14-3-486-493)
33. Khalyasmaa A., Matrenin P. Initial Data Corruption Impact on Machine Learning Models' Performance in Energy Consumption Forecast. 2021 Ural-Siberian Smart Energy Conference (USSEC), 13-15 November 2021, Novosibirsk, Russian Federation. IEEE, 2021, p. 5. DOI: [10.1109/USSEC53120.2021.9655724](https://doi.org/10.1109/USSEC53120.2021.9655724)
34. Bouktif S., Fiaz A., Ouni A., Serhani M.A. Optimal Deep Learning LSTM Model for Electric Load Forecasting using Feature Selection and Genetic Algorithm: Comparison with Machine Learning Approaches. *Energies*. 2018. Vol. 11. Iss. 7. N 1636. DOI: [10.3390/en11071636](https://doi.org/10.3390/en11071636)
35. Manusov V.Z. Neural networks: forecasting of electrical loads and power losses in electric grids. From romanticism to pragmatism. Novosibirsk: NSTU Publisher, 2018, p. 303 (in Russian).
36. Tianqi Chen, Guestrin C. XGBoost: A Scalable Tree Boosting System. KDD'16: Proceedings of the 22nd ACM SIGKDD International Conference on Knowledge Discovery and Data Mining, 13-17 August 2016, San Francisco, CA, USA. New York: Association for Computing Machinery, 2016, p. 785-794. DOI: [10.1145/2939672.2939785](https://doi.org/10.1145/2939672.2939785)
37. Ahmed I., Jeon G., Piccialli F. From Artificial Intelligence to Explainable Artificial Intelligence in Industry 4.0: A Survey on What, How, and Where. *IEEE Transactions on Industrial Informatics*. 2022. Vol. 18. Iss. 8, p. 5031-5042. DOI: [10.1109/TII.2022.3146552](https://doi.org/10.1109/TII.2022.3146552)
38. Adadi A., Berrada M. Peeking Inside the Black-Box: A Survey on Explainable Artificial Intelligence (XAI). *IEEE Access*. 2018. Vol. 6, p. 52138-52160. DOI: [10.1109/ACCESS.2018.2870052](https://doi.org/10.1109/ACCESS.2018.2870052)
39. Ribeiro M.T., Singh S., Guestrin C. "Why Should I Trust You?": Explaining the Predictions of Any Classifier. The 2016 Conference of the North American Chapter of the Association for Computational Linguistics: Human Language Technologies. Proceedings of the Demonstrations Session, 12-17 June 2016, San Diego, CA, USA. Stroudsburg: Association for Computational Linguistics, 2016, p. 97-101. DOI: [10.48550/arXiv.1602.04938](https://doi.org/10.48550/arXiv.1602.04938)
40. Selvaraju R.R., Cogswell M., Das A. et al. Grad-CAM: Visual Explanations from Deep Networks via Gradient-Based Localization. *International Journal of Computer Vision*. 2020. Vol. 128. Iss. 2, p. 336-359. DOI: [10.1007/s11263-019-01228-7](https://doi.org/10.1007/s11263-019-01228-7)
41. Lundberg S.M., Su-In Lee. A unified approach to interpreting model predictions. NIPS'17: Proceedings of the 31st International Conference on Neural Information Processing Systems, 4-9 December 2017, Long Beach, CA, USA. Red Hook: Curran Associates Inc., 2017, p. 4768-4777. DOI: [10.48550/arXiv.1705.07874](https://doi.org/10.48550/arXiv.1705.07874)
42. Kuzlu M., Cali U., Sharma V., Güler Ö. Gaining Insight Into Solar Photovoltaic Power Generation Forecasting Utilizing Explainable Artificial Intelligence Tools. *IEEE Access*. 2020. Vol. 8, p. 187814-187823. DOI: [10.1109/ACCESS.2020.3031477](https://doi.org/10.1109/ACCESS.2020.3031477)
43. Hengbo Liu, Ziqing Ma, Linxiao Yang et al. SADI: A Self-Adaptive Decomposed Interpretable Framework for Electric Load Forecasting Under Extreme Events. ICASSP 2023 – 2023 IEEE International Conference on Acoustics, Speech and Signal Processing, 4-10 June 2023, Rhodes Island, Greece. IEEE, 2023, p. 5. DOI: [10.1109/ICASSP49357.2023.10096002](https://doi.org/10.1109/ICASSP49357.2023.10096002)

Authors: Pavel V. Matrenin, Candidate of Engineering Sciences, Leading Researcher, Associate Professor, matrenin.2012@corp.nstu.ru, <https://orcid.org/0000-0001-5704-0976> (Ural Federal University named after the first President of Russia B.N.Yeltsin, Yekaterinburg, Russia; Novosibirsk State Technical University, Novosibirsk, Russia), Alina I. Stepanova, Junior Researcher, <https://orcid.org/0000-0002-3484-2295> (Ural Federal University named after the first President of Russia B.N.Yeltsin, Yekaterinburg, Russia).

The authors declare no conflict of interests.



Development of equipment and improvement of technology for inertial thickening of backfill hydraulic mixtures at the final stages of transportation

Aleksandra A. Volchikhina, Mariya A. Vasilyeva✉

Empress Catherine II Saint Petersburg Mining University, Saint Petersburg, Russia

How to cite this article: Volchikhina A.A., Vasilyeva M.A. Development of equipment and improvement of technology for inertial thickening of backfill hydraulic mixtures at the final stages of transportation. Journal of Mining Institute. 2025. Vol. 271. N 16360, p. 168-180.

Abstract

The results of the study of the functioning of the developed thickening equipment as part of the stowing complex for the formation of a flow of high-concentration hydromixture are presented. To explain the operation of the hydrotransport system of the stowing complex, equipped with a thickener of the developed design, its basic diagram is presented. A mathematical model has been created that describes the mechanism of inertial sedimentation of a solid component of a hydraulic mixture in a working chamber equipped with hydrodynamic profiles. Interaction with the profile leads to flow stratification due to a change in the trajectory of movement and a decrease in speed. The interval of rational velocity of primary pulp entering the input of the working chamber of the inertial thickener is substantiated. The synthesis of solutions of the thickening process model is performed in the COMSOL Multiphysics and Ansys Fluent programs. This made it possible to eliminate physical contradictions in the operation of the equipment and justify the overall dimensions of its main elements, ensuring the implementation of the mechanism of inertial sedimentation of the slurry. It was found that the concentration of the thickened flow at the outlet branch pipe of the thickener working chamber is determined by the level of the primary hydraulic fluid velocity, the characteristic length of the section of interaction with the deflecting profile, and the ratio of the flow and attack angles. A nomogram of the dynamics of the change in the hydraulic fluid concentration in the section of the outlet branch pipe depending on the ratios of the overall dimensions of the deflecting profile of the working chamber was compiled. The results of the study allowed formulating recommendations for selecting the dimensions of the thickener's deflecting hydrodynamic profile to form a flow of hydraulic mixture with a concentration of about 50 % by weight. The developed equipment can be used in a stowage complex and will increase the range of supply of the stowage mixture. This is due to the fact that a flow of primary slurry with a low concentration, due to lower pressure losses, can be moved in a pipeline system over a greater distance than a flow with a high filler content. The use of a thickener at the final stage of transportation is intended to increase the concentration of the hydraulic mixture immediately before production.

Keywords

backfill mixtures; inertial thickening; highly concentrated slurry; rheological properties; thickener; mine workings; parametric synthesis

Received: 15.12.2023

Accepted: 13.06.2024

Online: 18.11.2024

Published: 25.02.2025

Introduction

The objectives of mining production and technologies related to hydraulic transport of mineral processing products include reducing energy costs, decreasing the energy intensity of technological processes and using waste-free technologies [1-3]. This is achieved by using underground mining systems with backfilling of mined-out spaces and using production waste [4, 5]. Filling the mined-out space is intended to ensure its geomechanical stability [6, 7].

Most mining enterprises use both dry and hydraulic mixtures for backfilling with the use of enrichment waste. In the last 20-25 years, the use of hydraulic mixtures in backfilling operations has reached 85 %, while dry backfilling is used in only 15 % of cases [8, 9]. Backfilling operations



with dry mixtures are carried out mechanically [10]. The material is transported by drift belt conveyors, and then delivered to the mined-out space by self-propelled cars [11]. Hydraulic mixtures are delivered to the mined-out space through a system of backfill pipelines under natural pressure, determined by the ratio of the lengths of the vertical and horizontal sections [12]. Pressure losses due to overcoming local resistance and linear pressure losses significantly limit the distance of transportation of hydraulic mixtures. To increase the supply range, mixtures with a high content of the carrier medium are used, pipes with low specific roughness are used, which reduce the contact friction of the flow on the working surfaces [13, 14]. Additionally, auxiliary equipment is required, for example, vibration activators, slurry pumps [15, 16].

In the preparation of the hardening backfill, only inorganic binders are used [17]. In the mining industry, many of the known binders are used: cements, lime, gypsum, anhydrite, ground granulated slags, boiler ash, pyrrhotite-containing tailings of processing plants, etc. [18-20]. Complex binders are used more often – various cements, the main component of which are silicates and calcium aluminates formed during high-temperature processing of raw materials, for example, at the Verkhnekamsk deposit, Tashtagol mine, Taimyr mine, etc. One of the most effective types of raw materials for the production of local binders for the hardening backfill is blast furnace granulated slag. They are silicate and aluminosilicate melts obtained during the smelting of iron.

According to the study [11], an artificial massif formed from a hydraulic mixture based on enrichment waste is subject to less deformation compared to an artificial massif formed from dry backfill material. This helps to minimize the subsidence of the artificial massif and subsequent disturbances of the workings [21, 22]. One of the main requirements for hydraulic backfill is to ensure the strength of the formed backfill massif, achieved by it during the hardening process, simultaneously with the separation of the carrier liquid and a decrease in humidity [23-25].

A typical roof management passport contains information on the sequence of work, as well as data on the brands of backfill mixtures used to form the bottom layer of the backfill in each of the backfill sections. The mixture is often supplied to the backfill workings through backfill wells and concrete pipelines. Water released from the backfill mixture is discharged by pumps and rubber hoses into a water-bypass well. High-quality installation of a concrete pipeline, an insulating bulkhead, and constant monitoring along the backfill mixture supply route prevent the backfill mixture from getting into active mine workings.

Methods

The rheological properties of the hardening mixtures must ensure stable, stratification-free transportation along the filling pipeline route, uniform, stratification-free spreading throughout the chamber, and the required depth of penetration into the rock when using a combined chamber filling method. The strength and compression properties of the constructed artificial massif must comply with the accepted standard indicators.

Mixtures with a high content of dispersed fraction allow to significantly reduce water infiltration, reducing flooding of workings and the risk of their subsequent violations. To reduce shear stress during movement of the backfill mixture, the content of the solid phase of about 45 μm in size should be no more than 15 %. Hydraulic mixtures of dispersed substances are dilatants. Due to the internal structure and intermolecular interaction, during which the dispersed phase is structured in a specific volume, a power-law dependence of the change in shear stress on the velocity gradient is observed. The flow movement obeys the Ostwald – de Waale rheological law [26]:

$$\tau = K \left(\frac{dv}{dy} \right)^n,$$

where K – coefficient of viscosity of a liquid; n – a nonlinearity index that characterizes the degree to which the behavior of a fluid deviates from Newtonian behavior.



The change in the exponent of the power dependence affects the form of the rheological curve. At $n < 1$, the liquid “liquefies” under shear, which corresponds to Bingham bodies and viscous-plastic liquids (Shvedov bodies). This can be traced, for example, in paraffinic oils or petroleum products at temperatures close to the freezing point. At $n > 1$, on the contrary, an increase in the resistance of the substance under shear is observed (suspensions of enrichment tailings, pastes) [5, 27]. This statement is consistent with what is observed with an increase in the content of the dispersed phase, leading to an increase in the value of n , an increase in the linear losses of the flow pressure. This is a consequence of the fact that in structured substances an increase in concentration and a decrease in size lead to the appearance of additional contact friction between the particles of the flow [28]. To take into account the total stress required to initiate fluid motion (overcoming the yield point), it is permissible to use a modified power law – the Herschel – Bulkley model [29, 30].

The interaction of solid particles in a slurry flow depends on their size, shape, and concentration in the slurry. Small particles form dense mixtures, and their effect on the liquid phase is determined by the concentration in the flow. Larger particles form mixtures with a high concentration in the core of the flow [19]. In this case, significant differentiation by the size of the dispersed medium leads to a violation of the homogeneity of the flow and a change in its rheological characteristics. To ensure the stability of the granulometric composition, fine grinding mills and disintegrators are used [31]. The positive effect of using such equipment is due to the fact that crushing of solid materials by a highly loaded impact occurs in places of fusion, structural defects and stress concentrators in the fraction of dispersed material. This allows for a more uniform form of the fraction, as well as minimizing its secondary destruction during transportation.

When the speed of the hydraulic mixture changes, the thickness of the bottom moving layer with a high concentration of the solid phase changes. The moving layer affects the flow of the hydraulic mixture similarly to the walls of a pipe with a high roughness of the working surface. The thickness, density and speed of movement of this layer depend on the average speed of the flow of the hydraulic mixture and the size of the solid phase. As the speed of the flow decreases, the concentration of solid particles in a suspended state decreases, while the thickness of the layer formed by them increases, turning into sediment [32].

To improve the quality of the filling mixture, the most common methods are the use of binders, as well as the use of thickening equipment.

Binding agents and plasticizers in backfill mixtures, such as cement, anhydrite or slag, accelerate the hydration process, increase the rate of strength gain and reduce liquefaction of the hydraulic mixture. However, the use of a large volume of binding components can lead to adhesion to the walls of pipelines and their subsequent clogging, and when the binder is activated; it leads to accelerated corrosion of the working surfaces of the equipment. The use of plasticizers increases the fluidity and density of the backfill mixture, reducing the required amount of the binding component [31, 33]. But all this leads to an additional significant increase in costs for the preparation of the filling mixture and filling operations.

The maximum range of gravity transport of hydraulic mixtures reaches about 1000 m. To intensify this process and further increase the range of mixture delivery, gravity-pneumatic and vibration-gravity flow activation methods are used [34]. Delivery of a mixture of increased concentration over a distance of more than 400-500 m can lead to an extreme decrease in specific pressure, causing flow stratification and subsequent backfilling of the pipeline.

The backfilling of the mined-out space is carried out in three stages with different volumes of hydraulic mixture: formation of the base of the massif with a mixture of increased concentration; formation of the main body of the massif with a mixture of lower concentration; supply of a mixture of increased concentration to fill the working under the roof with minimal formation of voids. It is especially important to carry out backfilling work with a strengthening layer when developing workings in a retreating order.

Modernization of the filling mixture preparation unit. The ratio of the vertical and horizontal components of the sections of the backfill pipelines determines the value of the geodetic pressure of the flow of the backfill mixture, determining the maximum transportation distance. When moving on



a horizontal section of the pipeline, a drop in pressure is observed, the mixture tends to stratify due to a decrease in the flow rate below critical values. This leads to an inevitable change in the rheological characteristics [32, 35]. When preparing the stowage mixture, the content of the solid component is determined by the distance of the stowage section at the stage of mixing the components. The mobility of the hydraulic mixture ensured by reducing the content of the dispersed phase, causes an increase in the time it takes for the formed massif to achieve its standard strength. In addition, this leads to the need for work on removing excess liquid and its subsequent disposal. To minimize the listed complications, the authors propose upgrading the technological chain of the stowage complex equipment by integrating the developed inertial thickener into the pipeline system (Fig.1). Thickening of the hydraulic mixture at the final stages of backfilling operations will increase the range of supply of low-concentration backfilling mixtures and reduce the water content of workings due to the implementation of a circulating water supply system [36]. The use of traditional thickeners is limited by their bulkiness and low operating speed, which will require significant changes in the filling process [37].

At the final stage, immediately before entering the mined-out space, the hydraulic mixture with a high content of the carrier phase enters the inertial thickener. Its design is a working chamber 1, in which two hydrodynamic profiles are installed. The hydraulic mixture enters the working chamber through the inlet pipe 3, where it accumulates and settles. When entering the working chamber, the solid particles of the hydraulic mixture collide with the deflecting hydrodynamic profile 2 and settle to the bottom under the action of inertial and gravitational forces. The solid particles remaining in the suspended state in the hydraulic mixture settle after interacting with the cylindrical hydrodynamic profile 4. A layer of thickened mixture is formed in the lower part of the chamber, which moves into the drain pipe, from where it enters the pump unit for further delivery to the space being filled. The liquid phase is sent to the drain or to the circulating water supply system of the mining enterprise.

The use of the inertial thickening principle is due to the need to implement a continuous technology for feeding the backfill material, as well as the compactness of the equipment dimensions. The equipment does not require connection to the power supply system and, using the original hydraulic mixture, allows it to be thickened to a concentration of about 50 %. The thickener design provides for the removal of the clarified flow of the carrier medium through a separate channel for subsequent use

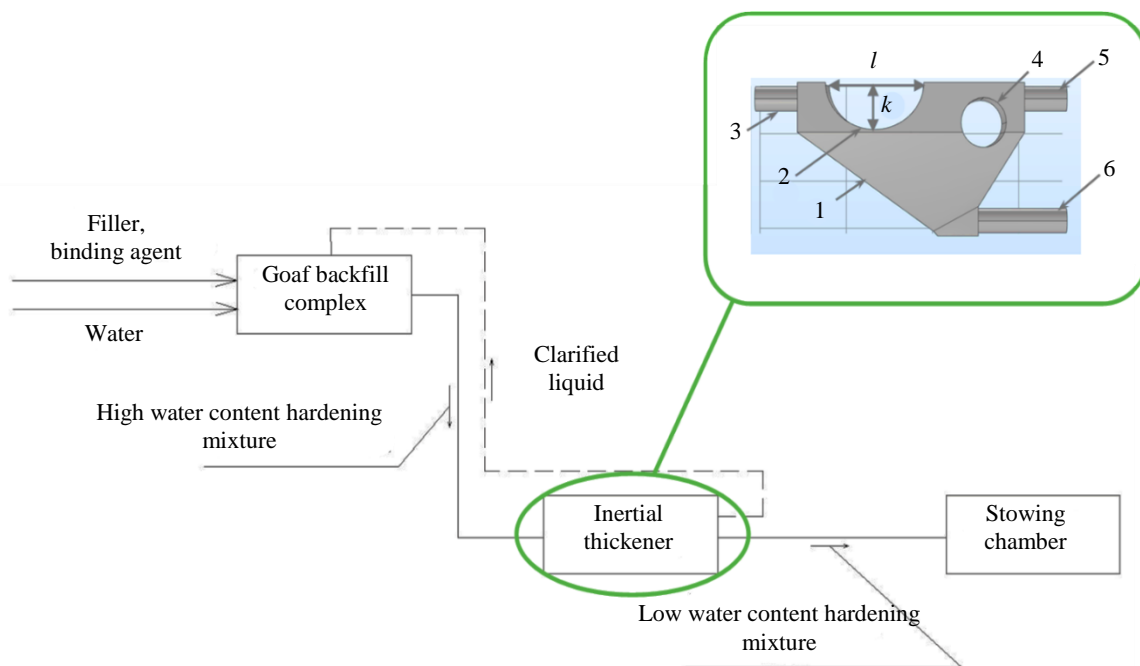


Fig.1. Technological scheme of hydraulic transport of stowage mixtures with thickening at the final stage of work

- 1 – working chamber; 2 – main deflecting hydrodynamic profile; 3 – inlet branch pipe;
4 – cylindrical hydrodynamic profile; 5 – outlet branch pipe of clarified water;
6 – outlet branch pipe of thickened mixture; l – longitudinal length of profile; k – transverse length of profile



in production needs. If it is not possible to implement a recycling water supply system, the clarified water removed can be fed into drainage ditches.

To study and predict the efficiency of the sedimentation process and the formation of a flow of thickened hydraulic mixture, as well as to assess the influence of the operating parameters of the initial hydraulic mixture, a multiphysical analysis model was developed in the COMSOL Multiphysics program (license number 6464550) [38-40]. The conducted studies made it possible to identify the pattern of influence of the design parameters of the deflection profile on the concentration of the generated flow and to substantiate a rational range of values for performing parametric synthesis.

When a solid body is flowed around by a filled stream, due to significant inertia determined by the specific gravity of a unit volume and the magnitude of the velocity, the particles of this stream continue to move along curved trajectories. The efficiency of inertial sedimentation is determined by the proportion of particles extracted from the stream. The initial parameters adopted in the study to form a multiphysical analysis model: the material of the thickener working chamber is St3 steel; particle shape – spherical; density of solid particles – 2300 kg/m³; density of hydraulic mixture – 1300 kg/m³; average reduced diameter of solid particles – 0.3 mm. To set the fraction size, the average value of the fractional composition of finely dispersed hydraulic mixtures was used: sand component 4-6 mm, enrichment tailings 0.2 mm (V.N.Pokrovskaya, 1972).

The number of particles at the thickener inlet is set to 1000 pcs/s. The particle content in the separated flows was estimated according to the Poincaré mapping principle [41]. The solution to the tracing problem allows one to determine the trajectories of a finite number of particles, eliminating the possibility of their secondary emission into the calculation region after interaction with the working surface of the deflecting hydrodynamic profile.

The calculation is based on the Euler – Lagrange method. The discrete phase model according to this method is constructed by solving the time-averaged Navier – Stokes equations for the liquid phase, considered as a constant medium (H.S.Fogler, 1992). The dispersed phase is described by tracing the trajectory of a given number of particles through the calculated flow fields [42-44]. The movement of the hydraulic mixture is specified by the modules: Turbulent flow k- ω for the general movement of the hydraulic mixture and Particle Tracing for Fluid Flow for modeling the movement of the discrete phase in the flow. To determine the trajectory of solid particles during the movement of the hydraulic mixture in the turbulent regime, a surface grid consisting of 115.5 thousand elements is specified (Table 1).

Table 1

Mathematical model of the thickening process

Specified parameter	Defining equations
Change in the mass of the mixture	$\frac{\partial \rho_h}{\partial t} + \nabla(\rho_h V_{hm}) = 0,$ <p>where ρ_h – density of hydraulic mixture, kg/m³; t – time, s; ∇ – differential operator; V_{hm} – averaged mass flow rate of hydraulic mixture, m/s.</p>
Changes in particle volume fraction	$\frac{\partial \alpha_p}{\partial t} + \nabla(\alpha_p V_{hp}) = 0,$ <p>where α_p – volume fraction of the dispersed phase in the flow of the hydraulic mixture in the range from 0 to 1; V_{hp} – average flow rate of hydraulic mixture in volume, m/s.</p>
Sliding speed	$V_{p1} = \frac{(\rho_p - \rho_w) d_p^2}{18 \mu f_d} \alpha_p - D_{tp} \left(\frac{\nabla \alpha_p}{\alpha_p} - \frac{\nabla \alpha_1}{\alpha_1} \right),$ <p>where ρ_p, ρ_w – density of solid particles and carrier medium, kg/m³; μ – dynamic viscosity coefficient of hydraulic mixture, Pa·s; f_d – distance traveled by a particle, m; α_1 – volume fraction of the carrier medium in the flow of the hydraulic mixture in the range from 0 to 1; D_{tp} – coefficient of turbulent diffusion of solid particles of a hydraulic mixture.</p>



End of Table 1

Specified parameter	Defining equations
The coefficient of turbulent diffusion of solid particles of a hydraulic mixture	$D_{ip} = KC_{\mu} \frac{k^2}{\varepsilon} \left(\frac{\gamma_k}{1 + \gamma_k} \right) \frac{1}{\sqrt{1 + C_{\beta k} \varepsilon^2}},$ <p>where K – Lagrange multiplier; C_{μ}, $C_{\beta k}$ – turbulence model constant $k - \varepsilon$; k – kinetic energy of turbulence, m^2/s^2; ε – turbulent dispersion velocity, m^2/s^3; γ_k – shear rate, time derivative of strain, s^{-1}.</p>
Trajectory of movement of solid particles in a hydraulic mixture	$f = \frac{d(m_{pv} V_p)}{dt} Ft,$ <p>where m_{pv} – mass of solid particles at a given speed, kg; V_p – average particle velocity; Ft – resultant of external forces, N.</p>
The amount of solid particles for the billing period	$N = \int_{t_0}^t \frac{1}{\tau_i} dt;$ $\tau_i = \min \left(2\tau_L - \tau_L \log \left(1 - \frac{I_e}{\tau_L V_w - V_p } \right) \right),$ <p>where τ_i – viscous stress tensor; τ_L – Lagrange response time; V_w – average speed of the carrier medium, m/s; I_e – unit tensor.</p>
The drag force per unit mass of a particle	$F_D = \frac{1}{\tau_p} m_p (V_w - V_p),$ <p>where τ_p – particle sedimentation time, s; m_p – particle mass, kg.</p>
Particle deposition time	$\tau_p = \frac{\rho_p d_p^2}{18\mu},$ <p>where d_p – diameter of solid particles, m.</p>
Lifting force	$F_L = 6,46 r_p^2 L_v \sqrt{\mu \rho_m \frac{ V_w - V_p }{ L_v }},$ $L_v = (V_w - V_p) (\nabla (V_w - V_p)),$ <p>where r_p – radius of solid particle, m; L_v – lift coefficient.</p>

To conduct the study, a numerical experiment method was chosen, which allows the most accurate characterization of the distribution of particles in the cross-section and their instantaneous position in changing velocity fields of the turbulent flow [45, 46]. The developed multiphysical model of the thickening process allows, in addition to changing the rheological parameters of the hydraulic mixture during its movement in the equipment, to estimate the change in the velocity of the carrier medium and the dispersed phase in the working area of the thickener during interaction with the profile surface. This made it possible to take into account velocity pulsations and the occurrence of ascending flows in the working area based on the specified parameters of the kinetic energy of the flow. The study of the movement of solid particles in the flow using the Euler – Lagrange method was performed with a volume fraction of the dispersed phase of 10 %.

A compacted discrete phase model was used for the solution, which overcomes the limitation on the acceptable volume fraction of solids by extending the Lagrange conservation equations, whereby the particles can achieve close packing. The governing equations were transformed into algebraic expressions. All working surfaces are subject to the boundary conditions of “non-slip walls”. The turbulent flow was calculated taking into account the force of gravity, while the particle trajectory was calculated taking into account the drag force and the force of gravity [33]. The verification of the recommended velocity is based on the assessment of the amount of solids in the outlet pipe of clarified water and thickened mixture using the method of cross-section mapping.

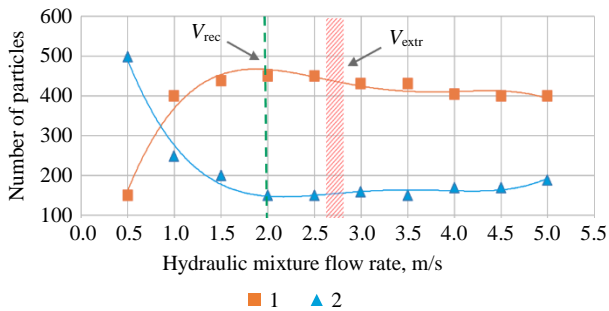


Fig.2. Content of solid component in the pipes of thickened mixture (1) and clarified water (2) for initial velocities of movement of hydraulic mixture

Discussion of results

The results of the study conducted to assess the distribution of the number of particles in the sections of the outlet pipes at different speeds of the primary mixture showed that at a flow rate of 2.0 m/s, the concentration of the dispersed phase in the section of the outlet pipe reaches 45 %. In the section of the outlet branch pipe for the clarified flow, the amount of solid particles was recorded at a level of 15 % of the initial one. Further studies showed that an increase in the velocity of the initial mixture entering the working zone contributes to a

decrease in the number of dispersed phase particles in the branch pipe of the thickened mixture and an insignificant increase in their content in the branch pipe of the clarified mixture (Fig.2).

The identified recommended feed rate of the initial hydraulic mixture into the thickener working chamber is within 2.0 m/s lower than the maximum permissible flow rate of the hydraulic mixture adopted at the plant – 2.65-2.76 m/s (depending on the productivity of the surface stowing complex). An increase in the feed rate of the initial hydraulic mixture slightly reduces the content of the dispersed phase in the thickened flow – no more than 8 %, while the content of solid particles in the clarified liquid flow remains virtually unchanged. The limiting value of the feed rate of the hydraulic mixture into the inertial thickener, upon reaching which its use is not effective, is 0.9 m/s. In this case, a high carryover of the dispersed phase by the ascending flow of clarified liquid is observed and the risk of bottom sediment formation is high.

To confirm the obtained results, studies were conducted on the distribution of flow density and the formed flow velocity fields in the working chamber of the inertial thickener.

The distribution of flow velocities during interaction with hydrodynamic profiles at a hydraulic inlet velocity is shown in Fig.3, *a*, the distribution of vectors of the flow velocity fields of the hydraulic mixture, performed in Ansys Fluent, in Fig.3, *b*.

The picture of particle velocity distribution in the calculation area complements the idea of the thickener operating principle. The conducted study of the distribution of the velocity fields and the flow density of the hydraulic mixture in the working chamber of the inertial thickener allowed us to reveal that there are several zones in the chamber in which processes occur that determine the efficiency of sedimentation. Zone A is the area of primary interaction of the mixture with the surface of the main deflecting hydrodynamic profile. In the area limited by zone B, the attack area of the flowing profile is formed in the flow. This contributes to the mixture significantly deviating from the initial trajectory and significantly losing speed – more than twice. Fig.3, *b* shows the directions of movement of the flow sections and the division of the flow into the sediment-forming zone C and the ascending flow – zone F, in which the velocity decreases to 0.25 of the initial one. The dispersed phase, carried

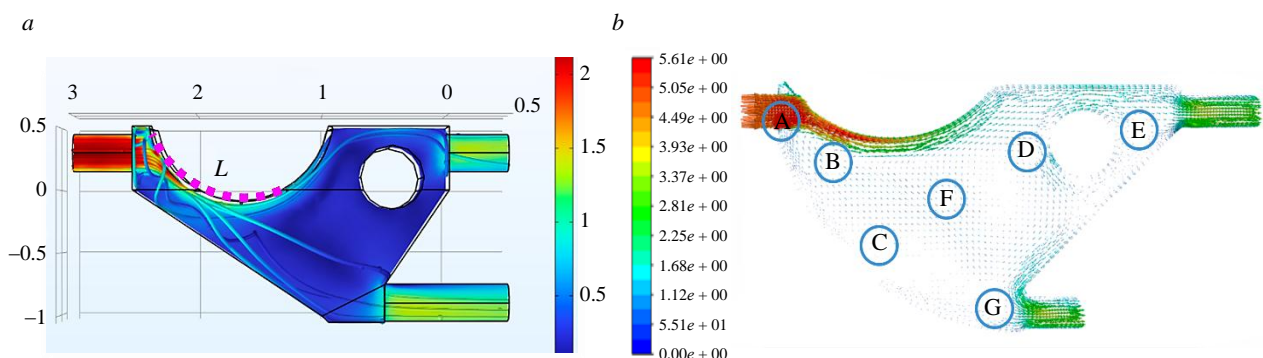


Fig.3. Distribution of the fields of parameters of the dynamic thickening process in the working zone of the thickener:
a – solid particle velocities; *b* – flow velocity vectors;
L – interaction section length



away by the ascending flow, collides with a cylindrical deflecting profile, which, cutting it, starts the process of secondary sedimentation. The particles enveloping its surface, descending along the inclined wall of the working chamber, form the final volume of the thickened flow – zone G, directed to the branch pipe for the thickened mixture for filling operations. Zone E designates the section for the removal of the dispersed phase particles remaining in suspension into the branch pipe for the clarified flow.

Inertial sedimentation is realized in the case when the kinetic energy of the particle is so great that the particle cannot follow the curved lines of flow and, colliding with an obstacle, settles in the allocated volume [47-49]. The inertial principle of thickening in the considered design is realized due to the force interaction of the dispersed phase with the deflecting hydrodynamic profiles. It is advisable to determine the ratios of its main design parameters. In parametric synthesis of equipment, this will ensure that the specified level of solid component concentration in the outlet pipe of the thickened mixture is achieved.

To substantiate the geometric parameters of the deflecting hydrodynamic profile, samples of the working chambers of the inertial thickener with different ratios of its longitudinal and transverse axes were studied. The dimensions of the inertial thickener may vary depending on the required flow concentration. To assess the impact of this on the efficiency of operation, a study was performed on the distribution of the dispersed phase in the working chamber and in the sections of the discharge pipes. Sets of rational combinations of parameters that ensure the formation of a thickened flow with the maximum possible content of the dispersed phase are presented in Table 2.

The obtained results made it possible to form a series of nomograms for the distribution of the dispersed phase in the flow to determine the rational ratio of the corresponding parameters (Fig.4).

Table 2

Distribution of the dispersed phase of the flow in the flow					
b, mm	Solids content, %				
	a, mm				
	1,000	1,150	1,250	1,350	1,450
400	52/32/16*	64/23/13	58/23/19	41/34/25	43/30/27
500	69/16/15	59/19/22	66/11/23	50/19/31	51/12/37
600	58/13/29	59/9/32	54/11/35	47/13/40	36/12/52
700	57/13/30	54/11/35	50/12/38	43/13/44	37/11/54

* Thickened mixture / clarified stream / sediment.

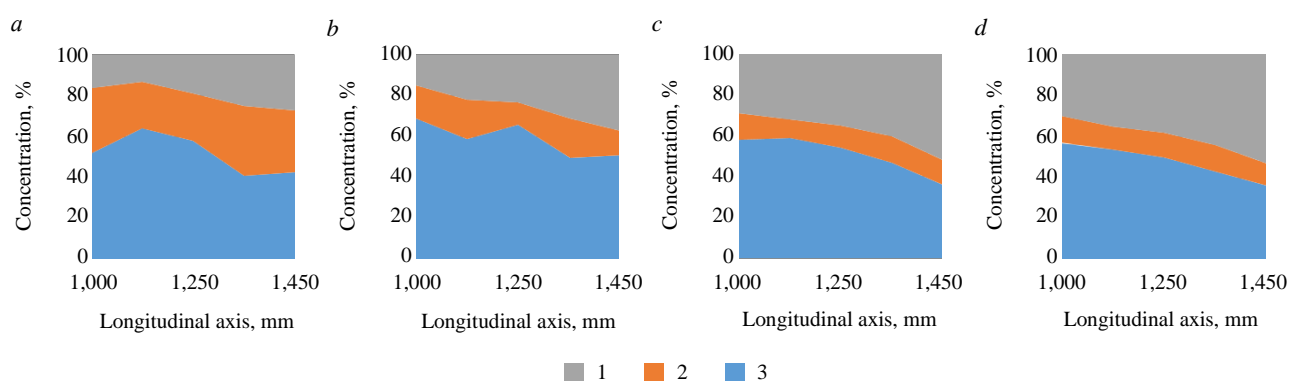


Fig.4. Nomograms of the distribution of the dispersed phase in the inertial thickener for different values of the transverse axis of the deflection profile:

a – 400 mm; b – 500 mm; c – 600 mm; d – 700 mm
1 – sediment; 2 – clarified liquid; 3 – thickened stream



The ratio of the lengths of the longitudinal and transverse axes of the deflecting profile $N = a/b$ is an invariant of geometric similarity. This value, independent of the dimensions of the natural and model object, can correspond to a change in the concentration of the formed flow in a wide range of values.

The ratio of characteristic parameters of the deflecting hydrodynamic profile sets the shape of the deflecting profile and determines the area of interaction of the profile with the flow entering the working chamber. Depending on the angle of attack of the flow, the inertial reflection of particles also occurs at different angles, determines the change in the direction of the flow and is accompanied by a change in the velocity of the dispersed phase (Fig.5).

The similarity criterion for inertial sedimentation is the Stokes criterion [32]:

$$St = 4r^2\rho VC/18\mu^2 L,$$

where V – flow velocity in the selected coordinate of the unsteady flow, m/s; r – radius of curvature of the streamlined surface, m; ρ – density of dispersed phase, kg/m³; μ – dynamic viscosity of the carrier medium, kg/m·s; L – characteristic linear size of the interaction area of a streamlined body, m (see Fig.3, a).

The calculation of the characteristic linear size of the interaction area of the streamlined body and the flow is performed according to the second Ramanujan formula for determining the length of the perimeter of an ellipse [50]:

$$L \approx \pi(a+b) \left[1 + \frac{3(Z)^2}{10 + \sqrt{4 - 3(Z)^2}} \right],$$

where a – value of longitudinal dimension of profile, m; b – value of transverse dimension of profile, m; $Z = (a-b)/(a+b)$ – ratio of major and minor semi-axes.

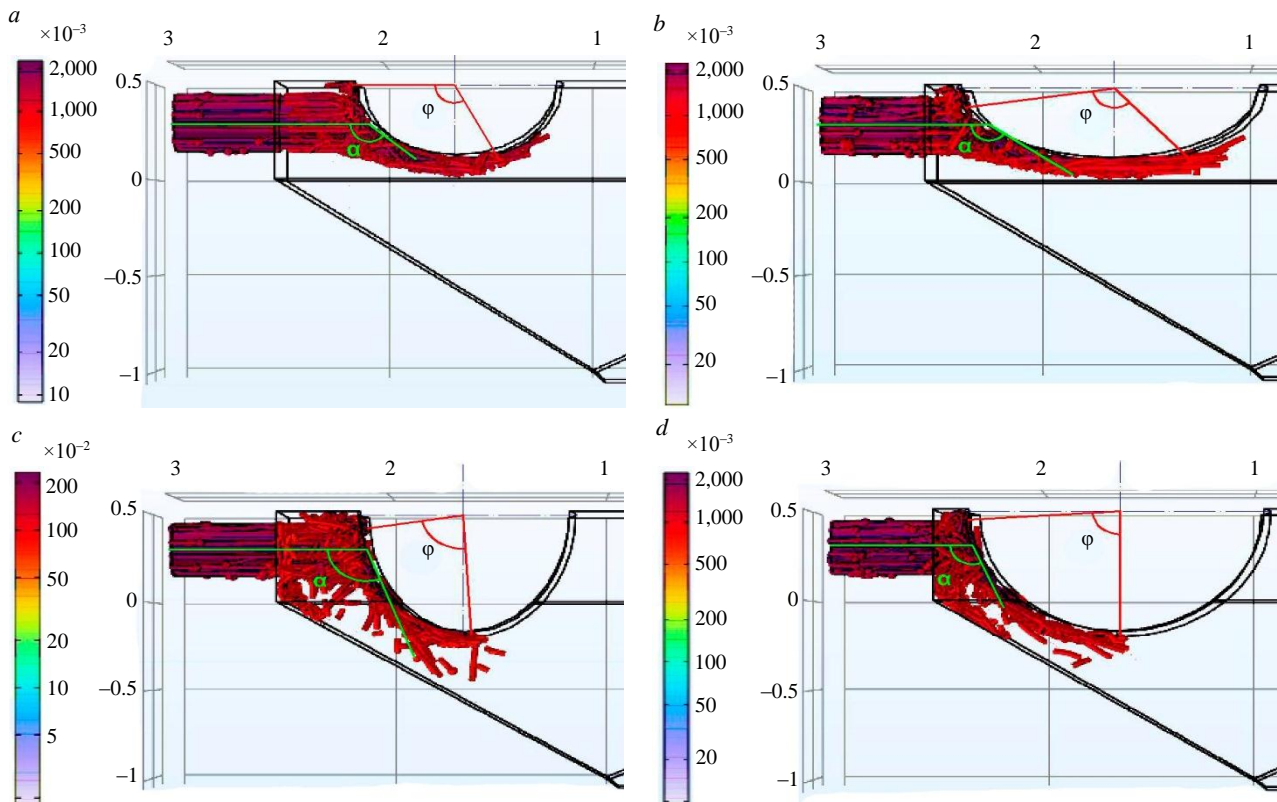


Fig.5. Formation of flow interaction areas
with different ratios of transverse and longitudinal axes of the deflection profile:
 a – 400/1000 mm; b – 400/1450 mm; c – 700/1000 mm; d – 400/1450 mm



As a result of the study of the distribution of the contact density of the flow, patterns of the distribution of the corresponding areas of interaction were obtained, forming the zones of flow around the surface of the hydrodynamic profile by the suspension-carrying flow (Fig.5). The formation of the trajectory of the flow movement is determined by the angle of attack of the flow α and the angle of flow around the profile φ , the value of which depends on the ratio of the lengths of the longitudinal and transverse dimensions of the profile.

The influence of the profile geometry on the flow parameters and subsequent inertial settling, determined by the characteristic length of the contact zone, can be estimated by the corresponding angle of attack of the flow α . The results of the assessment of their change depending on the profile parameters are presented in Fig.6. As follows from Fig.5, the length of the section of interaction of the flow with the profile is characterized by the flow angle φ . The dynamics of the increase in angle φ corresponds to the change in the characteristic length of the interaction section L . An increase in the longitudinal profile dimension has little effect on the change in the angle φ , accompanied by an increase in L due to an increase in the overall length of the profile. An increase in the transverse profile dimension leads to a relative decrease in this angle due to a change in the overall shape. At the same time, the tendency to increase the length of the interaction section L is preserved. The angles of attack and flow around the flow are significantly reduced with an increase in the transverse profile dimension.

Analysis of the parameters of the distribution of suspension-carrying flows and the formed trajectories of particle motion showed that an increase in the ratio of the lengths of the longitudinal and transverse dimensions of the deflecting profile is accompanied by an increase in the characteristic length of the section of interaction with the flow L (Fig.7, *a*). Results of a comprehensive analysis, including an assessment of the effect of an independent change in the characteristic overall parameters of the deflecting profile on the concentration of the formed condensed flow at the outlet of the working chamber. In addition, the corresponding lengths of the formed flow zones were determined. A nomogram has been compiled, displaying the selected area of flow concentration change and allowing to correlate it with the corresponding dimensions of the deflecting profile (Fig.7, *b*). The dotted lines mark the corresponding process of formation of areas of interaction with the flow, characterizing the flow zones, occurring within the framework of the selected profile geometry.

According to the obtained nomogram, an increase in the longitudinal dimension of the profile is accompanied by a decrease in the concentration of the thickened flow of the hydraulic mixture. An increase in the transverse dimension of the profile within the specified limits does not lead to a decrease

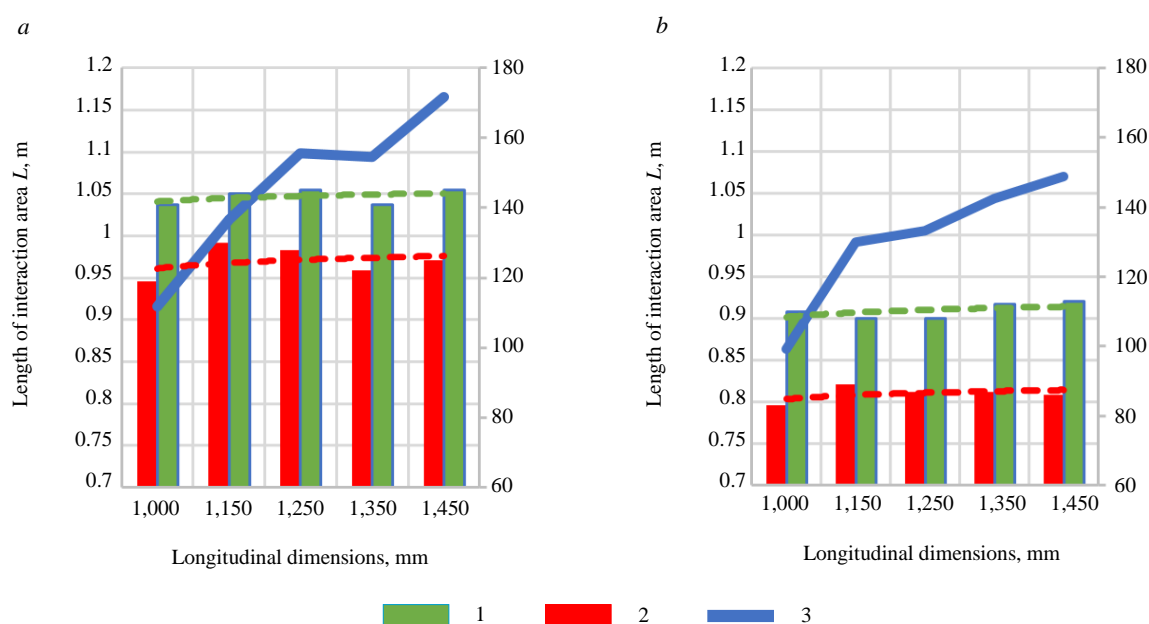


Fig.6. Change in the characteristic length of the interaction section L from the characteristic angles of interaction with the deflecting profile: *a* – longitudinal dimension 1000 mm, transverse dimension 400 mm; *b* – longitudinal dimension 1,450 mm, cross dimension 700 mm

1 – flow angle, deg; 2 – angle of attack, deg; 3 – L , m

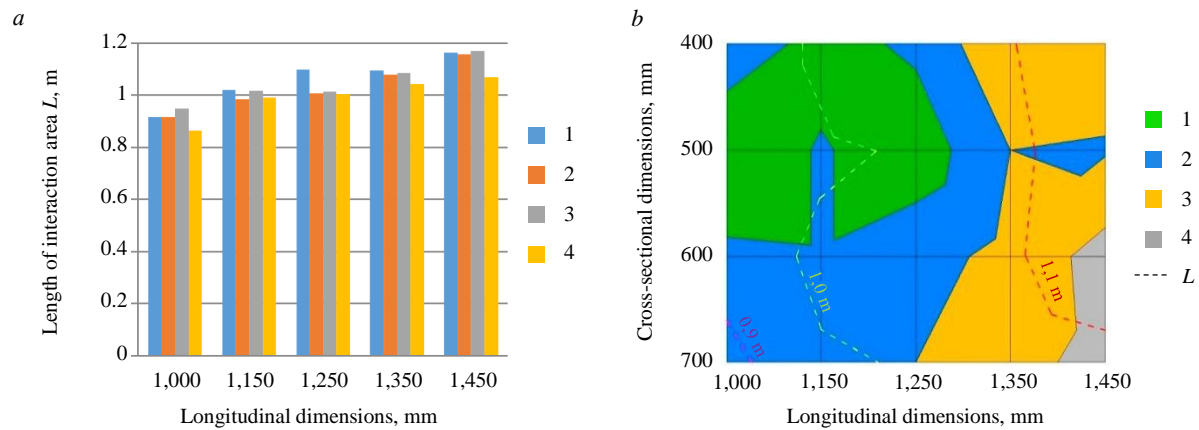


Fig.7. Dynamics of change of characteristic parameters of thickening depending on the ratios of characteristic overall parameters of the deflection profile:
a – change of characteristic length of the interaction section
(1 – transverse dimension 400 mm; 2 – 500 mm; 3 – 600 mm; 4 – 700 mm);
b – nomogram of change of concentration of thickened flow
(1 – 60-70 %; 2 – 50-60 %; 3 – 40-50 %; 4 – 30-40 %)

in the concentration of the formed flow. In some cases, this allows for the conditions for achieving the content of the dispersed phase within 70 % by weight. An increase in the length of the flow zone leads to a decrease in concentration due to a decrease in the inertial effect on the flow, determined by the angle of attack of the flow, accompanied by a change in the trajectory of dispersed particles.

Conclusion

As a result of the research carried out, a number of conclusions were made that have scientific and practical significance:

1. The supply of backfill mixtures over long distances is significantly limited by the reduction in specific hydrodynamic pressure, determined by the ratio of the vertical and horizontal components of the backfill pipeline, as well as the complex resistance of the channel, which forces the use of flowing mixtures with a low solid phase content in the technological process.

2. Hydraulic mixtures for backfilling work containing inorganic binders are dilatant substances which, due to the internal interaction of the particles of the dispersed phase, are structured in the volume. This corresponds to the observed power dependence of the change in shear stress on the velocity gradient during flow movement, known as the Ostwald – de Waale rheological law, and corresponding to the generalized Herschel – Bulkley model.

3. The determining factors in the use of thickening equipment are the productivity of the stowage pipeline, the degree of thickening and the granulometric composition of the mixture. The type of thickener must correspond to the features of the stowage complex. The use of the inertial principle of thickening is due to the need to implement a continuous technology for feeding the stowage material, as well as the compactness of the equipment dimensions.

4. Thickening of the hydraulic mixture used during stowage operations is recommended to be carried out at the final stage of transportation of the stowage material. This allows the use of the initial hydraulic mixture with a low content of the dispersed phase in the technological process and to implement reverse water drainage.

5. A mathematical model for determining the trajectories of the dispersed phase using the Euler – Lagrange method, constructed by solving the time-averaged Navier – Stokes equations for the liquid phase, considered as a constant medium. This made it possible to analyze the efficiency of the process of particle deposition and the formation of a condensed flow, as well as to evaluate the influence of the parameters of the initial hydraulic mixture. The trajectories of a limited number of particles through the calculated flow fields are considered as a discrete dynamic system, and Poincare sections are used for their analysis.

6. The content of the dispersed phase in the thickened flow depends on the trajectories of the particles, determined by the value of the characteristic length of the interaction section L , varied by changing



the ratio of the longitudinal and transverse dimensions of the deflecting hydrodynamic profile of the working chamber of the inertial thickener, the angles of attack and flow around the flow.

7. An increase in the transverse dimension of the deflecting profile is accompanied by a decrease in the angle of attack of the flow, significantly changing the trajectory of the flow of dispersed particles, and contributes to the effective implementation of the inertial thickening mechanism.

REFERENCES

1. Zubov V.P., Anisimov K.A. Resource-saving underground mining technology for diamond-bearing kimberlite ore under protective cushion below open pit mine bottom. *Gornyi zhurnal*. 2023. N 4, p. 26-37 (in Russian). DOI: [10.17580/gzh.2023.04.05](https://doi.org/10.17580/gzh.2023.04.05)
2. Kaplunov D.R., Ryl'nikova M.V., Radchenko D.N. Prospects for the development of technology for backfilling mined-out space during underground mining of ore deposits. *Mining Informational and Analytical Bulletin*. 2011. N 12, p. 5-10.
3. Belikov A.A., Belyakov N.A. Method of predicting the stress-strain state of interchamber pillars lined with a compliant rope fastener. *Mining Informational and Analytical Bulletin*. 2023. N 4, p. 20-34. DOI: [10.25018/0236-1493-2023-4-0-20](https://doi.org/10.25018/0236-1493-2023-4-0-20)
4. Sokolov I.V., Antipin Yu.G., Nikitin I.V. Basic principles and assessment criteria of technological strategy for underground mining in transition zones. *Mining Informational and Analytical Bulletin*. 2017. N 9, p. 151-160 (in Russian). DOI: [10.25018/0236-1493-2017-9-0-151-160](https://doi.org/10.25018/0236-1493-2017-9-0-151-160)
5. Atroshchenko V.A., Alexandrov V.I. Increasing the Efficiency of the Transport Pipelines of the Stowing Complex with the Application of a Polyurethane Coating. *Mining Informational and Analytical Bulletin*. 2022. Vol. 10-1, p. 25-38. DOI: [10.25018/0236-1493-2022-101-0-25](https://doi.org/10.25018/0236-1493-2022-101-0-25)
6. Mengyi Liu, Haijun Lu, Qingkai Deng et al. Shear strength, water permeability and microstructure of modified municipal sludge based on industrial solid waste containing calcium used as landfill cover materials. *Waste Management*. 2022. Vol. 145, p. 20-28. DOI: [10.1016/j.wasman.2022.04.031](https://doi.org/10.1016/j.wasman.2022.04.031)
7. Raffaldi M.J., Seymour J.B., Richardson J. et al. Cemented Paste Backfill Geomechanics at a Narrow-Vein Underhand Cut-and-Fill Mine. *Rock Mechanics and Rock Engineering*. 2019. Vol. 52. Iss. 12, p. 4925-4940. DOI: [10.1007/s00603-019-01850-4](https://doi.org/10.1007/s00603-019-01850-4)
8. Montyanova A.N., Trofimov A.V., Rumyantsev A.E. et al. Experience and efficiency of application of plasticized backfilling concrete. *Vestnik of Nosov Magnitogorsk State Technical University*. 2019. Vol. 17. N 1, p. 18-25 (in Russian). DOI: [10.18503/1995-2732-2019-17-1-18-25](https://doi.org/10.18503/1995-2732-2019-17-1-18-25)
9. Kovalski E.R., Gromtsev K.V., Petrov D.N. Modeling deformation of rib pillars during backfill. *Mining Informational and Analytical Bulletin*. 2020. N 9, p. 87-101 (in Russian). DOI: [10.25018/0236-1493-2020-8-0-87-101](https://doi.org/10.25018/0236-1493-2020-8-0-87-101)
10. Shuai Li, Zeming Zhao, Haoxuan Yu, Xinmin Wang. The Recent Progress China Has Made in the Backfill Mining Method, Part II: The Composition and Typical Examples of Backfill Systems. *Minerals*. Vol. 11. Iss. 12. N 1362. DOI: [10.3390/min11121362](https://doi.org/10.3390/min11121362)
11. Kovalskii E.R., Gromtsev K.V. Development of the technology of stowing the developed space during mining. *Journal of Mining Institute*. 2022. Vol. 254, p. 202-209. DOI: [10.31897/PMI.2022.36](https://doi.org/10.31897/PMI.2022.36)
12. Anisimov K.A., Nikiforov A.V. Modern technologies of the development of diamondiferous deposits. *Bulletin of the Tomsk Polytechnic University. Geo Assets Engineering*. 2023. Vol. 334. N 1, p. 196-208 (in Russian). DOI: [10.18799/24131830/2023/1/3837](https://doi.org/10.18799/24131830/2023/1/3837)
13. Kuskildin R.B., Vatlina A.M. Method of accelerated industrial testing of hydroabrasive wear of polymer coatings of steel pipes. *Journal of Physics: Conference Series*. 2021. Vol. 1728. N 012029. DOI: [10.1088/1742-6596/1728/1/012029](https://doi.org/10.1088/1742-6596/1728/1/012029)
14. Golik V.I., Razorenov Yu.I., Dzeranov B.V. Combined delivery of hardening mixtures to remote deposit sites. *Bulletin of the Kuzbass State Technical University*. 2017. N 4, p. 14-19 (in Russian). DOI: [10.26730/1999-4125-2017-4-14-19](https://doi.org/10.26730/1999-4125-2017-4-14-19)
15. Lyashenko V.I., Golik V.I., Dmitrak Yu.V., Franchuk V.P. Rationale for the Parameters of the Vibration Gravity Transportation of Solidifying Filling Mixtures to Mines. *Vestnik of Nosov Magnitogorsk State Technical University*. 2021. Vol. 19. N 1, p. 4-16 (in Russian). DOI: [10.18503/1995-2732-2021-19-1-4-16](https://doi.org/10.18503/1995-2732-2021-19-1-4-16)
16. Protosenya A.G., Kutepov Yu.Yu. Stability estimation of hydraulic fills in undermined areas. *Mining Informational and Analytical Bulletin*. 2019. N 3, p. 97-112 (in Russian). DOI: [10.25018/0236-1493-2019-03-0-97-112](https://doi.org/10.25018/0236-1493-2019-03-0-97-112)
17. Svakhina Y.A., Titova M.E., Pyagay I.N. Products of Apatite-Nepheline Ore Processing in the Synthesis of Low-Modulus Zeolites. *Indonesian Journal of Science & Technology*. 2023. Vol. 8. N 1, p. 49-64. DOI: [10.17509/ijost.v8i1.51979](https://doi.org/10.17509/ijost.v8i1.51979)
18. Volkov E.P., Vokhmin S.A., Anushenkov A.N., Golovanov A.I. Development of Formulations and the Mechanism of Activation of Mixtures for Underground Mining with use of Mill Tailings. *Journal of Siberian Federal University. Engineering & Technologies*. 2014. Vol. 7. N 3, p. 295-303 (in Russian).
19. Stovmanenko A.Yu., Anushenkov A.N. Increase of system effectiveness of pipeline transport of cast stowage mixes at their mechanical activation, in the conditions of underground mining of mineral deposits. *News of the Ural State Mining University*. 2016. Iss. 1 (41), p. 94-102 (in Russian).
20. Golik V.I., Komashchenko V.I., Shkuratskyi D.N. Optimization of composition of hardening mixes on geomechanical conditions by mining ore fields. *News of the Tula state university. Sciences of Earth*. 2016. N 3, p. 164-176 (in Russian).
21. Hengfeng Liu, Jixiong Zhang, Baiyi Li et al. Environmental behavior of construction and demolition waste as recycled aggregates for backfilling in mines: Leaching toxicity and surface subsidence studies. *Journal of Hazardous Materials*. 2020. Vol. 389. N 121870. DOI: [10.1016/j.jhazmat.2019.121870](https://doi.org/10.1016/j.jhazmat.2019.121870)
22. Jiahao Qin, Jian Zheng, Li Li. An analytical solution to estimate the settlement of tailings or backfill slurry by considering the sedimentation and consolidation. *International Journal of Mining Science and Technology*. 2021. Vol. 31. Iss. 3, p. 463-471. DOI: [10.1016/j.ijmst.2021.02.004](https://doi.org/10.1016/j.ijmst.2021.02.004)
23. Smirnov O.Iu. Investigating the conditions of applying the filling method of field development in various mining and geological conditions. *News of the Higher Institutions. Mining Journal*. 2019. N 5, p. 14-20 (in Russian). DOI: [10.21440/0536-1028-2019-5-14-20](https://doi.org/10.21440/0536-1028-2019-5-14-20)



24. Golik V.I., Tsidaev T.S., Tsidaev B.S. Improving the efficiency of ore mining by combining traditional and innovative technologies. *Mining Informational and Analytical Bulletin*. 2012. N 4, p. 11-18.
25. Pirogov G.G., Voronov E.T. Composite granular backfill in stoping by stripes. *Mining Informational and Analytical Bulletin*. 2021. N 3-2, p. 125-132 (in Russian). DOI: [10.25018/0236_1493_2021_32_0_125](https://doi.org/10.25018/0236_1493_2021_32_0_125)
26. Matveenkov V.N., Kirsanov E.A. Structural rationale of a non-Newtonian flow. *Moscow University Chemistry Bulletin*. 2017. Vol. 72. N 2, p. 69-91. DOI: [10.3103/S0027131417020031](https://doi.org/10.3103/S0027131417020031)
27. Matvienko O.V., Bazuev V.P., Cherkasov I.S., Aseeva A.E. Hydraulic properties of sand slurry flow in a pipe. *Journal of Construction and Architecture*. 2020. Vol. 22. N 2, p. 129-144 (in Russian). DOI: [10.31675/1607-1859-2020-22-2-129-144](https://doi.org/10.31675/1607-1859-2020-22-2-129-144)
28. Daihui Lu, Christov I.C. Physics-informed neural networks for understanding shear migration of particles in viscous flow. *International Journal of Multiphase Flow*. 2023. Vol. 165. N 104476. DOI: [10.1016/j.ijmultiphaseflow.2023.104476](https://doi.org/10.1016/j.ijmultiphaseflow.2023.104476)
29. Shammazov I., Karyakina E. The LNG Flow Simulation in Stationary Conditions through a Pipeline with Various Types of Insulating Coating. *Fluids*. 2023. Vol. 8. Iss. 2. N 68. DOI: [10.3390/fluids8020068](https://doi.org/10.3390/fluids8020068)
30. Matvienko O.V., Litvinova A.E. Steady flow of high-paraffin bituminous binder in cylindrical tube in terms of Herschel – Bulkley fluid. *Journal of Construction and Architecture*. 2021. Vol. 23. N 4, p. 79-99 (in Russian). DOI: [10.31675/1607-1859-2021-23-4-79-99](https://doi.org/10.31675/1607-1859-2021-23-4-79-99)
31. Ilinov M.D., Petrov D.N., Kolontsevsky E.V., Straupnik I.A. Usability of acrylates in damp proofing in deep-level salt mining. *Gornyi zhurnal*. 2023. N 8, p. 77-87 (in Russian). DOI: [10.17580/gzh.2023.08.10](https://doi.org/10.17580/gzh.2023.08.10)
32. Seiphoori A., Gunn A., Kosgodagan Acharige S. et al. Tuning Sedimentation Through Surface Charge and Particle Shape. *Geophysical Research Letters*. 2021. Vol. 48. Iss. 7. N e2020GL091251. DOI: [10.1029/2020GL091251](https://doi.org/10.1029/2020GL091251)
33. Vasilyeva M.A., Volchikhina A.A., Morozov M.D. Re-backfill technology and equipment. *Mining Informational and Analytical Bulletin*. 2021. N 6, p. 133-144 (in Russian). DOI: [10.25018/0236_1493_2021_6_0_133](https://doi.org/10.25018/0236_1493_2021_6_0_133)
34. Lyashenko V.I., Khomenko O.E., Chekushina T.V. et al. Technologies and equipment for mining and metallurgy waste management. *Mining Informational and Analytical Bulletin*. 2021. N 12, p. 132-148 (in Russian). DOI: [10.25018/0236_1493_2021_12_0_132](https://doi.org/10.25018/0236_1493_2021_12_0_132)
35. Aleksandrova T., Nikolaeva N., Afanasova A. et al. Justification for Criteria for Evaluating Activation and Destruction Processes of Complex Ores. *Minerals*. 2023. Vol. 13. Iss. 5. N 684. DOI: [10.3390/min13050684](https://doi.org/10.3390/min13050684)
36. Kibirev V.I., Bauman A.V., Nikitin A.E. On the creation of modern Russian thickeners. *Gornaya promyshlennost*. 2017. N 5 (135), p. 32-34.
37. Bauman A.V. Upon modernization of domestically produced radial thickeners. *Obogashchenie rud*. 2013. N 1, p. 44-49 (in Russian).
38. El Moutea O., El Amri H., El Akkad A. Finite Element Method for the Stokes–Darcy Problem with a New Boundary Condition. *Numerical Analysis and Applications*. 2020. Vol. 13. N 2, p. 136-151. DOI: [10.1134/S1995423920020056](https://doi.org/10.1134/S1995423920020056)
39. Scutaru M.L., Guendaoui S., Koubaiti O. et al. Flow of Newtonian Incompressible Fluids in Square Media: Isogeometric vs. Standard Finite Element Method. *Mathematics*. 2023. Vol. 11. Iss. 17. N 3702. DOI: [10.3390/math11173702](https://doi.org/10.3390/math11173702)
40. Togun H., Homod R., Sadeghinezhad E., Kazi S.N. Navier-Stokes Equations and High-Resolutions: Advancements in Accurate Incompressible Flow Simulations. *Knowledge-Based Engineering and Sciences*. 2023. Vol. 4. N 2, p. 51-59. DOI: [10.51526/kbes.2023.4.2.51-59](https://doi.org/10.51526/kbes.2023.4.2.51-59)
41. Vasilyeva M.A., Vöth S. Multiphysical Model of Heterogeneous Flow Moving Along a Channel of Variable Cross-section. *Journal of Mining Institute*. 2017. Vol. 227, p. 558-562. DOI: [10.25515/PMI.2017.5.558](https://doi.org/10.25515/PMI.2017.5.558)
42. Adameczyk W.P., Klimanek A., Bialecki R. et al. Comparison of the standard Euler – Euler and hybrid Euler – Lagrange approaches for modeling particle transport in a pilot-scale circulating fluidized bed. *Particuology*. 2014. Vol. 15, p. 129-137. DOI: [10.1016/J.PARTIC.2013.06.008](https://doi.org/10.1016/J.PARTIC.2013.06.008)
43. Esgandari B., Rauchenzauner S., Goniva C. et al. A comprehensive comparison of Two-Fluid Model, Discrete Element Method and experiments for the simulation of single- and multiple-spout fluidized beds. *Chemical Engineering Science*. 2023. Vol. 267. N 118357. DOI: [10.1016/j.ces.2022.118357](https://doi.org/10.1016/j.ces.2022.118357)
44. Yongchao Li, Defu Che, Yinhe Liu. CFD simulation of hydrodynamic characteristics in a multiple-spouted bed. *Chemical Engineering Science*. 2012. Vol. 80, p. 365-379. DOI: [10.1016/J.CES.2012.06.003](https://doi.org/10.1016/J.CES.2012.06.003)
45. Careaga J., Gatica G.N. Coupled mixed finite element and finite volume methods for a solid velocity-based model of multidimensional sedimentation. *ESAIM: Mathematical Modelling and Numerical Analysis*. 2023. Vol. 57. N 4, p. 2529-2556. DOI: [10.1051/m2an/2023057](https://doi.org/10.1051/m2an/2023057)
46. Fukui T., Kawaguchi M., Morinishi K. Numerical study on the inertial effects of particles on the rheology of a suspension. *Advances in Mechanical Engineering*. 2019. Vol. 11. Iss. 4, p. 10. DOI: [10.1177/1687814019847000](https://doi.org/10.1177/1687814019847000)
47. Tak Shing Lo, Koplik J. Channeling and stress during fluid and suspension flow in self-affine fractures. *Physical Review E*. 2014. Vol. 89. Iss. 2. N 023010. DOI: [10.1103/PhysRevE.89.023010](https://doi.org/10.1103/PhysRevE.89.023010)
48. Voulgaropoulos V., Jamshidi R., Mazzei L., Angeli P. Experimental and numerical studies on the flow characteristics and separation properties of dispersed liquid-liquid flows. *Physics of Fluids*. 2019. Vol. 31. Iss. 7. N 073304. DOI: [10.1063/1.5092720](https://doi.org/10.1063/1.5092720)
49. Wenwei Liu, Chuan-Yu Wu. Analysis of inertial migration of neutrally buoyant particle suspensions in a planar Poiseuille flow with a coupled lattice Boltzmann method-discrete element method. *Physics of Fluids*. 2019. Vol. 31. Iss. 6. N 063301. DOI: [10.1063/1.5095758](https://doi.org/10.1063/1.5095758)
50. Ce Xu. Some Evaluation of Infinite Series Involving Trigonometric and Hyperbolic Functions. *Results in Mathematics*. 2018. Vol. 73. Iss. 4. N 128. DOI: [10.1007/s00025-018-0891-9](https://doi.org/10.1007/s00025-018-0891-9)

Authors: Aleksandra A. Volchikhina, Postgraduate Student, <https://orcid.org/0000-0001-7142-1935> (Empress Catherine II Saint Petersburg Mining University, Saint Petersburg, Russia), Mariya A. Vasilyeva, Candidate of Engineering Sciences, Associate Professor, Vasilyeva_MA@pers.spmi.ru, <https://orcid.org/0000-0003-2594-748X> (Empress Catherine II Saint Petersburg Mining University, Saint Petersburg, Russia).

The authors declare no conflict of interests.



Behaviour of cerium (III) phosphate in a carbonate-alkaline medium

Tatyana E. Litvinova, Stepan A. Gerasev✉

Empress Catherine II Saint Petersburg Mining University, Saint Petersburg, Russia

How to cite this article: Litvinova T.E., Gerasev S.A. Behaviour of cerium (III) phosphate in a carbonate-alkaline medium. *Journal of Mining Institute*. 2024. Vol. 271. N 16416, p. 181-188.

Abstract

The article investigates the behaviour of rare earth metals in carbonate-alkaline systems. The results of experimental studies on rare earth element extraction from phosphogypsum, a large-tonnage industrial waste forming in production of phosphoric acid are presented. Using the liquid phase leaching method, it was possible to extract more than 53 % of rare earth elements from old phosphogypsum and more than 69 % from fresh phosphogypsum due to solid phase treatment with a 4 mol/l potassium carbonate solution at temperature 90 °C. The behaviour of model cerium (III) phosphate in a carbonate-alkaline medium is characterized: a solubility isotherm is obtained as well as the dependences of the degree of cerium extraction into solution on temperature, carbonate ion concentration, interphase ratio, stirring intensity, and pH. The ability of soluble rare earth element complexes to precipitate over time was established, which was confirmed using cerium and neodymium as an example. Within 240 h after the end of the experiment, approximately 25 % of cerium and 17 % of neodymium were precipitated from the liquid phase. A similar property was recorded in representatives of the light group and was not noted in elements of the heavy group. The ability to self-precipitate in future can serve as a basis for developing an alternative approach to separating rare earth metals into groups after extraction in a carbonate ion medium. Also, based on the analysis of experimental data, the mechanism of cerium (III) phosphate dissolution in a carbonate-alkaline medium was characterized. An assumption was made that rare earth metal phosphates dissolve sequentially passing into an insoluble carbonate and then into a soluble carbonate complex.

Keywords

rare earth metals; lanthanoids; cerium; carbonate leaching; phosphogypsum; complexation; precipitation

Received: 22.03.2024

Accepted: 24.09.2024

Online: 18.11.2024

Published: 25.02.2025

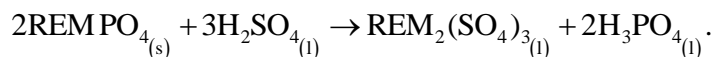
Introduction

Rare earth metals (REM) are a group consisting of 15 lanthanoids, scandium and yttrium [1, 2]. These metals are widely used in catalysis, defence industry, manufacturing of magnets, batteries, superconductors, etc. [3-5]. REM are strategic metals, and a promising trend for their production is processing of REM-containing technogenic raw materials [6, 7].

Natural apatite is used as a raw material for producing phosphoric acid and phosphorus fertilizers, however, during its beneficiation and processing, the waste forms: refinement tailings and phosphogypsum (PG) [8, 9]. REM found in apatite pass into target products and waste as impurities, with 20-30 % of REM migrating into refinement tailings, 10-15 % into H_3PO_4 and 60-70 % into phosphogypsum [10-12]. Thus, PG is a by-product of phosphoric acid production technology and contains approximately 0.5-0.6 % REM (mainly light ones). Considering that more than 6 billion tons of such waste accumulated in the world, it can be regarded as an accessible source of REM [13]. It is noteworthy that the predominant REM phases in GF are monazite (PO_4^{3-}) and gypsum (SO_4^{2-}) containing rare earth elements in the oxidation state +3 [14]. Among the possible phases, phosphate form of REM is less soluble and less extractable than the other ones; therefore, in order to develop the REM extraction technology, it is necessary to proceed from its properties [15].

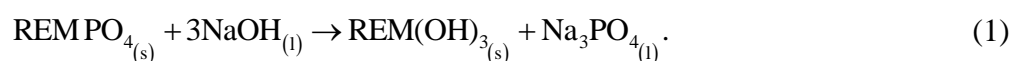


A method of acid leaching of rare earth elements from phosphogypsum is known [16]. Most recent studies focus on their extraction by treatment with citric or sulfuric acids. This approach allows achieving a high extraction degree (over 90 %), but requires the use of autoclaves, since the process occurs at elevated temperatures (at least 250 °C) and reagent concentrations (2 mol/l H₂SO₄) [17, 18]. In case of using sulfuric acid for leaching REM, the reaction equation has the following form:



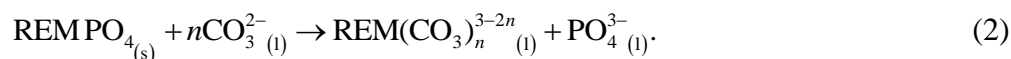
Among the disadvantages of this method are its non-environmentally friendly nature (the impact of acid solutions on the environment) and the impossibility to extract calcium as the main component of phosphogypsum (conversion of calcium into a valuable product is excluded) [19, 20].

Another method for extracting REM involves treating phosphates of rare earth elements (III) with alkali [21, 22]:



It is proposed to use sodium hydroxide solution with concentration 50-70 % at temperature 150 °C [16]. Reaction (1) is accompanied by formation of solid REM (III) hydroxide which is unstable and can transform into REM oxide (especially typical for cerium) [23]. Thus, the separation of solid mixture of products is a task for solving which the additional technological operations are required [24].

The behaviour of lanthanoids in REM (III) – CO₃²⁻ – H₂O system was investigated [25, 26]. Based on the analysis of published data, carbonate ions can act as a ligand and form soluble complex compounds [27]:

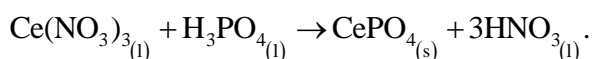


The mechanism of reaction (2) is poorly understood. Although n can take values from 1 to 4, carbonate complexes with $n = 1; 2$ are considered to be more stable [28, 29]. Moreover, due to the hydrolysis process, the forming OH⁻ and HCO₃⁻ can also be ligands. Approach (2) seems to be most suitable for processing phosphogypsum, since gypsum (CaSO₄·nH₂O) at temperature 50-90 °C for 4-6 h also reacts with carbonate ion to form valuable calcium carbonate [30-32].

Thus, the aim of this study is an attempt to characterize the dissolution mechanism of REE (III) phosphates in a carbonate-alkaline medium using cerium as the most widespread REM in GF and to propose further separation of rare earth elements from carbonate complexes.

Methods

Synthetic cerium (III) phosphate, which was previously obtained by mixing the solutions of cerium nitrate (0.2 mol/l), and phosphoric acid (0.2 mol/l): was used as the starting material containing REM:



Cerium (III) phosphate precipitation was carried out at stirring for 30 min with priming. After washing and drying, the average particle size of the precipitate was determined using “Microsizer 201” analyser: from 30 to 60 μm. Phosphates of other rare earth elements were obtained by a similar procedure.

In addition to synthetic lanthanoid precipitates, samples of fresh and old phosphogypsum from the Kingisepp dumps (Russian Federation) were used for the studies. Fresh phosphogypsum was obtained directly from production, and old phosphogypsum was stored at the landfill for at least one



year. According to mass spectrometric analysis, the following REM were found in the samples: Ce, Dy, Er, La, Nd, Pr, and Y. The results of analysis are presented in Table 1.

Table 1

Results of mass spectrometric analysis of phosphogypsum samples, wt. %

PG	SO ₃	CaO	P ₂ O ₅	K ₂ O	REM ₂ O ₃	Na ₂ O	SrO	Fe ₂ O ₃	Al ₂ O ₃	MgO	BaO
Old	54.84	41.39	1.73	0.77	0.32	0.28	0.22	0.19	0.18	0.02	0.01
Fresh	54.40	41.01	2.49	0.80	0.33	0.38	0.20	0.19	0.10	0.07	0.01

All experimental studies presented in the article were conducted using potassium carbonate as a leaching agent.

The solubility of cerium (III) phosphate in carbonate-alkaline systems was studied at temperature 25-90 °C, potassium carbonate concentration 1-4.5 mol/l, interphase ratio 10-3,000 ml/g, and stirring intensity 50-1,200 rpm. Thus, the solubility isotherm of cerium (III) phosphate at 90 °C was experimentally obtained as well as the dependences of the extraction degree into solution on time at different concentrations of carbonate ion, temperatures, L:S ratios, and stirring intensity. Each experiment was performed in the HEL Automate Reactor System at least twice. REM content in solutions was determined by trilonometric titration in the presence of arsenazo (III) indicator. The degree of REM extraction into solution was calculated from the formula

$$E(\text{REM}) = \frac{C(\text{TB})V(\text{TB})V(L)M(\text{REMPO}_4)}{m(\text{REMPO}_4)V(A)} \cdot 100\%,$$

where $C(\text{TB})$ is concentration of Trilon B, M; $V(\text{TB})$, volume of Trilon B, ml; $V(L)$, volume of liquid phase after the experiment, l; $M(\text{REMPO}_4)$, molar mass of REM phosphate, g/mol; $m(\text{REMPO}_4)$, mass of REM phosphate sample weight, g; $V(A)$, volume of aliquot, ml.

Secondary precipitate forming in the course of experiment at interphase ratio 100 ml/g was sent for Raman scattering spectroscopy (Raman spectra) for identification after filtration, washing and drying.

Based on the results presented in Table 1, both PG samples contain 0.3 wt.% REM (in terms of oxides), therefore, the experiments were also performed on concomitant extraction of REM into solution during calcium sulfate conversion. Based on the properties of model REM precipitates, leaching should be carried out at temperature 90 °C, L:S ratio 2,000 ml/g, stirring rate 650 rpm, and potassium carbonate concentration 4 mol/l for three hours. Upon completion of leaching, the solid phase was separated from the solution and, after washing and drying, was sent for mass spectrometric analysis.

Discussion of results

Solubility isotherm of cerium (III) phosphate (Fig.1) was obtained at 90 °C, L:S = 2,100 ml/g, and 650 rpm and is presented as a functional dependence of the extraction degree on the potassium carbonate concentration. Investigations were carried out in a wide range of potassium carbonate concentrations. It was found that in the range 1-2.5 mol/l the solution acquired a yellow colour, and at concentration above 3 mol/l – an orange colour. This fact can indicate a change in the shape of the complex ion from CeCO_3^+ to $\text{Ce}(\text{CO}_3)_2^-$, which is theoretically possible.

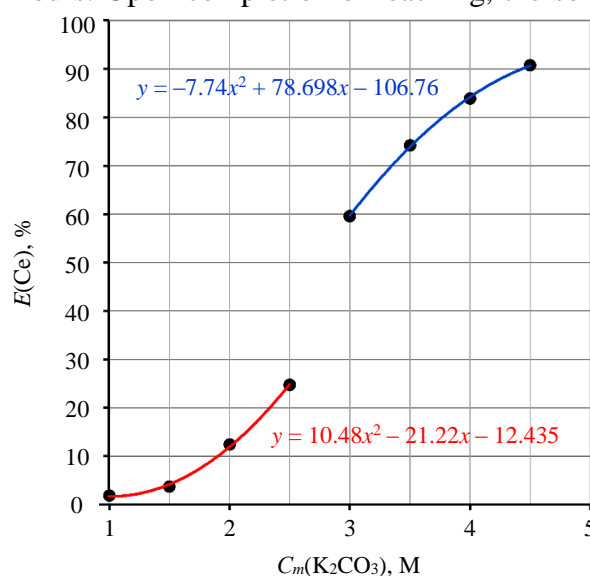


Fig.1. Cerium (III) phosphate solubility isotherm



The obtained isotherm is, probably, characterized by the presence of three intervals: the first one is 1-2.5 mol/l; the second one, 2.5-3 mol/l; and the third one, 3-4.5 mol/l. The first and the third intervals are described in Table 2.

Table 2

Characteristic of cerium (III) phosphate solubility isotherm

$C(K_2CO_3)$, mol/l	Ionic strength, mol/kg	E , %	Equation	Possible soluble form
1.0-2.5	3.0-7.5	1.9-24.7	$y = 10.48x^2 - 21.22x + 12.435$	$CeCO_3^+(l)$
3.0-4.5	9.0-13.5	59.6-90.8	$y = -7.74x^2 + 78.698x - 106.76$	$Ce(CO_3)_2^-(l)$

Solubility of phosphates is due to complexation process occurring under the influence of carbonate ion. In case of cerium (III) phosphate, the interphase ratio (Fig.2) and the concentration of carbonate ion (Fig.3) are the factors that have a significant effect on the dissolution process.

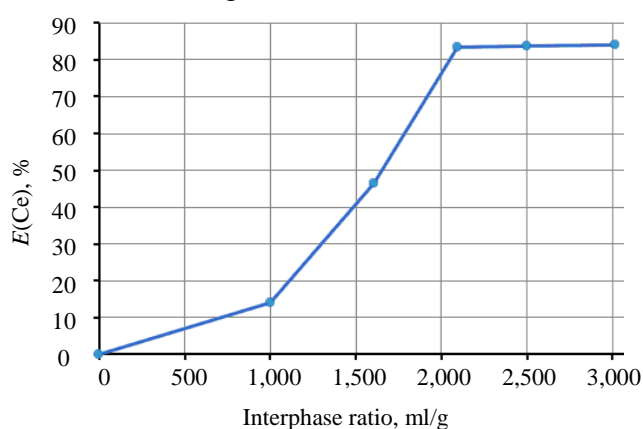


Fig.2. Effect of interphase ratio on the degree of cerium extraction into solution

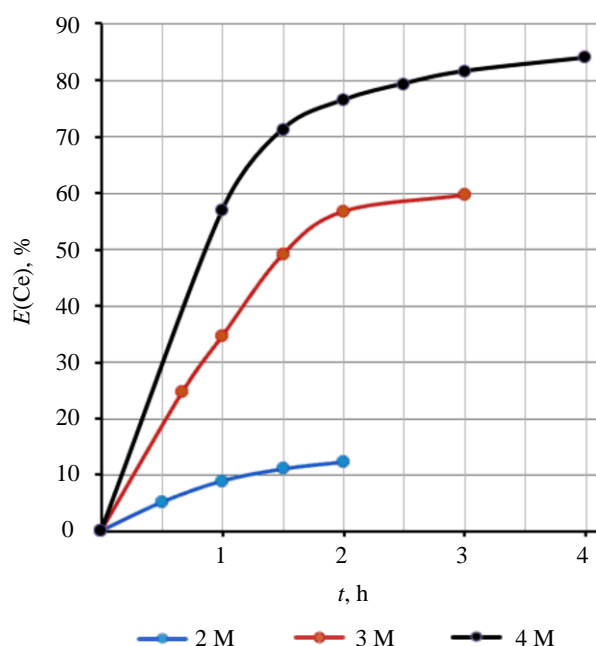
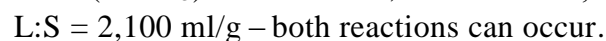
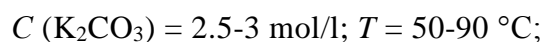
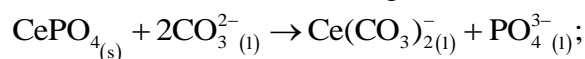
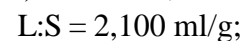
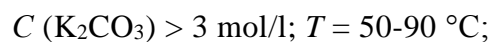
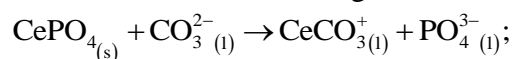
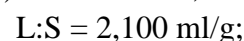
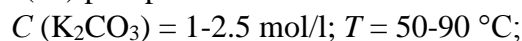


Fig.3. Dependence of degree of cerium extraction into solution on stirring time at different concentrations of carbonate ion

According to the solubility isotherm, the maximum degree of cerium extraction at temperature 90 °C corresponds to potassium carbonate concentration 4.5 M and is 90.8 %. Thus, the following resulting reactions are possible for cerium (III) phosphate:



The effect of L:S ratio was investigated at 90 °C and potassium carbonate concentration 4 M at stirring for two hours. According to the data obtained, it affects the degree of extraction, so that a significant excess of potassium carbonate solution is necessary to increase the solubility.

An increase in carbonate ion concentration naturally leads to an increasing degree of cerium extraction. A long time is required to achieve the state close to equilibrium, which can point to a possible diffusion limitations (caused, in particular, by pulp viscosity). A growing extraction degree with increasing concentration indirectly indicates the formation of an anionic complex in the form of an ion pair.

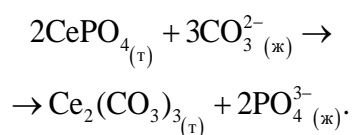


It was ascertained that temperature also affects the dissolution process. Figure 4 shows three kinetic curves obtained in the temperature range 50-90 °C at initial potassium carbonate concentration equal to 2 M. It was experimentally determined that at least 4 h of stirring are required to achieve the equilibrium state, and the dependencies have a similar appearance. With growing temperature, the extraction degree and the rate of the process increase from 50 to 90 °C, as indicated by a decrease in time required for attaining the equilibrium state.

The effect of stirring rate on solubility was investigated under the following conditions: 90 °C; 4 M K_2CO_3 ; L:S = 2,100 ml/g; $t = 1$ h. From the dependence in Fig.5 it follows that stirring significantly affects solubility to a value 650 rpm. Consequently, the process of cerium (III) phosphate dissolution is limited by diffusion.

Solid phase was analysed by Raman scattering spectroscopy (Fig.6) to determine the nature of precipitate and its components after treatment with potassium carbonate solution. The experiment was conducted for three hours with 4 M K_2CO_3 solution at temperature 90 °C, stirring rate 650 rpm, and L:S ratio 100 ml/g. After leaching, the precipitate was repeatedly washed to remove potassium carbonate. The analysis results were interpreted using the RRUFF database and publications [33, 34].

Spectral peaks of phosphate and carbonate anions are particularly prominent among the others indicating a possibility of cerium (III) carbonate formation as a secondary precipitate. It can be presumed that conversion of cerium phosphate to carbonate is the first stage of the overall dissolution process:



The results of investigating the kinetics of REM (III) carbonates dissolution process in carbonate-alkaline systems were presented

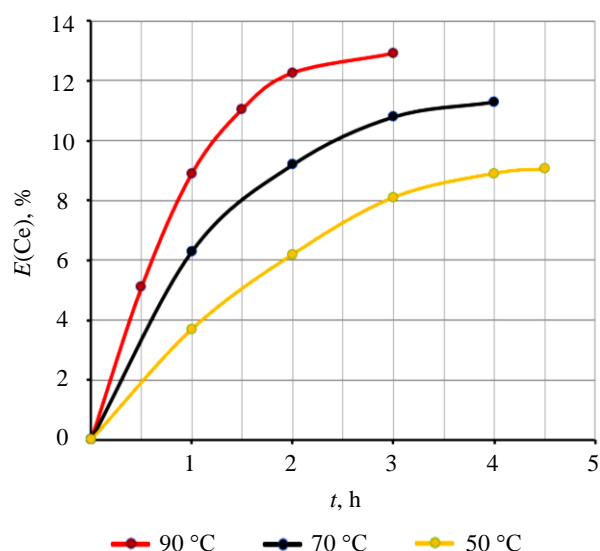


Fig.4. Temperature effect on degree of cerium extraction into solution

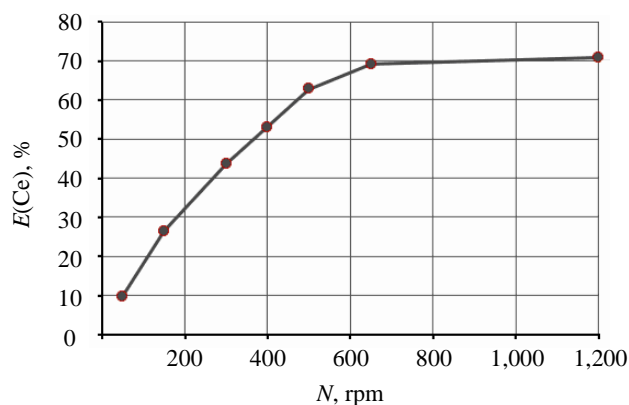


Fig.5. Effect of stirring rate on degree of cerium extraction into solution

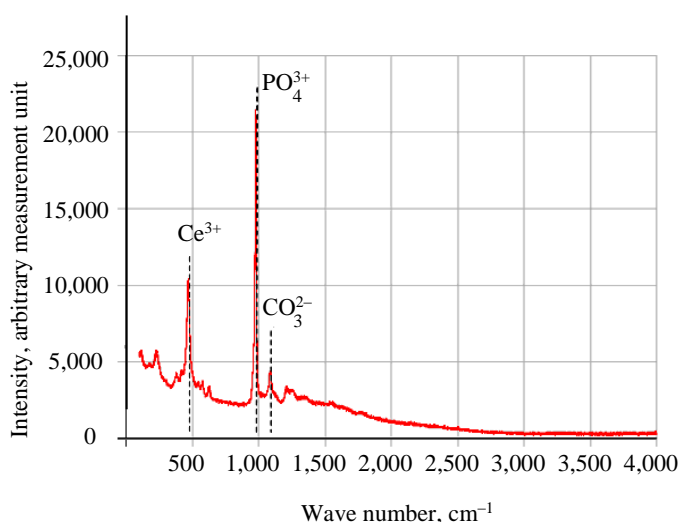


Fig.6. Raman scattering spectroscopy of secondary cerium precipitate

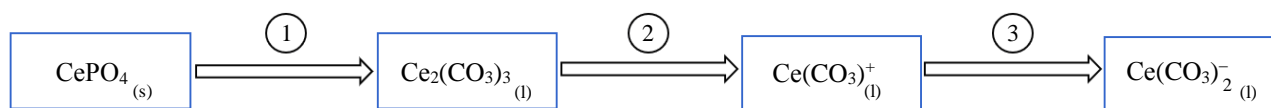


Fig.7. Possible dissolution mechanism of cerium (III) phosphate

in [35]. It is noteworthy that dissolution of carbonates occurs faster than dissolution of phosphates. Therefore, it can be presumed that the process of phosphate reprecipitation is the longest stage. The mechanism of REM phosphates dissolution can be described by three successive stages – reprecipitation and two stages of complexation (Fig.7).

Another factor affecting the degree of cerium extraction into solution is pH level. The effect is similar to that described in article [36]: addition of both acid and alkali to a mixture of cerium (III) phosphate and potassium carbonate solution in both cases leads to a decreasing solubility. Probably, along with carbonate anion, hydroxide anion and bicarbonate anion act as ligands which form less stable complexes. Considering the ability of REM (III) phosphates to transform into REM (III) carbonates a combined addition of OH^- and CO_3^{2-} can cause formation of REM (III) hydroxycarbonates. Thus, to achieve high solubility values, only the addition of carbonate solution without additional reagents is required.

It was found that some solutions containing REM carbonate complexes become turbid over time and form a precipitate. Similar behaviour was recorded for some representatives of light REM, while heavy REM complexes did not form a precipitate. Thus, self-precipitation of REM from lye can be used as a method for further separation of a mixture of rare earth elements into individual components or groups. Among rare earth elements, cerium can be characterized as more capable of self-precipitation of metal from carbonate complexes: 24.7 % of its complexes were destroyed after 240 hours of settling, while in the case of neodymium only 17.1 % precipitated.

Carbonate leaching method was used in processing technogenic waste, in particular phosphogypsum. The investigations indicate a possibility of extracting rare earth metals from PG into solution. The degree of REM extraction from samples of old and fresh phosphogypsum differs. As a result of experiments conducted for three hours at temperature 90 °C and potassium carbonate solution concentration 4 M, it was possible to extract 53.6 % REM from samples of old PG and 69.6 % REM from fresh PG. Difference in extraction degree is caused by differences in morphology of PG powders, as indicated by their difference in colour (a sample of old PG is dark grey, a sample of fresh PG is light grey). Such a difference can be caused by phase changes while in the dump.

Conclusion

A presumptive mechanism of cerium phosphate dissolution in a carbonate-alkaline medium (as one of the most common representatives of REM in phosphogypsum) was determined. Cerium (III) phosphate is successively converted into cerium (III) carbonate and then passes into a soluble carbonate complex. It was ascertained that the degree of REM extraction is affected by many factors: temperature, carbonate ion concentration, L:S ratio, stirring rate, and pH level. Parameters at which the maximum solubility of synthetic cerium phosphate is experimentally achieved were established for the conversion of technogenic phosphogypsum samples.

Thus, the method of carbonate-alkaline conversion can be used for processing phosphogypsum, resulting in formation of calcium carbonate, potassium sulphate, and carbonate complexes of rare earth metals. This approach is complex, unlike the previously developed acid methods, since it is simultaneously possible to extract a significant amount of REM into solution: it was possible to extract 53.6-69.6 % of total REM from different phosphogypsum samples.

A promising trend for further research is separation of rare earth elements in carbonate-alkaline systems, which is technically possible, since some lanthanoids can self-precipitate, in particular, representatives of the light REM group.



REFERENCES

1. Tominc S., Ducman V., Wisniewski W. et al. Recovery of Phosphorus and Metals from the Ash of Sewage Sludge, Municipal Solid Waste, or Wood Biomass: A Review and Proposals for Further Use. *Materials*. 2023. Vol. 16. Iss. 21. N 6948. DOI: [10.3390/ma16216948](https://doi.org/10.3390/ma16216948)
2. Saidakhmetov P., Piyanzina I., Faskhutdinova A. et al. Ab Initio Magnetic Properties Simulation of Nanoparticles Based on Rare Earth Trifluorides RE_3 ($RE = Tb, Dy, Ho$). *Crystals*. 2023. Vol. 13. Iss. 10. N 1487. DOI: [10.3390/cryst13101487](https://doi.org/10.3390/cryst13101487)
3. Ormerod J., Karati A., Baghel A.P.S. et al. Sourcing, Refining and Recycling of Rare-Earth Magnets. *Sustainability*. 2023. Vol. 15. Iss. 20. N 14901. DOI: [10.3390/su152014901](https://doi.org/10.3390/su152014901)
4. Pathapati S.V.S.H., Free M.L., Sarswat P.K. A Comparative Study on Recent Developments for Individual Rare Earth Elements Separation. *Processes*. 2023. Vol. 11. Iss. 7. N 2070. DOI: [10.3390/pr11072070](https://doi.org/10.3390/pr11072070)
5. Yunping Ji, Ming-Xing Zhang, Huiping Ren. Roles of Lanthanum and Cerium in Grain Refinement of Steels during Solidification. *Metals*. 2018. Vol. 8. Iss. 11. N 884. DOI: [10.3390/met8110884](https://doi.org/10.3390/met8110884)
6. Dzhevaga N., Lobacheva O. Reduction in Technogenic Burden on the Environment by Flotation Recovery of Rare Earth Elements from Diluted Industrial Solutions. *Applied Sciences*. 2021. Vol. 11. Iss. 16. N 7452. DOI: [10.3390/app11167452](https://doi.org/10.3390/app11167452)
7. Petrova T.A., Rudzisha E., Alekseenko A.V. et al. Rehabilitation of Disturbed Lands with Industrial Wastewater Sludge. *Minerals*. 2022. Vol. 12. Iss. 3. N 376. DOI: [10.3390/min12030376](https://doi.org/10.3390/min12030376)
8. Chernysh Y., Yakhnenko O., Chubur V., Roubik H. Phosphogypsum Recycling: A Review of Environmental Issues, Current Trends, and Prospects. *Applied Sciences*. 2021. Vol. 11. Iss. 4. N 1575. DOI: [10.3390/app11041575](https://doi.org/10.3390/app11041575)
9. Mukaba J.-L., Eze C.P., Pereao O., Petrik L.F. Rare Earths' Recovery from Phosphogypsum: An Overview on Direct and Indirect Leaching Techniques. *Minerals*. 2021. Vol. 11. Iss. 10. N 1051. DOI: [10.3390/min11101051](https://doi.org/10.3390/min11101051)
10. Xiaosheng Yang, Makkonen H.T., Pakkanen L. Rare Earth Occurrences in Streams of Processing a Phosphate Ore. *Minerals*. 2019. Vol. 9. Iss. 5. N 262. DOI: [10.3390/min9050262](https://doi.org/10.3390/min9050262)
11. Cheremisina O., Ponomareva M., Sergeev V. et al. Extraction of Rare Earth Metals by Solid-Phase Extractants from Phosphoric Acid Solution. *Metals*. 2021. Vol. 11. Iss. 6. N 991. DOI: [10.3390/met11060991](https://doi.org/10.3390/met11060991)
12. Mitrofanova G.V., Chernousenko E.V., Kompanchenko A.A., Kalugin A.I. Specific action of collector from phosphoric acid alkyl esters class in flotation of apatite-nepheline ores. *Journal of Mining Institute*. 2024. Vol. 268, p. 637-645.
13. Bin Xu, Aodong Gao, Zhouxiang Chen et al. Mechanical Properties and Optimal Mix Design of Phosphogypsum Cement Mineral Admixture Foam Light Soil. *Coatings*. 2023. Vol. 13. Iss. 11. N 1861. DOI: [10.3390/coatings13111861](https://doi.org/10.3390/coatings13111861)
14. Kaczorowska M.A. The Latest Achievements of Liquid Membranes for Rare Earth Elements Recovery from Aqueous Solutions – A Mini Review. *Membranes*. 2023. Vol. 13. Iss. 10. N 839. DOI: [10.3390/membranes13100839](https://doi.org/10.3390/membranes13100839)
15. Lobacheva O.L. Ion Flotation of Ytterbium Water-Salt Systems – An Innovative Aspect of the Modern Industry. *Water*. 2021. Vol. 13. Iss. 24. N 3493. DOI: [10.3390/w13243493](https://doi.org/10.3390/w13243493)
16. Brückner L., Elwert T., Schirmer T. Extraction of Rare Earth Elements from Phospho-Gypsum: Concentrate Digestion, Leaching, and Purification. *Metals*. 2020. Vol. 10. Iss. 1. N 131. DOI: [10.3390/met10010131](https://doi.org/10.3390/met10010131)
17. Lütke S.F., Oliveira M.L.S., Waechter S.R. et al. Leaching of rare earth elements from phosphogypsum. *Chemosphere*. 2022. Vol. 301. N 134661. DOI: [10.1016/j.chemosphere.2022.134661](https://doi.org/10.1016/j.chemosphere.2022.134661)
18. Virolainen S., Repo E., Sainio T. Recovering rare earth elements from phosphogypsum using a resin-in-leach process: Selection of resin, leaching agent, and eluent. *Hydrometallurgy*. 2019. Vol. 189. N 105125. DOI: [10.1016/j.hydromet.2019.105125](https://doi.org/10.1016/j.hydromet.2019.105125)
19. Sokolov I.V., Antipin Yu.G., Rozhkov A.A., Solomein Yu.M. Environmental geotechnology for low-grade ore mining with the creation of conditions for the concurrent disposal of mining waste. *Journal of Mining Institute*. 2023. Vol. 260, p. 289-296. DOI: [10.31897/PMI.2023.21](https://doi.org/10.31897/PMI.2023.21)
20. Pashkevich M.A., Alekseenko A.V., Nureev R.R. Environmental damage from the storage of sulfide ore tailings. *Journal of Mining Institute*. 2023. Vol. 260, p. 155-167. DOI: [10.31897/PMI.2023.32](https://doi.org/10.31897/PMI.2023.32)
21. Ochiai A., Utsunomiya S. Crystal Chemistry and Stability of Hydrated Rare-Earth Phosphates Formed at Room Temperature. *Minerals*. 2017. Vol. 7. Iss. 5. N 84. DOI: [10.3390/min7050084](https://doi.org/10.3390/min7050084)
22. Castro L., Blázquez M.L., González F., Muñoz J.A. Bioleaching of Phosphate Minerals Using *Aspergillus niger*: Recovery of Copper and Rare Earth Elements. *Metals*. 2020. Vol. 10. Iss. 7. N 978. DOI: [10.3390/met10070978](https://doi.org/10.3390/met10070978)
23. Srivastava S., Pandey N.K. Low-Cost Hydrothermally Synthesized Multifunctional Rare Earth Metal Yttrium Cerium Oxide. *Materials Proceedings*. 2023. Vol. 14. Iss. 1. N 26. DOI: [10.3390/IOCN2023-14542](https://doi.org/10.3390/IOCN2023-14542)
24. Lutskiy D.S., Ignatovich A.S. Study on hydrometallurgical recovery of copper and rhenium in processing of substandard copper concentrates. *Journal of Mining Institute*. 2021. Vol. 251, p. 723-729. DOI: [10.31897/PMI.2021.5.11](https://doi.org/10.31897/PMI.2021.5.11)
25. Ferri D., Grenthe I., Hietanen S. et al. Studies on Metal Carbonate Equilibria. 5. The Cerium (III) Carbonate Complexes in Aqueous Perchlorate Media. *Acta Chemica Scandinavica*. 1983. Vol. 37a, p. 359-365. DOI: [10.3891/acta.chem.scand.37a-0359](https://doi.org/10.3891/acta.chem.scand.37a-0359)
26. Yu-Ran Luo, Byrne R. Carbonate complexation of yttrium and the rare earth elements in natural waters. *Geochimica et Cosmochimica Acta*. 2004. Vol. 68. Iss. 4, p. 691-699. DOI: [10.1016/S0016-7037\(03\)00495-2](https://doi.org/10.1016/S0016-7037(03)00495-2)
27. Lee J.H., Byrne R.H. Complexation of trivalent rare earth elements (Ce, Eu, Gd, Tb, Yb) by carbonate ions. *Geochimica et Cosmochimica Acta*. 1993. Vol. 57. Iss. 2, p. 295-302. DOI: [10.1016/0016-7037\(93\)90432-V](https://doi.org/10.1016/0016-7037(93)90432-V)
28. Wood S.A. The aqueous geochemistry of the rare-earth elements and yttrium: 1. Review of available low-temperature data for inorganic complexes and the inorganic REE speciation of natural waters. *Chemical Geology*. 1990. Vol. 82, p. 159-186. DOI: [10.1016/0009-2541\(90\)90080-Q](https://doi.org/10.1016/0009-2541(90)90080-Q)
29. Pyagai I., Zubkova O., Babykin R. et al. Influence of Impurities on the Process of Obtaining Calcium Carbonate during the Processing of Phosphogypsum. *Materials*. 2022. Vol. 15. Iss. 12. N 4335. DOI: [10.3390/ma15124335](https://doi.org/10.3390/ma15124335)
30. Chan-Ung Kang, Sang-Woo Ji, Hwanju Jo. Recycling of Industrial Waste Gypsum Using Mineral Carbonation. *Sustainability*. 2022. Vol. 14. Iss. 8. N 4436. DOI: [10.3390/su14084436](https://doi.org/10.3390/su14084436)



31. Cheremisina O., Sergeev V., Ponomareva M. et al. Kinetics Study of Solvent and Solid-Phase Extraction of Rare Earth Metals with Di-2-Ethylhexylphosphoric Acid. *Metals*. 2020. Vol. 10. Iss. 5. N 687. DOI: [10.3390/met10050687](https://doi.org/10.3390/met10050687)
32. Amirshahi S., Jorjani E. Preliminary Flowsheet Development for Mixed Rare Earth Elements Production from Apatite Leaching Aqueous Solution Using Biosorption and Precipitation. *Minerals*. 2023. Vol. 13. Iss. 7. N 909. DOI: [10.3390/min13070909](https://doi.org/10.3390/min13070909)
33. Chuting Zhang, Chaoyang Chen, Zhibin Li, Andy H. Shen. Chemical Composition and Spectroscopic Characteristics of Alexandrite Effect Apatite from the Akzhailau Mountains of Kazakhstan. *Minerals*. 2023. Vol. 13. Iss. 9. N 1139. DOI: [10.3390/min13091139](https://doi.org/10.3390/min13091139)
34. Biying Lai, Bo Xu, Yi Zhao. U–Pb Dating, Gemology, and Chemical Composition of Apatite from Dara-e-Pech, Afghanistan. *Crystals*. 2024. Vol. 14. Iss. 1. N 34. DOI: [10.3390/cryst14010034](https://doi.org/10.3390/cryst14010034)
35. Litvinova T., Kashurin R., Zhadovskiy I., Gerasev S. The Kinetic Aspects of the Dissolution of Slightly Soluble Lanthanoid Carbonates. *Metals*. 2021. Vol. 11. N 1793. DOI: [10.3390/met11111793](https://doi.org/10.3390/met11111793)
36. Lee J.H., Byrne R.H. Examination of comparative rare earth element complexation behavior using linear free-energy relationships. *Geochimica et Cosmochimica Acta*. 1992. Vol. 56. Iss. 3, p. 1127-1137. DOI: [10.1016/0016-7037\(92\)90050-S](https://doi.org/10.1016/0016-7037(92)90050-S)

Authors: **Tatyana E. Litvinova**, Doctor of Engineering Sciences, Professor, <https://orcid.org/0000-0002-0133-3400> (Empress Catherine II Saint Petersburg Mining University, Saint Petersburg, Russia), **Stepan A. Gerasev**, Postgraduate Student, gerasev111@mail.ru, <https://orcid.org/0000-0003-0612-7283> (Empress Catherine II Saint Petersburg Mining University, Saint Petersburg, Russia).

The authors declare no conflict of interests.